ACTUAL PROBLEMS OF MICROWORLD PHYSICS

Proceedings of XII International School-Seminar

Gomel, Belarus, July 22 – August 2, 2013

Joint Institute for Nuclear Research, Dubna

National Center for Particle and High Energy Physics
of the Belarussian State University, Minsk, Belarus

B. Stepanov Institute of Physics of the National Academy
of Sciences of Belarus, Minsk, Belarus

Gomel Branch of the National Academy of Sciences of Belarus,
Gomel, Belarus

F. Skorina Gomel State University, Gomel, Belarus

P. Sukhoi Gomel State Technical University, Gomel, Belarus

Volume 1

Dubna 2015

УДК 539.12(063)
ББК 22.382я431

The contributions are reproduced directly from the originals presented by the Organizing Committee.

ISBN 978-5-9530-0413-8

Contents

Volume 1

Volume 2

1 Accelerator Physics

ATLAS Physics Results

Vasiliki A. Mitsou*
Instituto de Física Corpuscular (IFIC), CSIC – Universitat de València,
Parc Científic de la U.V., C/ Catedrático José Beltrán 2,
E-46980 Paterna (Valencia), Spain

Abstract

The ATLAS experiment at the Large Hadron Collider at CERN has been successfully taking data since the end of 2009 in proton-proton collisions at centre-of-mass energies of 7 and 8 TeV, and in heavy ion collisions. In these lectures, some of the most recent ATLAS results will be given on Standard Model measurements, the discovery of the Higgs boson, searches for supersymmetry and exotics and on heavy-ion results.

1 Introduction

Particle Physics aims at explaining the known content and forces of the Universe at a fundamental level. This knowledge is summarised in the Standard Model (SM) [1]: It includes 12 elementary matter particles, whereas their interactions are induced by requiring local gauge invariance.

The Standard Model provides an excellent description of collider experimental data so far. LEP, SLC, Tevatron, B-factories and LHC data show that SM describes physics at energies up to $\sqrt{s} \sim 200$ GeV with respect to QCD and hadronic structure, precision EW physics, top quark properties and flavour physics. Despite its success, the SM suffers from a number of shortcomings: How we solve the hierarchy problem in the electroweak symmetry breaking (Higgs mechanism)? How are the neutrino masses generated? Are the neutrinos Dirac or Majorana particles? New

*E-mail: vasiliki.mitsou@ific.uv.es

sources for CP violation are needed in the SM to explain the observed matter – antimatter baryon asymmetry. Gravitation is the only known force not included in the SM. The strong and electroweak interactions are not unified to a single coupling (grand unification). What is the nature of the dark matter and dark energy components of the Universe?

The Large Hadron Collider (LHC) [2] at CERN is designed, constructed and operated precisely in order to address these open issues of the Standard Model. In particular, the ATLAS experiment [3] has been successfully taking data since the end of 2009 till the first months of 2013 in proton-proton collisions at centre-of-mass energies of 7 and 8 TeV, and in heavy ion collisions. An overview of the physics results obtained so far is given here.

The ATLAS detector [3] consists of an inner tracking system (inner detector, or ID) surrounded by a superconducting solenoid providing a 2 T magnetic field, electromagnetic and hadronic calorimeters, and a muon spectrometer (MS) incorporating three large superconducting toroid magnets arranged with an eight-fold azimuthal coil symmetry around the calorimeters. The ID [4] consists of silicon pixel [5] and microstrip [6] detectors, surrounded by a transition radiation tracker [7]. The electromagnetic calorimeter is a lead/liquid-argon (LAr) detector [8]. Hadron calorimetry is based on two different detector technologies, with scintillator tiles or LAr as active media, and with either steel, copper, or tungsten as the absorber material [8, 9]. The MS comprises three layers of chambers for the trigger and for track measurements [10].

The structure of this paper is as follows. Section 2 provides an overview of the SM measurements carried out with ATLAS. Sections 3 and 4 highlight recent results on top quark and flavour physics, respectively. In Section 5, the runs and latest observations with heavy-ion collisions are discussed. The Higgs boson discovery and its studied properties are given in Section 6. In Sections 7 and 8, the latest results in searches for supersymmetry and for other beyond-the-SM (BSM) scenarios, respectively, are presented. The paper concludes with a summary and an outlook in Section 9.

2 Standard Model measurements

The measurement of the high-mass Drell-Yan differential cross section in proton-proton collisions at a centre-of-mass energy of 7 TeV at the LHC

is reported in Ref. [11]. Based on an integrated luminosity of 4.9 fb^{-1}, the differential cross-section in the $Z \to e^+e^-$ channel is measured with the ATLAS detector as a function of the invariant mass, m_{ee}, in the range $116 < m_{ee} < 1500$ GeV, for a fiducial region in which both the electron and the positron have transverse momentum $p_{\mathrm{T}} > 25$ GeV and pseudorapidity $|\eta| < 2.5$. A comparison is made to various event generators and to the predictions of perturbative QCD calculations at next-to-next-to-leading order.

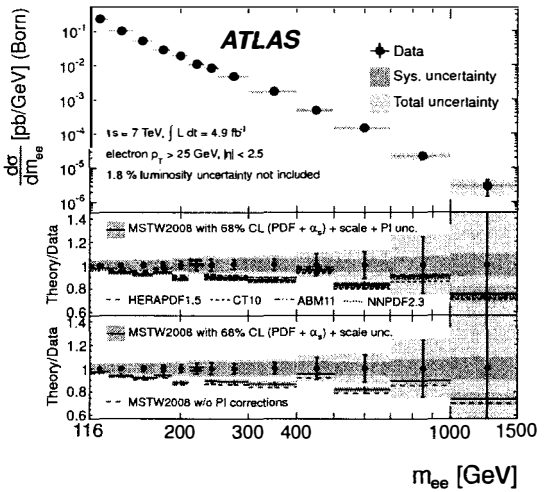

Figure 1: The measured differential cross section at the Born level within the fiducial region with statistical, systematic, and combined statistical and systematic (total) uncertainties. From Ref. [11].

The measured differential cross section at the Born level within the fiducial region (electron $p_{\mathrm{T}} > 25$ GeV and $|\eta| < 2.5$) with statistical, systematic, and combined statistical and systematic (total) uncertainties, excluding the 1.8% uncertainty on the luminosity is shown in Fig. 1. The measurement is compared to FEWZ 3.1 calculations at NNLO QCD with NLO electroweak corrections using the G_μ electroweak parameter scheme. The predictions include an additional small correction from single-boson production in which the final-state charged lepton radiates a real W or Z boson. In the upper ratio plot, the photon-induced corrections have

been added to the predictions obtained from the MSTW2008, HERA-PDF1.5, CT10, ABM11 and NNPDF2.3 NNLO parton distribution functions (PDFs), and for the MSTW2008 prediction the total uncertainty band arising from the PDF, α_s, renormalisation and factorisation scale, and photon-induced uncertainties is drawn. The lower ratio plot shows the influence of the photon-induced corrections on the MSTW2008 prediction, the uncertainty band including only the PDF, α_s and scale uncertainties. The comparison with event generators and PDFs show good agreement, therefore no sign of new physics is observed.

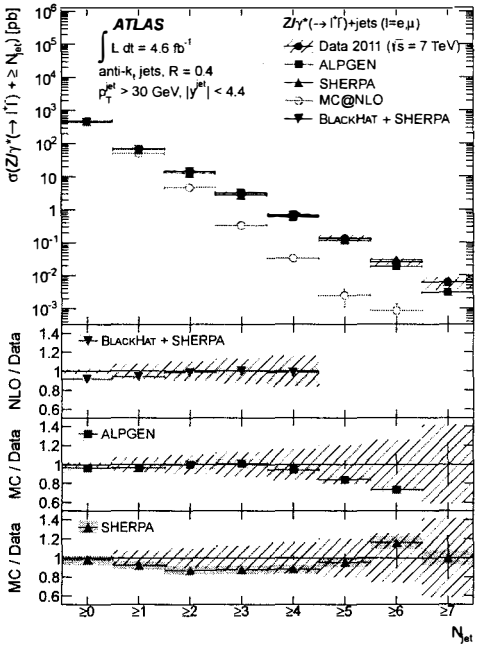

Figure 2: Measured cross section for $Z(\rightarrow \ell\ell)$+jets as a function of the inclusive jet multiplicity, N_{jet}. From Ref. [12].

Measurements of the production of jets of particles in association with a Z boson in pp collisions at $\sqrt{s} = 7$ TeV are presented in Ref. [12], using data corresponding to an integrated luminosity of 4.6 fb^{-1} collected by the ATLAS at the LHC. Inclusive and differential jet cross sections in Z events,

with Z decaying into electron or muon pairs, are measured for jets with transverse momentum $p_{\mathrm{T}} > 30$ GeV and rapidity $|\eta| < 4.4$. The results are compared to next-to-leading-order perturbative QCD calculations, and to predictions from different Monte Carlo (MC) generators based on leading-order and next-to-leading-order matrix elements supplemented by parton showers.

Measured cross section for $Z(\rightarrow \ell\ell)$+jets as a function of the inclusive jet multiplicity, N_{jet} are depicted in Fig. 2. The data are compared to NLO pQCD predictions from BH+SHERPA corrected to the particle level, and the ALPGEN, SHRPA and MCatNLO event generators (see legend for details). The error bars indicate the statistical uncertainty on the data, and the hatched (shaded) bands the statistical and systematic uncertainties on data (prediction) added in quadrature. This analysis confirms the Poisson scaling for exclusive bins in the high-p_{T} regime.

3 Top physics

The study of the top quark is important for High Energy Physics for a number of reasons. It is the heaviest fermion —near the electroweak (EW) symmetry-breaking scale—, therefore it features a large coupling to the Higgs boson. The top-quark production cross sections provide a test of QCD, since it is produced at very small distances. The top decays before hadronisation, allowing the study of spin characteristics (production mechanisms) and the W-helicity measurement (test of EW V-A structure). Its cross sections are sensitive to new physics, e.g. through the decay $t \rightarrow H^{+}b$. Besides these, it is an important background for Higgs studies and most searches for BSM scenarios.

The measurement of the top quark pair ($t\bar{t}$) inclusive production cross section in pp collisions at $\sqrt{s} = 8$ TeV is discussed in Ref. [13]. The analysis has been done in the lepton+jets final state in a dataset corresponding to an integrated luminosity of 5.8 fb^{-1}. A multivariate technique and b-jet identification were employed to separate the signal $t\bar{t}$ events from the various backgrounds. The inclusive $t\bar{t}$ production cross section is measured to be $\sigma_{t\bar{t}} = 241 \pm 2(\mathrm{stat}) \pm 31(\mathrm{syst}) \pm 9(\mathrm{lumi})$ pb and is in good agreement with the theoretical prediction $\sigma_{t\bar{t},\mathrm{th}} = 238^{+22}_{-24}$ pb. The overview of the $t\bar{t}$ cross section measurement for various centre-of-mass energies is presented in Fig. 3.

The top quark mass, on the other hand, has been measured using

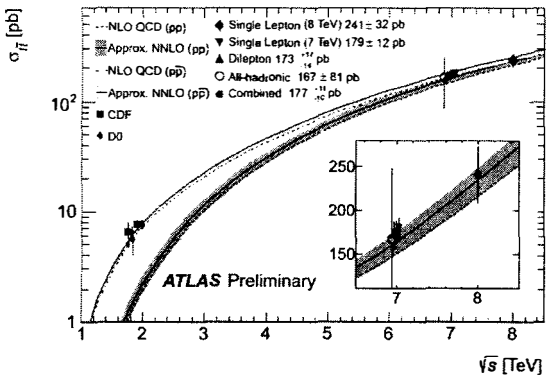

Figure 3: Summary plot showing the top pair production cross section as a function of the proton-(anti)proton centre-of-mass energy. The experimental results in the various top decay channels (and their combination) at 7 TeV and the recent result at 8 TeV are compared to an approximate NNLO QCD calculation based on Hathor 1.2. From Ref. [14].

the template method in the channel $t\bar{t} \to$ lepton + jets (lepton $= e, \mu$) based on ATLAS data recorded in the year 2011 [15]. The data were taken at a proton-proton centre-of-mass energy of $\sqrt{s} = 7$ TeV and correspond to an integrated luminosity of about 4.7 fb^{-1}. This analysis uses a 3-dimensional template technique which determines the top quark mass together with a global jet energy scale factor (JSF), and a relative b-jet to light-jet energy scale factor (bJSF), where light jets refers to u, d, c, s quark jets. The top quark mass is measured to be: $m_{\text{top}} = 172.31 \pm 0.23(\text{stat}) \pm 0.27(\text{JSF}) \pm 0.67(\text{bJSF}) \pm 1.35(\text{syst})$ GeV or, equivalently, $m_{\text{top}} = 172.31 \pm 0.75(\text{stat + JSF + bJSF}) \pm 1.35(\text{syst})$ GeV, where the uncertainties labelled JSF and bJSF refer to the statistical uncertainties on m_{top} induced by the in-situ determination of these scale factors. The summary of all ATLAS direct m_{top} measurements compared with the Tevatron and CMS ones is shown in Fig. 4.

The top quark polarisation in $t\bar{t}$ events using the lepton plus jets final state, where one W boson decays leptonically and the other hadronically, has been measured with ATLAS [16]. The decay of the $t\bar{t}$ pair is fully reconstructed using a likelihood method in order to calculate the rest frame

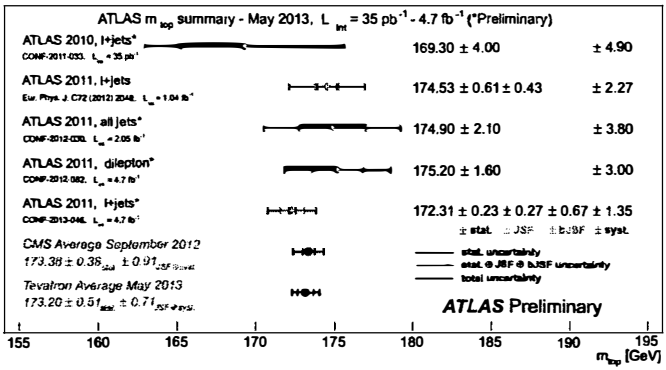

Figure 4: Summary of the ATLAS direct m_{top} measurements. The results are compared to the 2013 Tevatron and 2012 CMS m_{top} combinations. For each measurement, the statistical uncertainty, the JSF and bJSF contributions (when applicable) as well as the sum of the remaining uncertainties are reported separately. From Ref. [14].

of the leptonically decaying top quark. A template fit to the distribution of lepton polar angles in the parent top quark's rest frame is used to extract the fraction of positively polarised top quarks. The full 2011 ATLAS 7 TeV centre of mass energy pp collisions dataset from the LHC (4.66 fb^{-1}) is used to perform the measurement. The fraction of positively polarised top quarks is found to be $f = 0.470 \pm 0.009(\text{stat}) \,^{+0.023}_{-0.032}(\text{syst})$, compatible with the Standard Model prediction of $f = 0.5$.

Recent measurements of the W-boson polarisation in top-quark decays performed by the ATLAS and CMS Collaborations have been combined in Ref. [17]. The measurements are based on proton-proton collision data corresponding to integrated luminosities ranging from 35 pb^{-1} to 2.2 fb^{-1} produced at the LHC at a centre-of-mass energy of $\sqrt{s} = 7$ TeV. The results are quoted as helicity fractions, i.e. the fractions of events which contain W bosons with longitudinal and left-handed polarisation. The combined helicity fractions are

$$F_0 = 0.626 \pm 0.034(\text{stat}) \pm 0.048(\text{syst}), \quad (1)$$

$$F_L = 0.359 \pm 0.021(\text{stat}) \pm 0.028(\text{syst}), \quad (2)$$

which are in agreement with predictions from NNLO QCD. The fraction of

W bosons with right-handed polarisation is calculated assuming the sum of all fractions to be unity:

$$F_R = 0.015 \pm 0.034, \tag{3}$$

where the uncertainty includes the statistical and systematic uncertainties. Exclusion limits on anomalous Wtb couplings are derived from these results.

4 B physics

Weak decays of hadrons containing heavy quarks are employed for tests of the Standard Model and measurements of its parameters. In particular, they offer the most direct way to determine the weak mixing angles, to test the unitarity of the Cabibbo-Kobayashi-Maskawa (CKM) matrix, and to explore the physics of CP violation. The latter may also provide some hints about New Physics beyond the Standard Model. On the other hand, hadronic weak decays also serve as a probe of that part of strong-interaction phenomenology which is least understood: the confinement of quarks and gluons inside hadrons. In ATLAS beauty-physics analyses also include heavy quarkonia and D-hadron production in a variety of channels and analyses.

A limit on the branching fraction of $B_s^0 \to \mu\mu$ has been set using an integrated luminosity of 4.9 fb^{-1} collected in 2011 by the ATLAS detector [18]. The decay $B^\pm \to J/\psi K^\pm$, with $J/\psi \to \mu^+\mu^-$, was used as a reference channel for the normalisation of the integrated luminosity, acceptance and efficiency. The final selection was based on a multivariate analysis which is trained on MC, leaving the events in the sidebands to be used for optimisation and background estimation. Furthermore, this result profits from an improved event reconstruction and the use of multidimensional unbinned maximum likelihood fits for the extraction of the reference channel yield, with respect to previous results. An upper limit on $BR(B_s^0 \to \mu\mu) < 1.5\ (1.2) \times 10^{-8}$ at 95% (90%) confidence level (CL) has been set, as observed in Fig. 5.

Using 4.9 fb^{-1} of integrated luminosity taken at $\sqrt{s} = 7$ TeV by the ATLAS experiment, $B_d^0 \to K^{*0}\mu^+\mu^-$ events have been reconstructed and the angular distribution of their final state particles hase been measured [19]. The forward-backward asymmetry A_{FB} and the K^{*0} longitudinal polarisation F_L have been measured as a function of the dimuon invariant mass

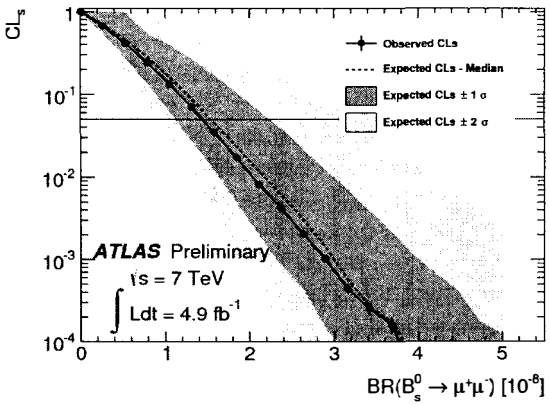

Figure 5: Observed CLs (circles) as a function of $B_s^0 \to \mu\mu$. The 95% CL limit is indicated by the horizontal (red) line. The dark (green) and light (yellow) bands correspond to the $\pm 1\sigma$ and $\pm 2\sigma$ ranges of the background-only pseudo-experiments with the median of the expected CLs given by the dashed line. From Ref. [18].

squared, q^2. The results obtained on A_{FB} and F_L are mostly consistent with theoretical predictions and measurements performed by other experiments. The results for F_L in the low-q^2 bins slightly deviate from Standard Model expectations, as reflected in Fig. 6.

5 Heavy-ion runs and results

During the operation in the years 2009-2013, besides collisions of proton beams, the LHC also delivered Pb+Pb collisions and p+Pb collisions, at the centre-of-mass energy $\sqrt{s_{NN}} = 2.76$ TeV and $\sqrt{s_{NN}} = 5.02$ TeV, respectively. Studies of heavy ion collisions explore complicated systems created in the volumes much larger than the size of the proton under the conditions of extreme energy density. Such conditions are similar to those at an early phase of the Universe evolution, when the matter was in the state of strongly interacting quark-gluon plasma. Results of nuclei collisions depend on the size of the volume and its shape, which are directly connected with the smallest distance of the nuclei centres during

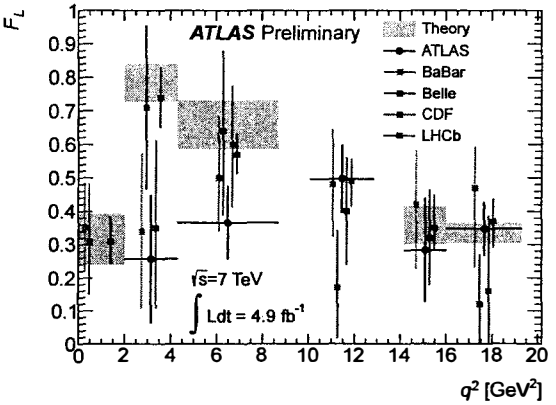

Figure 6: Fraction of longitudinal polarised K^{*0} mesons F_L as a function of q^2 measured by ATLAS (black dots). In each q^2 bin, ordered from right to left, results of other experiments are shown as coloured squares: BaBar, Belle, CDF and LHCb. All errors including statistical and systematic uncertainties. The experimental results are compared to theoretical Standard Model predictions including theoretical uncertainties. From Ref. [19].

the collision. Commonly, centrality of the nuclei collisions is denoted by the percentage of the cross section (starting from the most central events) or is characterised by the number of nucleons participating in inelastic interactions or by the number of binary nucleon-nucleon collisions.

Two-particle correlations in relative azimuthal angle $\Delta\phi$ and pseudo-rapidity $\Delta\eta$ were measured in $\sqrt{s_{NN}} = 5.02$ TeV p+Pb collisions using the ATLAS detector at the LHC [20]. The measurements were performed using approximately 1 μb^{-1} of data as a function of p_{T} and the transverse energy $\sum E_{\mathrm{T}}^{\mathrm{Pb}}$ summed over $3.1 < \eta < 4.9$ in the direction of the Pb beam. The correlation function, constructed from charged particles, exhibits a long-range ($2 < |\Delta\eta| < 5$) near-side ($\Delta\phi \sim 0$) correlation that grows rapidly with increasing $\sum E_{\mathrm{T}}^{\mathrm{Pb}}$. A long-range away-side ($\Delta\phi \sim \pi$) correlation, obtained by subtracting the expected contributions from recoiling dijets and other sources estimated using events with small $\sum E_{\mathrm{T}}^{\mathrm{Pb}}$, is found to match the near-side correlation in magnitude, shape (in $\Delta\eta$ and $\Delta\phi$) and $\sum E_{\mathrm{T}}^{\mathrm{Pb}}$T dependence, as shown in Fig. 7 (right). The resultant $\Delta\phi$ correlation is approximately symmetric about $\pi/2$, and is consistent with

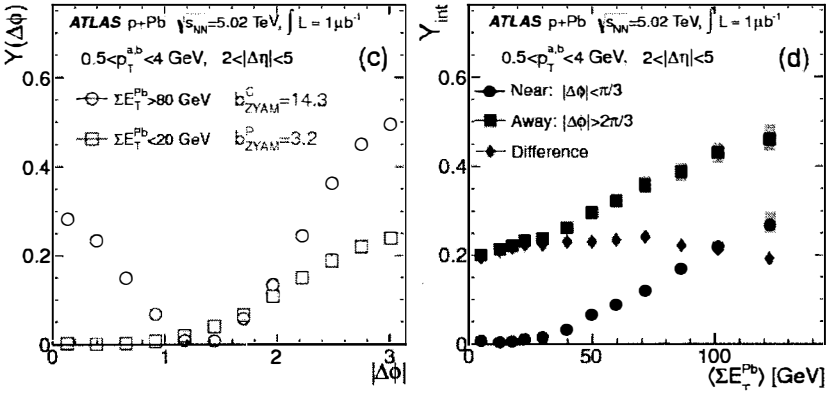

Figure 7: *Left:* Per-trigger yield $\Delta\phi$ distribution together with pedestal levels for peripheral ($b^{\mathrm{P}}_{\mathrm{ZYAM}}$) and central ($b^{\mathrm{C}}_{\mathrm{ZYAM}}$) events. *Right:* Integrated per-trigger yield as a function of $\sum E_{\mathrm{T}}^{\mathrm{Pb}}$ for pairs in $2 < |\Delta\eta| < 5$. The shaded boxes represent the systematic uncertainties, and the statistical uncertainties are smaller than the symbols. From Ref. [20].

a $\cos(2\Delta\phi)$ modulation for all $\sum E_{\mathrm{T}}^{\mathrm{Pb}}$ ranges and particle p_{T}, as shown in Fig. 7 (left). The amplitude of this modulation is comparable in magnitude and p_{T} dependence to similar modulations observed in heavy-ion collisions, suggestive of final-state collective effects in high multiplicity events.

6 Higgs boson discovery and properties

The Brout-Englert-Higgs mechanism [21] plays a central role in the unification of the electromagnetic and weak interactions by providing mass to the W and Z intermediate vector bosons without violating local gauge invariance. Within the Standard Model, the Higgs mechanism is invoked to break the electroweak symmetry; it implies the existence of a single neutral scalar particle, the Higgs boson. In July 2012 the ATLAS [22] and CMS [23] Collaborations announced the discovery of a new particle, with evidence of decays to photons as well as Z and W bosons. In the following year the LHC has produced more data, allowing for a more detailed understanding of this new resonance. With this dataset, the ATLAS experiment

has studied the properties of the particle, including its spin, mass, and couplings to SM particles, and found these properties to be consistent with those of the Standard Model Higgs boson.

Crucial experimental aspects of ATLAS for the observation of the diphoton decay of the Higgs boson are the excellent $\gamma\gamma$ mass resolution to observe the narrow signal peak above irreducible background and the powerful γ/jet separation to suppress $\gamma -$ jet and jet-jet background with jet $\rightarrow \pi^0$ faking single photons. Measurements of the properties [24], the spin [25] and the cross section [26] of the Higgs boson in the $H \rightarrow \gamma\gamma$ channel have been performed using the complete dataset of ~ 20 fb^{-1} of pp collision data at a centre-of-mass energy of 8 TeV.

The diphoton invariant-mass distributions for the $N_{\text{jets}} \geq 3$ bin is shown in the left panel of Fig. 8 [26]. The curves show the results of the single simultaneous fit to data for all N_{jets} bins. The red line is the combined signal and background, and the dashed line shows the background. The difference of the two curves is the extracted signal yield. The bottom inset displays the residuals of the data with respect to the fitted background component, and the dotted red line corresponds to the signal. The lower local probability of the background fluctuating beyond the observation in the data at a particular m_H (p_0 value) of $\sim 10^{-13}$ (7.4σ significance) was found at $m_H = 126.5$ GeV. The best-fit m_H value was found to be $126.8 \pm 0.2(\text{stat}) \pm 0.7(\text{syst})$ GeV. The dominant contribution to the systematic uncertainty on m_H comes from the uncertainties on the photon energy scale. At the best-fit value of $m_H = 126.8$ GeV, the signal strength, i.e. the ratio of the observed cross section to the expected SM cross section, was found to be $\mu = 1.65^{+0.34}_{-0.30}$.

Also known as the "golden" decay channel, $H \rightarrow ZZ^{(*)} \rightarrow 4\ell$ features by far the cleanest sample ($S/N \sim 1$) due to its unique signature of two high energy lepton pairs. However for m_H below 180 GeV, the ZZ decay is sub-threshold, thus forcing one of the Z^0 off-shell, thereby significantly reducing the branching ratio. The ATLAS detector was conceived to measure high-energy muons and electrons with great precision, also incorporating recognition of fast leptons already at the first (hardware) stage of the trigger. The distributions of the four-lepton invariant mass, $m_{4\ell}$, for the selected candidates compared to the background expectation in the mass range $80 - 170$ GeV are shown in Fig. 8 [27]. The signal expectation for the $m_H = 125$ GeV hypothesis is also shown. The resolution of the reconstructed Higgs boson mass is dominated by detec-

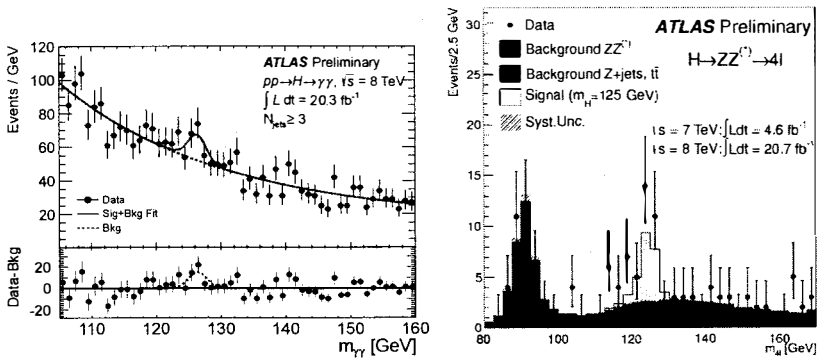

Figure 8: *Left:* Diphoton invariant-mass distribution for the $N_{\text{jets}} \geq 3$ bin. From Ref. [26]. *Right:* The distributions of the four-lepton invariant mass, $m_{4\ell}$, compared to the background expectation for the combined $\sqrt{s} = 8$ TeV and $\sqrt{s} = 7$ TeV data sets in the mass range $80 - 170$ GeV. From Ref. [27].

tor resolution at low m_H values and by the Higgs boson width at high m_H. The results are based on 4.6 fb^{-1} of 7 TeV pp collision data combined with 20.7 fb^{-1} of 8 TeV. A clear excess of events over the background is observed at $m_H = 124.3$ GeV in the combined analysis of the two datasets with a significance of 6.6σ, corresponding to a background fluctuation probability of 2.7×10^{-11}. The mass of the Higgs-like boson is measured to be $m_H = 124.3^{+0.6}_{-0.5}(\text{stat})^{+0.5}_{-0.3}(\text{syst})$ GeV in this channel, and the signal strength at this mass is found to be $\mu = 1.7^{+0.5}_{-0.4}$.

The full datasets recorded by ATLAS in 2011 and 2012, corresponding to an integrated luminosity of up to 25 fb^{-1} at $\sqrt{s} = 7$ TeV and $\sqrt{s} = 8$ TeV, have been analysed to determine several properties of the recently discovered Higgs boson using the $H \to \gamma\gamma$, $H \to ZZ^* \to 4\ell$ and $H \to WW^* \to \ell\nu\ell\nu$ decay modes [28]. The reported results include measurements of the mass and signal strength, evidence for production through vector-boson fusion, and constraints on couplings to bosons and fermions as well as on anomalous contributions to loop-induced processes.

The measured production strengths for a Higgs boson of mass $m_H = 125.5$ GeV, normalised to the SM expectations, for diboson final states and their combination is visible in Fig. 9. The best-fit values are indicated by the solid vertical lines. The total $\pm 1\sigma$ uncertainty is indicated

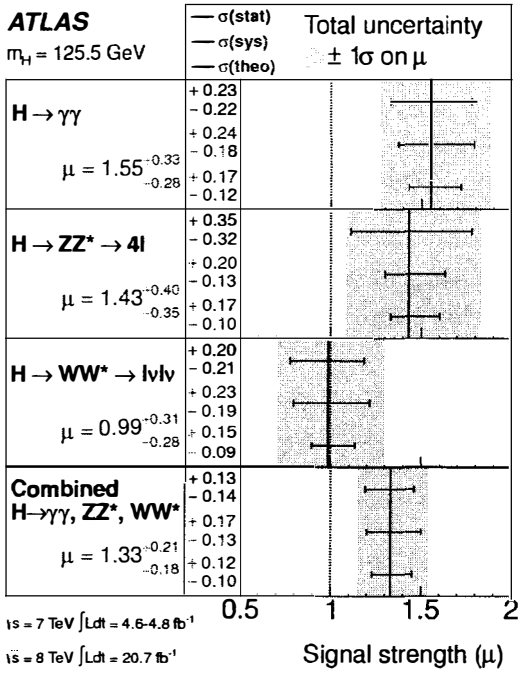

Figure 9: Measured production strengths for a Higgs boson of mass $m_H = 125.5$ GeV, normalised to the SM expectations, for diboson final states and their combination. From Ref. [28].

by the shaded band, with the individual contributions from the statistical uncertainty (top), the total (experimental and theoretical) systematic uncertainty (middle), and the theoretical uncertainty (bottom) on the signal cross section (from QCD scale, PDF, and branching ratios) shown as superimposed error bars. The overall compatibility between the signal strengths measured in the three final states and the SM predictions is about 14%, with the largest deviation ($\sim 1.9\sigma$) observed in the $H \to \gamma\gamma$ channel [28].

Good consistency between the measured and expected signal strengths is also found for the various categories of the $H \to \gamma\gamma$, $H \to ZZ^* \to 4\ell$ and $H \to WW^* \to \ell\nu\ell\nu$ analyses, which are the primary experimental inputs to the fit. If the preliminary $H \to \tau\tau$ [29] and $H \to b\bar{b}$ [30] results, for which only part of the 8 TeV dataset is used ($13\ \mathrm{fb}^{-1}$), were included,

the combined signal strength would be $\mu = 1.23 \pm 0.18$ [28].

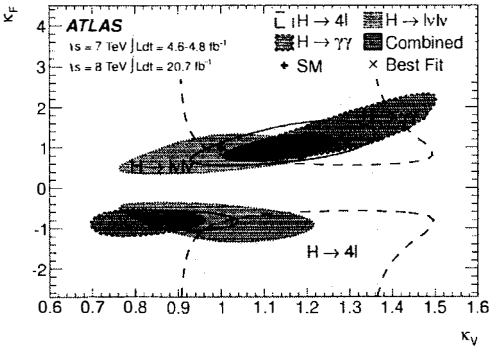

Figure 10: Likelihood contours (68% CL) of the coupling scale factors κ_F and κ_V for fermions and bosons, as obtained from fits to the three individual channels and their combination (for the latter, the 95% CL contour is also shown). The best-fit result ($\times$) and the SM expectation ($+$) are also indicated. From Ref. [28].

The benchmark model for the Higgs couplings presented here assumes one coupling scale factor for fermions, κ_F, and one for bosons, κ_V; in this scenario, the $H \to \gamma\gamma$ and $gg \to H$ loops and the total Higgs boson width depend only on κ_F and κ_V, with no contributions from physics beyond the Standard Model. The strongest constraint on κ_F comes indirectly from the $gg \to H$ production loop. Figure 10 shows the results of the fit to the data for the three channels and their combination. Since only the relative sign of κ_F and κ_V is physical, in the following $\kappa_V > 0$ is assumed. Some sensitivity to this relative sign is provided by the negative interference between the W-boson loop and t-quark loop in the $H \to \gamma\gamma$ decay. The data prefer the minimum with positive relative sign, which is consistent with the SM prediction, but the local minimum with negative sign is also compatible with the observation (at the $\sim 2\sigma$ level). The two-dimensional compatibility of the SM prediction with the best-fit value is 12%.

The Standard Model $J^P = 0^+$ hypothesis for the Higgs boson has been compared to alternative spin-parity hypotheses using 8 TeV (20.7 fb^{-1}) and 7 TeV (4.6 fb^{-1}) proton-proton collision data collected by ATLAS [31]. The Higgs boson decays $H \to \gamma\gamma$, $H \to ZZ^* \to 4\ell$ and $H \to WW^* \to$

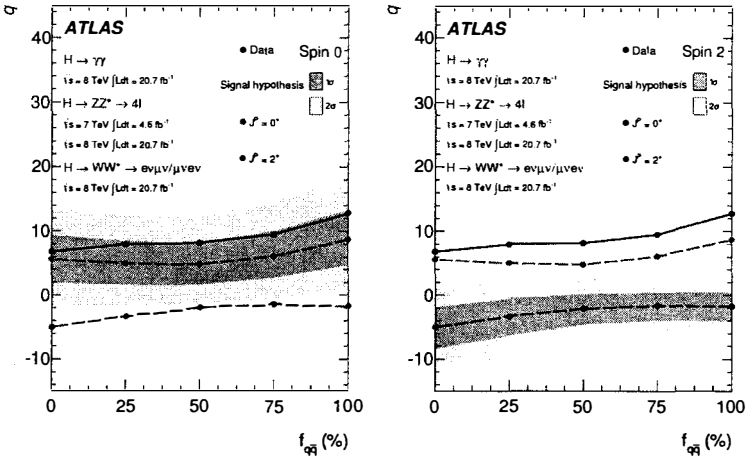

Figure 11: Expected distributions of the log-likelihood ratio q, for the combination of channels as a function of the fraction of the $q\bar{q}$ spin-2 production mechanism. The green and yellow bands represent, respectively, the 1σ and 2σ bands for 0^+ (left) and for 2^+ (right). From Ref. [31].

$\ell\nu\ell\nu$ have been used to test several specific alternative models, including $J^P = 0^-, 1^+, 1^-$ and a graviton-inspired $J^P = 2^+$ model with minimal couplings to SM particles. The data favour the Standard Model quantum numbers of $J^P = 0^+$. The 0^- hypothesis is rejected at 97.8% CL by using the $H \to ZZ^* \to 4\ell$ decay alone. The 1^+ and 1^- hypotheses are rejected with a CL of at least 99.7% by combining the $H \to ZZ^* \to 4\ell$ and $H \to WW^* \to \ell\nu\ell\nu$ channels. Finally, the $J^P = 2^+$ model is rejected at more than 99.9% CL by combining all three bosonic channels, independent of the assumed admixture of gluon-fusion and quarkantiquark production, as observed in Fig. 11. All these alternative models are excluded without assumptions on the strength of the couplings of the Higgs boson to SM particles. These studies provide evidence for the spin-0 nature of the Higgs boson, with positive parity being strongly preferred.

7 Hunt for supersymmetry

Supersymmetry (SUSY) [32, 33] is an extension of the Standard Model which assigns to each SM field a superpartner field with a spin differing by a half unit. SUSY provides elegant solutions to several open issues in the SM, such as the hierarchy problem, the identity of dark matter, and grand unification.

SUSY searches in collider experiments typically focus on events with high transverse missing energy ($E_{\mathrm{T}}^{\mathrm{miss}}$) which can arise from (weakly interacting) Lightest Supersymmetric Particles (LSPs), in the case of R-parity conserving SUSY, or from neutrinos produced in LSP decays, when R-parity is broken. Hence, the event selection criteria of inclusive channels are based on large $E_{\mathrm{T}}^{\mathrm{miss}}$, no or few leptons ($e$, μ), many jets and/or b-jets, τ-leptons and photons.

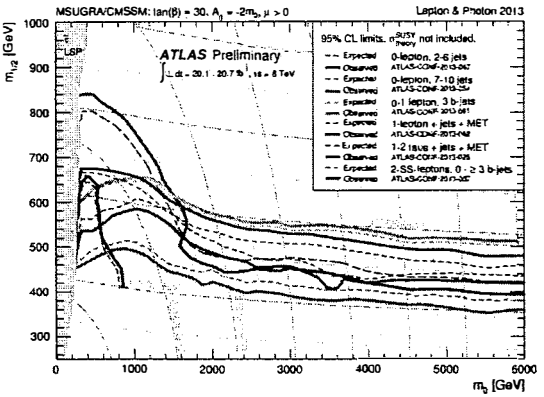

Figure 12: Exclusion limits at 95% CL for 8 TeV analyses in the (m_0, $m_{1/2}$) plane for the MSUGRA/CMSSM model. From Ref. [14].

In the absence of deviations from SM predictions, limits for squark and gluino production are set. Figure 12 illustrates the 95% CL limits set by ATLAS under the minimal Supergravity (mSUGRA) model in the (m_0, $m_{1/2}$) plane. The remaining parameters are set to $\tan\beta = 30$, $A_0 = -2\,m_0$, $\mu > 0$, so as to acquire parameter-space points where the predicted mass of the lightest Higgs boson, h_0, is near 125 GeV, i.e. compatible with the recently observed Higgs-like boson [22, 23]. Exclusion limits are

obtained by using the signal region with the best expected sensitivity at each point.

The mixing of left- and right-handed gauge states which provides the mass eigenstates of the scalar quarks and leptons can lead to relatively light 3rd generation particles. Stop ($\tilde{t}_1$) and sbottom ($\tilde{b}_1$) with a sub-TeV mass are favoured by the naturalness argument, while the stau ($\tilde{\tau}_1$) is the lightest slepton in many models. Therefore these could be abundantly produced either directly or through gluino production and decay. Such events are characterised by several energetic jets (some of them b-jets), possibly accompanied by light leptons, as well as high $E_{\mathrm{T}}^{\mathrm{miss}}$.

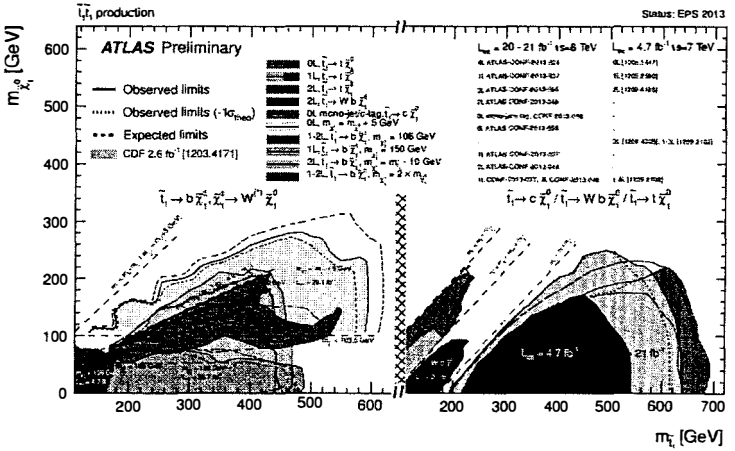

Figure 13: Summary of the dedicated ATLAS searches for stop pair production based on $20 - 21$ fb^{-1} of pp collision data taken at $\sqrt{s} = 8$ TeV, and 4.7 fb^{-1} of pp collision data taken at $\sqrt{s} = 7$ TeV. From Ref. [14].

If the gluino is too heavy to be produced at the LHC, direct $\tilde{t}_1\tilde{t}_1$ and $\tilde{b}_1\tilde{b}_1$ production is the only remaining possibility. If stop pairs are considered, two decay channels can be distinguished depending on the mass of the stop: $\tilde{t}_1 \to b\tilde{\chi}_1^{\pm}$ and $\tilde{t}_1 \to t\tilde{\chi}_1^0$. ATLAS has carried out a wide range of different analyses in each of these modes at both 7 TeV and 8 TeV centre-of-mass energy. In all these searches, the number of observed events has been found to be consistent with the SM expectation. Limits have been set on the mass of the scalar top for different assumptions on the mass hierarchy scalar top-chargino-lightest neutralino, as shown in the left (right) panel

of Fig. 13 for $\tilde{t}_1 \to b\tilde{\chi}_1^{\pm}$ ($\tilde{t}_1 \to t\tilde{\chi}_1^0$) decays.

For the former scenario, a scalar top quark of mass of up to 480 GeV is excluded at 95% CL for a massless neutralino and a 150 GeV chargino. For a 300 GeV scalar top quark and a 290 GeV chargino, models with a neutralino with mass lower than 180 GeV are excluded at 95% CL. For the case of a high-mass stop decaying to a top and a $\tilde{\chi}_1^0$, analyses requiring one, two or three isolated leptons, jets and large $E_{\mathrm{T}}^{\mathrm{miss}}$ have been carried out. Stop masses are excluded between 200 GeV and 680 GeV for massless neutralinos, and stop masses around 500 GeV are excluded along a line which approximately corresponds to neutralino masses up to 250 GeV. It is worth noting that a monojet analysis with c-tagging is deployed to cover part of the low-$m_{\tilde{t}_1}$, low-$m_{\tilde{\chi}_1^0}$ region through the $\tilde{t}_1 \to c\tilde{\chi}_1^0$ channel [34].

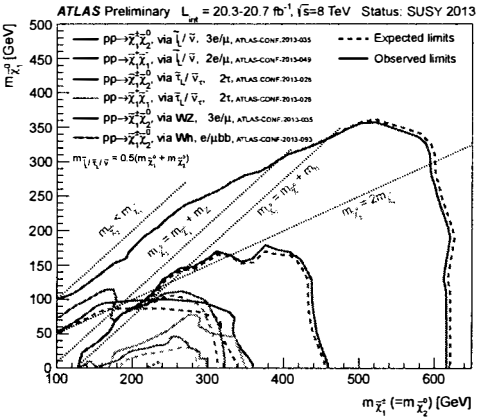

Figure 14: Summary of ATLAS searches for electroweak production of charginos and neutralinos based on 20 fb^{-1} of pp collision data at $\sqrt{s}$ = 8 TeV. From Ref. [14].

If all squarks and gluinos are above the TeV scale, weak gauginos with masses of few hundred GeV may be the only sparticles accessible at the LHC. As an example, at $\sqrt{s}$ = 7 TeV, the cross-section of the associated production $\tilde{\chi}_1^{\pm}\tilde{\chi}_2^0$ with degenerate masses of 200 GeV is above the 1-TeV gluino-gluino production cross section by one order of magnitude. Chargino pair production is searched for in events with two opposite-sign leptons and $E_{\mathrm{T}}^{\mathrm{miss}}$ using a jet veto, through the decay $\tilde{\chi}_1^{\pm} \to \ell^{\pm}\nu\tilde{\chi}_1^0$. A

summary of related analyses performed by ATLAS is shown in Fig. 14. Exclusion limits at 95% confidence level are shown in the ($m_{\tilde{\chi}_0^{\pm}}$, $m_{\tilde{\chi}_1^0}$) plane. The dashed and solid lines show the expected and observed limits, respectively, including all uncertainties except the theoretical signal cross section uncertainties.

Charginos with masses between 140 and 560 GeV are excluded for a massless LSP in the chargino-pair production with an intermediate slepton/sneutrino between the $\tilde{\chi}_1^{\pm}$ and the $\tilde{\chi}_1^0$. If $\tilde{\chi}_1^{\pm}\tilde{\chi}_2^0$ production is assumed instead, the limits range from 11 to 760 GeV. The corresponding limits involving intermediate W, Z and/or H are significantly weaker.

Searches are also performed in ATLAS for several signatures associated with the violation of R-parity (RPV). As an example we highlight here the interpretation of null inclusive searches in the one-lepton channel [35] in the context of a model where RPV is induced through bilinear terms, depicted in the left panel of Fig. 15. The results are obtained by combining the electron and muon channels. The band around the median expected limit shows the $\pm 1\sigma$ variations on the median expected limit, including all uncertainties except theoretical uncertainties on the signal. The dotted lines around the observed limit indicate the sensitivity to $\pm 1\sigma$ variations on these theoretical uncertainties. The thin solid black contours show the LSP lifetime. The result from the previous ATLAS search [36] for this model is also shown.

In view of the null results in other SUSY searches, it became mandatory to fully explore the SUSY scenario predicting meta-stable or long-lived particles. These particles, not present in the Standard Model, would provide striking signatures in the detector and rely heavily on a detailed understanding of its performance. For instance, gluino, top squark, or bottom squark R-hadrons that have come to rest within the ATLAS calorimeter, and decay at some later time to hadronic jets and a neutralino have been searched for, using 5.0 and 22.9 fb^{-1} of pp collisions at 7 and 8 TeV, respectively. Selections based on jet shape and muon-system activity are applied to discriminate signal events from cosmic ray and beam-halo muon backgrounds. In the absence of an excess of events, limits are set on gluino, stop, and sbottom masses for different decays, lifetimes, and neutralino masses. As shown in the right panel of Fig. 15, with a neutralino of mass 100 GeV, the analysis excludes gluinos with mass below 832 GeV(with an expected lower limit of 731 GeV), for a gluino lifetime between 10 μs and 1000 s in the generic R-hadron model with equal branching ratios for

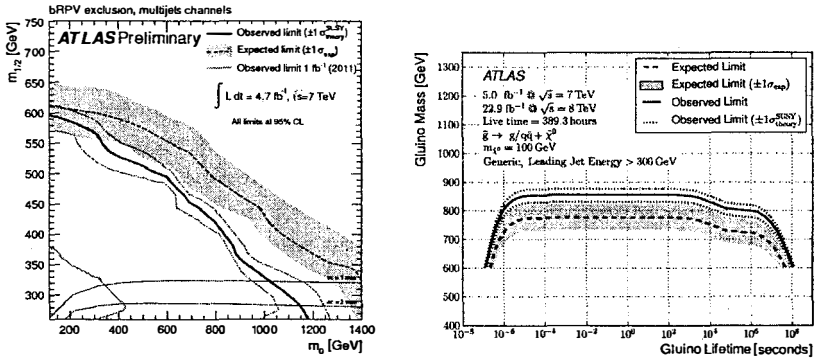

Figure 15: *Left:* Expected and observed 95% CL exclusion limits in the bilinear R-parity violating model. From Ref. [35]. *Right:* Bayesian lower limits on gluino mass versus its lifetime with R-hadron lifetimes in the plateau acceptance region between 10^{-5} and 10^{3} seconds. From Ref. [37].

decays to $q\bar{q} + \tilde{\chi}_1^0$ and $g + \tilde{\chi}_1^0$. Under the same assumptions for the neutralino mass and squark lifetime, top squarks and bottom squarks in the Regge R-hadron model are excluded with masses below 379 and 344 GeV, respectively.

8 Searches for exotic scenarios

Various theoretical scenarios that attempt to short out some of the Standard Model problems, in addition to supersymmetry, have also been enquired by ATLAS. Several signature-driven analyses have been pursued:

- resonances: dileptons, jets, photons, bosons, ...;
- special particles: slow-moving, long-lived, ...;
- $E_{\mathrm{T}}^{\mathrm{miss}}$ plus other object(s);
- other non-conventional signatures.

Subsequently the outcome of these searches are interpreted in the context of specific models to obtain exclusion limits on masses, scales, etc: Extra-dimension scenarios, heavy gauge bosons, contact interactions, leptoquarks, new quarks, excited fermions, magnetic monopoles, new gauge bosons, etc. Given the wide range of possibilities, it is not possible to cover every analysis here, hence only some recent results are highlighted.

A search for a dijet resonance with an invariant mass in the range between 130 and 300 GeV has been performed in the processes $pp \to W\mathrm{jj}+X$ with $W \to \ell\nu$ and $pp \to Z\mathrm{jj}+X$ with $Z \to \ell^+\ell^-$ ($\ell = e, \mu$) [38]. The data used correspond to 20.3 fb^{-1} of pp collision data recorded at $\sqrt{s} = 8$ TeV with ATLAS. The results are interpreted in terms of constraints on the Low Scale Technicolor (LSTC) model. No significant deviation from the Standard Model background prediction is observed. Upper limits on the production cross section times branching fraction are set for a hypothetical technipion (π_{T}) produced in association with a W or Z boson from the decay of a technirho (ρ_{T}) particle. The limits for the W boson are shown in the left panel of Fig. 16, assuming the mass relation of $m_{\rho_{\mathrm{T}}} = 3/2 \times m_{\pi_{\mathrm{T}}} + 55$ GeV. The inner and outer bands on the expected limit represent $\pm 1\sigma$ and $\pm 2\sigma$ variations, respectively. The LSTC predictions for the ρ_{T} cross section are also shown in blue.

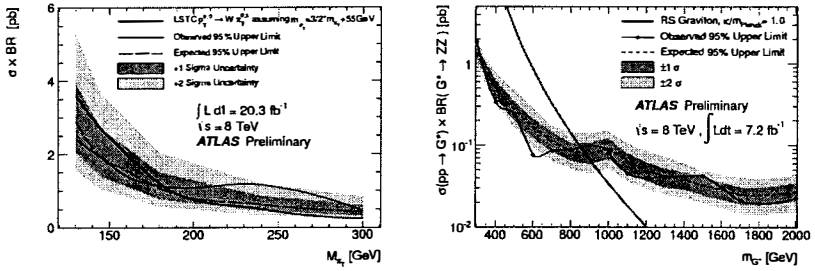

Figure 16: *Left:* Observed and expected 95% CL upper limits on the $W\pi_{\mathrm{T}}$ cross section as a function of the mass of the technipion in the $W\mathrm{jj}$ channel. From Ref. [38]. *Right:* Observed and expected 95% credibility level upper limits on $\sigma(pp \to G^*) \times BR(G^* \to ZZ)$ for the bulk RS graviton. From Ref. [39].

A search for a heavy particle that decays to a pair of Z bosons has been carried out using events recorded by ATLAS in pp collisions at $\sqrt{s} = 8$ TeV corresponding to an integrated luminosity of 7.2 fb^{-1}. The analysis considers the $\ell\ell qq$ final state and uses the diboson mass reconstructed from the leptons and jets as the discriminating variable. No significant deviation in the mass distribution from a smoothly falling background distribution is observed. The upper limits set on the production cross section times branching fraction into a ZZ boson pair for the bulk Randall-Sundrum

(RS) graviton with coupling parameter of $\kappa/\bar{m}_{\rm Pl} = 1.0$ are shown in the right panel of Fig. 16. The leading-order theoretical prediction for the bulk RS model is also shown. The inner and outer bands on the expected limit represent $\pm 1\sigma$ and $\pm 2\sigma$ variations, respectively. The corresponding 95% credibility level observed (expected) lower limit on the mass for the graviton is 850 (870) GeV.

Weakly-interacting massive particles (WIMPs, χ), stable neutral states, which exist in many extensions of the SM, provide a good candidate to explain the cosmological dark matter. The leading generic diagrams responsible for DM production at hadron colliders [40] involve the WIMP pair-production plus the initial- or final-state radiation (ISR/FSR) of a gluon, photon, weak gauge boson Z, W or a Higgs boson. The ISR/FSR particle is necessary to balance the two WIMPs' momentum, so that they are not produced back-to-back resulting in negligible $E_{\rm T}^{\rm miss}$. Therefore the search is based on selecting events high-$E_{\rm T}^{\rm miss}$ events, due to the WIMPs, and a single jet [41], photon [42] or boson [43] candidate.

In the context of $pp \to \chi\bar{\chi} + W/Z$ production, ATLAS has searched for the production of W or Z bosons decaying hadronically and reconstructed as a single massive jet in association with large $E_{\rm T}^{\rm miss}$ from the undetected $\chi\bar{\chi}$ particles [43]. For this analysis, the jet candidates are reconstructed using a filtering procedure referred to as large-radius jets. The 90% limits on χ-nucleon cross sections for spin-independent scattering are shown in Fig. 17 (left). They are compared to previous limits set by direct dark matter detection experiments and by the ATLAS 7 TeV monojet analysis [41]. For the spin-independent case with the opposite-sign up-type and down-type couplings, the limits are improved by about three orders of magnitude.

This search is sensitive to WIMP pair production, as well as to other DM-related models, such as invisible Higgs boson decays (WH or ZH production with $H \to \chi\bar{\chi}$). Moreover the monojet analysis [41] is pertinent for exploring the production of light gravitinos in association with gluinos or squarks in a gauge-mediated supersymmetric model. The cross section times acceptance times efficiency for the gravitino plus $\tilde{q}/\tilde{g}$ production as a function of the $\tilde{q}/\tilde{g}$ mass in the case of mass degenerate squark and gluinos is shown in Fig. 17 (right). The comparison of these curves with the acquired model-independent upper limit from the monojet search leads to the best lower bound to date on the gravitino mass. Exclusion limits on models with large extra spatial dimensions and on pair production of

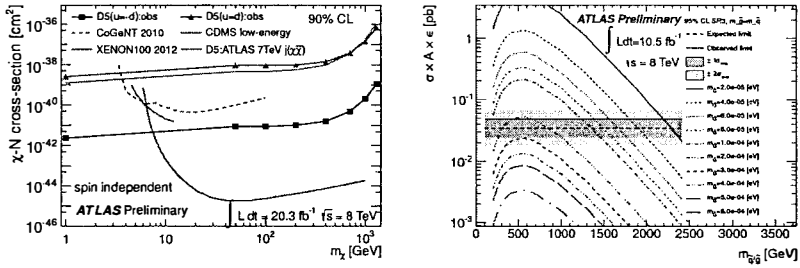

Figure 17: *Left:* 90% limits on χ-nucleon cross sections for spin-independent scattering obtained by the mono-W/Z analysis. From Ref. [43]. *Right:* Cross section times acceptance times efficiency for the gravitino plus $\tilde{q}/\tilde{g}$ production as a function of the $\tilde{q}/\tilde{g}$ mass for different values of the gravitino mass. From Ref. [41].

weakly interacting dark matter candidates have been obtained as well.

The leading quadratically-divergent contribution to the Higgs mass is the top quark loop, making particles closely coupled to the top quark natural candidates for relatively light manifestations of new physics. Vector-like top partners, i.e. fermions for which the right- and left-chiral components follow the same transformation rules, present a rich phenomenology. For heavy top-like partners, new decay modes open up: $T \to Wb$, $T \to Ht$ and $T \to Zt$ are possible. In addition, such partners can be part of multiplets that can include for example a charge 5/3 quark ($T_{5/3}$), a heavy B quark or a charge $-4/3$ quark ($Y_{-4/3}$). This can lead to a rich set of signatures which generally include many third-generation particles in the final state.

In the case of pair production of $T_{5/3}$, the decay chain $T^+_{5/3} \to W^+t \to W^+W^+b$ can lead to a pair of same-sign leptons, if both W bosons decay leptonically [44]. In the charge 2/3 case, for pair production the $T \to Wb$ decay mode leads to the same signature as SM $t\bar{t}$ production, so that a good discriminant is needed, such as the reconstructed heavy quark mass [45]. The $T \to Ht$ decay mode leads to an abundance of b-jets, since the final state consists of $WbbbX$, where X represents the decay products of the second T quark, and contains at least one b quark [46]. This allows the application of hard selection cuts in this channel, requiring at least six jets of which at least four should be b-tagged. For the third decay mode, $T \to Zt$, requiring a leptonically-decaying Z boson offers excellent

background suppression. After imposing a high p_{T} cut on the Z, ATLAS uses the reconstructed Zb mass (using the leading b-jet) as a discriminating variable [47]. This search is also sensitive to production of a heavy B quark decaying to Zb, for which this discriminating variable is even more powerful. Figure 18 summarises the limits obtained by the different ATLAS T quark searches.

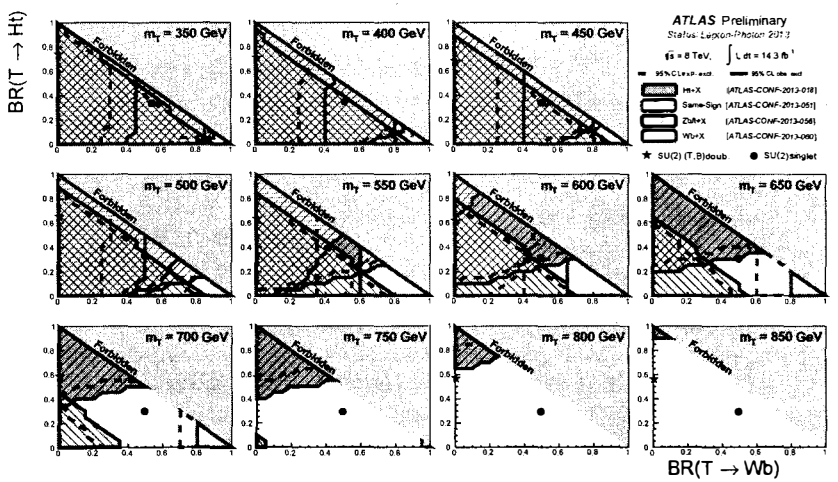

Figure 18: Full summary of ATLAS searches for vector-like T quark with 14 fb^{-1} of 8 TeV data. Excluded regions are drawn sequentially for each of the analyses in chronological order and overlaid (rather than combined) in each of the figures. From Ref. [14].

9 Summary and outlook

Excellent performance from ATLAS experiment and the LHC has been observed during the 7 TeV and 8 TeV runs in 2011-2012. The first results from Run-I include high precision in measurements of SM processes, the discovery of a boson consistent with the SM Higgs and improved limits on BSM scenarios. The analysis of the latest data is still on-going and more exciting results are expected to be released soon. The Particle Physics community is looking forward to LHC resuming collisions at $13-14$ TeV after the 2013-2014 LHC long shutdown.

Acknowledgments

The author acknowledges support by the Spanish Ministry of Economy and Competitiveness (MINECO) under the projects FPA2009-13234-C04-01 and FPA2012-39055-C02-01, by the Generalitat Valenciana through the project PROMETEO II/2013-017 and by the Spanish National Research Council (CSIC) under the JAE-Doc program co-funded by the European Social Fund (ESF).

References

[1] S. L. Glashow, *Nucl. Phys.* **22** (1961) 579; A. Salam, Weak and Electromagnetic Interactions, in *Elementary Particle Theory, Proc. of the Nobel Symposium*, ed. N. Svartholm, (Almquvist & Wiksell, Stockholm, 1968), p. 367; S. Weinberg, *Phys. Rev. Lett.* **19** (1967) 1264.

[2] L. Evans and P. Bryant, *JINST* **3** (2008) S08001.

[3] ATLAS Collab. (G. Aad *et al.*), *JINST* **3** (2008) S08003.

[4] G. Aad *et al.* [ATLAS Collaboration], Eur. Phys. J. C **70** (2010) 787 [arXiv:1004.5293 [physics.ins-det]].

[5] G. Aad *et al.*, JINST **3** (2008) P07007.

[6] A. Ahmad *et al.*, Nucl. Instrum. Meth. A **578** (2007) 98.

[7] E. Abat *et al.*, JINST **3** (2008) P02013.

[8] G. Aad *et al.* [ATLAS Collaboration], Eur. Phys. J. C **70** (2010) 723 [arXiv:0912.2642 [physics.ins-det]].

[9] G. Aad *et al.* [ATLAS Collaboration], Eur. Phys. J. C **70** (2010) 1193 [arXiv:1007.5423 [physics.ins-det]].

[10] G. Aad *et al.* [ATLAS Collaboration], Eur. Phys. J. C **70** (2010) 875 [arXiv:1006.4384 [physics.ins-det]].

[11] G. Aad *et al.* [ATLAS Collaboration], Phys. Lett. B **725** (2013) 223 [arXiv:1305.4192 [hep-ex]].

[12] G. Aad *et al.* [ATLAS Collaboration], JHEP **1307** (2013) 032 [arXiv:1304.7098 [hep-ex]].

[13] ATLAS Collaboration, "Measurement of the top quark pair production cross section in the single-lepton channel with ATLAS in proton-proton collisions at 8 TeV using kinematic fits with b-tagging," ATLAS-CONF-2012-149 (2012).

[14] `https://twiki.cern.ch/twiki/bin/view/AtlasPublic/CombinedSummaryPlots`

[15] ATLAS Collaboration, "Measurement of the Top Quark Mass from $\sqrt{s} = 7$ TeV ATLAS Data using a 3-dimensional Template Fit," ATLAS-CONF-2013-046 (2013).

[16] ATLAS Collaboration, "Measurement of top quark polarisation in $t\bar{t}$ events with the ATLAS detector in proton-proton collisions at $\sqrt{s} = 7$ TeV," ATLAS-CONF-2012-133 (2012).

[17] ATLAS Collaboration, "Combination of the ATLAS and CMS measurements of the W-boson polarization in top-quark decays," ATLAS-CONF-2013-033 (2013).

[18] ATLAS Collaboration, "Limit on $B_s^0 \to \mu\mu$ branching fraction based on 4.9 fb^{-1} of integrated luminosity," ATLAS-CONF-2013-076 (2013).

[19] ATLAS Collaboration, "Angular analysis of $B_d^0 \to K^{*0}\mu^+\mu^-$ with the ATLAS Experiment," ATLAS-CONF-2013-038 (2013).

[20] G. Aad *et al.* [ATLAS Collaboration], Phys. Rev. Lett. **110** (2013) 182302 [arXiv:1212.5198 [hep-ex]].

[21] P. W. Higgs, Phys. Rev. Lett. **13** (1964) 508; *idem,* Phys. Lett. **12** (1964) 132; *idem,* Phys. Rev. **145** (1966) 1156; F. Englert and R. Brout, Phys. Rev. Lett. **13** (1964) 321; G. S. Guralnik, C. R. Hagen and T. W. B. Kibble, Phys. Rev. Lett. **13** (1964) 585.

[22] ATLAS Collab. (G. Aad *et al.*), *Phys. Lett. B* **716** (2012) 1 [arXiv:1207.7214 [hep-ex]].

[23] CMS Collab. (S. Chatrchyan *et al.*), *Phys. Lett. B* **716** (2012) 30 [arXiv:1207.7235 [hep-ex]].

[24] ATLAS Collaboration, "Measurements of the properties of the Higgs-like boson in the two photon decay channel with the ATLAS detector using 25 fb^{-1} of proton-proton collision data," ATLAS-CONF-2013-012 (2013).

[25] ATLAS Collaboration, "Study of the spin of the Higgs-like boson in the two photon decay channel using 20.7 fb^{-1} of pp collisions collected at $\sqrt{s} = 8$ TeV with the ATLAS detector," ATLAS-CONF-2013-029 (2013).

[26] ATLAS Collaboration, "Differential cross sections of the Higgs boson measured in the diphoton decay channel with the ATLAS detector using 8 TeV proton-proton collision data," ATLAS-CONF-2013-072 (2013).

[27] ATLAS Collaboration, "Measurements of the properties of the Higgs-like boson in the four-lepton decay channel with the ATLAS detector using 25 fb^{-1} of proton-proton collision data," ATLAS-CONF-2013-013 (2013).

[28] G. Aad *et al.* [ATLAS Collaboration], Phys. Lett. B **726** (2013) 88 [arXiv:1307.1427 [hep-ex]].

[29] ATLAS Collaboration, "Search for the Standard Model Higgs boson in $H \to \tau\tau$ decays in proton-proton collisions with the ATLAS detector," ATLAS-CONF-2012-160 (2012).

[30] ATLAS Collaboration, "Search for the Standard Model Higgs boson in produced in association with a vector boson and decaying to bottom quarks with the ATLAS detector," ATLAS-CONF-2012-161 (2012).

[31] G. Aad *et al.* [ATLAS Collaboration], Phys. Lett. B **726** (2013) 120 [arXiv:1307.1432 [hep-ex]].

[32] H. P. Nilles, Phys. Rept. **110** (1984) 1.

[33] For a comprehensive review on SUSY searches, see e.g.: V. A. Mitsou, J. Phys. Conf. Ser. **447** (2013) 012019 [arXiv:1304.1414 [hep-ph]].

[34] ATLAS Collaboration, "Search for pair-produced top squarks decaying into charm quarks and the lightest neutralinos using 20.3 fb^{-1} of

pp collisions at $\sqrt{s} = 8$ TeV with the ATLAS detector at the LHC," ATLAS-CONF-2013-068 (2013).

[35] ATLAS Collaboration, "Search for supersymmetry at $\sqrt{s} = 7$ TeV in final states with large jet multiplicity, missing transverse momentum and one isolated lepton with the ATLAS detector," ATLAS-CONF-2012-140 (2012).

[36] G. Aad *et al.* [ATLAS Collaboration], Phys. Rev. D **85** (2012) 012006 [arXiv:1109.6606 [hep-ex]].

[37] G. Aad *et al.* [ATLAS Collaboration], "Search for long-lived stopped R-hadrons decaying out-of-time with pp collisions using the ATLAS detector," arXiv:1310.6584 [hep-ex], Phys. Rev. D, *to appear* (2013).

[38] ATLAS Collaboration, "Search for a dijet resonance produced in association with a leptonically decaying W or Z boson with the ATLAS detector at $\sqrt{s} = 8$ TeV," ATLAS-CONF-2013-074 (2013).

[39] ATLAS Collaboration, "Search for resonant ZZ production in the $ZZ \to \ell\ell qq$ channel with the ATLAS detector using 7.2 fb^{-1} of $\sqrt{s} =$ 8 TeV pp collision data," ATLAS-CONF-2012-150 (2013).

[40] For a comprehensive review on searches, see e.g.: V. A. Mitsou, "Shedding Light on Dark Matter at Colliders," arXiv:1310.1072 [hep-ex], Int. J. Mod. Phys. A, *to appear* (2013).

[41] ATLAS Collaboration, "Search for new phenomena in monojet plus missing transverse momentum final states using 10 fb^{-1} of pp collisions at $\sqrt{s} = 8$ TeV with the ATLAS detector at the LHC," ATLAS-CONF-2012-147 (2012).

[42] G. Aad *et al.* [ATLAS Collaboration], Phys. Rev. Lett. **110** (2013) 011802 [arXiv:1209.4625 [hep-ex]].

[43] ATLAS Collaboration, "Search for dark matter pair production in events with a hadronically decaying W or Z boson and missing transverse momentum in pp collision data at $\sqrt{s} = 8$ TeV with the ATLAS detector," ATLAS-CONF-2013-073 (2013).

[44] ATLAS Collaboration, "Search for anomalous production of events with same-sign dileptons and b jets in 14.3 $\text{fb}^{-1}$of pp collisions at $\sqrt{s} = 8$ TeV with the ATLAS detector," ATLAS-CONF-2013-051 (2013).

[45] ATLAS Collaboration, "Search for pair production of heavy top-like quarks decaying to a high-p_{T} W boson and a b quark in the lepton plus jets final state in pp collisions at $\sqrt{s} = 8$ TeV with the ATLAS detector," ATLAS-CONF-2013-060 (2013).

[46] ATLAS Collaboration, "Search for heavy top-like quarks decaying to a Higgs boson and a top quark in the lepton plus jets final state in pp collisions at $\sqrt{s} = 8$ TeV with the ATLAS detector," ATLAS-CONF-2013-018 (2013).

[47] ATLAS Collaboration, "Search for pair production of new heavy quarks that decay to a Z boson and a third generation quark in pp collisions at $\sqrt{s} = 8$ TeV with the ATLAS detector," ATLAS-CONF-2013-056 (2013).

Physics highlights at ILC and CLIC

S. Lukić*
Vinča Institute of Nuclear Sciences, University of Belgrade, Serbia
On behalf of the FCAL Collaboration and the
CLIC detector and physics study

Abstract

In this lecture, the physics potential for the e^+e^- linear collider experiments ILC and CLIC is reviewed. The experimental conditions are compared to those at hadron colliders and their intrinsic value for precision experiments, complementary to the hadron colliders, is discussed. The detector concepts for ILC and CLIC are outlined in their most important aspects related to the precision physics. Highlights from the physics program and from the benchmark studies are given. It is shown that linear colliders are a promising tool, complementing the LHC in essential ways to test the Standard Model and to search for new physics.

1 Introduction

In the European strategy for particle physics, linear electron-positron colliders represent an important component of the future High-Energy physics program. They are designed for precision measurements, complementary to the present Large Hadron Collider (LHC), as well as to its possible upgrades and successors at CERN [1]. At present, two international projects are devoted to the design of the future linear colliders - the International Linear Collider (ILC) [2] and the Compact Linear Collider (CLIC) [3].

One of the main goals of the linear collider experiments is to test the Standard Model (SM), in particular regarding the mechanism of the Electroweak Symmetry Breaking (EWSB). The recent discovery of a new scalar boson at

*E-mail:slukic@vinca.rs

LHC [4], with properties consistent with those of the SM Higgs boson, has given a very strong impetus to this area of research. Precision measurements of the Higgs sector can test different existing theories describing EWSB. Another important area is the search for new physics. This area is driven by the quest to resolve open questions in particle physics, as well as by the evidence from cosmology of phenomena that cannot be explained within the framework of the SM.

The crucial motivation and potential of the linear colliders is that of fundamental advance in knowledge. This lecture will underline *new* knowledge that can be gained through precision measurements [2, 5].

1.1 The experimental environment at hadron versus lepton colliders

The difference in nature of the colliding particles lies at the origin of all of the major differences between the hadron and lepton collider experiments.

Since hadrons are compound objects, the initial state of individual partons is not uniquely defined. In the general case, initial states are realized as quantum superposition of states distributed according to the proton structure functions. In the analysis, distributions of initial parton states are calculated using QCD models tuned to data from deep inelastic scattering experiments [6].

At lepton colliders the colliding particles are elementary, therefore the inital state is well defined at the fundamental level. This allows for full reconstruction of the final state from conservation principles, up to the distribution of initial center-of-mass (CM) energies. The distribution of initial particle energies due to beam-beam effects can be precisely measured in the course of the experiment [7, 8, 9, 10, 11].

Each collision at a hadron collider creates a large number of elementary processes. Most of these processes represent background for the physics analysis, and deposit high doses of radiation energy in the detector. Complex trigger schemes, with the retention rate of only $\sim$ 1 event in 10^6, have to be employed during the data taking in order to select events that are of interest for the physics analysis. Moreover, due to high radiation levels, an important issue for the detector design is the radiation hardness of detectors at all angles.

By contrast, the total cross section at lepton colliders is relatively small. The total radiation levels are moderate, and the radiation dose does not represent an issue for the detector design except in the very forward region. The pulsed beam structure allows for the readout of all detector data. The readout

is thus triggerless, and the experiment is cleaner with regards to the physics background. In terms of cross sections, lepton colliders have high sensitivity to electroweak processes, allowing very precise measurements in the Higgs sector, as well as in the search for new physics.

2 The accelerator concepts

2.1 ILC accelerator

The electrons for the ILC beam are produced by a polarized photocathode DC gun electron source. The electrons are first accelerated to 15 GeV in the bunch compressor, and then in the main linac to the nominal energy. The positrons are generated by pair conversion of high-energy photons produced by passing the high-energy electron beam through an undulator. The beam acceleration in the ILC main linac is provided by niobium superconducting nine-cell cavities. The beam delivery systems then bring the two beams into collision with a crossing angle of 14 mrad.

The ILC beam is structured in bunch trains arriving at a rate of 5 Hz. The length of the bunch trains is 1 ms. The bunch spacing within the train is 370 ns, allowing full separation of events from different bunches by detector timing techniques. At 500 GeV in CM, each bunch contains 2×10^{10} electrons in a quasi-Gaussian spatial distribution with σ_x = 470 nm, σ_y = 5.9 nm and σ_z = 300 μm, resulting in instantaneous luminosity of $2 \times 10^{34} cm^{-2} s^{-1}$ [12].

The present state of the art of the superconducting RF technology is a result of several decades of development [13]. The field gradient in superconductors is limited by the field emission, as well as by the quench-causing surface defects. The FLASH FEL facility at DESY, Hamburg, has been in operation since 2004 with an average gradient of 20 MV/m in the main accelerator [14]. For the European XFEL program, gradients up to 35 MV/m have been realised in TESLA prototype cryomodules using surface electropolishing [15]. Many of the beam-tuning techniques required by the ILC have also been demonstrated at the FLASH FEL. R&D on creation of small emittance beams, as well as their focusing and alignment, is done at the Accelerator Test Facility (ATF) at KEK, Japan. Suppression of the electron cloud formation in the beam tube is studied within the CesrTA program at the Cornell University [12].

2.2 CLIC accelerator

The main objective of the CLIC project is to build a linear collider for the multi-TeV range at reasonable cost and size. This requires very high acceleration gradients, which cannot be reached with the superconducting technology. Therefore, CLIC is based on the novel two-beam acceleration technology, in which a low-energy high-current drive beam provides the RF power for the acceleration of the physics beam. The acceleration cavities for the main beam operate at room temperature, and can sustain field gradients over 100 MV/m .

In order to maintain a low breakdown rate, the length of the CLIC bunch train has to be limited to about 150 ns. At the same time, in order to achieve high luminosity, the bunch focusing has to be very strong, the bunch population high, and the bunch spacing very short. In the standard beam parameter set at 3 TeV, RMS bunch dimensions are σ_x = 40 nm, σ_y = 1 nm and σ_z = 44 μm, bunch population is 3.7×10^9 and bunch spacing is only 0.5 ns, which results in a luminosity value of $5.9 \times 10^{34} cm^{-2} s^{-1}$ [3]

The two-beam acceleration scheme is the subject of study of the CTF3 project at CERN. Some of the most important milestones achieved until now include the generation of an acceleration field well above 100 MV/m, as well as excellent performance of the accelerating structures at the nominal field of 100 MV/m without beam load [3].

3 The detectors for a linear collider

Two detector concepts are foreseen for the future linear collider, the International Large Detector (ILD) and the Silicon Detector (SiD) [16, 17]. The basic layout of both detectors is very similar (Fig. 1). The main tracker of ILD is based on a Time-Projection Chamber (TPC) for quasi-continuous track reconstruction, supplemented by inner and outer barrel silicon strip layers for precise track reference, and a forward silicon strip tracker. SiD is a compact cost-effective detector with a 5 Tesla magnetic field and all-silicon tracking with 5 layers in the barrel and 7 layers in the endcap region. Both detectors are planned to be implemented using a push-pull configuration which allows installing one detector in the beam line while the other is in the hangar for maintenance.

Vertex detector consists of a number of thin pixelized semiconductor layers with extremely light support structure. Its purpose is to allow reconstruction of the secondary vertices by precise tracking, avoiding multiple scattering in the material. The innermost barrel layer has a radius of 16 mm.

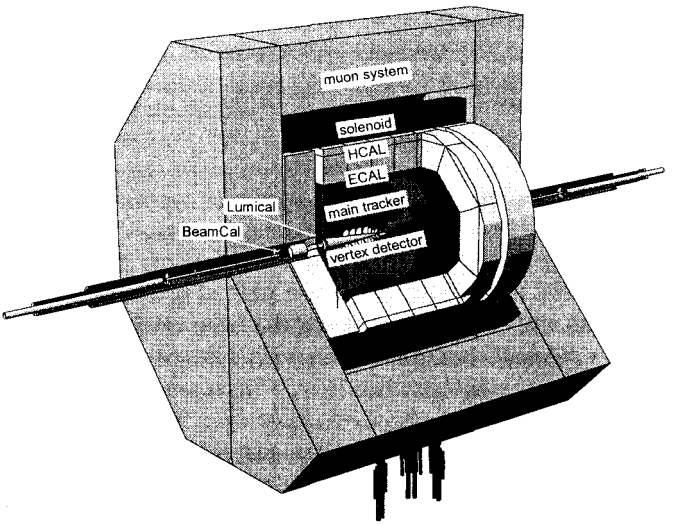

Figure 1: Schematic view of the International Large Detector concept for the linear collider.

Depending on the angle and energy of the detected particles, the impact parameter resolution is between a few μm and several ten μm [2].

Main tracker performs precise 3D reconstruction of particle tracks in the magnetic field. Both the ILD and the SiD tracker systems satisfy the design goal for the transverse momentum resolution of charged particles of $\Delta(1/p_T) \leq 2 \times 10^{-5}\mathrm{GeV}^{-1}$ [16, 17].

Electromagnetic calorimeter (ECAL) reconstructs electromagnetic (EM) showers and provides distinction of EM showers from the hadronic ones. The ECAL is designed with tungsten absorber layers, interspersed with scintillator tiles or silicon pads with high granularity. Because of the large difference between EM radiation length and nuclear interaction length in tungsten, hadronic showers develop slower, and start at larger depth of material than the EM showers.

Hadronic calorimeter (HCAL) is designed with steel absorbers and either scintillator tiles or gas detectors, with sufficient thickness for full containment of hadronic showers. The main aim of HCAL is to measure the energy of neutral hadrons, identified by the absence of tracks in the main

tracker. The long EM radiation length in steel allows fine longitudinal sampling with a reasonable number of layers.

Forward calorimeters In the very forward region of the detector, two calorimeters are installed, LumiCal for precise luminosity measurement by counting Bhabha-scattering events and BeamCal for fast luminosity estimate and for monitoring of the beam parameter by measurement of beam-induced processes at low angles. Both calorimeters are centered around the outgoing beam axis. BeamCal covers angles from below 1° to 2°, and LumiCal from about 2° to 6°. LumiCal is designed for precise reconstruction of EM showers, while the main challenge for BeamCal is radiation hardness because of the relatively high radiation dose at small angles [18].

Both detector concepts have also been adapted for the CLIC environment [5]. Main differences include calorimeter thickness, and the use of tungsten absorber, in order to contain higher-energy showers, higher semiconductor granularity to cope with the occupancy and a larger diameter of the innermost barrel layer of the vertex detector because of higher radiation.

3.1 Particle flow calorimetry

About 10% of energy of a typical jet is carried by long-lived neutral hadrons, 62% by charged particles, mostly hadrons, another 27% by photons and 1.5% by neutrinos [19]. If visible jet energy is entirely reconstructed from calorimetric information, the precision is limited by the relatively poor energy resolution of HCAL. To improve the jet energy resolution, the Particle Flow concept aims at full identification of all constituent particles in the detector system, so that charged particle energies can be reconstructed from track curvatures. To this aim, finely granulated calorimeters are required to separate and reconstruct showers. This allows for precise reconstruction of invariant masses of jets and accurate identification of physics events.

Figure 2 shows a typical reconstructed jet in a simulation of the CLIC_ILD. Electrons are identified by a curved track in the main tracker, and a fast-developing shower in the ECAL. Showers induced by photons develop fast as well, but there is no associated track in the tracker, due to the low interaction cross section in the low-density material of the tracker. Hadrons develop showers slower and deposit a large fraction of their energy in the HCAL. Neutral

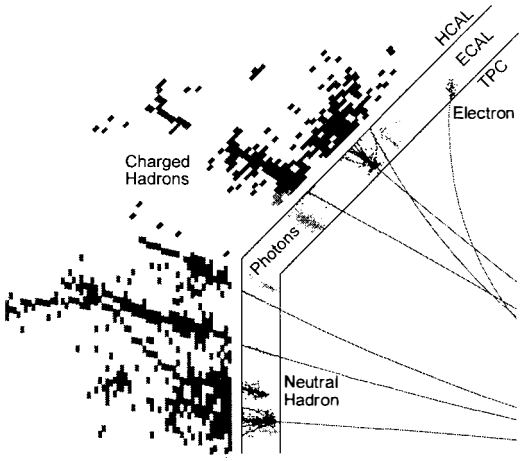

Figure 2: Particle tracks from a simulated jet in CLIC_ILD (from Ref. [19]).

hadrons have no associated track in the tracker. It has been shown by simulation that a jet energy resolution between 3 and 3.7% is achievable in the entire energy range from 0 to 1.5 TeV in the barrel region of the CLIC_ILD [19].

4 Physics program

Both in the ILC and the CLIC projects, the accelerator is planned to be built in stages defined with the physics potential in view. At each stage, each of the accelerators can be tuned to lower energy, at some cost in luminosity.

At 250 GeV, the Higgs boson production by Higgsstrahlung (HZ) has its maximum (see Fig. 3). This point gives access to first precise measurements of the Higgs couplings and mass. At an accelerator built for a 250 GeV CM energy, high-precision W mass study can be also performed by tuning the accelerator down to 160 GeV in CM. The "Giga-Z" program [20] is also within reach at 91 GeV in CM, provided that luminosity can be measured with the required precision. The 250 GeV CM energy is the first stage of the ILC program.

At 350 GeV, the Higgsstrahlung and the WW fusion ($H\nu_e\bar{\nu}_e$) processes of Higgs production have comparable cross sections. This allows for the measurement of absolute Higgs couplings, as well as a model-independent measurement of the total Higgs width. The top quark mass can be precisely measured in a

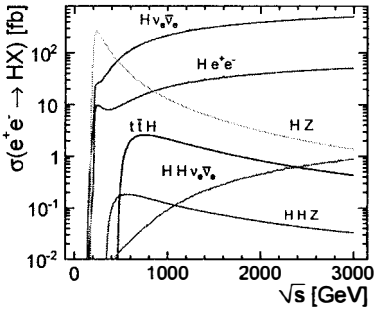

Figure 3: Higgs production cross section as a function of the CM energy.

production threshold scan. In the CLIC project, 350 GeV is considered as the first energy stage. In the ILC program, the top-pair threshold scan is performed at the 500 GeV stage with the accelerator tuned down to 350 GeV.

Above 350 GeV, Higgs production is accessed predominantly by the *WW* fusion, allowing higher precision of Higgs couplings. Precise measurement of most couplings of the gauge bosons is best performed at 500 GeV. New physics is best accessed at higher energies. Production thresholds for supersymmetric particles are expected to start just below 1 TeV, and the mass reach for searches such as the search for the Z' boson in the $e^+e^- \rightarrow f\bar{f}$ channel is higher for higher CM energies.

The ILC program is thus planned in three building stages. The 250 GeV stage for the first precise measurements of the Higgs sector, the nominal design energy of 500 GeV, and the ultimate CM energy of 1 TeV, achievable by extension of the main linac and the use of cavities with higher gradient, so that the total length of the facility reaches 50 km.

The CLIC machine is designed for searches for new physics at multi-TeV energies, with the goal to reach 3 TeV in the CM frame. Currently a lowest energy stage of 350 GeV is considered, followed by an upgrade to 1.4 TeV, and the final stage of 3 TeV, for which the accelerator facility will be 48 km long.

Benchmark studies of physics performance of the ILC and CLIC experiments have been performed using dedicated tool-chains consisting of process generation with realistic beam- and Beamstrahlung spectra, relevant physics- and beam-induced background, complete and realistic simulation of the interaction of the final particles with the detector, as well as event reconstruction using Particle Flow algorithms developed for the linear colliders.

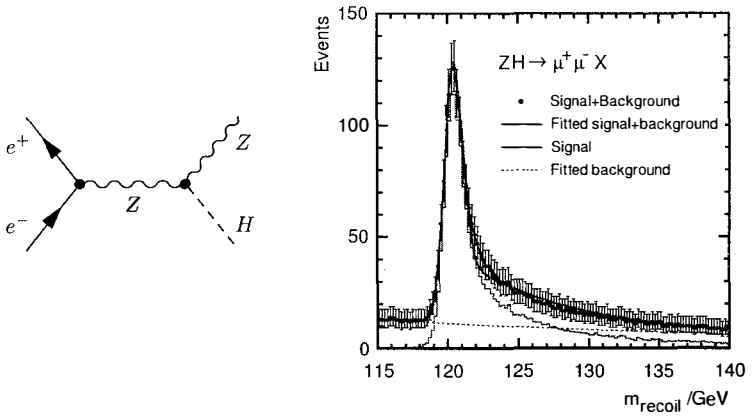

Figure 4: Left: Higgsstrahlung Feynmann diagram; right: recoil-mass distribution of muon pairs from the Z decay at 250 GeV ILC (figure taken from Ref. [16], see also [21]).

4.1 Highlights from the Standard Model

4.1.1 The Higgs boson

The program of precise measurements in the Higgs sector is an excellent illustration of the capacity of the linear collider to advance our understanding of particle physics. The entry point into this field is the Higgsstrahlung process, in which a Z boson is created in the annihilation of the initial electron-positron pair and emits a Higgs boson in the final state (Fig. 4, left). Experimental identification of the Higgsstrahlung is achieved by selecting lepton pairs with invariant mass consistent with the Z mass. The distribution of the recoil mass, calculated under the assumption that all events occur at the nominal CM energy, features a clear peak at the Higgs mass, and a high-energy tail due to the luminosity spectrum (Fig. 4, right). In the analysis of the $Z \to \mu^+\mu^-$ decay, the absolute value of g^2_{HZZ} is determined from the number of events in the peak with a precision of 2.5% at ILC [2] and 4.2% at CLIC [22]. The Higgs mass is determined from the position of the peak with a statistical precision of 40 MeV at the 250 GeV ILC [2] and 120 MeV at the 350 GeV CLIC [22]. If the analysis of the $Z \to e^+e^-$ decay is combined, the precision reaches 32 MeV at ILC [2].

At CM energies of 350 GeV and higher, Higgs production by WW fusion

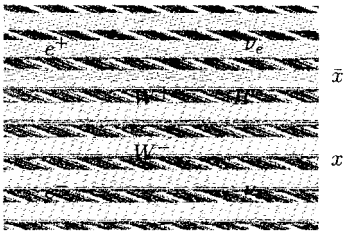

Figure 5: Feynmann diagram for Higgs production by WW fusion, and subsequent decay to a particle-antiparticle pair.

allows for the measurement of Higgs couplings via the branching ratios (BR) for the Higgs decay to a pair of fermions or gauge bosons (Fig. 5).

Using the value of g^2_{HZZ} obtained in the Higgsstrahlung measurement, the Higgs coupling to W is obtained from the relationship,

$$\frac{\sigma(e^+e^- \to ZH) \times BR(H \to x\bar{x})}{\sigma(e^+e^- \to \nu_e\bar{\nu}_e H) \times BR(H \to x\bar{x})} \propto \left(\frac{g_{HZZ}}{g_{HWW}}\right)^2, \tag{1}$$

where the best statistical precision is reached in the case when x stands for the b quark. Higgs total decay width, Γ_H, can be obtained from either the $H \to WW^*$ or the $H \to ZZ^*$ decay,

$$\sigma(e^+e^- \to \nu_e\bar{\nu}_e H) \times BR(H \to WW^*) \propto \frac{g^4_{HWW}}{\Gamma_H}. \tag{2}$$

Finally, Γ_H can be used to determine the absolute value of all other measured couplings.

At 1 TeV or above, the cross section for the WW^* fusion process is sufficiently high to allow for the measurement of rare Higgs decays such as the decay to a pair of muons, for which the BR is calculated to be 2.14×10^{-4} [23]. In such measurements, after subtraction of background by selection cuts or multivariate analysis (MVA), the shape of the dimuon invariant mass distribution of the signal on top of the remaining background is fitted to the data (Fig. 6). The statistical precision of BR($h \to \mu\mu$) is 32% at the 1 TeV ILC [2], 29% at the 1.4 TeV CLIC [22], and 16% at the 3 TeV CLIC [22, 24]. An overview of achievable uncertainties in various Higgs measurements can be found in the ILC Technical Design Report [2], as well as in the CLIC Snowmass paper [22].

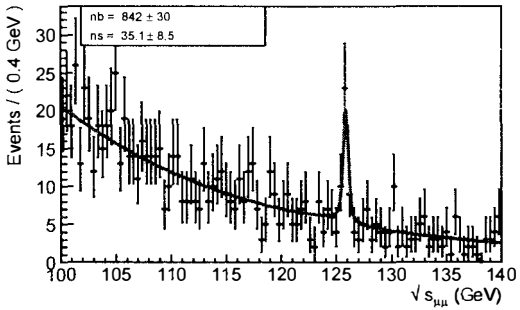

Figure 6: Fit of the model of the dimuon invariant mass distribution of the signal on top of the background remaining after an MVA selection at 1.4 TeV CLIC.

4.1.2 Top pair threshold scan

The top pair threshold scan is a very precise method of experimental determination of the top quark mass. The effective cross section for top pair production is measured in several energy points near the threshold, with $\sim 10 \text{fb}^{-1}$ of dedicated beam time per point. The position of the rising edge of the measured cross-section curve is sensitive to the top-quark mass. The precise value of the mass is extracted by fitting the theoretical calculation of the cross-section curve to the data. The luminosity spectrum, as well as the initial-state radiation (ISR) distribution have to be taken into account in the calculation, as can be seen in Fig. 7. The statistical uncertainty of the top mass obtained in this way at either ILC or CLIC is 34 MeV. The overall uncertainty is, however, limited by the uncertainties of the theoretical calculation to about 100 MeV [25].

4.2 Searches for new physics

Open questions in particle physics itself, as well as observations in other fields, such as cosmology, indicate that the SM does not cover all known phenomena. Such questions include the gauge hierarchy problem of the SM, the nature of elementary constituents of Dark Matter in the universe, or the source of CP violation in the evolution of the universe. Existing theoretical extensions of the SM that seek to address these questions drive the program of searches for new physics at future collider experiments.

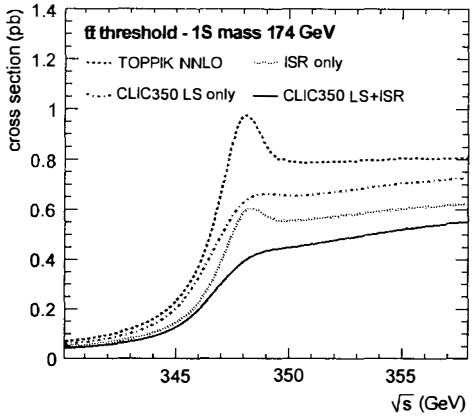

Figure 7: Influence of the luminosity spectrum on the measured cross-section curve in the top-pair threshold scan (taken from Ref. [25]).

4.2.1 New gauge boson

A common consequence of many extensions of the SM, in which the SM gauge group is embedded into a larger mathematical structure with additional U(1) symmetry groups, is the existence of one or more new, heavy and electrically neutral gauge bosons, denoted Z'. If the mass of Z' is within the kinematical reach of the collider, it is observable as a resonance in the $e^+e^- \to f\bar{f}$ channel. However, even if the Z' mass is higher than the CM energy of the collider, its existence can be observed via loop corrections of the $e^+e^- \to f\bar{f}$ cross section. The mass scale at which Z' is detectable by such effects depends on the precision of the $e^+e^- \to f\bar{f}$ measurement. Depending on the model, the sensitivity of the 500 GeV ILC to the Z' boson reaches between 4 and 10 TeV in terms of the 95% CL for exclusion [2]. The reach of the 1 TeV ILC is almost twice as high. At 3 TeV CLIC, depending on the couplings of Z' to fermions, 5σ discovery of the Z' boson will be possible for $m_{Z'}$ between 8 and 50 TeV, using the measured cross sections and forward-backward asymmetries [22].

4.2.2 Supersymmetry

Supersymmetric theories postulate symmetry between bosons and fermions at a TeV scale. They offer a natural candidate for dark matter, as well as a possibility

New particle	LHC (14 TeV)	HL-LHC	CLIC3
squarks [TeV]	2.5	3	$\lesssim$1.5
sleptons [TeV]	0.3	-	$\lesssim$1.5
Z′ (SM couplings) [TeV]	5	7	20
2 extra dims M_D [TeV]	9	12	20–30
TGC (95%) (λ_γ coupling)	0.001	0.0006	0.0001
μ contact scale [TeV]	15	-	60
Higgs composite scale [TeV]	5–7	9–12	70

Table 1: Discovery reach in various theory models for different colliders. LHC at 14 TeV refers to integrated luminosity of 100 fb^{-1}, HL-LHC 1 ab^{-1}, and the 3 TeV CLIC up to 2 ab^{-1}. Taken from Ref. [22].

of unification of forces at high energies. The potential for discovery of the supersymmetric partners of the SM leptons is higher at CLIC than at the 14 TeV LHC (Tab. 1, [22]). Depending on the supersymmetric model, the production threshold for the lightest sparticles, which have not yet been excluded by the LHC, lies just below 1 TeV, requiring linear colliders of 1 TeV or more for their discovery. If supersymmetric particles are discovered, linear colliders offer unique opportunity to measure their masses and couplings, and thus test the existing theories.

4.2.3 Discovery reach

A brief overview of the discovery reach of the 3 TeV CLIC in comparison with the LHC and the HL-LHC is given in Tab. 1 from Ref. [22]. Beside the discovery potential for the supersymmetric particles, and the Z' boson, energy scale for theories with extra spatial dimensions is listed, the sensitivity level for anomalous triple coupling of the gauge bosons (TGC), the μ contact interaction scale, as well as the composite Higgs boson mass scale [5].

5 Conclusions

In this lecture, basic motivation for building a next-generation linear collider was given, together with the accelerator and detector concepts. The physics program was outlined in its main aspects, including the SM studies and the search for new physics, and several higlights from the benchmark studies were

given. In these benchmark studies, based on detailed and realistic simulations, the precision capabilities of linear colliders were confirmed and significant discovery potential has been demonstrated for the searches for new physics. Linear collider is a promising tool, complementing the LHC in essential ways to test the SM and to search for new physics.

The linear collider study is a broad field for R&D in accelerator technology and in detector hardware, as well as for physics analysis work. Once built, the physics program of the linear collider unfolds in energy stages, and spans over 20 years of research work with potentially ground-breaking physics opportunities at each stage.

References

[1] *The European Strategy Session of the CERN Council in Brussels*, 30 May, 2013. http://council.web.cern.ch/council/en/EuropeanStrategy/ESParticlePhysics.html.

[2] H. Baer et al., eds., *The International Linear Collider - Technical Design Report*, vol. 2: Physics. International Linear Collider, 2013. ILC-REPORT-2013-040, http://www.linearcollider.org/ILC/TDR.

[3] M. Aicheler et al., eds., *A multi-TeV linear collider based on CLIC technology: CLIC Conceptual Design Report.* CERN European organization for nuclear research, 2012. CERN-2012-007.

[4] G. Aad et al., *Physics Letters B* **716** (2012) 1.

S. Chatrchyan et al., *Physics Letters B* **716** (2012) 30.

[5] L. Linssen, A. Miyamoto, M. Stanitzki, and H. Weerts, eds., *Physics and Detectors at CLIC: CLIC Conceptual Design Report.* CERN European organization for nuclear research, 2012. CERN-2012-003.

[6] F. Aaron et al., *Journal of High Energy Physics* **01** (2010) 1–63.

[7] K. Mönig, *Measurement of the differential luminosity using bhabha events in the forward-tracking region at TESLA*, LC Note LC-PHSM-2000-60-TESLA, TESLA project, 2000.

[8] C. Rimbault, P. Bambade, K. Mönig, and D. Schulte, *Journal of Instrumentation* **2** (2007) P09001.

[9] S. Lukić, I. Božović-Jelisavčić, M. Pandurović, and I. Smiljanić, *Journal of Instrumentation* **8** (2013) P05008, [arXiv:1301.1449]. LCD-Note-2012-008.

[10] I. Božović-Jelisavčić, S. Lukić, G. Milutinović-Dumbelović, M. Pandurović, and I. Smiljanić, *Journal of Instrumentation* **8** (2013) P08012, [arXiv:1304.4082].

[11] S. Poss and A. Sailer, *Luminosity spectrum reconstruction at linear colliders*, Note LCD-Note-2013-010, CERN, 2013.

[12] C. Adolphsen et al., eds., *The International Linear Collider - Technical Design Report*, vol. 3: Accelerator. International Linear Collider, 2013. ILC-REPORT-2013-040, http://www.linearcollider.org/ILC/TDR.

[13] http://tesla-new.desy.de.

[14] http://flash.desy.de/accelerator/.

[15] L. Lilje et al., *NIM* **A 524** (2004) 1.

[16] ILD Concept Group, *The International Large Detector - Letter of Intent*, Report DESY 2009/87 - Fermilab PUB-09-682-E - KEK Report 2009-6, 2010. http://ilcild.org/.

[17] H. Aihara, P. Burrows, and M. Oreglia, eds., *SiD Letter of Intent*. 2009.

[18] H. Abramowicz et al., *Journal of Instrumentation* **5** (2010) P12002.

[19] J. S. Marshall, A. Münnich, and M. A. Thomson, arXiv:1209.4039.

[20] R. Hawkings and K. Mönig, *Eur. Phys. J direct* **1** (2000) 1.

[21] H. Li et al., *HZ recoil mass and cross section analysis in ILD*, LC Note LC-PHSM-2009-006, DESY, 2009.

[22] H. Abramowicz et al., arXiv:1307.5288.

[23] LHC Higgs Cross Section Working Group, arXiv:1201.3084.

[24] C. Grefe, *Light Higgs decay into muons in the CLIC SiD detector*, Note LCD-Note-2011-035, CERN, 2011.

[25] K. Seidel, F. Simon, M. Tesař, and S. Poss, *Eur. Phys. J* **C 73** (2013) 2530.

Precise luminosity measurement at a Linear Collider

S. Lukić*

Vinča Institute of Nuclear Sciences, University of Belgrade, Serbia

On behalf of the FCAL Collaboration

Abstract

The high charge density and high energy at future linear colliders will present challenges to the luminosity measurement that have not been there in the past. The intense electromagnetic interaction between the electron bunches influences the luminosity measurement at the level of several percent. Precise correction of the beam-beam effects, based on experimentally measurable quantities, is described here. In addition, a comprehensive list of systematic effects in luminosity measurement is given, with their individual contributions to the final uncertainty of the luminosity figure.

1 Introduction

High-precision capabilities of linear electron-positron colliders earn such experiments a significant place in the program of elementary particle physics. A crucial condition necessary to fully realize the precision potential of the linear colliders is precise measurement of luminosity. Luminosity is a key figure relating the observed number of events of a given process to its cross section. In the most straightforward sense, it can be defined by the expression,

$$L = N_1 N_2 \frac{f}{A} \tag{1}$$

*E-mail:slukic@vinca.rs

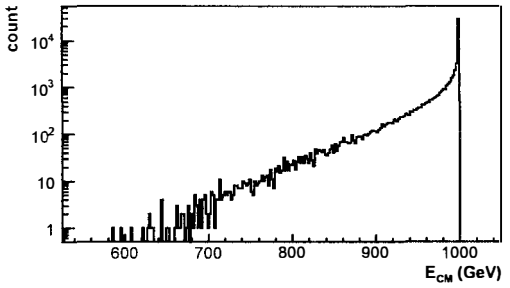

Figure 1: Luminosity spectrum at 1 TeV ILC, simulated using Guinea-Pig [1]

Here N_1 and N_2 are the average populations of the colliding bunches, f is the overall bunch-crossing rate, and A is the overlap integral of the 2D density distributions of the two bunches in the perpendicular plane.

The *luminosity spectrum* $\mathcal{L}(E_{CM})$ is defined as the distribution of the center-of-mass (CM) energy E_{CM} available to individual collisions in the experiment. Due to beam-beam effects (see Sec. 2), the luminosity spectrum features the characteristic low-energy tail (Fig. 1)

The basic expression,

$$L\sigma_a = N_a \tag{2}$$

relates the luminosity, the cross section σ_a of an elementary process a in a given part of the phase space defined by experimental selection cuts, and the number of detected events N_a of the process a in the same part of the phase space.

In production threshold scans, the luminosity spectrum, including the luminosity peak shape, as well as the low-energy tail, affect the results of the scan in a considerable way [2]. It is thus indispensable to know the luminosity spectrum to sufficient precision in order to be able to fit the theoretical distributions of the kinematic parameters to the measurement.

Presently the most precise way to measure luminosity at a linear collider is to use Bhabha-scattering as the gauge process. Bhabha scattering is characterized by low angles (the cross section scales approximately with θ^{-3}), as well as by final energies close to the beam energy. The cross section is relatively high, ensuring good statistical accuracy. Precision better than 10^{-3} was reached with this method at LEP, thanks to a careful experimental setup, and precise QED calculations [3, 4, 5, 6]. At future linear colliders, the International Linear

Collider (ILC) [7] and the Compact Linear Collider (CLIC) [8], the CM energy will be 3 to 30 times higher, and luminosity up to thousand times higher. In such conditions, intense beam-beam effects induce severe counting biases of Bhabha-events which require dedicated correction procedures, as pointed out in Ref. [9].

1.1 The luminosity calorimeter - LumiCal

The luminometer for the future linear colliders (LumiCal, Fig. 2) is designed as a pair of sampling calorimeters with cylindrical geometry, centered around the outgoing beam axis at ~ 2.5 m from the interaction point (IP) on both sides. The calorimeters consist of a number of layers in the longitudinal direction, each layer containing a tungsten disk and a segmented sensor plate. Electromagnetic (EM) showers developing in tungsten are sampled in the sensor plates. The absorber plates are each 3.5 mm thick, corresponding to one radiation length in tungsten. The number of layers is 30 for ILC, and 40 for CLIC. The Molière radius of LumiCal is ~ 1.5 cm. The sensor plates are segmented both radially and azimuthally, allowing full reconstruction of the four momenta of the detected particles. The outer radius of the LumiCal is 196 mm in the ILC case, and ca. 300 mm in the CLIC case. The inner radius is 80 mm in the ILC case, and 100 mm in the CLIC case.

The fiducial volume (FV) of the calorimeters is defined as the angular range with optimal energy resolution, and covers angles from 41 to 67 mrad at ILC, and 43 to 80 mrad at CLIC.

Bhabha events are recognized by coincident detection of showers in the FV of both halves of the luminometer in a given energy range near the peak energy. According to Eq. 2, the luminosity figure is then obtained by dividing the number of detected events by the Bhabha cross section integrated in the corresponding region of the phase space.

In Sec. 2, the physical processes affecting the luminosity measurement will be outlined, and the event simulation methods used in this work will be briefly described. In Sec. 3, a method of handling the counting bias due to beam-beam effects will be described and tested on simulated events. In the conclusions, the performance of the method for the final precision of the luminosity measurement will be summarized and discussed.

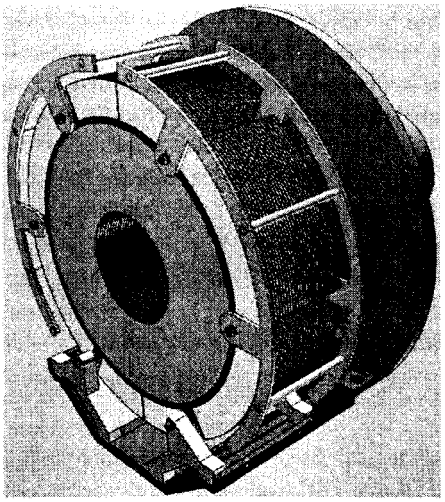

Figure 2: LumiCal sketch

2 Physics of the luminosity measurement

2.1 Physical processes affecting the luminosity measurement

Beamstrahlung

In order to reach the projected luminosity at future linear colliders, the electron[1] beams will be focused to a few nm in the vertical direction, and a few ten to few hundred nm in the horizontal directions [7, 8] at the interaction point (IP), resulting in extremely high local charge densities, and extremely intense EM interaction between the opposing bunches. In case of a charge moving with relativistic velocity $\vec{v}$, the component of EM field perpendicular to $\vec{v}$ scales the Lorentz factor $\gamma = 1/\sqrt{1 - v^2/c^2}$. At future linear colliders, the Lorentz factor of the bunches is of the order of 10^6 in the lab frame, or 10^{12} in the rest frame of the opposing bunch. Since the bunches have opposite charge signs, the direction of the perpendicular component of the Lorentz force points towards the bunch center. This results in a very strong focusing effect of the bunches – the *pinch effect*. The pinch effect enhances the luminosity, but induces emission of intense and energetic EM radiation, *Beamstrahlung*, from the electrons in the

[1] Unless stated otherwise, electron always refers to electron or positron

bunch. For an elaborate treatment of the beam-beam effects, see Refs. [10, 1].

The angular distribution of Beamstrahlung is contained in several hundred μrad around the beam axis. The distribution of energy loss of individual electrons is very wide, and depending on the conditions, may reach up to the beam energy. This leads to the creation of the low-energy tail of the luminosity spectrum (see Fig. 1). At the level of individual e^+e^- collision events, Beamstrahlung energy loss prior to the collision is asymmetric between the two colliding particles, resulting in non-zero velocity of the CM frame of the collision with respect to the lab frame.

Initial and Final State Radiation

The Bhabha process is accompanied by emission of the initial- and final state radiation (ISR, FSR). ISR and FSR are QED phenomena, and their energy- and angular distributions can be precisely calculated [11]. Due to the quantum interference terms, ISR and FSR cannot be cleanly separated at the fundamental level. The resulting angular distribution is quasi-continuous, with sharp peaks around the initial and final electron momenta.

Boost of the collision frame

In the frame of the two Bhabha electrons after emission of Beamstrahlung and ISR, and before emission of FSR, the *collision frame*[2], the deflection angle is the same for both particles, according to the momentum-conservation principle. This angle is denoted the *scattering angle*, θ^{coll}.

As the collision frame is recoiling against the photons radiated before the scattering, it has a velocity $\vec{\beta}_{coll}$ with respect to the lab frame. $\vec{\beta}_{coll}$ is collinear with the beam axis, axcept in rare cases when ISR is emitted under significant angle with respect to the beam. In the lab frame, the final particles have angles θ_1^{lab} and θ_2^{lab}, which correspond to the scattering angle θ^{coll} and its mirror image $\pi - \theta^{coll}$ boosted by $\vec{\beta}_{coll}$. Because of the boost, even if θ^{coll} was in the angular range of the FV of the LumiCal, one or both of the final angles in the lab frame may be outside FV. In this way, Beamstrahlung induces an *angular counting loss* of Bhabha events.

At LEP, the intensity of the beam-beam effects was small, and application of asymmetric selection cuts was sufficient to minimize the uncertainties arising from the Beamstrahlung to the required level. At future linear colliders, where

[2]Also denoted the *hard-scattering frame* in literature, see [11]

the beam-beam effects are far more intense, the angular counting loss is of the order of several percent. If one endeavors to correct this counting bias using bunch-crossing simulations, the ultimate precision will be limited by the precision of the simulation, and by the uncertainties in the determination of beam parameters. A method of event-by-event correction of the angular counting loss by direct measurement of the boost of the collision frame [12] is described in sec 3.

Processes after scattering

After scattering, the final electrons may emit FSR. Beside that, their trajectories are deflected inwards by a fraction of mrad under the influence of the EM field of the opposing bunch, thus inducing a small additional angular counting loss termed Electromagnetic Deflection (EMD) effect. Beamstrahlung may be emitted at this stage as well, but since it is emitted under very small angles with respect to the final electrons, it is summed with the electrons in the calorimeter.

Bhabha event spectrum

For the reconstruction of the luminosity spectrum from the energy spectrum of the Bhabha scattering events, it is important to take into account the energy dependence of the Bhabha cross section,

$$\mathcal{B}(E_{CM}) = \mathcal{L}(E_{CM})\frac{\mathrm{d}\sigma_B}{\mathrm{d}E_{CM}} \propto \mathcal{L}(E_{CM})/E_{CM}^2 \tag{3}$$

Since ISR mostly misses the luminometer, the CM energy reconstructed from the detected particles is $E_{CM,rec} < E_{CM}$, and the corresponding spectrum can be represented as a generalized convolution of $\mathcal{B}(E_{CM})$ and the function $\mathcal{I}(x)$ describing the fractional CM energy loss due to the ISR,

$$h(E_{CM,rec}) = \int_0^{E_{max}} \mathcal{B}(E_{CM})\frac{1}{E_{CM}}\mathcal{I}(\frac{E_{CM,rec}}{E_{CM}})\,\mathrm{d}E_{CM} \tag{4}$$

In the frame of the two-electron system after emission of ISR and before emission of the FSR, i.e. the *collision frame*, the deflection angles in the collision are the same for both particles, according to the momentum-conservation principle. One can, therefore, define a unique *scattering angle* θ^{coll}.[3]

[3]Rigorous definition of the collision frame is not straightforward because of the quantum

2.2 Simulation tools for the analysis of the physics of the luminosity measurement

To estimate the precision of the luminosity measurement, Bhabha events in the bunch-collision were simulated using the Guinea-Pig software for the simulation of the bunch crossing [1], and the BHLUMI Bhabha event generator [11]. For details on feeding BHLUMI events to Guinea-Pig, see Ref. [12].

The simulations were run with the standard parameter set from the ILC Technical Progress Report 2011 [13] as the basis for both the 500 GeV and the 1 TeV ILC cases, as well as with the standard simulated bunch density and momentum distributions for CLIC from Ref. [14]. In the ILC case, beside the standard parameter set, simulations were also performed with 24 different variations of individual beam-parameters, in order to determine the influence of the beam-parameter uncertainties on the performance of the presented methods. The simulated beam-parameter variations included symmetric variations of the bunch size parameters $\sigma_{x,y,z}$ and the bunch charge q by ± 10 and $\pm 20\%$, one-sided variations of $\sigma_{x,y,z}$ ans q by $+20\%$, as well as beam misalignment in x- and y-direction by up to one $\sigma_{x,y}$, respectively.

The interaction with the detector was approximated by parametrization of the detector resolutions, as well as by summing together the four-momenta of all particles that are closer together than one Molière radius, as described in detail in Ref. [12].

3 Correction of the beam-beam effects

The analysis of the Bhabha count proceeds as follows: correction of the angular counting loss, deconvolution of the ISR energy loss, numerical correction for the counting bias due to the LumiCal energy resolution [12], and finally the correction of the EMD counting bias.

3.1 Angular counting loss

Since the angles of the detected showers, θ_1^{lab} and θ_2^{lab}, are boosted by $\vec{\beta}_{coll}$ with respect to the scattering angle θ_{coll}, $\vec{\beta}_{coll}$ can be reconstructed to a good approximation from θ_1^{lab} and θ_2^{lab}. If β_{coll} is taken to be collinear with the z-axis, the

interference between ISR and FSR. In practice, the collision frame is defined as the CM frame of the final electrons together with all radiation within a given tollerance angle with respect to the respective final electron momenta.

system of two equations given by the expressions for the boost of the final particle momenta allows reconstructing β_{coll} and θ_{coll},

$$\beta_{coll} = \frac{\sin(\theta_1^{lab} + \theta_2^{lab})}{\sin\theta_1^{lab} + \sin\theta_2^{lab}} \quad ; \quad \frac{1}{\tan\theta_{coll}} = \gamma_{coll}\left(\frac{1}{\tan\theta_1^{lab}} - \beta_{coll}\frac{1}{\sin\theta_1^{lab}}\right) \qquad (5)$$

The effective acceptance of Bhabha events in the luminometer decreases with increasing β_{coll}. The effective limiting scattering angles θ_{min}^{coll} and θ_{max}^{coll} in the collision frame for a given β_{coll} are obtained by boosting θ_{min} and θ_{max} into the collision frame. This allows calculating the event-by-event weighting factor to compensate for the loss of acceptance,

$$w(\beta_{coll}) = \frac{\int_{\theta_{min}}^{\theta_{max}} \frac{d\sigma}{d\theta}\, d\theta}{\int_{\theta_{min}^{coll}}^{\theta_{max}^{coll}} \frac{d\sigma}{d\theta}\, d\theta}. \qquad (6)$$

The results of correction are shown in Fig. 3 for the 1 TeV case. The control spectrum (black) contains all events that would hit the FV of the LumiCal if there were no boost of the collision frame. The detected spectrum is shown in red, and the corrected spectrum green. The blue line represents the events for which β_{coll} is higher than some limiting value β^*, at which the effective acceptance of LumiCal is reduced to zero. Due to kinematic constraints, high values of β_{coll} are possible only with high energy loss, which explains the sudden drop of such events at 80% of the nominal CM energy. However, a small number of events with apparent $\beta_{coll} > \beta^*$ is present also at energies above 80% of the nominal CM energy, because occasionally the assumption that β_{coll} is collinear with the beam axis is broken due to off-axis ISR. This is visible in the zoomed figure (Fig. 3, right), where these events are scaled by a factor 100.

The following is the list of sources of systematic uncertainty of the collision-frame method:

1. Off-axis ISR. In rare events with significant off-axis ISR, the assumption that β_{coll} is collinear with the beam axis does not hold,

2. The implicit assumption that the cluster around the most energetic shower always contains the Bhabha electron. In a fraction of events of the order of a few permille, this is not the case, and the reconstructed polar angles $\theta_{1,2}^{lab}$ may differ from the final electron angles.

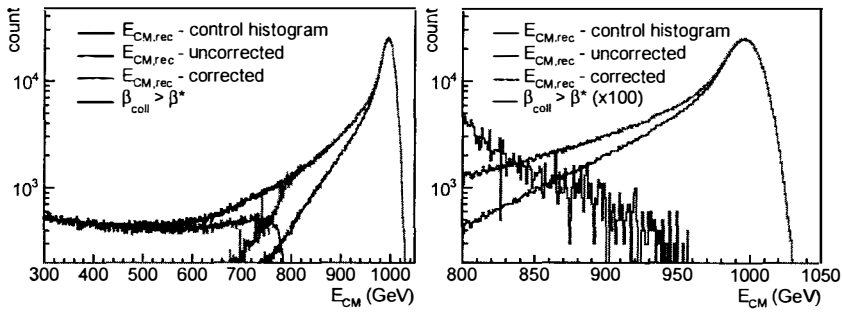

Figure 3: Correction of the counting loss due to Beamstrahlung and ISR at 1 TeV. Left: whole spectrum; right: zoom on energies above 800 GeV. Black: Simulated control spectrum without counting loss due to Beamstrahlung and ISR; red: Reconstructed E_{CM} spectrum affected by the counting loss; green: Reconstructed spectrum with correction for the counting loss due to Beamstrahlung and ISR; blue: events inaccessible to the correction

3. The use of the approximate angular differential cross section for the Bhabha scattering in the calculation of the correction weight,

4. Assumption that all ISR is lost, and all FSR is detected, in the calculation of β_{coll} and w.

The relative bias due to the off-axis ISR is if the order of one permille. This bias is related to the energy- and angular distribution of the ISR, which is reliably predicted by the generator. Thus this bias can be reliably corrected, and it is not sensitive to beam-parameter variations.

The uncertainty introduced by the implicit assumption that the cluster around the most energetic shower always contains the Bhabha electron depends on the beam parameters, and it may even depend on the specifics of the position-reconstruction algorithm in the luminometer. Its correction is beyond the scope of the present study. The contribution of the effects 3 and 4 is smaller than the statistical uncertainty of the present analysis. The final quoted uncertainty, containing the contributions from the effects 2, 3 and 4 in the upper 20% of the luminosity spectrum is as follows: For the 500 GeV ILC, the uncertainty is $(+0.4 \pm 0.1) \times 10^3$, for the 1 TeV ILC, it is $(+0.7 \pm 0.1) \times 10^3$. The absolute size of these final biases can be taken as the present estimate of the uncertainty of the luminosity measurement induced by beamstrahlung and ISR.

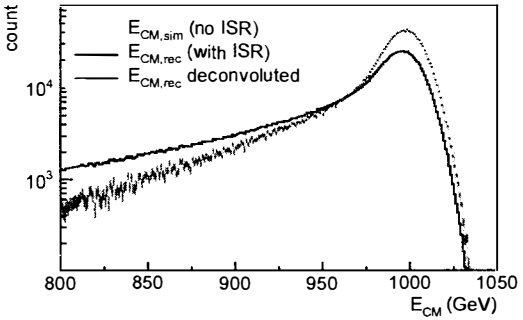

Figure 4: Deconvolution of the ISR deformation of the luminosity spectrum. Yellow: the control histogram – simulated E_{CM} before emission of ISR, smeared with a normalized Gaussian; black: the histogram affected by the ISR energy loss – reconstructed E_{CM} from the detected showers, green: deconvoluted spectrum.

3.2 ISR energy loss

To obtain the Bhabha CM energy distribution $\mathcal{B}(E_{CM})$, the ISR energy loss should be deconvoluted from $h(E_{CM,rec})$. This deconvolution can be performed using the theoretical form of the distribution $\mathcal{I}(x)$ of the ISR fractional energy loss, and by solving the system of linear equations resulting from the discretization of Eq. 4 [12]. To obtain the function $\mathcal{I}(x)$, the distribution of $x = E_{CM,rec}/E_{CM}$ was taken from the BHLUMI file, and the beta distribution was fitted to it for $x > 0.8$.

The results of the deconvolution are shown in Fig. 4. The control histogram (yellow) contains simulated CM energies before ISR emission, smeared by the energy resolution of the LumiCal. The histogram with ISR energy loss (black) is simply the histogram resulting from the correction of the angular counting loss in the previous step. The deconvoluted histogram is shown as green points with error bars.

The uncertainty estimate of the deconvolution procedure alone for the integral luminosity in the upper 20% of the spectrum is given by the relative integral difference between the deconvoluted and the control spectrum in the upper 20%. This uncertainty is $(+0.81 \pm 0.22) \times 10^{-3}$ at 1 TeV, and $(+0.35 \pm 0.21) \times 10^{-3}$ at 500 GeV.

3.3 Energy resolution

Since full energy information of the detected particles is used to determine the luminosity spectrum, the energy resolution of LumiCal induces a bias in the Bhabha count by asymmetric redistribution of events around the CM energy cut because of the slope in the form of the spectrum at the cut energy. This can be corrected by integration of the fitted parametrized form of $\mathcal{B}(E_{CM})$. When the cut is made at 80% of the nominal energy, the size of this correction is between 1 and 4×10^{-4}. It has been shown in Ref. [12] that the energy-resolution effect can be corrected to better than 1×10^{-4}.

3.4 Angular loss due to the EMD

The EMD shifts the polar angles of the outgoing particles consistently towards smaller angles. Since the Bhabha cross section is monotonously decreasing with the polar angle, the net effect of the EMD is a decrease in the Bhabha count. Since the EMD bias is small, correction by MC simulation of the bunch crossing has sufficient precision. The precision is limited by the beam-parameter uncertainties in the MC simulation. If the conservative beam-parameter uncertainty described in Sec. 2.2 is taken, the precision of EMD correction is $\pm 5 \times 10^{-4}$ of the total luminosity at 500 GeV, and $\pm 2 \times 10^{-4}$ at 1 TeV. If the beam parameters are known with better precision than 20% (see Ref. [15]), the residual uncertainty will be correspondingly smaller.

4 Overview of the systematic uncertainties in luminosity measurement

Beside the uncertainties remaining after correction of the beam-beam effects, a number of further systematic effects limits the achievable luminosity precision at future linear colliders. These will be briefly reviewed here.

4.1 Physics background

A major systematic effect in the luminosity measurement originates from the four-fermion neutral-current processes of the type $e^+e \to e^+e\bar{f}f$. These processes have a signature similar to Bhabha scattering, characterized by the outgoing e^+e pairs at low angles carrying a large fraction of the beam energy so

they can be miscounted as signal. Using event selection based on coplanarity and CM energy, the fraction is reduced to 2.2 permille at 500 GeV and 0.8 permille at 1 TeV [16].

At present there are no accurate estimates of the theoretical precision with which the fraction of physics background events is calculated. Thus the above quoted fractions, obtained using the WHIZARD generator, will be taken as a full-size effect.

4.2 Systematics of the polar angle reconstruction

Matching of the experimental and the theoretical selection cuts in Eq. 2 depends crucially on the precision of the reconstruction of the polar-angle of the shower.

The inner radius of the active volume of the LumiCal has to be known with precision of 10 μm in order to keep the resulting luminosity uncertainty well below 1 permille [17, 18].

Position uncertainty LumiCal – IP reflects directly on the polar angle uncertainty. It is affected by the lateral positioning uncertainty of the Lumical relative to the final beam-delivery quadrupole, by the uncertainty of the lateral IP position determined by the beam-position monitors, and by the longitudinal uncertainty in the relative positioning of the two calorimeters. All three of these parameters must be known at the level of several hundred μm in order to keep the resulting luminosity uncertainty at the one-permille level [17, 18].

Intrinsic reconstruction uncertainties due to the shower reconstruction algorithm of the LumiCal introduce a polar angle bias of 3.2×10^{-3} mrad and polar angle resolution of 2.2×10^{-2} mrad [19]. Each of these effects adds an independent contribution of 0.16 permille to the luminosity uncertainty [17].

4.3 Cross section

The Bhabha cross-section calculation for the LEP experiment reached a precision of 0.54 permille [6]. For the future linear colliders, new calculations are necessary, because the contribution of the virtual Z-boson exchange alters the cross section significantly. Presently a new Bhabha generator is under development [20] which will include beam polarization, the background processes, as well as the wide-angle measurement.

The uncertainty on the beam polarization affects the luminosity figure via the cross-section calculation at the level of 0.19 permille [17].

5 Conclusions

Precise luminosity measurement is essential at linear colliders in order to fully exploit their intrinsic precision physics capabilities. A number of systematic effects, of whoch the most dramatic are the beam-beam effects, limit the achievable precision.

The collision-frame method corrects the beam-beam effects by directly measuring the counting losses via experimentally observable quantities related to the beam-beam effects in a fundamental way. Precision of below 1 permille is reached, essentially independent of the precision with which the key beam parameters are known.

Contributions of the beam-beam effect correction, as well as from other sources, to the overall systematic uncertainty of the luminosity measurement are listed in Tab. 1.

Table 1: Systematic uncertainties in luminosity measurement.

Source of uncertainty	500 GeV (10^{-3})	1 TeV (10^{-3})
Bhabha cross section	0.54	0.54
Polar-angle resolution	0.16	0.16
Polar-angle bias	0.16	0.16
IP lateral position	0.1	0.1
Energy resolution	0.1	0.1
Energy scale	1	1
Beam polarization	0.19	0.19
Correction of angular losses due to Beamstrahlung	0.4	0.7
ISR deconvolution	0.4	0.8
EMD correction	0.5	0.2
Physics background	2.2	0.8
Total	2.6	1.8

The final uncertainty is 2.6, respectively 1.8 permille in the 500 GeV and the 1 TeV cases. This satisfies the requirement for the largest part of the Physics programme at the ILC. However, for high-precision measurements such as the Giga-Z programme, precision of 10^{-4} is required [21]. Uncertainties pre-

sented here may be refined towards this goal as more precise knowledge becomes available on beam-parameter physical correlations, the cross section of the physics background, as well as with further refinement of the correction methods.

References

[1] D. Schulte, *Study of Electromagnetic and Hadronic Background in the Interaction Region of the TESLA Collider*. PhD thesis, Hamburg University, 1996.

[2] F. Simon, *Optimum lumi spectrum and required accuracy for a tt scan near threshold*, in *FCAL workshop, DESY Zeuthen, Germany*, 7-9 May, 2012. https://indico.desy.de/conferenceDisplay.py?confId=5333.

[3] OPAL Collaboration, *Eur.Phys.J.* **C14** (2000) 373–425, [hep-ex/9910066].

[4] **ALEPH Collaboration** Collaboration, ALEPH Collaboration, *Eur.Phys.J.* **C14** (2000) 1–50.

[5] **L3 Collaboration** Collaboration, L3 Collaboration, *Eur.Phys.J.* **C16** (2000) 1–40, [hep-ex/0002046].

[6] A. Arbuzov et al., *Physics Letters B* **383** (1996) 238.

[7] ILC Collaboration, *The International Linear Collider - Technical Design Report*. International Linear Collider, 2013. ILC-REPORT-2013-040, http://www.linearcollider.org/ILC/TDR.

[8] M. Aicheler et al., eds., *A multi-TeV linear collider based on CLIC technology: CLIC Conceptual Design Report*. CERN European organization for nuclear research, 2012. CERN-2012-007.

[9] C. Rimbault, P. Bambade, K. Mönig, and D. Schulte, *Journal of Instrumentation* **2** (2007) P09001.

[10] K. Yokoya and P. Chen, *Beam-beam phenomena in linear colliders*, in *Frontiers of Particle Beams: Intensity Limitations*, vol. 400 of *Lecture Notes in Physics*, pp. 415–445, Springer Verlag, 1991. US-CERN School on Particle Accelerators.

[11] S. Jadach, W. Placzek, E. Richter-Was, B. Ward, and Z. Was, *Computer Physics Communications* **102** (1997) 229.

[12] S. Lukić, I. Božović-Jelisavčić, M. Pandurović, and I. Smiljanić, *Journal of Instrumentation* **8** (2013) P05008, [arXiv:1301.1449]. LCD-Note-2012-008.

[13] E. Elsen et al., eds., *International Linear Collider - A technical progress report*. International Linear Collider, 2011. ILC-REPORT-2011-30, ISBN: 978-3-935702-56-0.

[14] D. Schulte et al., *CLIC simulations from the start of the linac to the interaction point*, in *Proceedings of EPAC 2002, Paris, France*, 2002. CERN-PS-2002-053-AE ; CLIC-Note-529.

[15] C. Grah and A. Sapronov, *Journal of Instrumentation* **3** (2008), no. 10 P10004.

[16] I. Božović-Jelisavčić, S. Lukić, G. Milutinović-Dumbelović, M. Pandurović, and I. Smiljanić, *Journal of Instrumentation* **8** (2013) P08012, [arXiv:1304.4082].

[17] H. Abramowicz et al., *Journal of Instrumentation* **5** (2010) P12002.

[18] A. Stahl, *Luminosity measurement via Bhabha scattering: Precision requirements for the luminosity calorimeter*, LC Note LC-DET-2005-004, SLAC, 2005.

[19] I. Sadeh, *Luminosity measurement at the International Linear Collider*, Master's thesis, Tel Aviv University, 2008.

[20] V. Makarenko, *New generator for Bhabha scattering*, in *The XII-th International School-Seminar, The Actual Problems of Microworld Physics, Gomel, Belarus*, July 22 - August 2, 2013.

[21] T. Behnke, C. Damerell, J. Jaros, and A. Miyamoto, eds., *International Linear Collider - Reference Design Report*, vol. 4. ILC Global Design Effort and World Wide Study, 2007.

Probing and Identifying New Physics Scenarios at International Linear Collider

A.A. Pankov*, I.A. Serenkova†, A.V. Tsytrinov‡, I.A. Pankov§
Abdus Salam ICTP Affiliated Centre at Gomel State Technical University

Abstract

Numerous non-standard dynamics are described by contact-like effective interactions that can manifest themselves in e^+e^- collisions only through deviations of the observables (cross sections, asymmetries) from the Standard Model predictions. If such a deviation were observed, it would be important to identify the actual source among the possible non-standard interactions as many different new physics scenarios may lead to very similar experimental signatures. Here we study the possibility of uniquely identifying the indirect effects of s-channel sneutrino exchange, as predicted by supersymmetric theories with R-parity violation, against other new physics scenarios in process $e^+e^- \to \mu^+\mu^-$ at the International Linear Collider. To evaluate the identification reach on sneutrino exchange, we use as basic observable a double polarization asymmetry, A_{double}. Also, we examine the effects of neutrino and electron mixing with exotic heavy leptons in the process $e^+e^- \to W^+W^-$ within E_6 models, in particular, the possibility of uniquely distinguishing and identifying such effects of heavy neutral lepton exchange from $Z-Z'$ mixing.

*E-mail:pankov@ictp.it
†E-mail:inna.serenkova@cern.ch
‡E-mail:tsytrin@rambler.ru
§E-mail:iv.pankov@tut.by

1 Introduction

Numerous new physics (NP) scenarios, candidates as solutions of Standard Model (SM) conceptual problems, are characterized by novel interactions mediated by exchanges of very heavy states with mass scales significantly greater than the electroweak scale. In many cases, theoretical considerations as well as current experimental constraints indicate that the new objects may be too heavy to be directly produced even at the highest energies of the CERN Large Hadron Collider (LHC) and at foreseen future colliders, such as the e^+e^- International Linear Collider (ILC). In this situation the new, non-standard, interactions would only be revealed by indirect, virtual, effects manifesting themselves as deviations from the predictions of the SM. In the case of indirect discovery the effects may be subtle since many different NP scenarios may lead to very similar experimental signatures and they may easily be confused in certain regions of the parameter space for each class of models.

There are many very different NP scenarios that predict new particle exchanges which can lead to contact interactions (CI) which may show up below direct production thresholds. These are compositeness [1], a Z' boson from models with an extended gauge sector, scalar or vector leptoquarks [2], R-parity violating sneutrino ($\tilde{\nu}$) exchange [3], bi-lepton boson exchanges [4], anomalous gauge boson couplings (AGC) [5], virtual Kaluza–Klein (KK) graviton exchange in the context of gravity propagating in large extra dimensions, exchange of KK gauge boson towers or string excitations [6], *etc.* Of course, this list is not exhaustive, because other kinds of contact interactions may be at play.

If R-parity is violated it is possible that the exchange of sparticles can contribute significantly to SM processes and may even produce peaks or bumps [3] in cross sections if they are kinematically accessible. Below threshold, these new spin-0 exchanges may make their manifestation known via indirect effects on observables (cross sections and asymmetries), including spectacular decays [7]. Here we will address the question of whether the effects of the exchange of scalar (spin-0) sparticles can be differentiated at linear colliders in process

$$e^+ + e^- \to \mu^+ + \mu^- \quad (\text{or } \tau^- + \tau^+), \tag{1}$$

from those associated with the wide class of other contact interactions

mentioned above.[1]

Another important reaction at ILC is

$$e^+ + e^- \to W^+ + W^-, \tag{2}$$

which is quite sensitive to NP effects, in particular, both the leptonic vertices and the trilinear couplings to W^+W^- of the SM Z and of any new heavy neutral boson or a new heavy lepton that can be exchanged in the s-channel or t-channel, respectively. A popular example in this regard, is represented by E_6 models. In particular, an effective $SU(2)_L \times U(1)_Y \times U(1)_{Y'}$ model, which originates from the breaking of the exceptional group E_6, leads to extra gauge bosons. Indeed, in the breaking of this group down to the SM symmetry, two additional neutral gauge bosons could appear and the lightest Z' is defined as

$$Z' = Z'_\chi \cos\beta + Z'_\psi \sin\beta, \tag{3}$$

where the angle β specifies the orientation of the $U(1)'$ generator in the E_6 group space. The values $\beta = 0$ and $\beta = \pi/2$ would correspond, respectively, to pure Z'_χ and Z'_ψ bosons, while the value $\beta = -\arctan\sqrt{5/3}$ would correspond to a Z'_η boson originating from the direct breaking of E_6 to a rank-5 group in superstring inspired models.

Another characteristic of extended models, apart from the Z', is the existence of new matter, new heavy leptons and quarks. In E_6 models the fermion sector is enlarged, since the matter multiplets are in larger representations (the $\underline{27}$ fundamental representation), that contains, in particular, a vector doublet of leptons. From the phenomenological point of view it is convenient to classify the fermions present in E_6 in terms of their transformation properties under $SU(2)$. We denote the particles with unconventional isospin assignments (right-handed doublets) as exotic fermions. We here consider two heavy left- and right-handed $SU(2)$ exotic lepton doublets

$$\begin{pmatrix} N \\ E^- \end{pmatrix}_L , \begin{pmatrix} N \\ E^- \end{pmatrix}_R , \tag{4}$$

and one Z' boson, with masses larger than M_Z and coupling constants that may be different from those of the SM. These leptons are called *vector leptons*. We also assume that the new, "exotic" fermions only mix with the

[1]For details of the analysis and original references, see [8,9]

standard ones within the same family (the electron and its neutrino being the ones relevant to process (2)), which assures the absence of tree-level generation-changing neutral currents [10]. In this paper, we also study the indirect effects induced by heavy lepton exchange in $W^{\pm}$ pair production (2) at the ILC, with a center of mass energy $\sqrt{s} = 0.5 - 1$ TeV and time-integrated luminosity of $\mathcal{L}_{\rm int} = 0.5 - 1$ ab^{-1}.

The paper is organized as follows. In Section 2 we evaluate discovery and identification reaches on sneutrinos in process (1). In Section 3 we study the heavy neutral lepton and boson mixings in the process (2) and determine the discovery and identification reaches on the NWe coupling constants. Concluding remarks are contained in Section 4.

2 Observables and NP parametrization in $\mu^+\mu^-$ production

For a sneutrino in an R-parity-violating theory, we take the basic couplings to leptons and quarks to be given by

$$\lambda_{ijk} L_i L_j \bar{E}_k + \lambda'_{ijk} L_i Q_j \bar{D}_k. \tag{5}$$

Here, L (Q) are the left-handed lepton (quark) doublet superfields, and $\bar{E}$ ($\bar{D}$) are the corresponding left-handed singlet fields. If just the R-parity violating $\lambda LL\bar{E}$ terms of the superpotential are present it is clear that observables associated with leptonic process (1) will be affected by the exchange of $\tilde{\nu}$'s in the t- or s-channels [3]. For instance, in the case only one nonzero Yukawa coupling is present, $\tilde{\nu}$'s may contribute to, e.g. $e^+e^- \to \mu^+\mu^-$ via t-channel exchange. In particular, if λ_{121}, λ_{122}, λ_{132}, or λ_{231} are nonzero, the $\mu^+\mu^-$ pair production proceeds via additional t-channel sneutrino exchange mechanism. However, if only the product of Yukawa, e.g. $\lambda_{131}\lambda_{232}$, is nonzero the s-channel $\tilde{\nu}_\tau$ exchange would contribute to the $\mu^+\mu^-$ pair final state. Below we denote by λ the relevant Yukawa coupling from the superpotential (5) omitting the subscripts.

With P^- and P^+ denoting the longitudinal polarizations of the electrons and positrons, respectively, and θ the angle between the incoming electron and the outgoing muon in the c.m. frame, the differential cross section of process (1) in the presence of contact interactions can be expressed

as ($z \equiv \cos\theta$):

$$\frac{\mathrm{d}\sigma^{\mathrm{CI}}}{\mathrm{d}z} = \frac{3}{8}\left[(1+z)^2\sigma_+^{\mathrm{CI}} + (1-z)^2\sigma_-^{\mathrm{CI}}\right]. \tag{6}$$

In terms of the helicity cross sections $\sigma_{\alpha\beta}^{\mathrm{CI}}$ (with $\alpha, \beta = \mathrm{L}, \mathrm{R}$), directly related to the individual CI couplings $\Delta_{\alpha\beta}$ (see Eq. (10)):

$$\sigma_+^{\mathrm{CI}} = \frac{1}{4}\left[(1-P^-)(1+P^+)\,\sigma_{\mathrm{LL}}^{\mathrm{CI}} + (1+P^-)(1-P^+)\,\sigma_{\mathrm{RR}}^{\mathrm{CI}}\right] \tag{7}$$

$$\sigma_-^{\mathrm{CI}} = \frac{1}{4}\left[(1-P^-)(1+P^+)\,\sigma_{\mathrm{LR}}^{\mathrm{CI}} + (1+P^-)(1-P^+)\,\sigma_{\mathrm{RL}}^{\mathrm{CI}}\right] \tag{8}$$

where the first (second) subscript refers to the chirality of the electron (muon) current. Moreover, in Eqs. (7) and (8):

$$\sigma_{\alpha\beta}^{\mathrm{CI}} = \sigma_{\mathrm{pt}}|\mathcal{M}_{\alpha\beta}^{\mathrm{CI}}|^2, \tag{9}$$

where $\sigma_{\mathrm{pt}} \equiv \sigma(e^+e^- \to \gamma^* \to \mu^+\mu^-) = (4\pi\alpha_{\mathrm{em}}^2)/(3s)$. The helicity amplitudes $\mathcal{M}_{\alpha\beta}^{\mathrm{CI}}$ can be written as

$$\mathcal{M}_{\alpha\beta}^{\mathrm{CI}} = \mathcal{M}_{\alpha\beta}^{\mathrm{SM}} + \Delta_{\alpha\beta} = Q_e Q_\mu + g_\alpha^e\, g_\beta^\mu\, \chi_Z + \Delta_{\alpha\beta}, \tag{10}$$

where $\chi_Z = s/(s - M_Z^2 + iM_Z\Gamma_Z)$ represents the Z propagator, $g_{\mathrm{L}}^l = (I_{3L}^l - Q_l s_W^2)/s_W c_W$ and $g_{\mathrm{R}}^l = -Q_l s_W^2/s_W c_W$ are the SM left- and right-handed lepton ($l = e, \mu$) couplings of the Z with $s_W^2 = 1 - c_W^2 \equiv \sin^2\theta_W$ and Q_l the leptonic electric charge. The $\Delta_{\alpha\beta}$ functions represent the contact interaction contributions coming from TeV-scale physics.

The structure of the differential cross section (6) is particularly interesting in that it is equally valid for a wide variety of NP models such as composite fermions, extra gauge boson Z', AGC, TeV-scale extra dimensions and ADD model. Parametrization of the $\Delta_{\alpha\beta}$ functions in different NP models ($\alpha, \beta = \mathrm{L}, \mathrm{R}$) can be found in [8].

The doubly polarized total cross section can be obtained from Eq. (6) after integration over z within the interval $-1 \le z \le 1$. In the limit of s, t small compared to the CI mass scales, the result takes the form

$$\begin{aligned}\sigma^{\mathrm{CI}} &= \sigma_+^{\mathrm{CI}} + \sigma_-^{\mathrm{CI}} = \frac{1}{4}\left((1-P^-)(1+P^+)\,(\sigma_{\mathrm{LL}}^{\mathrm{CI}} + \sigma_{\mathrm{LR}}^{\mathrm{CI}}) + \right.\\ &+ \left.(1+P^-)(1-P^+)\,(\sigma_{\mathrm{RR}}^{\mathrm{CI}} + \sigma_{\mathrm{RL}}^{\mathrm{CI}})\right).\end{aligned} \tag{11}$$

It is clear that the formula in the SM has the same form where one should replace the superscript CI $\dashrightarrow$ SM in Eq. (11).

Since the $\tilde{\nu}$ exchanged in the s-channel does not interfere with the s-channel SM γ and Z exchanges, the differential cross section with both electron and positron beams polarized can be written as [11]

$$\frac{\mathrm{d}\sigma^{\tilde{\nu}}}{\mathrm{d}z} = \frac{3}{8}\left[(1+z)^2\sigma_+^{\mathrm{SM}} + (1-z)^2\sigma_-^{\mathrm{SM}} + 2\,\frac{1+P^-P^+}{2}\,(\sigma_{\mathrm{RL}}^{\tilde{\nu}} + \sigma_{\mathrm{LR}}^{\tilde{\nu}})\right]. \quad (12)$$

Here, $\sigma_{\mathrm{RL}}^{\tilde{\nu}}(=\sigma_{\mathrm{LR}}^{\tilde{\nu}}) = \sigma_{\mathrm{pt}}\,|\mathcal{M}_{\mathrm{RL}}^{\tilde{\nu}}|^2$, $\mathcal{M}_{\mathrm{RL}}^{\tilde{\nu}} = \mathcal{M}_{\mathrm{LR}}^{\tilde{\nu}} = \frac{1}{2}\,C_{\tilde{\nu}}^s\chi_{\tilde{\nu}}^s$, and $C_{\tilde{\nu}}^s$ and $\chi_{\tilde{\nu}}^s$ denote the product of the R-parity violating couplings and the propagator of the exchanged sneutrino. For the s-channel $\tilde{\nu}_\tau$ sneutrino exchange they read

$$C_{\tilde{\nu}}^s\,\chi_{\tilde{\nu}}^s = \frac{\lambda_{131}\lambda_{232}}{4\pi\alpha_{\mathrm{em}}}\,\frac{s}{s - M_{\tilde{\nu}_\tau}^2 + iM_{\tilde{\nu}_\tau}\Gamma_{\tilde{\nu}_\tau}} \quad (13)$$

Below we will use the abbreviation $\lambda^2 = \lambda_{131}\lambda_{232}$.

As seen from Eq. (12) the polarized differential cross section picks up a z-independent term in addition to the SM part. The corresponding total cross section can be written as

$$\begin{aligned}\sigma^{\tilde{\nu}} &= \frac{1}{4}\,(1-P^-)(1+P^+)\,(\sigma_{\mathrm{LL}}^{\mathrm{SM}} + \sigma_{\mathrm{LR}}^{\mathrm{SM}}) + \frac{1}{4}\,(1+P^-)(1-P^+)\,\times \\ &\times\ (\sigma_{\mathrm{RR}}^{\mathrm{SM}} + \sigma_{\mathrm{RL}}^{\mathrm{SM}}) + \frac{3}{2}\,\frac{1+P^-P^+}{2}\,(\sigma_{\mathrm{RL}}^{\tilde{\nu}} + \sigma_{\mathrm{LR}}^{\tilde{\nu}}). \end{aligned} \quad (14)$$

It is possible to uniquely identify the effect of the s-channel sneutrino exchange exploiting the double beam polarization asymmetry defined as [11]

$$A_{\mathrm{double}} = \frac{\sigma(P_1,-P_2) + \sigma(-P_1,P_2) - \sigma(P_1,P_2) - \sigma(-P_1,-P_2)}{\sigma(P_1,-P_2) + \sigma(-P_1,P_2) + \sigma(P_1,P_2) + \sigma(-P_1,-P_2)}, \quad (15)$$

where $P_1 = |P^-|$, $P_2 = |P^+|$. From (11) and (15) one finds

$$A_{\mathrm{double}}^{\mathrm{SM}} = A_{\mathrm{double}}^{\mathrm{CI}} = P_1P_2 = 0.48, \quad (16)$$

where the numerical value corresponds to electron and positron degrees of polarization: $P_1 = 0.8$, $P_2 = 0.6$. This is because these contact interactions contribute to the same amplitudes as shown in (10). Eq. (16) demonstrates

that $A^{\rm SM}_{\rm double}$ and $A^{\rm CI}_{\rm double}$ are indistinguishable for any values of the contact interaction parameters, $\Delta_{\alpha\beta}$, i.e. $\Delta A_{\rm double} = A^{\rm CI}_{\rm double} - A^{\rm SM}_{\rm double} = 0$.

On the contrary, the $\tilde{\nu}$ exchange in the s-channel will force this observable to a smaller value, $\Delta A_{\rm double} = A^{\tilde{\nu}}_{\rm double} - A^{\rm SM}_{\rm double} \propto -P_1 P_2 \, |C^s_{\tilde{\nu}} \chi^s_{\tilde{\nu}}|^2 < 0$. The value of $A_{\rm double}$ below $P_1 P_2$ can provide a signature of scalar exchange in the s-channel. All those features in the $A_{\rm double}$ behavior are shown in Fig. 1.

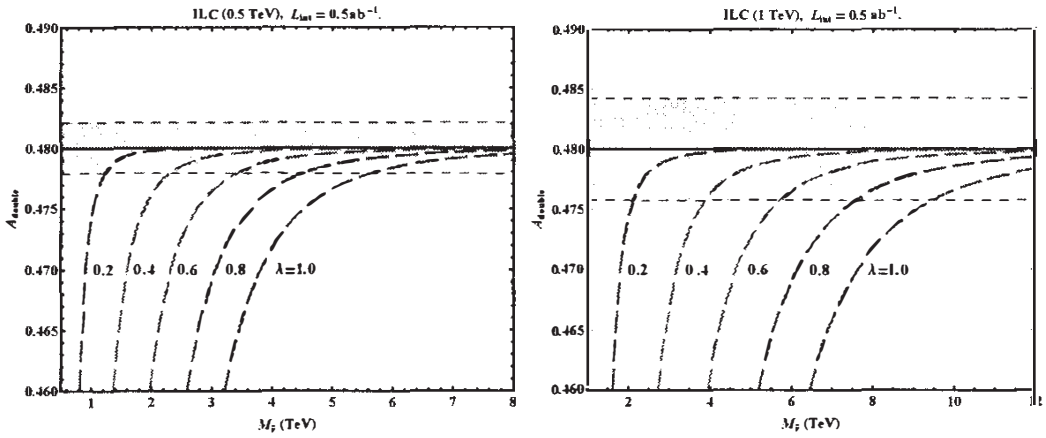

Figure 1: Double beam polarization asymmetry $A^{\tilde{\nu}}_{\rm double}$ as a function of sneutrino mass $M_{\tilde{\nu}}$ for different choices of λ (dashed lines) at the ILC with $\sqrt{s} = 0.5$ TeV (left panel) and $\sqrt{s} = 1.0$ TeV (right panel), $\mathcal{L}_{\rm int} = 0.5$ ab^{-1}. From left to right, λ varies from 0.2 to 1.0 in steps of 0.2. The solid horizontal line corresponds to $A^{\rm SM}_{\rm double} = A^{\rm CI}_{\rm double}$. The yellow bands indicate the expected uncertainty in the SM case.

In the numerical analysis, cross sections are evaluated including initial- and final-state radiation by means of the program ZFITTER, together with ZEFIT, with $m_{\rm top} = 175$ GeV and $m_H = 125$ GeV.

As numerical inputs, we shall assume the identification efficiencies of $\epsilon = 95\%$ for $\mu^+\mu^-$ final states, integrated luminosity of $\mathcal{L}_{\rm int} = 0.5$ ab^{-1} with uncertainty $\delta\mathcal{L}_{\rm int}/\mathcal{L}_{\rm int} = 0.5\%$, and a fiducial experimental angular range $|\cos\theta| \leq 0.99$. Also, regarding electron and positron degrees of polarization, we shall consider the following values: $P^- = \pm 0.8$; $P^+ = \pm 0.6$, with $\delta P^-/P^- = \delta P^+/P^+ = 0.5\%$.

Discovery and identification reaches on the sneutrino mass $M_{\tilde{\nu}}$ (95% C.L.) plotted in Fig. 2 are obtained from conventional χ^2 analysis.

For comparison, current limits from low-energy data are also shown. From Fig. 2 one can see that identification of sneutrino exchange effects in

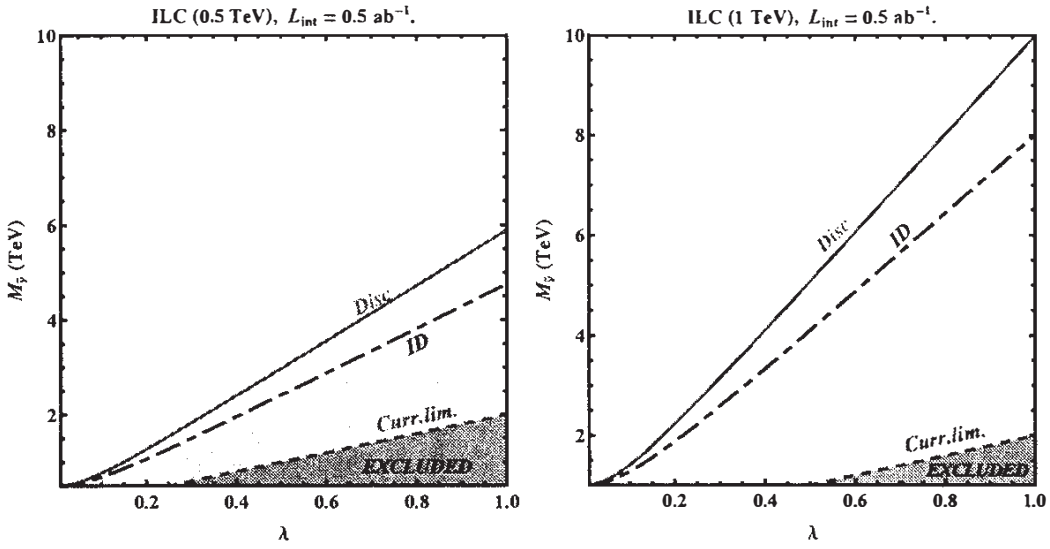

Figure 2: Discovery and identification reaches on sneutrino mass $M_{\tilde{\nu}}$ (95% C.L.) as a function of λ for the process $e^+e^- \to \mu^+\mu^-$ at the ILC with $\sqrt{s} = 0.5$ TeV (left panel) and $\sqrt{s} = 1.0$ TeV (right panel), $\mathcal{L}_{\rm int} = 0.5$ ab^{-1}. For comparison, current limits from low energy data are also displayed.

the s-channel with $A_{\rm double}$ is feasible in the region of parameter and mass space far beyond the current limits.

3 Lepton and $Z - Z'$ mixing in W^+W^- production

In process (2) fermionic coupling constants modified by leptonic mixing can be written as [9]:

$$g_a^e = g_a^{e^0} c_{1a}^2 + g_a^{E^0} s_{1a}^2, \qquad g_a'^e = g_a'^{e^0} c_{1a}^2 + g_a'^{E^0} s_{1a}^2; \tag{17}$$

$$G_L^\nu = c_{1L}c_{2L} - 2\,T_{3L}^E\, s_{1L}\, s_{2L}, \qquad G_R^\nu = -2\,T_{3R}^E\, s_{1R}s_{2R}; \tag{18}$$

$$G_L^{Ne} = -s_{2L}c_{1L} - 2\,T_{3L}^E c_{2L}\, s_{1L}, \qquad G_R^{Ne} = -2\,T_{3R}^E\, c_{2R}s_{1R}. \tag{19}$$

Here, $(\varepsilon^0 = e^0,\ E^0)$, $g_a^{\varepsilon^0} = (T_{3a}^{\varepsilon^0} - Q_{{\rm em},a}^{\varepsilon^0} s_W^2) g_Z$ and $T_{3a}^{\varepsilon^0}$ is the third isospin component, $g_Z = 1/s_W c_W$, with $c_W = \cos\theta_W$, $c_{1a} = \cos\psi_{1a}$, $c_{2a} = \cos\psi_{2a}$, $s_{1a} = \sin\psi_{1a}$ and $s_{2a} = \sin\psi_{2a}$. ψ_{1a} and ψ_{2a} being the mixing angles in charged and neutral lepton sectors, respectively.

Z-Z' mixing can be parametrized as

$$\begin{pmatrix} Z_1 \\ Z_2 \end{pmatrix} = \begin{pmatrix} \cos\phi & \sin\phi \\ -\sin\phi & \cos\phi \end{pmatrix} \begin{pmatrix} Z \\ Z' \end{pmatrix}, \tag{20}$$

where Z, Z' are weak eigenstates, Z_1, Z_2 are mass eigenstates and ϕ is the Z-Z' mixing angle. Taking Eq. (20) into account, the lepton neutral current couplings to Z_1 and Z_2 are, respectively:

$$g^e_{1a} = g^e_a \cos\phi + g'^e_a \sin\phi\,; \qquad g^e_{2a} = -g^e_a \sin\phi + g'^e_a \cos\phi. \tag{21}$$

In the Born approximation the process (2) is described by the set of five diagrams shown in Fig. 3 and corresponding to mass-eigenstate exchanges (i.e. γ, ν, N, Z_1 and Z_2), with couplings given by Eqs. (17)-(19) and (21).

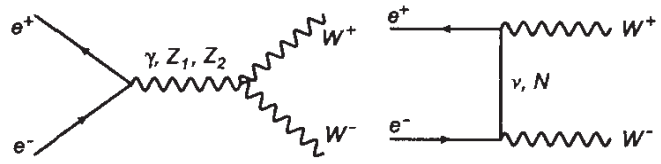

Figure 3: Feynman diagrams.

The polarized cross section for the process (2) can be written as

$$\begin{aligned} \frac{d\sigma(P_L^-, P_L^+)}{d\cos\theta} &= \frac{1}{4}\left[(1+P_L^-)(1-P_L^+)\frac{d\sigma^{RL}}{d\cos\theta} + \right. \\ &+ (1-P_L^-)(1+P_L^+)\frac{d\sigma^{LR}}{d\cos\theta} + (1+P_L^-)(1+P_L^+)\frac{d\sigma^{RR}}{d\cos\theta} + \\ &+ \left.\left(1-P_L^-\right)\left(1-P_L^+\right)\frac{d\sigma^{LL}}{d\cos\theta}\right], \end{aligned} \tag{22}$$

where P_L^- (P_L^+) are degrees of longitudinal polarization of e^- (e^+), θ the scattering angle of the W^- with respect to the e^- direction. The superscript "RL" refers to a right-handed electron and a left-handed positron, and similarly for the other terms. The relevant polarized differential cross sections for $e_a^- e_b^+ \to W_\alpha^- W_\beta^+$ contained in Eq. (22) can be expressed as [12]

$$\frac{d\sigma^{ab}_{\alpha\beta}}{d\cos\theta} = C \sum_{k=0}^{k=2} F_k^{ab}\, \mathcal{O}_{k\,\alpha\beta}, \tag{23}$$

where $C = \pi\alpha^2_{e.m.}\beta_W/2s$, $\beta_W = (1 - 4M_W^2/s)^{1/2}$ the W velocity in the CM frame, and the helicities of the initial e^-e^+ and final W^-W^+ states are labeled as $ab = (RL,\ LR,\ LL,\ RR)$ and $\alpha\beta = (LL,\ TT,\ TL)$, respectively. The $\mathcal{O}_k$ are functions of the kinematical variables dependent on energy $\sqrt{s}$, the scattering angle θ and the W mass, M_W, which characterize the various possibilities for the final W^+W^- polarizations (TT, LL, $TL + LT$ or the sum over all W^+W^- polarization states for unpolarized W's).

The F_k are combinations of lepton and trilinear gauge boson couplings, g_{WWZ_1} and g_{WWZ_2}, including lepton and Z-Z' mixing as well as propagators of the intermediate states. For instance, for the LR case one finds

$$\begin{aligned} F_0^{LR} &= \frac{1}{16s_W^4}\left[(G_L^\nu)^2 + r_N\left(G_L^{Ne}\right)^2\right]^2, \\ F_1^{LR} &= 2\left[1 - g_{WWZ_1}g_{1L}^e\chi_1 - g_{WWZ_2}g_{2L}^e\chi_2\right]^2, \\ F_2^{LR} &= -\frac{1}{2s_W^2}\left[(G_L^\nu)^2 + r_N\left(G_L^{Ne}\right)^2\right] \times \\ &\times \left[1 - g_{WWZ_1}g_{1L}^e\chi_1 - g_{WWZ_2}g_{2L}^e\chi_2\right], \end{aligned} \tag{24}$$

where the χ_j $(j = 1, 2)$ are the Z_1 and Z_2 propagators, i.e. $\chi_j = s/(s - M_j^2 + iM_j\Gamma_j)$, $r_N = t/(t - m_N^2)$, with $t = M_W^2 - s/2 + s\cos\theta\beta_W/2$, and m_N is the neutral heavy lepton mass. Also, in Eq. (24), $g_{WWZ_1} = g_{WWZ}\cos\phi$ and $g_{WWZ_2} = -g_{WWZ}\sin\phi$ where $g_{WWZ} = \cot\theta_W$. Note that Eq. (24) is obtained in the approximation where the imaginary parts of the Z_1 and Z_2 boson propagators are neglected, which is fully appropriate far away from the poles.

The first term F_0^{LR} describes the contributions to the cross section caused by neutrino ν and heavy neutral lepton N exchanges in the t-channel while the second one, F_1^{LR}, is responsible for s-channel exchange of the photon γ and the gauge bosons Z_1 and Z_2. The interference between s- and t-channel amplitudes is contained in the term F_2^{LR}. The RL case is simply obtained from Eq. (24) by exchanging $L \to R$.

For the LL and RR cases there is only N-exchange contribution,

$$F_0^{LL} = F_0^{RR} = \frac{1}{16s_W^4}r_N^2\left(G_L^{Ne}G_R^{Ne}\right)^2. \tag{25}$$

Concerning the $\mathcal{O}_{k\,\alpha\beta}$ multiplying the expression in Eq. (25) (see Eq. (23)) their explicit expressions for polarized and unpolarized final states W^+W^- can be found in, e.g.

Let us start the analysis with a case where there is only lepton mixing and no Z-Z' mixing, i.e., $\phi = 0$. Since the mixing angles are bounded by s_i^2 at most of order 10^{-2}, we can expect that retaining only the terms of order s_1^2, s_2^2 and $s_1 s_2$ in the cross section (22) should be an adequate approximation. To do that we expand the couplings of Eqs. (17)-(19) taking $g_a^{\epsilon^0} = (T_{3a}^{\epsilon^0} - Q_{\mathrm{em},a}^{\epsilon^0} s_W^2) g_Z$ into account. We find for E_6 models, where $T_{3L}^E = T_{3R}^E = -1/2$:

$$\begin{aligned} G_L^{Ne} &= s_{1L} - s_{2L}, & G_R^{Ne} &= s_{1R} \\ g_L^e &= g_L^{e^0}, & g_R^e &= g_R^{e^0} - \frac{1}{2}(G_R^{Ne})^2 g_Z, \\ G_L^\nu &= G_L^{\nu^0} - \tfrac{1}{2}(G_L^{Ne})^2, & G_R^\nu &= s_{1R}\, s_{2R}. \end{aligned} \tag{26}$$

From Eqs. (24)-(26) one can see that in the adopted approximation the cross section (22) allows to constrain basically the pair of heavy lepton couplings squared, $((G_L^{Ne})^2, (G_R^{Ne})^2)$, it is not possible to constrain s_{2R}^2, which represents mixing in the right-handed neutral-lepton sector.

The sensitivity of the polarized differential cross section (22) to the couplings G_L^{Ne} and G_R^{Ne} is evaluated numerically by dividing the angular range $|\cos\theta| \leq 0.98$ into 10 equal bins, and defining a χ^2 function in terms of the expected number of events $N(i)$ in each bin for a given combination of beam polarizations [13]:

$$\chi^2 = \sum_{\{P_L^-, P_L^+\}} \sum_i^{\text{bins}} \left[\frac{N_{\text{SM+NP}}(i) - N_{\text{SM}}(i)}{\delta N_{\text{SM}}(i)} \right]^2, \tag{27}$$

where $N(i) = \mathcal{L}_{\text{int}}\, \sigma_i\, \varepsilon_W$ with $\mathcal{L}_{\text{int}}$ the time-integrated luminosity. Furthermore,

$$\sigma_i = \sigma(z_i, z_{i+1}) = \int_{z_i}^{z_{i+1}} \left(\frac{d\sigma}{dz} \right) dz, \tag{28}$$

where $z = \cos\theta$ and polarization indices have been suppressed. Also, ε_W is the efficiency for W^+W^- reconstruction, for which we take the channel of lepton pairs ($e\nu$+$\mu\nu$) plus two hadronic jets, giving $\varepsilon_W \simeq 0.3$ basically from the relevant branching ratios. The procedure outlined above is followed to evaluate both $N_{\text{SM}}(i)$ and $N_{\text{SM+NP}}(i)$.

Also, in our numerical analysis to evaluate the sensitivity of the differential distribution to model parameters we include initial-state QED

corrections to on-shell $W^{\pm}$ pair production in the flux function approach that assures a good approximation within the expected accuracy of the data.

Now we turn to the generic case where both lepton mixing and Z-Z' mixing occur, so that the leptonic coupling constants are as in Eq. (21) and the Z_1, Z_2 couplings to $W^{\pm}$ are as in Eq. (24). In this case, in order to evaluate the influence of the Z-Z' mixing on the allowed discovery region on the heavy lepton coupling plane $((G_L^{Ne})^2, (G_R^{Ne})^2)$ one should vary the mixing angle ϕ within its current constraints which depend on the specific Z' model, namely $-0.0018 < \phi < 0.0009$ for the ψ model and $-0.0016 < \phi < 0.0006$ for the χ model. Within a specific Z' model and with fixed m_N, the χ^2 function basically depends on three parameters: ϕ, G_L^{Ne} and G_R^{Ne}. In this case, $\chi^2 \leq \chi^2_{\rm min} + \chi^2_{\rm CL}$ describes a tree-dimensional surface. Its projection on the $((G_L^{Ne})^2, (G_R^{Ne})^2)$ plane demonstrates the interplay between leptonic and Z-Z' mixings. Fig. 4 shows, as a typical example, the results of this analysis for the χ-model (left panel) and the ψ-model (right panel), respectively, with fixed $m_N = 0.3$ TeV. As one can see, the shapes of the allowed regions for the coupling constants G_L^{Ne} and G_R^{Ne} are quite dependent on the Z' model and different for these two cases. From the explicit calculation it turns out that this is due to the different relative signs between the lepton and Z-Z' mixing contributions to the deviations of the cross section $\Delta\sigma$.

Concerning Fig. 4 and the corresponding analysis for the χ and ψ models, we should note that the bounds on the lepton couplings $(G_L^{Ne})^2$ and $(G_R^{Ne})^2$ are somewhat looser than in the case $\phi = 0$ discussed above (roughly, by a factor as large as two), but still numerically competitive with the current situation. Also, we can remark that the cross sections for longitudinal W^+W^- production provide by themselves the most stringent constraints for this model.

By "identification" we shall here mean *exclusion* of a certain set of competitive models, including the SM, to a certain confidence level. For this purpose, we use the double beam polarization asymmetry, defined in (15). From Eqs. (22) and (15) one finds for the $A_{\rm double}$ of the process (2)

$$A_{\rm double} = P_1 P_2 \frac{(\sigma^{RL} + \sigma^{LR}) - (\sigma^{RR} + \sigma^{LL})}{(\sigma^{RL} + \sigma^{LR}) + (\sigma^{RR} + \sigma^{LL})}. \tag{29}$$

We note that this asymmetry is only available if both initial beams are polarized.

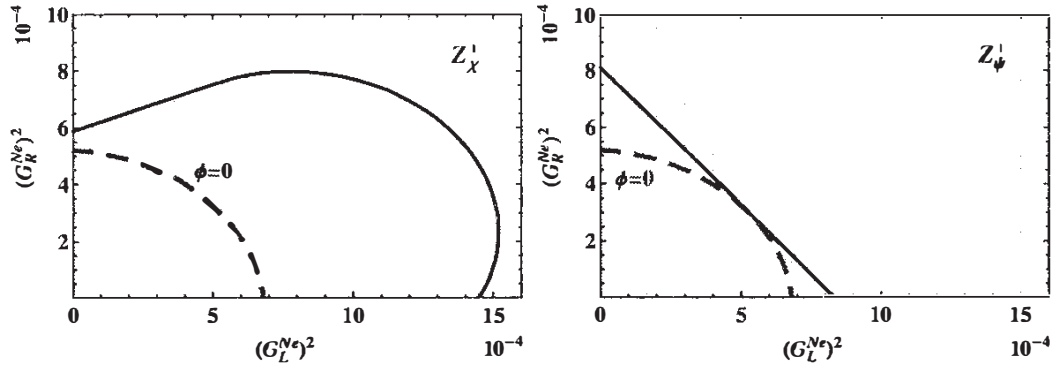

Figure 4: Discovery reach at 95% CL on the heavy neutral lepton coupling plane $((G_L^{Ne})^2, (G_R^{Ne})^2)$ at $m_N = 0.3$ TeV in the case where both lepton mixing and Z-Z' mixing are simultaneously allowed for the Z'_χ model (left panel) and the Z'_ψ model (right panel), obtained from combined analysis of polarized differential cross sections $d\sigma(W_L^+W_L^-)/dz$ at different sets of polarization, $P_L^- = \pm 0.8$, $P_L^+ = \mp 0.6$, at the ILC with $\sqrt{s} = 0.5$ TeV and $\mathcal{L}_{\rm int} = 1$ ab^{-1}. The dashed curves labelled "$\phi = 0$" refer to the case of no Z-Z' mixing..

It is important to also note that the SM gives rise only to σ^{LR} and σ^{RL} such that the structure of the integrated cross section has the form

$$\sigma_{\rm SM} = \frac{1}{4}\left[\left(1+P_L^-\right)\left(1-P_L^+\right)\sigma_{\rm SM}^{RL} + \left(1-P_L^-\right)\left(1+P_L^+\right)\sigma_{\rm SM}^{LR}\right]. \qquad (30)$$

This is also the case for anomalous gauge couplings (AGC) [12], and Z'-boson exchange (including Z-Z' mixing and Z_2 exchange) [13]. The corresponding expressions for those cross sections can be obtained from (30) by replacing the specification SM $\to$ AGC and Z', respectively. Accordingly, the double beam polarization asymmetry has a common form for all those cases:

$$A_{\rm double}^{\rm SM} = A_{\rm double}^{\rm AGC} = A_{\rm double}^{\rm Z'} = P_1 P_2 = 0.48, \qquad (31)$$

where the numerical value corresponds to the product of the electron and positron degrees of polarization: $P_1 = 0.8$, $P_2 = 0.6$. Eq. (31) demonstrates that $A_{\rm double}^{\rm SM}$, $A_{\rm double}^{\rm AGC}$ and $A_{\rm double}^{\rm Z'}$ are indistinguishable for any values of NP parameters, AGC or Z' mass and strength of Z-Z' mixing, i.e. $\Delta A_{\rm double} = A_{\rm double}^{\rm AGC} - A_{\rm double}^{\rm SM} = A_{\rm double}^{\rm Z'} - A_{\rm double}^{\rm SM} = 0$.

On the contrary, the heavy neutral lepton N-exchange in the t-channel will induce non-vanishing contributions to σ^{LL} and σ^{RR}, and thus force $A_{\rm double}$ to a smaller value, $\Delta A_{\rm double} = A_{\rm double}^{N} - A_{\rm double}^{\rm SM}$ and $\Delta A_{\rm double} \propto$

$-P_1P_2\, r_N^2\, \left(G_L^{Ne}G_R^{Ne}\right)^2 < 0$ irrespectively of the simultaneous lepton and Z-Z' mixing contributions to σ^{RL} and σ^{LR}. A value of $A_{\rm double}$ below P_1P_2 can provide a signature of heavy neutral lepton N-exchange in the process (2).

The identification reach (ID) on the plane of heavy lepton coupling $((G_L^{Ne})^2, (G_R^{Ne})^2)$ (at 95% C.L.) for various lepton masses m_N plotted in Fig. 5 is obtained from conventional χ^2 analysis with $A_{\rm double}$. Note that discovery is possible in the green and yellow regions, whereas identification is only possible in the green region. The hyperbola-like limit of the identification reach is due to the appearance of a product of the squared couplings $(G_L^{Ne})^2$ and $(G_R^{Ne})^2$ in the deviation from the SM cross section, given by Eq. (25).

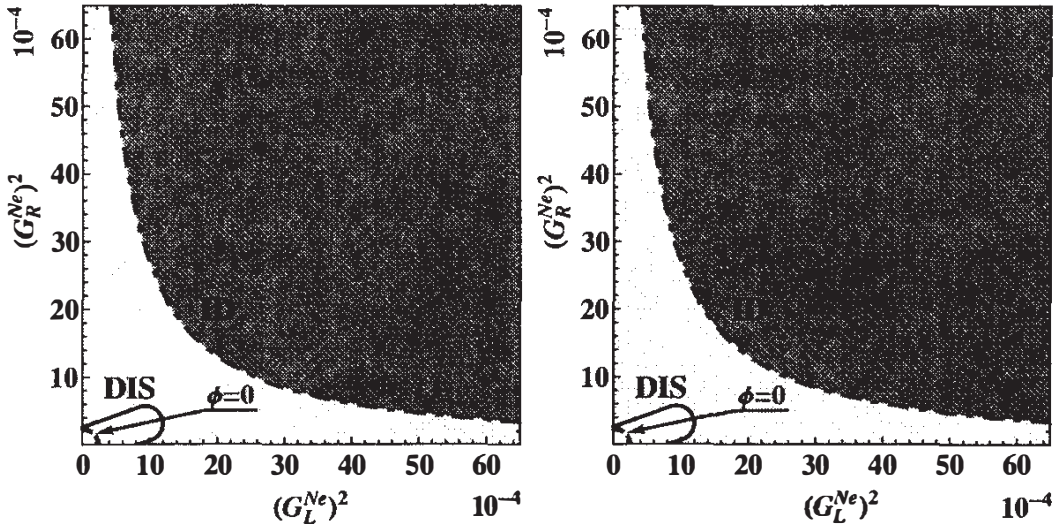

Figure 5: Left panel: discovery (DIS) and identification (ID) reaches at 95% CL on the heavy neutral lepton coupling plane $((G_L^{Ne})^2, (G_R^{Ne})^2)$, obtained from a combined analysis of polarized differential cross sections $d\sigma(W_L^+W_L^-)/dz$ at different sets of polarization, $P_L^- = \pm 0.8$, $P_L^+ = \mp 0.6$, and exploiting the double polarization asymmetry. Furthermore, $m_N =$ 0.3 TeV, $\sqrt{s} = 0.5$ TeV and $\mathcal{L}_{\rm int} = 1$ ab^{-1}. Right panel: similar, with $\sqrt{s} = 1.0$ TeV and for $m_N = 0.6$ TeV. The dashed curves labelled "$\phi = 0$" refer to the case of no Z-Z' mixing, whereas the outer contour labelled "DIS" refer to the minimum discovery reach in the presence of mixing..

4 Concluding remarks

In this note we have studied how uniquely identify the indirect (propagator) effects of spin-0 sneutrino predicted by supersymmetric theories with R-parity violation, against other new physics scenarios in high energy e^+e^- annihilation into lepton-pairs at the ILC in process (1).

To evaluate the identification reach on the sneutrino exchange signature, we develop a technique based on a double polarization asymmetry formed by polarizing both beams in the initial state, that is particularly suitable to directly test for such s-channel sneutrino exchange effects in the data analysis.

We have also studied the process $e^+e^- \to W^+W^-$ and seen how to identify the propagator and exotic-lepton mixing effects of a heavy neutral lepton exchange in the t-channel. Discovery of new physics, meaning exclusion of the Standard Model, does not depend on having both initial beams polarized, but the sensitivity is improved with beam polarization. We shown that the availability of both beams being polarized, plays a crucial rôle in identifying those new physics scenarios.

References

[1] E. Eichten, K. D. Lane and M. E. Peskin, Phys. Rev. Lett. **50**, 811 (1983); R. Rückl, Phys. Lett. B **129**, 363 (1983).

[2] W. Büchmuller, R. Rückl and D. Wyler, Phys. Lett. B **191**, 442 (1987) [Erratum-ibid. B **448**, 320 (1999)].

[3] J. Kalinowski, R. Rückl, H. Spiesberger and P. M. Zerwas, Phys. Lett. B **406**, 314 (1997) [hep-ph/9703436]; Phys. Lett. B **414**, 297 (1997).

[4] F. Cuypers and S. Davidson, Eur. Phys. J. C **2**, 503 (1998) [hep-ph/9609487].

[5] G. J. Gounaris, D. T. Papadamou and F. M. Renard, Phys. Rev. D **56**, 3970 (1997) [hep-ph/9703281].

[6] N. Arkani-Hamed, S. Dimopoulos and G. R. Dvali, Phys. Lett. B **429**, 263 (1998) [hep-ph/9803315]; L. Randall and R. Sundrum, Phys. Rev. Lett. **83**, 3370 (1999) [hep-ph/9905221].

[7] N.-E. Bomark, D. Choudhury, S. Lola and P. Osland, JHEP **1107**, 070 (2011) [arXiv:1105.4022 [hep-ph]].

[8] G. Moortgat-Pick, P. Osland, A. A. Pankov and A. V. Tsytrinov, Phys. Rev. D **87**, 095017 (2013) [arXiv:1303.3845 [hep-ph]].

[9] A. V. Tsytrinov, J. Kalinowski, P. Osland and A. A. Pankov, Phys. Lett. B **718** (2012) 94 [arXiv:1207.6234 [hep-ph]].

[10] J. Beringer *et al.* [Particle Data Group Collaboration], Phys. Rev. D **86** (2012) 010001.

[11] P. Osland, A. A. Pankov and N. Paver, Phys. Rev. D **68**, 015007 (2003) [arXiv:hep-ph/0304123].

[12] G. Gounaris, J. Layssac, G. Moultaka and F. M. Renard, Int. J. Mod. Phys. A **8** (1993) 3285.

[13] V. V. Andreev, G. Moortgat-Pick, P. Osland, A. A. Pankov and N. Paver, Eur. Phys. J. C **72** (2012) 2147 [arXiv:1205.0866 [hep-ph]].

The performance of the MPD detector for measurements of heavy-ion collisions

Victor Kireev*
VBLHEP, JINR

Abstract

In my report I present the results of MPD performance study. A full detector simulation was carried out for central Au+Au collisions using as an input the UrQMD generator. The simulation was performed with realistic shape of the beam interaction zone.

1 Intoduction

A new scientific program on heavy-ion physics NICA/MPD [1] was launched at JINR (Dubna) for comprehensive exploration of the QCD phase diagram with ion species ranging from protons to Au^{79+} over the energy range $4 < \sqrt{s} < 11$ GeV. The major goal of the NICA/MPD Project is the study of in-medium properties of hadrons and the nuclear matter equation of state, including a search for possible signals of deconfinement and/or chiral symmetry restoration phase transitions and the QCD critical endpoint.

Here we studed the process of propagation of particles through the detector setup, identification and MPD phase-space coverage.

2 MPD detector at JINR

The MPD detector [2] comprises the central detector and two forward spectrometers situated along the beam line symmetrically with respect

*E-mail: skvitek@gmail.com

to the centre of MPD. The central detector consits of a barrel part and two endcaps located inside the magnetic field. The barrel part is a shell-like set of various detector systems surrounding the interaction point and aimed to reconstruct and identify both charged and neutral particles in the pseudorapidity region of $|\eta| \leq 1.2$. The endcaps are aimed for precise tracking over pseudorapidity range ($1.2 < |\eta| < 2$).

The barrel part consists of tracker and particle identification system (Fig. 2.1). The principal tracker is the time projection chamber supplemented by the inner tracker surrounding the interaction region. Both subdetectors has to provide precise track finding, momentum determination, vertex reconstruction and pattern recognition. The high performance time-of-flight system must be able to identify charged hadrons and nuclear clusters in the wide rapidity range and up to total momentum of 2 GeV/c. The fast forward detectors will provide the TOF system with the start signal. The main goal of electromagnetic calorimeter is to identify electrons, photons and measure their energy with high precision. Two end-caps trackers are located on both sides of the TPC along the z axis. The ECT is designed to provide tracking information for particles travelling at small radii. Particles emitted in very forward/backward directions are detected by fast forward detectors, beam-beam counters and zero degree calorimeters. They are used for trigger definition, centrality determination and reconstruction of the position of the interaction point.

3 MPD performance study

All MPD characteristics was studied in MpdRoot with Au+Au collisions from the UrQMD [3] event generator. The track reconstruction algorithm in the MPD simulation chain is based on a Kalman-filter [4] approach. The position of the collision vertex is found by extrapolating all the tracks reconstructed in the TPC back to the beam line. The found position Z_{found} is compared then with the true one (Z_{MC}), the RMS of the difference ($Z_{found} - Z_{MC}$) is the vertex resolution along the beam line σ_Z. Basically, σ_Z depends on track multiplicity: it gets worse in peripheral collisions and/or in the events with a displaced vertex when some part of tracks has only few space points in the TPC and do not reconstructed. In order to disentangle these two effects, we plot in the left panel of Fig. 3.1 the primary vertex resolution as a function of the TPC track multiplicity for minimum bias collisions taking place in the center of the detector; while

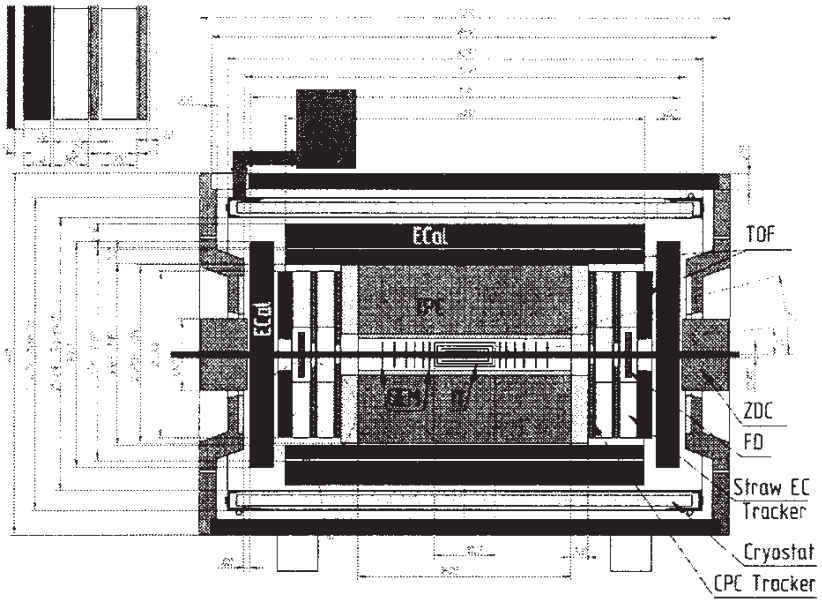

Figure 2.1: Cutaway side view of the Central Detector of MPD with based dimensions.

the right panel of the same figure demonstrates a σ_z dependence on the coordinate of the primary collision along the beam line for events with the same particle multiplicity (here peripheral Au+Au collisions at b $\approx$ 10 fm with $N_{tracks} \approx 50$ were used). As one can see, even in peripheral collisions at the lowest NICA energy the accuracy of the primary vertex reconstruction in MPD is good enough at distances from the detector center well beyond the limits of the beam diamond (which is distributed along z with $\sigma_{Gauss} \approx 24$ cm). The precision of the vertex reconstruction decreases considerably only at the edges of the MPD TPC. As it was observed, IP spread in the transverse direction has no effect in event vertex reconstruction.

MPD tracking efficiency is shown as a function of pseudorapidity on Fig 3.2 (left plot), and versus p_T (right plot). For p_T plot we use the momenta cut $p > 200$ MeV/c. The efficiency is plotted for two intervals of the vertex coordinate of an interaction point along z-axis: $|Zvertex| < 5$ cm (blue symbols) and $|Zvertex| < 80$ cm (red circles). There is no dependency of tracking efficiency for η up to 1.7.

The overall MPD efficiency for detecting of protons was studied with central Au+Au collisions: we apply an impact parameter cut $b < 4$ fm. The procedure was as follows. The reconstructed in the TPC tracks were propagated to the TOF and matched with the corresponding TOF hits.

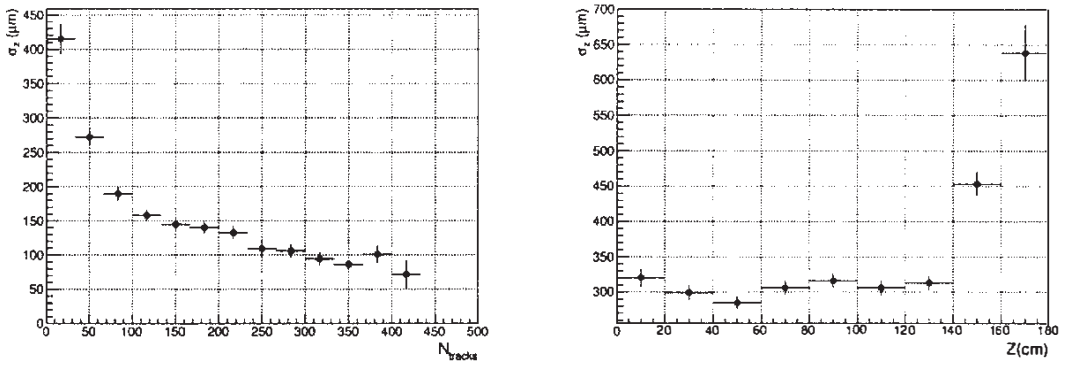

Figure 3.1: (Left panel) Vertex resolution versus track multiplicity (N_{tracks}) for minimum bias collisions at the MPD center. (Right panel) σ_Z as a function of the Z-coordinate of the event collision vertex for peripheal Au+Au collisions.

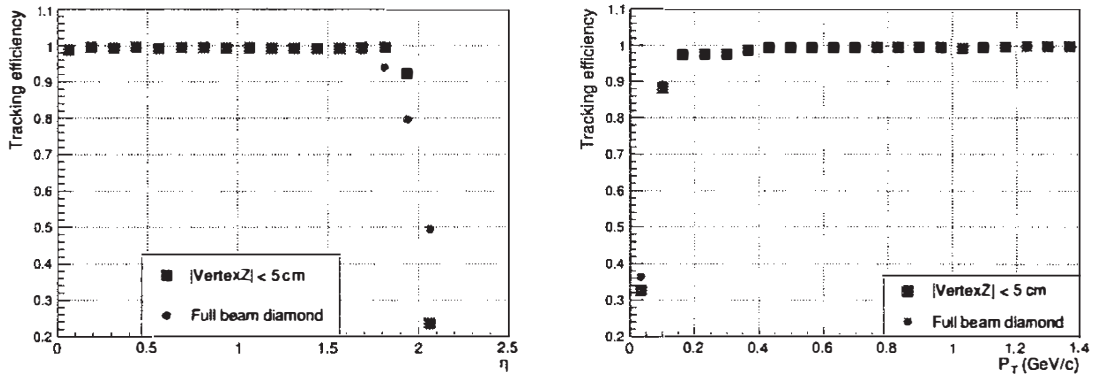

Figure 3.2: Track reconstruction efficiency versus η for tracks with momenta $p > 200$ MeV/c (left panel), and p_T within $|\eta| < 1$ (right panel). UrQMD, central Au+Au collisions with beam diamond. Blue symbols: $|VertexZ| < 5$ cm, red circles: no contsrain on VertexZ.

Here only the barrel part of the TOF detector used. The mass squared for each TOF matching was calculated using the information about the particles momentum, track length and time-of-flight. In Fig. 3.3 (left panel) the mass-squared and momentum correlation plot is shown for pions, kaons and protons. This picture is for the flat distribution of the IPs Z-coordinate. As one can see, the proton candidates can be selected from other species up to total momentum of 3 GeV/c. Proton identification was

achieved by a window cut $0.45 < m^2 < 1.6\ GeV^2/c^4$.

All the identified in an event protons were counted and the event-by-event ratio of the number of the registered protons to the total number of protons in bins of the IPs Z-coordinate is plotted in Fig. 3.3 (right panel). The overall efficiency, which includes the acceptance, as well as tracking, matching and PID efficiencies is of about 73% in the center and drops up to 63% at Z = 75 cm. In central Au+Au collisions at $\sqrt{s} = 4$ GeV we are able to register by the TPC and barrel-TOF of about 100 protons per event if the collision vertex is at Z = 0 and of about 78 protons in a central collision at Z = 75 cm. In the studies aimed in searching for the QCD Critical End Point by means of event-by-event baryon number fluctuations, a loss in the overall MPD proton efficiency for displaced collision vertices may be crucial. To minimize a negative effect of this efficiency loss on physics results, either a cut on Z-position of the reconstructed vertex can be applied off-line, or the shape of the beam diamond can be changed during the data taking period by squeezing Z-distribution with some loss in the event rate due to decrease in luminosity - the latter solution is suggested by the NICA accelerator team.

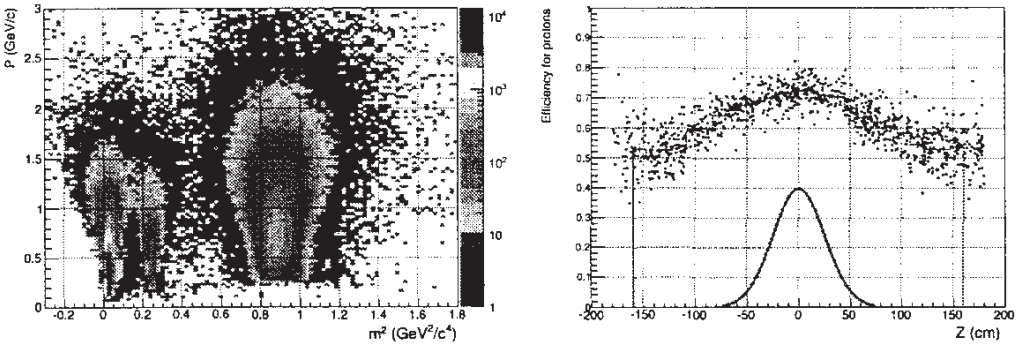

Figure 3.3: (Left panel) Total momentum versus mass squared for π, K, p. Central Au+Au, TPC + TOF-barrel, flat Z-distribution $|Z_{Vertex}| < 170$ cm. (Right panel) Overall proton efficiency versus Z-coordinate of the collision vertex, the red line is the profile of the event-by-event efficiencies. The real IP shape is shown by the solid blue line.

MPD phase-space coverage for identified kaons and protons is plotted in terms of transverse momentum and rapidity in Fig. 3.4.

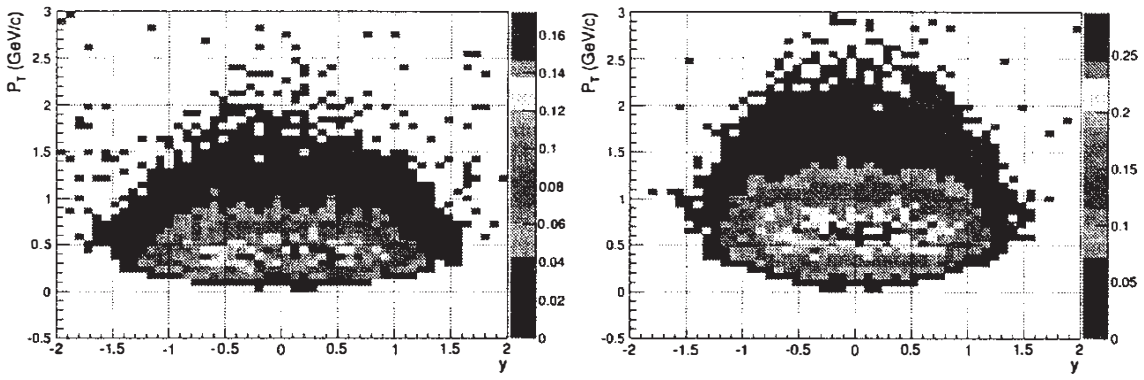

Figure 3.4: MPD phase-space in terms of y and p_T for identified kaons (left) and protons (right). Au+Au at $\sqrt{s} = 9$ GeV (UrQMD), realistic PID, full beam diamond.

4 Summary

The MPD project is progressing well, substantial design work has been almost completed. Significant progress has been achieved in simulation, performance studies and detector prototyping. Track reconstruction efficiency is 100% for $|\eta| < 1.7$. Even in peripheral collisions at the lowest NICA energy the accuracy of the primary vertex reconstruction in MPD is good enough for very distant from the detector center collisions. The precision of the vertex reconstruction decreases considerably only at the edges of the MPD TPC. As it was observed, IP spread in the transverse direction has no effect in event vertex reconstruction.

References

[1] A. Sissakian et al., Design and Construction of Nuclotron-based Ion Collider facility (NICA), Conceptual design report (JINR, Dubna, 2008).

[2] Kh.U. Abraamyan et al. (MPD Collaboration) NIM A 628 (2011) 99-102

[3] M. Bleicher et al., J. Phys. G25, 1859 (1999), hep-ph/9909407.

[4] R. Fruhwirth, Nucl. Instr. and Meth. A262, 444 (1987).

Model-independent search for Z' at hadron colliders

Skalozub V.V.,* Tukhtarov A.V.†

Dnipropetrovsk National University, 49010 Dnipropetrovsk, Ukraine

Abstract

The model-independent search for Z' boson at hadron collides is described. In this approach, not only the mass $m_{Z'}$ but also the couplings of the Z' to the standard model (SM) fermions are arbitrary parameters. The key element here is that the specific relations between the couplings take place. The most important is the universality of the axial-vector coupling a_f^2 which is the same for all the leptons and quarks and independent of the type of them.

On the base of these relations, we construct the observable which uniquely picks out the signals of the virtual (as well as real) Z' boson for both type the Tevatron and LHC experiments. This variable accounts for the specific role of the a_f^2 coupling. It is constructed on the base of the process: $\bar{q}q \to \mu^+\mu^-(e^+e^-)$, with PDFs taken into consideration. Then, the results of different experiments can be analyzed. Recent data of the CMS collaboration on the forward-backward asymmetry for the Drell-Yan process at the LHC are analyzed and the estimates of $m_{Z'}$ and a_f^2 are obtained.

1 Abelian Z' boson

The already finished precision experiments at LEP have determined the SM parameters and particle masses at the level of radiative corrections. They also afforded an opportunity for searching for signals of new heavy particles beyond the SM.

*E-mail:skalozubv@daad-alumni.de

†E-mail:anvitu@gmail.com

At LEP1 and LEP2 experiments no new particles were discovered and the energy scale of new physics was estimated as of the order 1 TeV.

Experiments at the LHC - new stage in high energy physics. The most important result of the finished experiments is the discovery of Higgs boson having the mass $m_H = 126$ GeV. No new particles beyond the SM were discovered at the first stage of experiments at 3 - 7 TeV of proton beams.

Among the most perspective new particles for searching for is the heavy Z' boson. A lot of extended models includes this particle which is a massive neutral vector particle associated usually with an extra $U(1)$ subgroup of the underlying group. Z' is predicted by a number of GUTs, (the E_6 and $SO(10)$ based models, $\chi - \psi$ and so on are often discussed). In fact, about hundred models includes Z' with different masses and couplings.

Present day status of Abelian Z' can be summarized as follows. Model-dependent (MD) search for Z' at LEP2 gave: $m_{Z'} > 400 - 800$ GeV. Model-dependent results from Tevatron: $m_{Z'} > 800$ GeV, and from LHC first run: $m_{Z'} > 2$ TeV.

In this approach, the effects of Z' are calculated within a specific model beyond SM. Free parameters are $m_{Z'}$ and $\Gamma_{Z'}$. All the couplings are fixed. It is usually believed that Z' is a narrow state with small width: $\Gamma/m_{Z'} \ll 1$.

In the model-independent (MinD) searching for Z', analysis is covering a lot of models. So, free parameters are the mass $m_{Z'}$ and the couplings to the SM fermions. Effects of Z' are calculated within a specific low energy effective lagrangian.

In Ref.[1] (see also review [2]) general relations which hold in any model of the Z' between low energy couplings have been derived. These relations (RG relations) are the consequences of a renormalizability . They were derived within the following assumptions:

1) Only one Z' exists at energy scale $1 - 10$ TeV;

2) At low energies, it phenomenologically is described by the known effective lagrangian (see, below);

3) Z' is decoupled at considered energies and the SM or the THDM are used as low energy effective theories;

4) SM is the subgroup of the extended gauge group. So, the only origin of possible three-level interaction Z' with the SM particles is $Z - Z'$ mixing.

2 Effective lagrangian at low energies

At low energies, the Z'-boson can manifest itself by means of the couplings to the SM fermions and scalars as a virtual intermediate state. The Z-boson couplings are also modified due to a Z–Z' mixing.

Significant signals beyond the SM can be inspired by the couplings of renormalizable types. Such couplings can be described by adding new $\tilde{U}(1)$-terms to electroweak covariant derivatives $D^{\rm ew}$ in the lagrangian [3], [4]

$$
\begin{aligned}
L_f &= i\sum_{f_L}\bar{f}_L\gamma^\mu\left(\partial_\mu - \frac{ig}{2}\sigma_a W_\mu^a - \frac{ig'}{2}B_\mu Y_{f_L} - \frac{i\tilde{g}}{2}\tilde{B}_\mu\tilde{Y}_{f_L}\right) f_L \qquad (1)\\
&+ i\sum_{f_R}\bar{f}_R\gamma^\mu\left(\partial_\mu - ig'B_\mu Q_f - \frac{i\tilde{g}}{2}\tilde{B}_\mu\tilde{Y}_{f_R}\right) f_R,\\
L_\phi &= \left|\left(\partial_\mu - \frac{ig}{2}\sigma_a W_\mu^a - \frac{ig'}{2}B_\mu Y_\phi - \frac{i\tilde{g}}{2}\tilde{B}_\mu\tilde{Y}_\phi\right)\phi\right|^2, \qquad (2)
\end{aligned}
$$

where $f_L = (f_u)_L, (f_d)_L$ are left-handed doublets, $f_R = (f_u)_R, (f_d)_R$ are right-handed singlets. The couplings $g, g', \tilde{g}$ are the charges associated with the $SU(2)_L, U(1)_Y$, and the Z' gauge groups, respectively, σ_a are the Pauli matrices, Q_f denotes the charge of f in positron charge units,Y_ϕ is the $U(1)_Y$ hypercharge, and $Y_{f_L} = -1$ for leptons and $1/3$ for quarks.

The generators $\tilde{Y}_{f_L} = \mathrm{diag}(\tilde{Y}_{f_u}, \tilde{Y}_{f_d})$ and $\tilde{Y}_\phi = \mathrm{diag}(\tilde{Y}_{\phi,1}, \tilde{Y}_{\phi,2})$ are diagonal 2×2 matrices.

As for the scalar sector, the lagrangian can be simply generalized for the case of the SM with two Higgs doublets (THDM).

Lagrangian (2) leads to the Z–Z' mixing. The mixing angle θ_0 is

$$
\theta_0 = \frac{\tilde{g}\sin\theta_W\cos\theta_W}{\sqrt{4\pi\alpha_{\rm em}}}\frac{m_Z^2}{m_{Z'}^2}\tilde{Y}_\phi + O\left(\frac{m_Z^4}{m_{Z'}^4}\right), \qquad (3)
$$

where θ_W is the SM Weinberg angle, and $\alpha_{\rm em}$ is the electromagnetic fine structure constant.

Other Z' couplings are

$$
v_f = \tilde{g}\frac{\tilde{Y}_{L,f} + \tilde{Y}_{R,f}}{2}, \qquad a_f = \tilde{g}\frac{\tilde{Y}_{R,f} - \tilde{Y}_{L,f}}{2}. \qquad (4)
$$

Lagrangian (1) leads to the following interactions:

$$\begin{aligned}\mathcal{L}_{Z\bar{f}f} &= \frac{1}{2} Z_\mu \bar{f}\gamma^\mu \left[(v_{fZ}^{\rm SM} + \gamma^5 a_{fZ}^{\rm SM})\cos\theta_0 + (v_f + \gamma^5 a_f)\sin\theta_0\right] f, \\ \mathcal{L}_{Z'\bar{f}f} &= \frac{1}{2} Z'_\mu \bar{f}\gamma^\mu \left[(v_f + \gamma^5 a_f)\cos\theta_0 - (v_{fZ}^{\rm SM} + \gamma^5 a_{fZ}^{\rm SM})\sin\theta_0\right] f, \quad (5)\end{aligned}$$

where f is a SM fermion state; $v_{fZ}^{\rm SM}$, $a_{fZ}^{\rm SM}$ are the SM couplings of the Z-boson.

At low energies, it is convenient to introduce the dimensionless couplings

$$\bar{a}_f = \frac{m_Z}{\sqrt{4\pi} m_{Z'}} a_f, \quad \bar{v}_f = \frac{m_Z}{\sqrt{4\pi} m_{Z'}} v_f, \quad (6)$$

which can be constrained by experiments.

3 RG relations

In a particular model, $\tilde{Y}_\phi$, $\tilde{Y}_{L,f}$, $\tilde{Y}_{R,f}$ take some specific values. If the model is unknown, these parameters remain potentially arbitrary numbers. This is not the case if the underlying extended model is a renormalizable one. The couplings are correlated [1]:

$$\tilde{Y}_{\phi,1} = \tilde{Y}_{\phi,2} \equiv \tilde{Y}_\phi, \qquad \tilde{Y}_{L,f} = \tilde{Y}_{L,f^*}, \quad \tilde{Y}_{R,f} = \tilde{Y}_{L,f} + 2T_{3f}\,\tilde{Y}_\phi. \quad (7)$$

Here f and f^* are the partners of the $SU(2)_L$ fermion doublet ($l^* = \nu_l, \nu^* = l$, $q_u^* = q_d$ and $q_d^* = q_u$), T_{3f} is the third component of weak isospin.

It is convenient to introduce the Z' couplings to the vector and axial-vector fermion currents (4),

$$v_f - a_f = v_{f^*} - a_{f^*}, \qquad a_f = T_{3f}\tilde{g}\tilde{Y}_\phi. \quad (8)$$

Hence it follows:

1) The couplings of Z' to the axial-vector fermion current have the universal absolute value proportional to the Z' coupling to the scalar doublet.

2) Z–Z' mixing angle (3) can be determined by the axial-vector coupling.

Since a_f is universal, we introduce the notation

$$\bar{a} = \bar{a}_d = \bar{a}_{e^-} = -\bar{a}_u = -\bar{a}_\nu, \quad (9)$$

and find

$$\theta_0 = -2\bar{a}\frac{\sin\theta_W \cos\theta_W}{\sqrt{\alpha_{em}}}\frac{m_Z}{m_{Z'}}. \tag{10}$$

From (8) it follows for each fermion doublet

$$\bar{v}_{f_d} = \bar{v}_{f_u} + 2\bar{a}. \tag{11}$$

Thus, Z' couplings can be parameterized by seven independent couplings

$$\bar{a}, \bar{v}_u, \bar{v}_c, \bar{v}_t, \bar{v}_e, \bar{v}_\mu, \bar{v}_\tau. \tag{12}$$

These variables are useful for either theoretical considerations or fitting data of experiments.

4 Estimates from LEP experiments

MinD limits on Z' couplings from LEP1 and LEP2 have been obtained at $1-2\sigma$ CL in [2]. The axial-vector coupling $\bar{a}$ can be constrained by LEP1 (through the mixing angle) and LEP2 ($e^+e^- \to \mu^+\mu^-, \tau^+\tau^-$) data with the maximal likelihood value

$$\bar{a}^2 = 1.3 \times 10^{-5} \tag{13}$$

and 2σ confidence level (CL) interval:

$$0 < \bar{a}^2 < 3.61 \times 10^{-4}. \tag{14}$$

The electron vector coupling $\bar{v}_e$ can be constrained by LEP2 data in the Bhabha process ($e^+e^- \to e^+e^-$) at 2σ CL interval:

$$4 \times 10^{-5} < \bar{v}_e^2 < 1.69 \times 10^{-4}. \tag{15}$$

Constrain $\bar{v}_u, \bar{v}_c, \bar{v}_t, \bar{v}_\mu, \bar{v}_\tau$ by the widest interval from 2σ CL intervals for $\bar{v}_e$, $\bar{a}$ gives

$$0 < \bar{v}_{other}^2 < 4 \times 10^{-4}. \tag{16}$$

Let us present expected parameters for Z' searching for

- spin 1
- charge 0

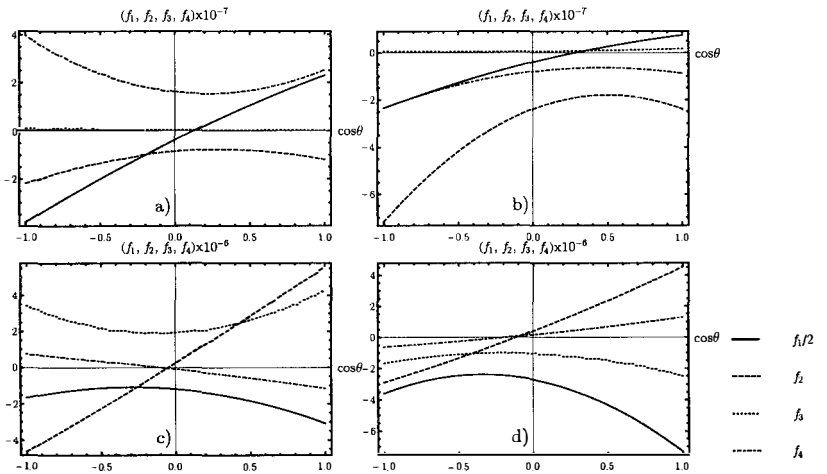

Figure 1: Plots for the form-factors given by Eq. (17). a) $M = 50$ GeV and c) $M = 100$ GeV are plots for $u\bar{u} \to l^+l^-$; b) $M = 50$ GeV and d) $M = 100$ GeV are plots for $d\bar{d} \to l^+l^-$; $m_{Z'} = 2.5$ TeV.

- mass $m_{Z'} \geq 2$ TeV, width $\Gamma_{Z'} = 150 - 200$ GeV
- mixing angle Θ_0
- coupling $\tilde{g}$
- axial-vector coupling constant $\bar{a}^2 = 1.3 \times 10^{-5}$
- vector coupling constant $4 \times 10^{-5} < \bar{v}_e^2 < 1.69 \times 10^{-4} (2\sigma \cdot CL)$

These values will serve us as a guide for analysis of experimental data obtained at hadron colliders. In what follows, we shall concentrate on recent data from LHC.

5 Z' in the quark-antiquark process

We begin our consideration with the basic process of quark-atiquark annihilation into lepton-antilepton pairs: $q\bar{q} \to l^+l^-$. Z' contribution comes as an interference between γ/Z and Z' states. The cross-section is

$$\frac{d\sigma}{d\hat{t}} = \left(\frac{d\sigma}{d\hat{t}}\right)^{SM} + f_1(M,z)\,\bar{a}^2 + f_2(M,z)\,\bar{a}\bar{v}_l + \\ + f_3(M,z)\,\bar{a}\bar{v}_q + f_4(M,z)\,\bar{v}_q\bar{v}_l + \ldots, \quad z = \cos\theta \tag{17}$$

where $\hat{t} = (p_{l^+} - p_q)^2$ is Mandelstam variable, θ is the emission angle of the lepton l^- relative to the quark momentum in the dilepton center-of-mass frame; M is dilepton mass.

In our investigation only $u\bar{u}$ and $d\bar{d}$ pairs are taking into account as dominant[5]. We also neglect fermions masses since amplitudes are calculated in the tree-level. All parton-level calculations are performed using FeynArts[6] and FormCalc[7] packages.

As it can be seen from Fig. (1), the f_1 and f_2 are dominant. The function f_3 is symmetric and its value can be neglected at the low energies. The last function f_4 requires extra research. These functions behavior suggests the idea of asymmetry-like observable.

6 The observable

The cross-section is the function of three kinematic variables. We use $\tanh y$ instead of y. This trick allows us to save angular dependence of the cross-section. Integration over Y depends on the magnitudes of the form-factors F_i but does not matter on their behavior. Fig. (2) shows F_i as functions of $\cos\theta = \tanh y$ for $M = 50$, 100 150 and 150 GeV and intermediate state pseudorapidities $Y < |1|$.

As it can be seen from Fig. (2) the functions F_1 and F_2 are dominant. The function F_3 can be neglected for a broad range of M that means av_u term is kinematically suppressed. The last term can be neglected by constructing an asymmetry. Let us denote

$$\Delta_i(M,Y) = \int_0^1 dz\, F_i(M,Y,z) - \int_{-1}^0 dz\, F_i(M,Y,z), \\ \Sigma_i(M,Y) = \int_0^1 dz\, F_i(M,Y,z) + \int_{-1}^0 dz\, F_i(M,Y,z), \quad z = \tanh y. \tag{18}$$

Values of the Δ_i are tabulated in the Tab. (1) for dilepton masses $M =$ 25, 50, 75, 100, 120, 150 and 200 GeV and Z' masses $m_{Z'} = 1.2$, 2.0, 2.5 and 3 TeV. Table is presented at the end of the paper.

As it can be seen Δ_i modula are slightly decreased with $m_{Z'}$ grows. Also starting from $M = 120$ GeV $v_u v_l$ term can not be neglected. That is why we take into account only $M < 120$ GeV for analysis. Using Eq. (18) forward-backward asymmetry can be written as

$$A_{FB}\left(a^2,\, av_l\right) = \frac{\Delta_{\rm SM} + \Delta_1 \bar{a}^2 + \Delta_2 \bar{a}\bar{v}_l}{\Sigma_{\rm SM} + \Sigma_1 \bar{a}^2 + \Sigma_2 \bar{a}\bar{v}_l}. \tag{19}$$

This asymmetry is our two-parameters observable. It also depends on M and Y but they are ignored as integration parameters. We use CMS collaboration data for Drell-Yan process forward-backward asymmetry [8], so SM terms can not be discarded.

7 Z' in the Drell-Yan process at LHC

At the LHC, the most convenient possibility for detecting the Z' signals is Drell-Yan $p\bar{p} \to l^+ l^-$ process. Our approach is based on tree-level parton scattering amplitudes, so there are no differences between final-state leptons. The cross-section of the considered process can be written as the parton-level cross-section combined with the parton distribution functions (PDFs)

$$\frac{\partial^3 \sigma_{p\bar{p}\to l^+l^-}}{\partial x_q \partial x_{\bar{q}} \partial t} = \sum_{q,\bar{q}} f_{q,p}(x_q, Q^2) f_{\bar{q},p}(x_{\bar{q}}, Q^2) \frac{\partial \sigma_{q\bar{q}\to l^+l^-}}{\partial t} \tag{20}$$

where $f_{q,p}(x_q, Q^2)$ is the pdf for parton q in proton with the momentum fraction x_q at the scale Q^2. We use MSTW PDF package[9].

This triple-differential cross-section is complete description of the Drell-Yan process. Experimental data are available with other set of variables. In experiments, events are selected using pseudorapidities $\eta^{\pm}$ and mass M (or transverse momenta $p_T^{\pm}$) of the final-state leptons. Momentum fractions x_q, $x_{\bar{q}}$ and Mandelstam variables $\hat{s}, \hat{t}$ are expressed as

$$\begin{aligned} x_q &= \frac{M}{\sqrt{S}} e^{\frac{\eta_+ + \eta_-}{2}}, \quad x_{\bar{q}} = \frac{M}{\sqrt{S}} e^{-\frac{\eta_+ + \eta_-}{2}}, \\ \hat{s} &= M^2 = 4p_T^2 \cosh^2 \frac{\eta_+ - \eta_-}{2}, \quad \hat{t} = -\frac{M^2}{1 + e^{(\eta_+ - \eta_-)/2}}. \end{aligned} \tag{21}$$

It is useful to denote $Y = (\eta_+ + \eta_-)/2$ — intermediate stare rapidity and $y = (\eta_+ - \eta_-)/2$ — scattering angle related variable; in dilepton center-of-mass frame $\cos\theta = \tanh y$. The kinematics of the lepton pair formation

is well-known and can be found in the literature (for example [10]). Using these variables, the cross-section is

$$\frac{\partial^3\sigma_{p\bar{p}\to l^+l^-}}{\partial M\partial Y\partial z}=\sum_{q,\bar{q}} f_{q,p}(M,Y)f_{\bar{q},p}(M,Y)\frac{\partial\sigma_{q\bar{q}\to l^+l^-}}{\partial z},\quad z=\tanh y. \tag{22}$$

Applying Eq. (17) to Eq. (22) the cross-section reads as

$$\begin{aligned}\frac{\partial^3\sigma}{\partial M\partial Y\partial z} &= \left(\frac{\partial^3\sigma}{\partial M\partial Y\partial z}\right)^{SM}+F_1(M,Y,z)\bar{a}\bar{v}_l+F_2(M,Y,z)\bar{a}\bar{v}_l+\\ &+F_3(M,Y,z)\bar{a}\bar{v}_u+F_4(M,Y,z)\bar{v}_l\bar{v}_u,\quad z=\tanh y.\end{aligned} \tag{23}$$

Note that Y enters PDF factors only, that allows us to neglect the second-generation quarks[5]. Its values is limited by the detector capabilities and conservation laws.

The functions F_i also depend on the Z' mass $m_{Z'}$ and the decay width $\Gamma_{Z'}$. The model-independent analysis of LEP data showed that $m_{Z'}\sim 1.2$ TeV and $\Gamma_{Z'}=0.1\,m_{Z'}\sim 120$ GeV [1, 11]. On the other hand, recent CMS experiments indicated (in model-dependent approaches) that $m_{Z'}\geq 1.79$ TeV. We use these values as starting point. We also suppose that $\Gamma_{Z'}=0.1\,m_{Z'}$.

To have a hint for constructing an observable in the Drell-Yan process we take into consideration the above analysis od the $q\bar{q}\to l^+l^-$ process.

8 Data fit

Observable (19) actually has one additional parameter $m_{Z'}$. We are going to calculate χ^2 for some given $m_{Z'}$ values and apply a $\chi^2\to$ min criterium. It this way we reduce errors caused by the many-parametric fits. For specific experimental data, a suiting value of $m_{Z'}$ will be related with positivity of a^2 parameter and smallness of χ^2 value.

We use general maximum-likelyhood method with χ^2 function

$$\chi^2\left(\bar{a}^2,\,\bar{a}\bar{v}_l\right)=\sum_i\left(\frac{A^i_{exp}-A^i_{FB}\left(\bar{a}^2,\,\bar{a}\bar{v}_l\right)}{\delta A_i}\right)^2. \tag{24}$$

Since we expect experimental data to be normally distributed, $l\left(\bar{a}^2,\,\bar{a}\bar{v}_l\right)\propto\exp\left[-\chi^2\left(\bar{a}^2,\,\bar{a}\bar{v}_l\right)\right]$ is maximum-likelyhood function. And χ^2

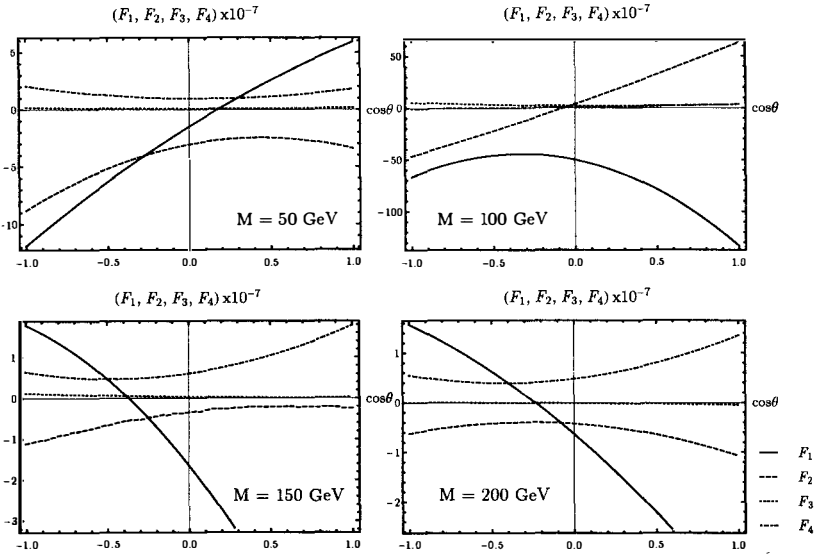

Figure 2: Plots for the form-factors given by Eq. (23). $m_{Z'} = 2.5$ TeV, $Y < |1|$.

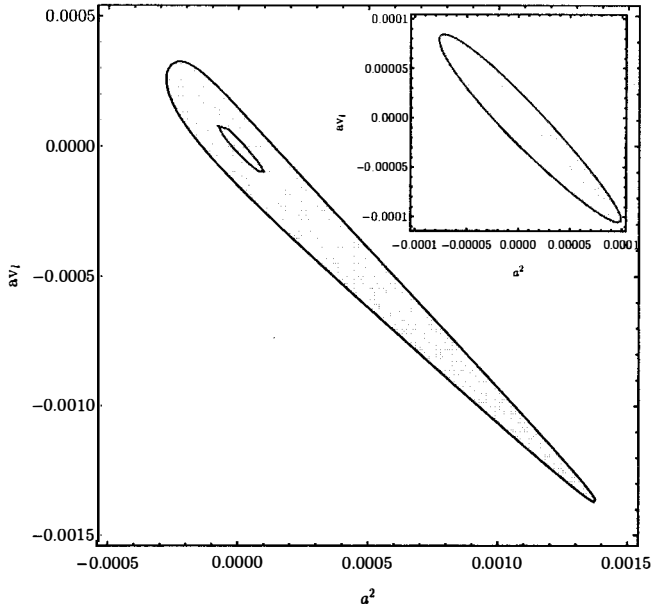

Figure 3: Confidence level areas (26) (yellow — 68% CL, blue — 95% CL) for $\chi^2_{\min}$ at $m_{Z'} = 2.5$ TeV. Zero point is $\bar{a}^2 = 9.86 \times 10^{-5}$ and $\bar{a}\bar{v}_l = -6.93 \times 10^{-5}$.

itself is logarithmic maximum-likelyhood function and its minimum can be found from the conditions

$$\frac{\partial \chi^2}{\partial \bar{a}^2} = 0, \quad \frac{\partial \chi^2}{\partial \bar{a}\bar{v}_l} = 0. \tag{25}$$

The confidence level (CL) areas are obtained from the condition

$$\chi^2\left(\bar{a}^2, \bar{a}\bar{v}_l\right) - \chi^2_{\min} \leq \chi^2_{\mathrm{CL},\alpha}(\nu), \tag{26}$$

where $\chi^2_{\min}$ is minimum value found from Eq. (25) and $\chi^2_{\min} \leq \chi^2_{\mathrm{CL},\alpha}(\nu)$ is chi-squared distribution critical value for ν degrees of freedom at α-level (CL% $= 100(1-\alpha)$).

We obtain min. $\chi^2_{\min} = 2.67649$ with $\bar{a}^2 = 9.86 \times 10^{-5}$ and $\bar{a}\bar{v}_l = -6.93 \times 10^{-5}$ for $m_{Z'} = 2.5$ TeV.

For other values of $m_{Z'}$ wich are local minimums of χ^2, the values of $\bar{a}^2$ become negative. So, the mass $m_{Z'} = 2.5$ TeV is reasonable.

9 Discussion

Nowadays, when the LHC is in upgrade stage and the experimental data accumulated already at energies up to 7 TeV are reported by the Collaboration, it is of interest to apply different methods of the data treating. This can open possibilities for discovering new particles in future experiments at higher energies. On the other hand, huge amount of data have been accumulated in finished experiments, that also opens perspectives for searching for new particles as virtual states. In the present report we described the model-independent analysis for searching for the Z' gauge boson on the base of the Drell-Yan process and applied it for the LHC experiments. In fact, the basic properties of the $q\bar{q} \to l^+l^-$ process were taken into considerations. So, formally, other hadronic initial states can be used. This will change the PDF parts of the cross-sections. We showed that the forward-backward asymmetry is the most perspective observable for detecting the Z' boson. Here, we have to stress that the RG relations between couplings of Z' to the SM fermions are key elements of our investigation. Just due to these relations the kinematics features proper to the Z' have been elucidated. These ensure the unique signals of the Z' virtual state. On the base of the data for forward-backward asymmetry of the Drell-Yan scattering process reported by CMS collaboration [8], we estimated the mass and $\bar{a}^2$ and $\bar{a}\bar{v}_l$ couplings to the SM fermions. These values could be accounted for as guide for future experiments.

It is also interesting to compare the present results with the ones coming from the LEP experiments adduced in Sect.4. We see that the mass of the virtual state is increased twice from 1.2 TeV to 2.5 TeV. The universal coupling's maximum likelyhood value $\bar{a}^2$ is increased nearly 10 times. One of the reasons why the discrepancy appeared may be the fact that in the analysis of the LEP data carried out already the order of the Z' coupling to the SM fermions was taken be $a^2 \sim 10^{-2}$. In contrast, in the present analysis any assumptions have been done. Other possibility is the fact that here we took into account the results of CMS collaboration accumulated at $\sqrt{s} = 7$ GeV, only. The results may change when a more complete data set will be analyzed.

Table 1: Tabulation of the Δ_i calculated for different Z' masses

M, GeV	$\Delta_1 \times 10^{-7}$	$\Delta_2 \times 10^{-8}$	$\Delta_4 \times 10^{-9}$
$m_{Z'} = 1.2$ TeV			
25	7.579	5.702	-1.486
50	8.829	26.899	-11.879
75	19.418	196.365	-69.942
100	-33.132	548.646	202.653
120	-10.290	42.245	86.278
150	-5.130	4.377	57.575
200	-2.905	-2.338	41.254
$m_{Z'} = 2.0$ TeV			
25	7.629	5.715	-1.486
50	8.869	26.946	-11.867
75	19.455	196.510	-69.767
100	-33.096	548.420	201.780
120	-10.252	42.198	85.737
150	-5.089	4.387	57.008
200	-2.857	-2.282	40.529
$m_{Z'} = 2.5$ TeV			
25	7.639	5.718	-1.486
50	8.877	26.955	-11.863
75	19.463	196.539	-69.733
100	-33.088	548.374	201.604
120	-10.245	42.188	85.628
150	-5.081	4.389	56.895
200	-2.848	-2.271	40.385
$m_{Z'} = 3.0$ TeV			
25	7.645	5.719	-1.486
50	8.881	26.960	-11.862
75	19.467	196.555	-69.715
100	-33.084	548.349	201.509
120	-10.241	42.183	85.569
150	-5.076	4.389	56.833
200	-2.843	-2.265	40.307

10 Acknowledgements

One of us (VS) is indebted to Organizing Committee of Gomel School for kind invitation, nice meeting and financial support of the stay.

References

[1] Skalozub V.V. Gulov A.V. Renormalizability and model-independent description of Z' signals at low energies. *Eur. Phys. J. C*, 17:685–694, 2000.

[2] Skalozub V.V. Gulov A.V. Fitting of Z' parameters. *Int.J.Mod.Phys. A*, 25:5787–5815, 2010, arXiv:1009.2320v1.

[3] Lynn B. W. Cvetic M. Gauge structures beyond the standard model and 100-GeV mass region. *Phys. Rev. D*, 35:51–69, 1987.

[4] Degrassi G. Sirlin A. Renormalization of constrained $SU(2)_L \times U(1)_Y \times U(1)$ models. *Phys. Rev. D*, 40:3066–3073, 1989.

[5] Kozhushko A.A. Gulov A.V. Two-parametric model-independent observables for Z' searching at the Tevatron, 2012, arXiv:1209.5022v2.

[6] Hahn T. Generating Feynman Diagrams and Amplitudes with FeynArts 3. *Comput.Phys.Commun.*, 140:418–431, 2001.

[7] Perez-Victoria M. Hahn T. Automatized One-Loop Calculations in four and D dimensions. *Comput.Phys.Commun.*, 118:153–165, 1999.

[8] CMS Collaboration. Forward backward asymmetry of DrellYan lepton pairs in pp collisions at $\sqrt{s} = 7$ TeV. *Phys. Let. B*, 718:752772, 2013.

[9] Thornec R.S. Martina A.D., Stirlingb W.J. and G. Watt. Parton distributions for the LHC. *Eur.Phys.J. C*, 63:189–285, 2009.

[10] Schroeder D.V. Peskin M.E. *An Introduction To Quantum Field Theory (Frontiers in Physics).* Westview Press, reprint edition, 1995.

[11] Skalozub V.V. Gulov A.V. Model-independent search for the Abelian Z' boson in the Bhabha process. *Phys. Rev.*, D70:115010, 2004.

Observables for Z' signal searches at the Tevatron and LHC

A.V. Gulov*, A.A. Kozhushko†
Dnipropetrovsk National University, 49010 Dnipropetrovsk, Ukraine

Abstract

We propose a scheme of searches for the Z' gauge boson at modern hadron colliders. The scheme utilizes model-independent relations between the Z' couplings to fermions. It includes a prescription for integrating the Drell-Yan cross section in the SM Z-boson peak region and leads to two-parametric observables, which are suitable for constraining the Z' vector and axial-vector couplings to SM fermions in a general phenomenological parameterization with non-universal Z' interactions. Also a one-parametric observable for searching for the popular leptophobic Z' boson is proposed.

1 Introduction

A new heavy neutral vector boson (Z' boson) [1, 2, 3] is a popular scenario of searching for physics beyond the standard model (SM) of elementary particles in modern collider experiments. Both the Tevatron and LHC collaborations try to catch the particle as a resonance in the Drell-Yan process. Observing no peak they conclude that the Z' mass is no less than approximately 2.2 TeV [4, 5] if one considers some predefined set of Z' models.

Significant amount of the Tevatron and LHC data is collected at the Z-boson peak at 66–116 GeV. At these energies the Z' boson also can manifest itself as an off-shell state, as the Z coupling constants are influenced by

*E-mail:alexey.gulov@gmail.com
†E-mail:a.kozhushko@yandex.ru

the $Z - Z'$ mixing, and these effects may allow to find Z' signals by fitting the experimental data.

In order to select Z' off-shell hints, proper observables have to be introduced to amplify possible signal [6, 7, 8]. The key problem for off-shell Z' detection is to maximally reduce the number of the Z' couplings in the observable that is used to fit the data. The ultimate scenario assumes a one-parametric observable. However, a two-parametric observable can be also useful and effective. For example, the strategy to construct observables driven by one or two parameters was successfully applied to analyze the final data of the LEP experiment leading to model-independent hints and constraints on Z' couplings [9, 10, 11].

In this paper we investigate possibilities of constructing few-parametric observables for the Drell-Yan process taking into account kinematics of the proton-(anti)proton collisions and model-independent parameterization of the Z' couplings. Here we consider the general case of a Z' boson with non-universal phenomenological Z' couplings to fermion generations. We conclude that two-parametric observables exist at energies corresponding to Z peak, and we obtain all of them. These observables can be used as a key to find possible signals of the off-shell Z' boson. Our suggestions and results are valid both for the minimal SM and for the two-Higgs doublet model (THDM).

All calculations in our paper are performed for the Tevatron case ($p\bar{p}$ collision, $\sqrt{S} = 1.96$ TeV, corresponding kinematical cuts). The generalization for the LHC case is mostly straightforward.

The paper is organized as follows. In section 2 we provide all necessary information on the low-energy Z' parameterization for our calculations. Section 3 contains specifics on Z' contribution to the Drell-Yan process, uncertainties, and kinematic variables suitable for hadron colliders. In section 4 we construct the observables in a step-by-step manner. In section 5 we briefly summarize and discuss the obtained results.

2 Abelian Z' couplings to leptons and quarks

Being decoupled at energies of order of m_Z, the Abelian Z' boson interacts with the SM particles as an additional $\tilde{U}(1)$ gauge boson. Its couplings to

the SM fermions are usually parameterized by the effective Lagrangian:

$$\begin{aligned}\mathcal{L}_{Z\bar{f}f} &= \frac{1}{2} Z_\mu \bar{f}\gamma^\mu \left[(v_{fZ}^{\rm SM} + \gamma^5 a_{fZ}^{\rm SM})\cos\theta_0 + (v_f + \gamma^5 a_f)\sin\theta_0\right] f, \\ \mathcal{L}_{Z'\bar{f}f} &= \frac{1}{2} Z'_\mu \bar{f}\gamma^\mu \left[(v_f + \gamma^5 a_f)\cos\theta_0 - (v_{fZ}^{\rm SM} + \gamma^5 a_{fZ}^{\rm SM})\sin\theta_0\right] f. \quad (1)\end{aligned}$$

(Further details on the parameterization can be found in [12, 13].) Here f is an arbitrary SM fermion state; a_f and v_f are the Z' couplings to the axial-vector and vector fermion currents, respectively; $v_{fZ}^{\rm SM}$, $a_{fZ}^{\rm SM}$ are the SM couplings of the Z-boson; θ_0 is the Z–Z' mixing angle. The a_f and v_f couplings are proportional to the Z' gauge coupling $\tilde{g}$.

This parameterization is suggested by a number of natural conditions:

- the Z' interactions of renormalizable types are to be dominant at low energies $\sim m_Z$. The non-renormalizable interactions generated at high energies due to radiation corrections are suppressed by the inverse heavy mass $1/m_{Z'}$ (or by other heavier scales $1/\Lambda_i \ll 1/m_{Z'}$) and, therefore, at low energies can be neglected;
- the Z' boson is the only neutral vector boson with the mass $\sim m_{Z'}$.

At low energies the Z' couplings enter the cross section together with the inverse Z' mass, so it is convenient to introduce the dimensionless couplings

$$\bar{a}_f = \frac{m_Z}{\sqrt{4\pi} m_{Z'}} a_f, \quad \bar{v}_f = \frac{m_Z}{\sqrt{4\pi} m_{Z'}} v_f, \quad (2)$$

which are constrained by experiments.

Below the Z' decoupling threshold the effective $\tilde{U}(1)$ symmetry is a trace of the renormalizability of an unknown complete model with the Z' boson, and it leads to additional relations between the Z' couplings

$$\bar{a}_{q_d} = \bar{a}_l = -\bar{a}_{q_u} = -\bar{a}_{\nu_l} = \bar{a}, \qquad \bar{v}_{q_d} = \bar{v}_{q_u} + 2\bar{a}, \qquad \bar{v}_l = \bar{v}_{\nu_l} + 2\bar{a}, \quad (3)$$

where q_u, q_d, l, and ν_l are an up-type and a down-type quark, a lepton, and a neutrino inside any fermion generation, correspondingly, and $\bar{a}$ is a universal coupling constant, which defines also the Z–Z' mixing angle in (1):

$$\theta_0 \approx -2\bar{a} \frac{\sin\theta_W \cos\theta_W}{\sqrt{\alpha_{\rm em}}} \frac{m_Z}{m_{Z'}}. \quad (4)$$

The discussed relations (3) and (4) are also true for the THDM case. More details on this matter can be found in [14]. The full Lagrangian is written out in [15].

As a result, Z' couplings can be parameterized by seven independent constants $\bar{a}$, $\bar{v}_u$, $\bar{v}_c$, $\bar{v}_t$, $\bar{v}_e$, $\bar{v}_\mu$, $\bar{v}_\tau$. These parameters must be fitted in experiments. In a particular model, one has some specific values for them. In case when the model is unknown, these parameters remain potentially arbitrary numbers.

3 Abelian Z' in the Drell-Yan process

At hadron colliders the most prominent signal of the Abelian Z' boson is expected in the pp or $(p\bar{p}) \to l^+l^-$ scattering process. The general idea of our approach is equally applicable both for dielectrons and dimuons in the final state. To be definite, we shall consider the dimuon case. Specifics concerning the dielectron final state are addressed to in [8].

The quantities that are directly measured in experiments and used for event selection are the pseudorapidities $\eta_\pm$ and transverse momenta $p_T^\pm$ of the final-state muons.

We use the cross section in the following standard form:

$$\begin{aligned} \frac{\partial^3 \sigma_{AB}}{\partial M \partial Y \partial y} &= \sum_{q,\bar{q}} F_{q\bar{q}}(M, \mu_{\mathrm{F,R}}, Y) \frac{\partial \sigma_{q\bar{q}\to\mu^+\mu^-}}{\partial y}, \\ \sigma_{q\bar{q}\to\mu^+\mu^-} &= \sigma_{q\bar{q}\to\mu^+\mu^-}(M, y), \end{aligned} \tag{5}$$

where $Y = (\eta_+ + \eta_-)/2$ is the well-known intermediate-state rapidity, $y = (\eta_+ - \eta_-)/2$ is related to the scattering angle in the $q\bar{q} \to \mu^+\mu^-$ process and governs the parton-level kinematics, and $M^2 = \hat{s} = (p_{\mu^+} + p_{\mu^-})^2$. The interacting hadrons are marked with A and B (p or $\bar{p}$), and $F_{q\bar{q}}$ is the PDF factor for each quark flavor q at the factorization scale μ_{F} and renormalization scale μ_{R}. To access the parton distribution data, we use the MSTW 2008 package [16]. The quantity $\sigma_{q\bar{q}\to\mu^+\mu^-}$ is the parton-level cross section. All parton-level calculations are performed using *FeynArts* [19] and *FormCalc* [20] packages.

Leading Z' contribution to the Drell-Yan process arises from interference between diagrams with γ^*/Z and Z' intermediate states, resulting in

corrections of order of $O(\tilde{g}^2)$. The cross section reads as

$$\begin{aligned}\sigma_{\rm DY} &= \sigma_{\rm SM} + \sigma_{Z'},\\ \sigma_{Z'} &= \bar{a}^2\sigma_{\bar{a}^2} + \bar{a}\bar{v}_e\sigma_{\bar{a}\bar{v}_\mu} + \bar{a}\bar{v}_u\sigma_{\bar{a}\bar{v}_u} + \bar{v}_u\bar{v}_\mu\sigma_{\bar{v}_u\bar{v}_\mu} + \bar{a}\bar{v}_c\sigma_{\bar{a}\bar{v}_c} + \bar{v}_c\bar{v}_\mu\sigma_{\bar{v}_c\bar{v}_\mu}\end{aligned} \quad (6)$$

Here $\bar{a}$ and $\bar{v}_f$ are the couplings defined in (2), (3), and $\sigma_{\bar{a}^2}$, $\sigma_{\bar{a}\bar{v}_f}$, $\sigma_{\bar{v}_f\bar{v}_{f'}}$ are the numerical factors that depend on M, Y, y. In this approximation there are six independent unknown quantities entering the Drell-Yan process cross section. In (6) the factors that include $\bar{v}_u$ and $\bar{v}_c$ arise only due to contributions of first and second generation fermions, respectively. The contribution from the third generation is neglected due to the nature of (anti)protons.

Both the PDF factor and the parton-level cross section are calculated in the leading order (LO) in α_S, and σ_{AB} in the LO is obtained in this way. The next-to-next-to-leading order (NNLO) QCD corrections are then taken into account by multiplying σ_{AB} by the NNLO K-factor, which is calculated using the *FEWZ 2.1* software [17]. To take into account the electroweak radiative corrections we use running couplings and decay widths, the main contribution comes with the running value of the QED coupling constant $\alpha_{\rm QED}$ at the Z-peak [18].

We also consider the PDF uncertainties $\Delta\sigma_{\rm PDF}$ in the 90% CL intervals and the uncertainties due to the factorization and renormalization scales variation, $\Delta\sigma_\mu$. To incorporate the latter uncertainties, we follow the common procedure: we set $\mu_{\rm R} = \mu_{\rm F} = \mu$ and vary μ from $\sqrt{\hat{s}}/2$ to $2\sqrt{\hat{s}}$.

The cross section then can be written as $\sigma_{\rm DY} \pm \Delta\sigma_{\rm PDF} \pm \Delta\sigma_\mu$.

We note that Y enters the PDF factors only, while y is included into the parton-level cross sections only. This is a crucial point for our analysis, as it allows us to treat $F_{q\bar{q}}$ and $\sigma_{q\bar{q}\to\mu^+\mu^-}$ separately. Therefore, we can try to use any peculiarities in the M-, Y-, and y-dependence of the PDF factors and partonic cross sections to suppress some of the numerical factors in (6). It is assumed that all the combinations of the Z' couplings in the cross section are of the same order of magnitude. The leptophobic Z' case, which seems to be a popular parameterization nowadays, is treated separately in section 4.

In addition to the Z' couplings, there are another two unknown Z' parameters that affect $\sigma_{\rm DY}$. These are the Z' mass $m_{Z'}$ and decay width $\Gamma_{Z'}$. The latest data from the CMS and ATLAS indicates that Z' is heavier than 2.27 TeV. This means, that for energies close to the Z peak the $\sigma_{\rm DY}$

dependencies on $m_{Z'}$ and $\Gamma_{Z'}$ can be neglected, assuming that the Z' peak is far away from this region.

The Y and y values that we can investigate are limited by detector performance and conservation laws.

The selection citerium for muons at the D0 Collaboration is that the muon pseudorapidity must be in the range $|\eta_{\pm}| \leq 2.0$ [21]. Therefore,

$$|Y| \leq 2.0. \tag{7}$$

The limits for y are the same as for Y. The CDF case is addessed in [8]. This section can be briefly summarized by saying the following: the cross section of the Drell-Yan process contains six unknown linear-independent terms inspired by Z' boson. The cross section depends on three kinematic variables, which will be used in what follows to suppress some of the contributions from the unknown Z' parameters. This will allow us to amplify the signal of Z' that is possibly hidden in the Tevatron experimental data.

4 The Observable

Of course, the most detailed description of a scattering process is contained in the differential cross section. But a possible Z' signal can be washed out by the interference between the six independent combinations of Z' couplings entering the cross section. In general, integration by kinematic variables can leave this situation without changes. We need to pay special attention to the integration scheme to reduce the number of interfering parameters in order to make a successful data fit possible. This scheme must derive benefits from kinematic properties of the cross section.

4.1 Integrating by Y

The intermediate-state rapidity Y enters the PDF factors only. Let us study the M- and Y-dependence of $F_{q\bar{q}}(M, Y)$ in eq. (5). At any fixed kinematically allowed Y value $F_{q\bar{q}}$ is a smooth monotonically decreasing function of M. Kinematic properties of $F_{q\bar{q}}$ are different for each flavor but independent of Z' properties. So, the Y-dependence of the cross section can be utilized to suppress the contributions of the second generation, i.e., the terms with $\bar{a}\bar{v}_c$ and $\bar{v}_c\bar{v}_\mu$ in eq. (6).

We use the following integration scheme

$$\sigma_1 = \int_{-Y_m}^{Y_m} dY\, W(M,Y) \frac{\partial^3 \sigma_{\rm DY}}{\partial Y \partial M \partial y} \tag{8}$$

with a simple piecewise-constant weight function

$$W(M,Y) = \begin{cases} A(M), & 0 < |Y| \le Y_1, \\ 1, & Y_1 < |Y| < Y_m. \end{cases} \tag{9}$$

In eq. (8) σ_1 denotes the value obtained by the integration of the triple-differential cross section $\sigma_{\rm DY}$ by Y. In fact, we integrate the PDF factor in eq. (5):

$$F_{q\bar{q}}(M) = 2 \int_0^{Y_m} dM\, W(M,Y)\, F_{q\bar{q}}(M,Y), \tag{10}$$

$$\sigma_1 = \sum_{q,\bar{q}} F_{q\bar{q}}(M) \frac{\partial^2 \sigma_{q\bar{q}\to\mu^+\mu^-}}{\partial M \partial y}. \tag{11}$$

So, in in this subsection we will study $F_{q\bar{q}}(M)$ for different quark generations. Note, that the Y-distribution for the Drell-Yan cross section is symmetric.

Consider the M values at the Z-peak. Both CDF and D0 collaborations define limits of this region to be symmetric with respect to the Z boson mass. These limits are often set to either 66 GeV $\le M \le$ 116 GeV or 71 GeV $\le M \le$ 111 GeV. In the present paper the former alternative is used. Actually, the choice of specific lower and upper limits does not affect our results. There are only two general requirements: the limits have to be symmetric with respect to m_Z and large enough so that we could set all quark masses to zero.

In figure 1 the plots for $F_{q\bar{q}}(M,Y)$ versus Y at different M values are shown for u, d, c, and s quarks. The relative contributions of second generation quarks amount up to 11% at $M = 66$ GeV and cannot be neglected. There is a qualitative difference between the PDF factors for the first and second generations. At some energies the factor for u quarks is convex for Y close to zero (at somewhat lower energies this is also the case for d). This is due to the nature of a proton.

For any given M value from the Z-peak region we can adjust the weight function in such a way that the factors $F_{c\bar{c}}(M)$ and $F_{s\bar{s}}(M)$ amount to less than 1% of each of the factors $F_{u\bar{u}}(M)$ and $F_{d\bar{d}}(M)$:

$$F_{c\bar{c},\, s\bar{s}}(M) \le 0.01 F_{u\bar{u},\, d\bar{d}}(M) \tag{12}$$

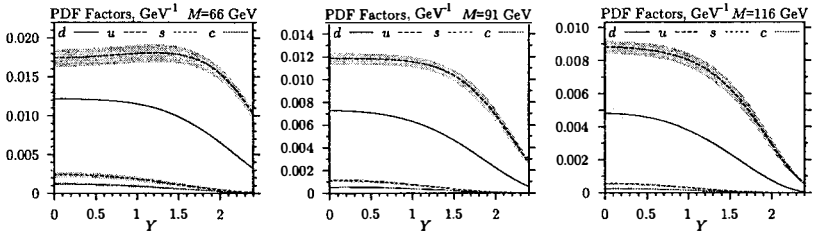

Figure 1: Plots for $F_{q\bar{q}}(M, Y)$ versus Y at different M values. The uncertainties that arise from the PDF errors and factorization scale variation are also shown (see section 3).

This is shown on figure 2 (b). Therefore, the contributions of the second-generation quarks are suppressed, and $\sigma_{\bar{a}\bar{v}_c}$ and $\sigma_{\bar{v}_c\bar{v}_\mu}$ are excluded from $\sigma_{\rm DY}$. The weight coefficient $A(M)$ can be determined for several M values and interpolated in the Z-peak region. For our specific case $A(M)$ is plotted in figure 2 (a). Here Y_m is set to 2.0, and Y_1 is 0.75.

As a result, we obtain the cross section σ_1, which depends on y and M and contains four linearly independent Z' terms instead of six:

$$\sigma_1 \;=\; \sigma_{1\,\rm SM} + \bar{a}^2\sigma_{1\,\bar{a}^2} + \bar{a}\bar{v}_\mu\sigma_{1\,\bar{a}\bar{v}_\mu} + \bar{a}\bar{v}_u\sigma_{1\,\bar{a}\bar{v}_u} + \bar{v}_u\bar{v}_\mu\sigma_{1\,\bar{v}_u\bar{v}_\mu}. \qquad (13)$$

Our next step is to use the remaining two kinematic variables, M and y, to get rid of another two unknown combinations of the Z' couplings.

4.2 Integrating by M and y

The difference of the pseudorapidities, y, enters the parton-level cross section of the Drell-Yan process, $\sigma_{q\bar{q}\to\mu^+\mu^-}$, only and is irrelevant for the PDF analysis. In general, the parton-level cross section depends also on M through four 'resonant' functions:

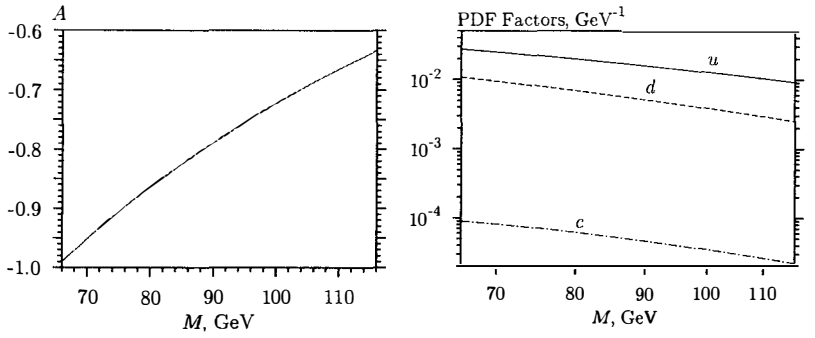

(a) (b)

Figure 2: (a) Weight coefficient $A(M)$ used for integration over the Z-peak region. $Y_m = 2.0$, $Y_1 = 0.75$; (b) A plot illustrating the suppression of the contributions of second-generation quarks to the Drell-Yan cross section in different regions of M values and with different integration schemes. The plotted values are $F_{u\bar{u}}$, $F_{d\bar{d}}$, and $F_{c\bar{c}}$ ($F_{s\bar{s}}$ is not shown on the right plot. Because of the utilized integration scheme at some M this PDF factor becomes negative, but its absolute value is even smaller than $F_{c\bar{c}}$) integrated by Y over the region $|Y| \leq 2.0$ with $A(M)$ from figure 2 (a), where Y_1 is set to 0.75.

$$
\begin{aligned}
f_1(M) &= \frac{1}{(M^2/m_Z^2 - 1)^2 + \Gamma_Z^2/m_Z^2}, \\
f_2(M) &= \frac{(M^2/m_Z^2 - 1)}{(M^2/m_Z^2 - 1)^2 + \Gamma_Z^2/m_Z^2}, \\
f_2'(M) &= \frac{(M^2/m_{Z'}^2 - 1)}{(M^2/m_{Z'}^2 - 1)^2 + \Gamma_{Z'}^2/m_{Z'}^2}, \\
f_3(M) &= \frac{M^2\Gamma_Z\Gamma_{Z'}/(m_Z^3 m_{Z'}) + (M^2/m_Z^2)(M^2/m_Z^2 - 1)(M^2/m_{Z'}^2 - 1)}{[(M^2/m_Z^2 - 1)^2 + \Gamma_Z^2/m_Z^2][(M^2/m_{Z'}^2 - 1)^2 + \Gamma_{Z'}^2/m_{Z'}^2]}.
\end{aligned}
\tag{14}
$$

Here $m_{Z,Z'}$ and $\Gamma_{Z,Z'}$ denote the masses and the widths of the Z and Z' bosons. We investigate the energy region close to the Z boson peak. As it was noted earlier, in this case we do not care about the specific values of the Z' mass and decay widths. But at this point for numerical calculations

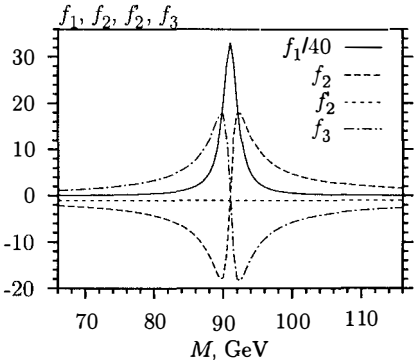

Figure 3: Plots for the resonant functions, which are given by eqs. 14, in the region 66 GeV $\leq M \leq$ 116 GeV.

we are going to set specific values for $m_{Z'}$ and $\Gamma_{Z'}$. Following the recent LHC results [4, 5], we set $m_{Z'}$ to 2.5 TeV and assume the decay width to be 10% of the mass. Actually, we use some asymptotics of f_2' and f_3 at $M \ll m_{Z'}$.

As it can be seen from figure 3, the f_1 function is dominant. In the discussed symmetric Z-peak region the functions f_2, f_3 are odd-like with respect to $M = m_Z$, and the function f_2' is small. As a consequence, after integrating by M over the region the functions f_2, f_2', and f_3 are negligible compared to f_1. We are going to use the discussed feature in what follows.

When investigating the M-dependence of the hadronic cross section σ_1, we deal not with the resonant functions themselves, but with their products with the PDF factors. The general form of σ_1 can be written as

$$\sigma_1 - \sigma_{1\,\mathrm{SM}} = \frac{\cosh 2y}{\cosh^4 y} \left[a(M) \tanh 2y + b(M) \right], \tag{15}$$

where $a(M)$ and $b(M)$ are some functions that include the unknown couplings $\bar{a}$, $\bar{v}_u$, and $\bar{v}_\mu$. The M-dependence arises from the 'resonant' functions multiplied by $F_{q\bar{q}}(M)$ from eq. (10). From the plots in figure 2 (b) we can conclude that the factors $F_{q\bar{q}}(M)$ are smooth, monotonic, and slowly-varying in the considered region. Therefore, we stress that all the discussed properties of f_1, f_2, f_2', and f_3 are generally maintained, when these functions are multiplied by $F_{q\bar{q}}(M)$.

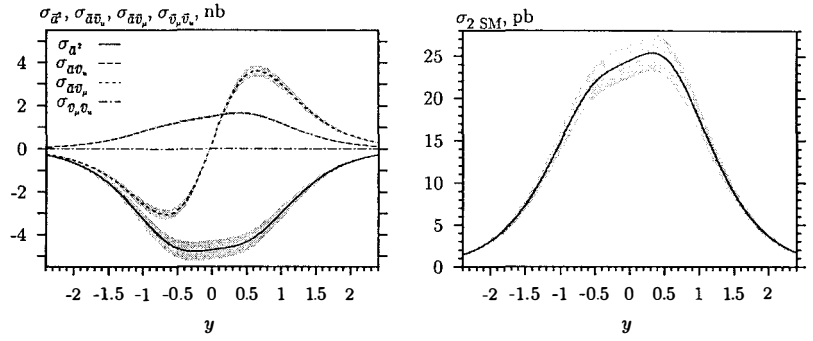

Figure 4: Plots for (a) the Z'-related factors and (b) $\sigma_{2\,\mathrm{SM}}$ from eq. (16). The uncertainty bands are also shown.

Naturally, f_2' and f_3 do not enter the SM part $\sigma_{1\,\mathrm{SM}}$. There are four factors entering the Z' contribution: $\sigma_{1\,\bar{a}^2}$, $\sigma_{1\,\bar{a}\bar{\nu}_\mu}$, $\sigma_{1\,\bar{a}\bar{\nu}_u}$, and $\sigma_{1\,\bar{\nu}_u\bar{\nu}_\mu}$ (see eq. (13)). The factor $\sigma_{1\,\bar{\nu}_u\bar{\nu}_\mu}$ does not depend on f_1, and, therefore, according to our discussion of properties of the 'resonant' functions we may eliminate it by the straightforward integration by M over the Z-peak region (66 GeV $\leq M \leq$ 116 GeV). The resulting value is denoted σ_2:

$$\begin{aligned}
\sigma_2 - \sigma_{2\,\mathrm{SM}} &= \int dM\,(\sigma_1 - \sigma_{1\,\mathrm{SM}}) = \frac{\cosh 2y}{\cosh^4 y}\,(a\tanh 2y + b)\,, \\
\sigma_2 &= \sigma_{2\,\mathrm{SM}} + \bar{a}^2\sigma_{2\,\bar{a}^2} + \bar{a}\bar{\nu}_\mu\sigma_{2\,\bar{a}\bar{\nu}_\mu} + \bar{a}\bar{\nu}_u\sigma_{2\,\bar{a}\bar{\nu}_u}, \\
a &= \int dM\,a(M), \qquad b = \int dM\,b(M). \qquad (16)
\end{aligned}$$

The factors $\sigma_{2\,\mathrm{SM}}$, $\sigma_{2\,\bar{a}^2}$, $\sigma_{2\,\bar{a}\bar{\nu}_\mu}$, $\sigma_{2\,\bar{a}\bar{\nu}_u}$, and $\sigma_{2\,\bar{\nu}_u\bar{\nu}_\mu}$ are plotted on figure 4. It can be seen that $\sigma_{2\,\bar{\nu}_u\bar{\nu}_\mu}$ is negligibly small compared to the other three factors indicating that our assumption is relevant.

We are not concerned about $\sigma_{2\,\mathrm{SM}}$ at the moment and shall turn to investigating the y-dependence of the Z'-related contribution presented in eq. (16). The behavior of the $\sigma_{2\bar{a}\bar{\nu}_u}$ factor is governed by its odd part, while the $\sigma_{2\bar{a}^2}$ and $\sigma_{2\bar{a}\bar{\nu}_\mu}$ factors are obviously dominated by their even parts. From the plots on figure 4 (a), one can conclude that it is possible to suppress one of the three factors by integrating the cross section by y over a symmetric region. Remember, that the integration limits for y are

the same as for Y. In our case

$$-2.0 \leq y \leq 2.0. \tag{17}$$

For integration by y we propose the following approach. The weight function that we use has a structure similar to the one in eq. (15):

$$\omega(y) = \tanh 2y + k. \tag{18}$$

Just like the Z' contribution to σ_2, this is a sum of odd and even functions of y. Here k is a numerical constant. We will adjust its value so that the contribution of one of the remaining three factors becomes negligible when integrated by y.

After the integration we obtain

$$\begin{aligned} \sigma^* - \sigma^*_{\rm SM} &= \int_{-Y_m}^{Y_m} dy\,(\tanh 2y + k)\,\sigma_2, \\ \sigma^* &= \sigma^*_{\rm SM} + \bar{a}^2\sigma^*_{\bar{a}^2} + \bar{a}\bar{v}_\mu\sigma^*_{\bar{a}\bar{v}_\mu} + \bar{a}\bar{v}_u\sigma^*_{\bar{a}\bar{v}_u}. \end{aligned} \tag{19}$$

Note, that due to the symmetric integration region only the even part of the function $\omega(y)\sigma_2$ survives. The factors $\sigma^*_{\rm SM}$, $\sigma^*_{\bar{a}^2}$, $\sigma^*_{\bar{a}\bar{v}_\mu}$, and $\sigma^*_{\bar{a}\bar{v}_u}$ are linear functions of k:

$$\begin{aligned} \sigma^*_{\rm SM} &= (3.40 + 63.5\,k)\ \text{pb} \pm (0.39 + 5.4\,k)\ \text{pb}, \\ \sigma^*_{\bar{a}^2} &= (0.354 - 12.2\,k)\ \text{nb} \pm (0.003 - 1.2\,k)\ \text{nb}, \\ \sigma^*_{\bar{a}\bar{v}_u} &= (0.468 + 3.89\,k)\ \text{nb} \pm (0.009 + 0.17\,k)\ \text{nb}, \\ \sigma^*_{\bar{a}\bar{v}_\mu} &= (7.12 + 0.802\,k)\,\text{nb} \pm (0.52 + 0.068\,k)\,\text{nb}. \end{aligned} \tag{20}$$

Let us construct an observable that is suitable for fitting of the axial-vector coupling $\bar{a}$ and the coupling to the up-quark vector current, $\bar{v}_u$. That is, the factor $\sigma^*_{\bar{a}\bar{v}_\mu}$ has to be suppressed. We choose the suppression criteria

$$|\sigma^*_{\bar{a}\bar{v}_\mu}| < 0.01|\sigma^*_{\bar{a}^2}|, \qquad |\sigma^*_{\bar{a}\bar{v}_\mu}| < 0.01|\sigma^*_{\bar{a}\bar{v}_u}| \tag{21}$$

to calculate k in eq. (20). Overlap of the intervals obtained from the upper and lower bounds for factors gives the resulting interval $-9.18 \leq k \leq -8.55$. If we set k = -9 in eq. (20), the resulting observable will contain only two unknown Z' parameters:

$$\begin{aligned} \sigma^* = \sigma^*_{\rm SM} + \bar{a}^2\sigma^*_{\bar{a}^2} + \bar{a}\bar{v}_u\sigma^*_{\bar{a}\bar{v}_u}, \qquad & \sigma^*_{\rm SM} = -569 \pm 48\ \text{pb}, \\ \sigma^*_{\bar{a}^2} = 111 \pm 10\ \text{nb}, \qquad & \sigma^*_{\bar{a}\bar{v}_u} = -34.5 \pm 1.5\ \text{nb}. \end{aligned} \tag{22}$$

Table 1: Couplings entering each of the two considered observables, together with the corresponding values of k, the SM contribution $\sigma^*_{\rm SM}$, and the factors $\sigma^*_{\bar{a}^2}$, $\sigma^*_{\bar{a}\bar{v}_u}$, and $\sigma^*_{\bar{a}\bar{v}_\mu}$.

couplings	k	$\sigma^*_{\rm SM}$, pb	$\sigma^*_{\bar{a}^2}$, nb	$\sigma^*_{\bar{a}\bar{v}_u}$, nb	$\sigma^*_{\bar{a}\bar{v}_u}$, nb
$\bar{a}^2$, $\bar{a}\bar{v}_u$	-9	-569 ± 48	111 ± 10	-34.5 ± 1.5	suppressed
$\bar{a}^2$, $\bar{a}\bar{v}_\mu$	-0.12	-4.23 ± 0.26	1.82 ± 0.14	suppressed	7.02 ± 0.52

This specific observable allows us to perform fitting of the $\bar{a}$ and $\bar{v}_u$ couplings.

There are two other possible observables in this approach: the one with suppressed $\sigma^*_{\bar{a}\bar{v}_u}$ and the one with suppressed $\sigma^*_{\bar{a}^2}$. However, the latter case cannot be realized in our scheme with suppression factor 0.01, because the intervals obtained for the lower and upper bounds from (20) do not overlap. Therefore, one has either to require weaker suppression in eq. (21) or to narrow down the margin of error reducing the confidence level. Furthermore, this observable contains three Z' couplings as opposed to two couplings in the case when $\sigma^*_{\bar{a}\bar{v}_u}$ or $\sigma^*_{\bar{a}\bar{v}_\mu}$ is suppressed. The mentioned flaws make this observable less attractive for data fitting, and we refrain from discussing it in the rest of our paper.

In table 1 we present the combinations of couplings that enter each of the proposed observables, together with the corresponding values of k and $\sigma^*_{\bar{a}^2}$, $\sigma^*_{\bar{a}\bar{v}_u}$, and $\sigma^*_{\bar{a}\bar{v}_\mu}$. Note, that we choose certain k values from the corresponding intervals.

The model-independent analysis of the LEP II data [12, 13] resulted in obtaining upper bounds for $\bar{a}^2$ and $\bar{v}_\mu^2$ at 95% CL, both of order of 10^{-4}. From figures 4 (a), (b) and table 1 (see also [15]) it can be seen that these upper bounds are too large, since when substituted into eq. (16) they lead to a large deviation from the SM, which is not confirmed by any of the experimental data. Therefore, we may expect at least some significant improvement of the LEP-motivated bounds.

Neither LEP data nor Tevatron or LHC data shows any explicit indications of the Abelian Z'. This provides motivation to investigate models with the so called leptophobic Z'. In these models Z' boson couplings to the SM leptons are strongly suppressed compared to the quark couplings. From the Lagrangian in eq. (1) and the relations in eq. (3) it follows that in the leptophobic case v_l, a_l, and a_q are small compared to v_q, and the

leading Z' contributions to the cross section are

$$\begin{aligned} \sigma_{\rm DY} &= \sigma_{\rm SM} + \sigma_{Z'}, \\ \sigma_{Z'} &= \bar{a}\bar{v}_u\sigma_{\bar{a}\bar{v}_u} + \bar{v}_u\bar{v}_\mu\sigma_{\bar{v}_u\bar{v}_\mu} + \bar{a}\bar{v}_c\sigma_{\bar{a}\bar{v}_c} + \bar{v}_c\bar{v}_\mu\sigma_{\bar{v}_c\bar{v}_\mu} + O(\bar{a}^2, \bar{a}\bar{v}_\mu). \end{aligned} \quad (23)$$

After applying all the integrations discussed in section 4, we end up with the observable where only the term $\bar{a}\bar{v}_u\sigma^*_{\bar{a}\bar{v}_u}$ survives. This observable is one-parametric:

$$\sigma^* = \sigma^*_{\rm SM} + \bar{a}\bar{v}_u\sigma^*_{\bar{a}\bar{v}_u}. \quad (24)$$

The numerical values are the same as in the second line of table 1.

Our results obtained for the dimoun case can be easily recalculated for dielectrons, taking into account the difference between event selection criteria for muons and electrons.

5 Discussion

The data analysis performed by the LHC and Tevatron collaborations resulted in setting model-dependent lower bounds on the Z' mass. In that analysis only the high-energy region of the Drell-Yan cross section was considered. In our paper we present a different approach that allows to search for a Z' signal in the $p\bar{p} \to l^+l^-$ process at the energies near m_Z. In this region the most important contributions at the Z peak come from the $Z - Z'$ mixing angle and Z'-induced contact couplings. The approach utilizes the model-independent relations between the effective Z' couplings. Therefore, in case no signal is observed one would still be able to derive constraints for different Z' models and compare them to the ones presented in [4, 5].

We provided the example of how to use the proposed procedure. The numerical values of the cutoffs Y_1, Y_m and k may vary, as they depend on specific experimental conditions, e.g. bin structure and available data. For example, the Y_m value can easily be moved closer to the detector coverage limit, and the weighting functions $W(M, Y)$ and $\omega(y)$ will have to be adjusted accordingly, but the general layout, including the qualitative form of the weighting functions, will remain unchanged.

The obtained two alternative observables can be used in fitting the experimental data on the $p\bar{p} \to l^+l^-$ scattering collected by the Tevatron

collaborations. This allows to constrain the Z' vector axial-vector couplings to SM fermions.

In case of the leptophobic Z' boson, there is a one-parametric observable containing the combination of couplings $\bar{a}\bar{v}_u$.

There is a large amount of data on leptonic scattering processes collected in the LEP and LEP II experiments. The second observable in table 1 contains the coupling combinations $\bar{a}^2$ and $\bar{a}\bar{v}_e$ that also enter lepton scattering processes. It seems to be attractive for combined fits of the LEP and Tevatron data.

References

[1] A. Leike, *Phys. Rep.* **317**, 143 (1999).

[2] P. Langacker, *Rev. Mod. Phys.* **81**, 1199-1228 (2008).

[3] T. Rizzo, e-print hep-ph/0610104.

[4] CMS Collaboration, *Phys. Lett. B* **720**, 63 (2013) e-print arXiv:1212.6175 [hep-ex].

[5] N. Hod, on behalf of the ATLAS collaboration, e-print arXiv:1303.4287 [hep-ex].

[6] P. Osland and A. Pankov, *Phys. Lett. B* **406**, 328-336 (1997).

[7] P. Osland, A. A. Pankov, N. Paver and A. V. Tsytrinov *Phys. Rev. D* **79**, 115021 (2009).

[8] A. Gulov and A. Kozhushko, e-print arXiv:1209.5022 [hep-ph].

[9] A. V. Gulov and V. V. Skalozub, *Phys. Rev. D* **61**, 055007 (2000).

[10] A. V. Gulov and V. V. Skalozub, *Phys. Rev. D* **70**, 115010 (2004).

[11] A. V. Gulov and V. V. Skalozub, *Phys. Rev. D* **76**, 075008 (2007).

[12] A. V. Gulov and V. V. Skalozub, e-print arXiv:0905.2596v2 [hep-ph].

[13] A. V. Gulov and V. V. Skalozub, *Int. J. Mod. Phys. A* **25**, 5787-5815 (2010).

[14] A. V. Gulov and V. V. Skalozub, *Eur. Phys. J. C* **17**, 685-694 (2000)

[15] A. V. Gulov and A. A. Kozhushko, *Int. J. Mod. Phys. A* **26**, 4083-4100 (2011).

[16] A.D. Martin, W.J. Stirling, R.S. Thorne and G. Watt, *Eur. Phys. J. C* **63**, 189 (2009); *ibid.* **64**, 653 (2009) http://projects.hepforge.org/mstwpdf/.

[17] http://gate.hep.anl.gov/fpetriello/FEWZ.html.

[18] K. Nakamura *et al.*, *J. Phys. G* **37**, 075021 (2010).

[19] T. Hahn, *Comput. Phys. Commun.* **140**, 418 (2001); http://www.feynarts.de/.

[20] T. Hahn and M. Perez-Victoria, *Comput. Phys. Commun.* **118**, 153 (1999); http://www.feynarts.de/formcalc/, http://www.feynarts.de/looptools/.

[21] V.M. Abazov *et al.*, *Phys. Rev. Lett.* **106**, 122001 (2011).

On the Influence of Crystal Geometry on the Efficiency of "Crystal Collimation" on the LHC

Viktor Tikhomirov*, Alexei Sytov
Research Institute for Nuclear Problems, Belarusian State University

Abstract

Future crystal based collimation system of the Large Hadron Collider is considered. We reveal that the collimation efficiency depends both on the crystal thickness and positive value of the miscut angle characterizing nonparallelity of the channeling plane and the crystal surface. In both cases the collimation efficiency is mostly determined by the number and amplitude of betatron oscillations of particles hitting the crystal the second time and can be described in terms of both beam phase space and particle deflection angle distribution after the first crystal passage. We demonstrate that a crystal thickness optimal for the collimation efficiency exist. Additionally, we prove that the miscut angle could considerably increase the inelastic nuclear interaction fraction even in the perfectly aligned crystal collimator in the UA9 experiment.

1 Introduction

The future collimation system at the LHC based on bent crystals can drastically increase the collimation efficiency in comparison with the traditional "amorphous" one [1], [2] to solve efficiently the problem of halo cleaning after the LHC luminosity upgrade.

In order to investigate the possibilities future LHC crystal based collimation system the UA9 experiment was conducted at the SPS [3]. The

*E-mail:vvtikh@mail.ru

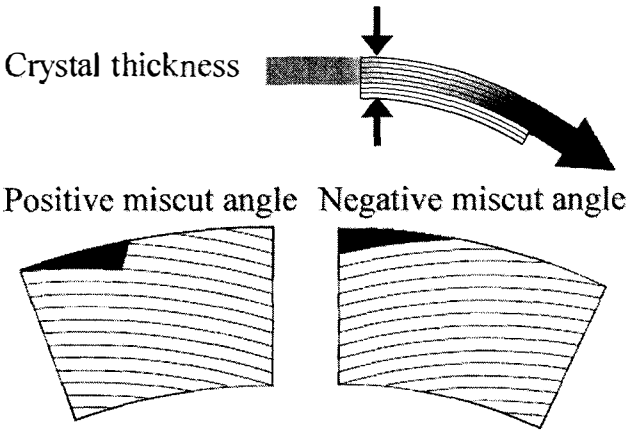

Figure 1: Parameters affecting the collimation efficiency.

considerable difference between simulation and experiment was observed. The experimental ratio of the nuclear reaction rate at channeling and amorphous orientation cases turned out to be equal to 5. So, the collimation efficiency at the channeling orientation obtained in the UA9 experiment was much lower than expected. As we will show below this disagreement can be explained in terms of the miscut angle measured between the channeling planes and crystal surface (see Fig. 1).

In most particle accelerators including the SPS and LHC it is possible to achieve practically zero angular divergence of the incident beam to the crystal. However the miscut angle can greatly influence for collimation efficiency. Even if the crystal alignment is perfect a small nonparallelity of the lateral crystal surface with atomic planes can become a reason of uncapturing the particle in the channeling regime in the case of the positive miscut angle or of early escape the particle from channeling in the case of the negative one. So, too many particles will not hit the absorber immediately and have to hit the crystal again after several turns in accelerator causing additional nuclear reaction.

According to our simulations some particles can pass on the opposite side of the crystal after the first crystal passage. We demonstrate that some of them can hit the absorber without additional crystal passage. It means that the existence of this kind of secondary halo particles can be

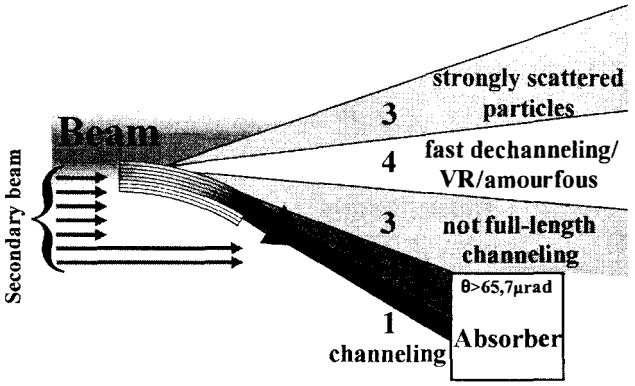

Figure 2: Particle groups.

considered as an important factor determining the collimation efficiency. Additionally, it is the reason of dependence of the collimation efficiency on the crystal thickness (see Fig. 1).

2 Particle deflection by the crystal at the first crystal passage

In the ideal case all particles hitting the crystal at the channeling orientation will be deflected in the channeling regime by an angle of crystal bending. However, in spite of nearly negligible beam angular divergence some particles will either not be captured into the channeling regime or dechannel before the crystal exit. Depending on the deflection angle all the particles deflected by the crystal for the first time can be separated into four groups (Fig. 2).

1. The first one consists of particles deflected by the crystal in the channeling regime approximately by an angle of crystal bending and hitting the absorber immediately. As it was mentioned above it is the ideal situation.

2. The second group includes the particles deflected quite enough to enter the absorber at the first time as the particles from the previous group. In general, these particles pass not full crystal length in the channeling

regime but are deflected enough to reach the absorber.

Both of these groups include good particles that will be absorbed just after the first crystal passage. So, these particles are not "interesting for us". However there are particles that will not enter the absorber immediately after the first crystal passage. These particles are included in the third and forth groups.

3. The third group includes particles deflected by either not full-length channeling or amorphous-like scattering. These particles acquire sufficiently high amplitude of betatron oscillations for hitting the absorber after several turns in the accelerator. However, they have not enough initial conditions after the first crystal passage in order to get into the absorber immediately. The main interest of such particles is that they could pass the crystal again. This can decrease their high amplitude of betatron oscillations by cooling. And what is even worth these particles can be scattered inelastically.

4. The forth group combines the particles deflected by either not full-length channeling or amorphous-like scattering or volume reflection by the angles small enough to reach the absorber whenever. So, such particles need additional crystal passage for hitting the latter.

Both of these groups comprise the secondary beam which has to hit the crystal again. That is why we should consider the second crystal passage in order to investigate the crystal collimation efficiency.

All of these particle groups will exist at the channeling orientation. Depending on some parameters the particle portion in corresponding group can vary. These parameters are the miscut angle and particle impact parameter of the first crystal hitting.

Note that particles from the third group and even some particles from the forth one can have sufficient amplitude of betatron oscillations to bypass the crystal from both sides including the opposite one and, of course, they can hit the crystal again. The probability of another crystal hit depends on the crystal thickness because the crystal becomes wider as a target with increasing of its thickness for particles hitting it at the second time. That is why the collimation efficiency must also depend on the crystal thickness.

As was mentioned above the collimation efficiency is determined by the particle second crystal passage in all cases. The problem is at which conditions particles can be captured at the channeling regime again or be deflected enough for hitting the absorber. This problem should be treated

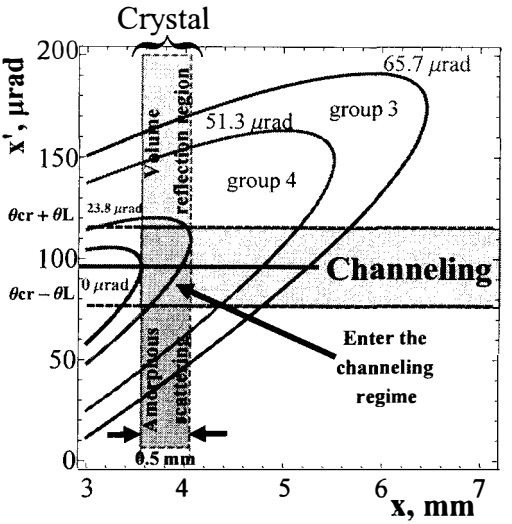

Figure 3: Phase space in accelerator.

in terms of phase space at the crystal longitudinal position and particle deflection angle distribution after the first crystal passage.

3 Conceptions for treating the second crystal passage

Consider the phase space in accelerator. It is shown in Fig. 3. Internal ellipse (51.3 μrad) separates the fourth and the third particle groups as well as the external one (65.7 μrad) bounds the third group. These ellipses are defined by equation

$$x^2\gamma_{cr} + 2\alpha_{cr}xx' + \beta_{cr}x'^2 = A^2, \tag{1}$$

where $\gamma_{cr} = (1 + \alpha_{cr}^2)/\beta_{cr}$, α_{cr} and β_{cr} are the Courant-Snyder coefficients at the crystal longitudinal coordinate, x and x' are particle transverse coordinate and angle in accelerator respectively [4]. These coordinates in phase space vary at different particle revolution and in the ideal case must

be random value uniformly distributed on the corresponding ellipse. The Courant-Snyder coefficients are constants at the respective longitudinal coordinate known for each accelerator. So, just the value A^2 defines the size of the ellipse. This value is an invariant equal to the beam emittance. It strictly depends on the particle deflection angle θ_d during the previous crystal passage.

$$A^2 = x_0^2/\beta_{cr} + \beta_{cr}\theta_d^2 + 2\theta_d(\beta_{cr}x_0' + \alpha_{cr}x_0), \tag{2}$$

where x_0 and x_0' are initial coordinate and angle at the crystal entrance. From the Fig. 3 one can see where the ellipses intersect the crystal i. e. the hit of the crystal occurs. However, the first crystal hit occurs approximately at the maximal coordinate in phase space. This coordinate is equal to the corresponding amplitude of betatron oscillations at which the crystal "scrapes" the beam at x_{cr}. The incident angle is expressed by x_{cr}: $x_{cr}' = -\alpha_{cr}x_{cr}/\beta_{cr}$ in this case. That's why Eq. (2) can be simplified:

$$A^2 = x_{cr}^2/\beta_{cr} + \beta_{cr}\theta_d^2. \tag{3}$$

So, we should just find the deflection angles to determine corresponding zone boundaries. The external boundary of the fourth particle group can be obtained from the condition that the transverse coordinate of the boundary of the absorber X_{TAL} is equal to the amplitude of betatron oscillations at the absorber longitudinal coordinate. So, one can conclude that

$$A_4^2 = X_{TAL}^2/\beta_{TAL} \tag{4}$$

and substituting this equation into Eq. (3), one can obtain the deflection angle

$$\theta_{d4} = \sqrt{X_{TAL}^2\beta_{cr}/\beta_{TAL} - x_{cr}^2}/\beta_{cr}, \tag{5}$$

where β_{TAL} is the Courant-Snyder coefficient at the absorber longitudinal coordinate. For the UA9 experiment such deflection angle is approximately equal to 51.3 μrad.

The external boundary of the third particle group can be obtained from the condition that the positive deflection angle is sufficient only for particle touching the absorber at its boundary X_{TAL}. The coordinate of incidence to the absorber x_{inTAL} depending on the transverse particle coordinate x_d and the deflection angle θ_d after the crystal passage can be written as:

$$\begin{aligned} x_{inTAL} = x_d\sqrt{\beta_{TAL}/\beta_{cr}}(\cos\Delta\Psi + \alpha_{cr}\sin\Delta\Psi) + \\ +(\theta_d + x_{cr}')\sqrt{\beta_{TAL}\beta_{cr}}\sin\Delta\Psi, \end{aligned} \tag{6}$$

where $\Delta\Psi$ is the difference between absorber and crystal betatron phases. Assuming that $x_d = x_{cr}$ for the first crystal passage and putting $x_{inTAL} = X_{TAL}$ one can obtain the required deflection angle

$$\theta_{d3} = \frac{X_{TAL} - x_{cr}\sqrt{\beta_{TAL}/\beta_{cr}}(\cos\Delta\Psi + \alpha_{cr}\sin\Delta\Psi)}{\sqrt{\beta_{TAL}\beta_{cr}}\sin\Delta\Psi} - x'_{cr}. \qquad (7)$$

This deflection angle is approximately equal to 65.7 μrad for the UA9 experiment. Unlike the external boundary of the fourth particle group the one of the third group is not so strict because if the deflection angle exceeds θ_{d3} but possesses negative sign, the particle will not hit the absorber immediately and, thus, will join the third particle group. But the case of large negative deflection angle is rather exotic because the volume reflection can't produce such considerable angle at the first particle crystal passage and the probability of scattering by nuclei by such angle at the UA9 crystal collimator length ($\sim$2 mm) and the beam energy (120 GeV) is sufficiently small. So, we can consider that at the second crystal passage the beam phase space is limited by the external boundary of the third particle group.

What effects are possible at the second crystal entrance? One can notice in the Fig. 3 the zone of possible capture in the channeling regime restricted by the Lindhard angle, the volume reflection zone and the zone of amorphous-like scattering. Here the same value of crystal thickness was taken as in the UA9 experiment: 0.5 mm. One can see that at such value of crystal thickness most of particle simply scattered during the first crystal passage will hit the crystal at the channeling zone because the r.m.s. angle of scattering at the crystal length 2 mm (as in the UA9) is approximately equal to 25 μrad. The entrance in the channeling zone doesn't mean automatic capture in the channeling regime, it only means that the entrance in the channeling regime is possible.

In the case of entrance in the zone of amorphous-like scattering particle can be deflected in different directions. According to (2) the amplitude of betatron oscillations can not only increase but also decrease. It means the possibility that some particles can lose their transverse energy and have a chance to enter the channeling regime at the next crystal passage. Also they can increase their amplitude of betatron oscillations and hit the absorber without additional crystal passage. But of course each crystal passage increases the probability of nuclear reaction, that's why the amorphous-like scattering is undesirable.

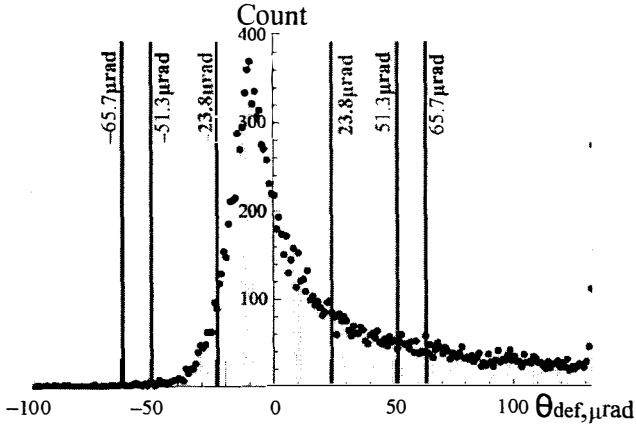

Figure 4: Particle distribution in deflection angle after the first crystal passage.

The volume reflection can be useful for particles from the forth group that need only small betatron oscillation amplitude increasing in order to reach the absorber.

In all cases the question is how many particles from this or that group will enter. In favorable cases the particles with low amplitude of betatron oscillations are good for the channeling regime and the particles with high amplitude of betatron oscillations are good for straight hit into absorber. So, we need the particle distribution in deflection angles after the first crystal passage simulated for the perfect channeling alignment of the crystal with zero miscut (Fig. 4). Vertical lines represent corresponding ellipses (that the relationship between them is given by Eq. (3)). One can see that most of particles will enter the channeling regime with high probability. But considerable part of them possess bad betatron oscillations amplitude both for channeling and for the immediate absorber hit.

All the conceptions in this section can be applied to investigation of both the miscut angle and the crystal thickness influence.

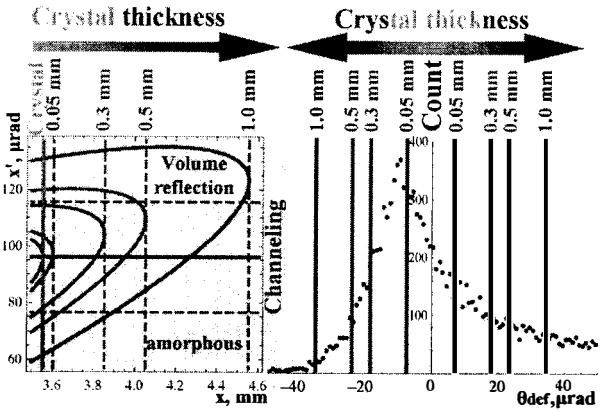

Figure 5: Phase space in accelerator and particle distribution of deflection angles after the first crystal passage.

4 Crystal thickness influence on the collimation efficiency

Imagine at first that we have a crystal of infinite thickness. It is clear that such configuration cannot be optimal because particles from the third group will hit the crystal every time instead of flight from the opposite crystal sight directly to the absorber. From the other hand if the crystal is very thin many particles will not enter the channeling regime at the second crystal passage as we can see from both the phase diagram and deflection angle distribution (the initial conditions at the first crystal passage remain the same because the particle impact parameter doesn't exceed $0.2 \div 0.3$ μm). So, this case also cannot be considered as optimal. That's why we can conclude that a crystal thickness optimal for the maximal collimation efficiency must exist.

Which optimal crystal thickness can we expect? In order to answer this question we can apply the conceptions of phase diagram and deflection angle distribution, shown in Fig. 5. Different possible values of the crystal thickness correspond to the maximal coordinates of the ellipses. The latter can be defined by the particle deflection angle at the first crystal passage, that's why we can connect the crystal thickness and the deflection angle.

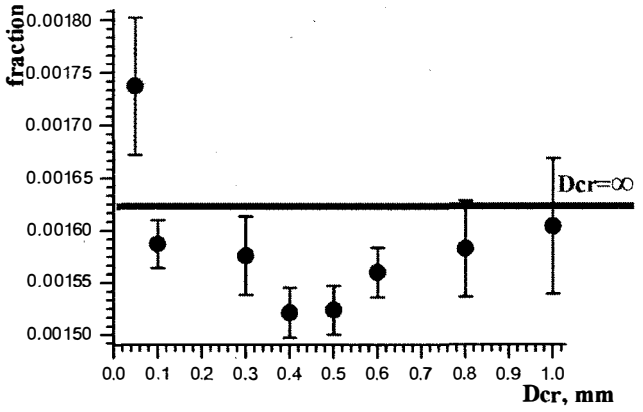

Figure 6: Dependence of the inelastic nuclear interaction fraction of protons on the crystal thickness.

One can see this correspondence in Fig. 5. So, we can conclude that for low probability of the amorphous-like scattering the crystal thickness must be at least less than 2 mm for the UA9 case in order not to include the forth particle group (see Fig. 3) completely. On the other hand it must exceed 0.2÷0.3 mm in order to include at least the peak of the deflection angle distribution in the channeling zone. The most expected value of the crystal thickness is a bit more than 0.3 mm because the ellipses with the maximal coordinate exceeding 0.3 mm don't belong to the channeling zone completely.

The dependence of inelastic nuclear interaction fraction of protons on the crystal thickness was simulated (Fig. 6). As we have expected before the optimal crystal thickness slightly exceed 0.3 mm and is considerably less than 2 mm. If the crystal thickness decreases, the nuclear interaction fraction will increase. While we increase it the nuclear interaction fraction will also do asymptotically approaching to the value of 0.00162.

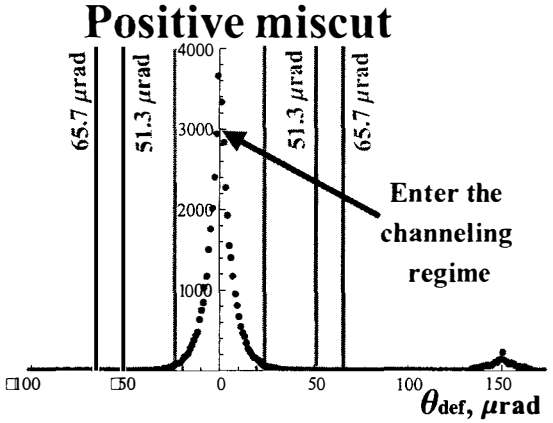

Figure 7: Distribution of deflection angles after the first crystal passage in the case of positive miscut angle of 200 μrad.

5 Miscut angle influence to the collimation efficiency

The technology of crystals with almost zero miscut is very complicated and expensive. But is the miscut angle so important for taking it into account? What is better the positive miscut angle or the negative one?

The first variant seems to be better [5] because the angular divergence of the beam hitting the crystal the second time is considerably higher in the case of negative miscut than in the case of the positive one (Fig. 7-8). It means that much more particles will enter in the channeling zone (see Fig. 3) in the positive miscut case than in the negative one. However, let us recall that the particles from the third and edge of the fourth group needn't another crystal passage or need only a small additional deflection by crystal. Much more of such particles appear in the negative miscut angle case than to the positive one. So, each sign of the miscut angle has its own advantage.

We simulated the dependence of inelastic nuclear interaction fraction of protons on the miscut angle (Fig. 9). At small values the positive miscut angle provides better collimation efficiency than the negative one. But the

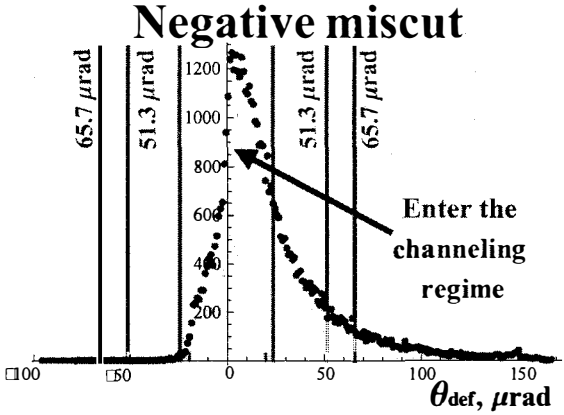

Figure 8: Distribution of deflection angles after the first crystal passage in the case of negative miscut angle of −200 μrad.

peaks of the dependence are approximately symmetric w. r. t. vertical axis and have approximately the same value. It is also important that the nuclear interaction fraction in both peaks is exceeds that at zero miscut approximately by a factor of four. Note that the UA9 experiment was provided at the miscut of 200 μrad, that is at the worst possible value for the collimation according to both our simulations and [6]. So, the miscut angle of both signs can considerably increase the nuclear interaction rate in the UA9 case in which the collimation efficiency of the positive miscut case is practically the same as in the case of negative one.

6 Conclusion

Thus, both the crystal thickness and the miscut angle can considerably affect the collimation efficiency. In particular, the influence of the latter increases the nuclear reaction probability in the crystal collimator up to four times. So, one can improve the crystal based collimation system by varying the miscut angle. At small values of about 10 μrad the positive sign of the latter is much more preferable than the negative one. However, the nuclear reaction probability will increase up to four times for both

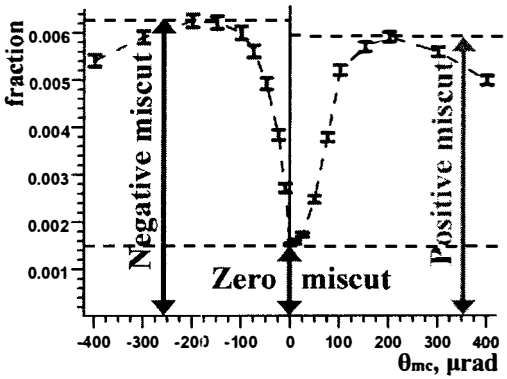

Figure 9: Dependence of inelastic nuclear interaction fraction of protons on the miscut angle.

signs of the miscut angle in the widely used 100 μrad region. Thus the UA9 experiment was carried out at optimal crystal thickness of 0.3÷0.5 mm and really unfortunate miscut angle value of 100÷200 μrad.

References

[1] V. M. Biryukov, et al. *NIM* B234, 23-30 (2005).

[2] R. Assmann, S. Redaelli, W. Scandale. *LHC Project Report 918* 4 p. (2006).

[3] W. Scandale, et al. *Phys. Lett.* B692, 78-82 (2010).

[4] A.G. Afonin et al. *Physics of Particles and Nuclei* 36, 42-99 (2005).

[5] K. Elsener, et al. *NIM* B119, 215-230 (1996).

[6] V.V. Tikhomirov, A.I. Sytov. *Prob. Atomic Sci. Technol.* 57 N1, 88-92 (2012).

2 Non-Accelerator Physics

Spacetime Quantum Fluctuations, Minimal Length and Einstein Equations

A.E.Shalyt-Margolin*
National Centre of Particles and High Energy Physics,
Minsk, Belarus

Abstract

In the process of work it has been found that space-time quantum fluctuations are naturally described in terms of the deformation parameter introduced on going from the well-known quantum mechanics to that at Planck's scales and put forward in the previous works of the author. As shown, with the use of quite natural assumptions, these fluctuations must be allowed for in Einstein Equations to lead to the dependence of the latter on the above-mentioned parameter, that is insignificant and may be ignored at low energies but is of particular importance at high energies. Besides, some inferences form the obtained results are maid.

1 Introduction

The notion "space-time foam", introduced by J. A. Wheeler about 60 years ago for the description and investigation of physics at Planck's scales (Early Universe) [1],[2], is fairly settled. Despite the fact that in the last decade numerous works have been devoted to physics at Planck's scales within the scope of this notion, for example [3]–[22], by this time still their no clear understanding of the "space-time foam" as it is.
On the other hand, it is undoubtful that a quantum theory of the Early Universe should be a deformation of the well-known quantum theory.
The deformation is understood as an extension of a particular

*E-mail: a.shalyt@mail.ru; alexm@hep.by

theory by inclusion of one or several additional parameters in such a way that the initial theory appears in the limiting transition [23].

In his works with the colleagues [24]–[32] the author has put forward one of the possible approaches to resolution of a quantum theory at Planck's scales on the basis of the density matrix deformation. This work demonstrates that space-time quantum fluctuations, in essence generating the space-time foam, may be naturally described in terms of the deformation parameter α_l introduced in [24]–[32], where l – measuring scale. Further it is shown that, with the use of quite natural assumptions, these fluctuations must be allowed for in Einstein Equations [33] to result in their dependence on the parameter α_l, insignificant and negligible at low energies (i.e. in the limit $l \to \infty$) but important at Planck's scales $l \to \propto l_P$.

Actually it is revealed that, if the metrics $g_{\mu\nu}$ is measured at some fixed energy scale $E \sim 1/l$ (as is always the case in real physics), Einstein Equations are α_l–deformed, and the known Einstein Equations [33] appear in the low-energy limit. However, this aspect may be ignored in all the known cases and the corresponding energy ranges because the scale l is very distant from l_P. Two clear illustrations of the high-energy α_l–deformation of Einstein Equations are given.

Some inferences from the results obtained are considered, in particular for the cosmological term Λ.

This work is a natural continuation of the paper [50]. In [50] it has been shown that in particular cases the General Relativity Einstein Equations may be written in the α_l–representation, i.e. they are dependent on the parameter α_l. Also, it has been demonstrated that for the indicated cases one can derive the high-energy (Planck) α_l - deformation of Einstein Equations. Then the question arises whether Einstein Equations are dependent on α_l in the most general case.

Proceeding from the present work, this question may be answered positively.

2 Quantum Fluctuations of Space-time and High-Energy Deformation

In accordance with the modern concepts, the space-time foam [2] notion forms the basis for space-time at Planck's scales (Big Bang). This object

is associated with the quantum fluctuations generated by uncertainties in measurements of the fundamental quantities, inducing uncertainties in any distance measurement. A precise description of the space-time foam is still lacking along with an adequate quantum gravity theory. But for the description of quantum fluctuations we have a number of interesting methods (for example, [34],[12]-[22]).
In what follows, we use the terms and symbols from [14]. Then for the fluctuations $\widetilde{\delta l}$ of the distance l we have the following estimate:

$$\widetilde{\delta l} \gtrsim l_P^{\gamma} l^{1-\gamma}, \tag{1}$$

where $0 \leq \gamma \leq 1$ and $l_P = (\hbar G/c^3)^{1/2}$ is the Planck length.
At the present time three principal models associated with different values of the parameter γ are considered:

A) $\gamma = 1$ that conforms to the initial (canonical) model from [2]

$$\widetilde{\delta l} \gtrsim l_P; \tag{2}$$

B) $\gamma = 2/3$ that conforms to the model [34],[14] compatible with the holographic principle [35]–[39]

$$\widetilde{\delta l} \gtrsim (l l_P^2)^{1/3} = l_P \left(\frac{l}{l_P}\right)^{1/3}; \tag{3}$$

C) $\gamma = 1/2$ - random-walk model [21] [22]

$$\widetilde{\delta l} \gtrsim (l l_P)^{1/2} = l_P \left(\frac{l}{l_P}\right)^{1/2}. \tag{4}$$

But, because of the experimental data obtained with the help of the Hubble Space Telescope [40], a random-walk model C) may be excluded from consideration (for example, see [19]) and is omitted in this work.

Moreover, in fact it is clear that **at Planck's scales, i.e. for**

$$l \to \propto l_P, \tag{5}$$

models A) are B) are coincident.
Using(2)–(4), we can derive the quantum fluctuations for all the primary

space-time characteristics, specifically for the time $\widetilde{\delta}t$, energy $\widetilde{\delta}E$, and metrics
$\widetilde{\delta}g_{\mu\nu}$ (formula (10) of [14]):

$$\widetilde{\delta}g_{\mu\nu} \gtrsim (l_P/l)^{\gamma}. \tag{6}$$

It is obvious that all of them are dependent on one and the same dimensionless parameter l_P/l and on the Planck length l_P, i.e. on the fundamental constants.
Note also that in fact this parameter is introduced as a deformation parameter on going from the well-known quantum mechanics (QM) to a quantum mechanics with the fundamental length (QMFL), provided this length l_{min} is on the order of Planck's length $l_{min} \propto l_P$, as revealed by the author in the works written with his colleagues [24] –[32]. Let us recollect in short the central idea of the above-mentioned works (pp. 1267,1268 in [25]).
The main object under consideration in this case is the density matrix ρ. We assume that in QMFL the measuring procedure adopted in QM is valid being defined by ρ. Then

$$Sp[(\rho\widehat{X}^2) - Sp^2(\rho\widehat{X})] \geq l_{min}^2 > 0, \tag{7}$$

where $\widehat{X}$ is the coordinate operator. Expression (7) gives the measuring rule used in QM. However, in the case considered here, in comparison with QM, the right part of (7) cannot be done arbitrarily near to zero since it is limited by $l_{min}^2 > 0$. A natural way for studying QMFL is to consider this theory as a deformation of QM, turning to QM at the low energy limit (during the expansion of the Universe after the Big Bang).
We will consider precisely this option. Here the following question may be formulated: how should be deformed density matrix conserving quantum-mechanical measuring rules in order to obtain self-consistent measuring procedure in QMFL? For answering to the question we will use the R-procedure. For starting let us to consider R-procedure both at the Planck's energy scale and at the low-energy one. At the minimal length scale $l \approx il_{min}$ where i is a small quantity. Further l tends to infinity and we obtain for density matrix [24]-[32]:

$$Sp[\rho l^2] - Sp[\rho l]Sp[\rho l] \simeq l_{min}^2 \;\; or \;\; Sp[\rho] - Sp^2[\rho] \simeq l_{min}^2/l^2. \tag{8}$$

Therefore:

1. When $l < \infty$, $Sp[\rho] = Sp[\rho(l)]$ and $Sp[\rho] - Sp^2[\rho] > 0$. Then, $Sp[\rho] < 1$ that corresponds to the QMFL case.

2. When $l = \infty$, $Sp[\rho]$ does not depend on l and $Sp[\rho] - Sp^2[\rho] \to 0$. Then, $Sp[\rho] = 1$ that corresponds to the QM case.

The above deformation parameter is as follows:

$$\alpha_l = l_{min}^2/l^2. \tag{9}$$

This parameter is variable within the interval

$$0 < \alpha_l \leq 1/4, \tag{10}$$

whereas the density matrix in QMFL becomes deformed and dependent on α_l: $\rho = \rho(\alpha_l)$, and we get

$$\lim_{\alpha_l \to 0} \rho(\alpha_l) \to \rho, \tag{11}$$

where ρ – known density matrix from QM.
When $l_{min} \propto l_P$, it is cleat that $\alpha_l \propto l_P^2/l^2$ and all the fluctuations above $\widetilde{\delta} l, \widetilde{\delta} g_{\mu\nu}, \widetilde{\delta} t, \widetilde{\delta} E$ may be expressed in terms of the deformation parameter α_l. For example, this is the case when the Generalized Uncertainty Principle (GUP) [41]–[48] is valid

$$\triangle x \geq \frac{\hbar}{\triangle p} + \ell^2 \frac{\triangle p}{\hbar}, \ell^2 = \lambda l_P^2, \tag{12}$$

and λ is the model-depended dimensionless numerical factor.
Then, as seen in (12), we have a minimal length on the order of the Planck length

$$l_{min} = 2\sqrt{\lambda} l_P. \tag{13}$$

Therefore, we obtain

$$(\frac{l_P}{l})^2 = \frac{1}{4\lambda} \alpha_l \tag{14}$$

and the factor $\frac{1}{4\lambda}$ is introduced into all of the formula (2)–(8) as soon as the fundamental quantities involved are expressed in terms of α_l. Specifically, the most important formula (6) in this case is of the form

$$\widetilde{\delta} g_{\mu\nu} \gtrsim (4\lambda)^{-\gamma/2} \alpha_l^{\gamma/2}. \tag{15}$$

In what follows we assume that a minimal length in a theory – l_{min} is existent no matter how it is introduced, from GUP (12) or in some other way. Then the parameter α_l (9) is quite naturally brought about from (7), (8).
With the use of this "coordinate system" the above-mentioned models A) and B) of the space-time quantum fluctuations may be "unified" as follows:

I. The minimal length l_{min} , similar to cases A) and B), is introduced at Planck's level

$$l_{min} \propto l_P.$$

II. In both cases fluctuations of the fundamental quantities may be expressed in terms of the parameter α_l.

III. The principal difference between A) and B) resides in the fact that in the second case a minimal fluctuation of the length is dependent on the measuring scale l, $(\widetilde{\delta}^{min}l) = (\widetilde{\delta}^{min}l)[l]$, whereas in the first case it is completely determined by the minimal length $\widetilde{\delta}^{min} \approx l_{min}$, being absolute in its character.

IV. As noted above, in the high-energy limit, i.e. for

$$l \to l_{min}, \tag{16}$$

both models are coincident.

3 Quantum Fluctuations and Einstein Equations

Thus, from the preceding section it follows that in any case we have minimal fluctuations $\widetilde{\delta}^{min}$ (dependent on the measuring scale l or on the energy $E \sim 1/l$) for all the fundamental physical quantities $l, t, E, g_{\mu\nu}, ...$, expressed in terms of the parameter α_l. Specifically, we have

$$(\widetilde{\delta}^{min}g_{\mu\nu})[l] = (\widetilde{\delta}^{min}g_{\mu\nu})[\alpha_l] \propto \alpha_l^{\gamma/2}. \tag{17}$$

Next we make the only natural assumption
if the metric $g_{\mu\nu}$ in General Relativity (GR) is measured at the scale l or, that is the same, on the scale of the energies $E \sim 1/l$, variation of the metric $\delta g_{\mu\nu}$ is governed by its fluctuation $(\widetilde{\delta}g_{\mu\nu})[l]$

and hence it is dependent on l or, actually, on α_l

$$\delta g_{\mu\nu} = (\delta g_{\mu\nu})[l] = (\delta g_{\mu\nu})[\alpha_l].$$

In particular, it can't be arbitrary small as its lower limit is the fixed value

$$(\widetilde{\delta^{min}} g_{\mu\nu})[\alpha_l] > 0.$$

That means

$$(\delta^{min} g_{\mu\nu})[\alpha_l] = \kappa \alpha_l^{\gamma/2}, \tag{18}$$

where $\kappa > 0$ – some model-dependent factor.
Obviously, we have

$$\lim_{l\to\infty} (\delta g_{\mu\nu})[l] = \lim_{\alpha_l \to 0} (\delta g_{\mu\nu})[\alpha_l] \to 0. \tag{19}$$

From this it follows immediately that in this case variation of the action of δS_G in General Relativity [33] is also dependent on α_l

$$\delta S_G = (\delta S_G)[\alpha_l] \tag{20}$$

and hence $G_{\mu\nu} \equiv R_{\mu\nu} - \frac{1}{2} R g_{\mu\nu}$ is dependent on α_l too:

$$G_{\mu\nu}^{[\alpha_l]} \equiv G_{\mu\nu}[\alpha_l]. \tag{21}$$

Then the knowns **Einstein tensor**

$$\lim_{l\to\infty} G_{\mu\nu}^{[\alpha_l]} = \lim_{\alpha_l \to 0} G_{\mu\nu}^{[\alpha_l]} \equiv G_{\mu\nu} \tag{22}$$

and **Einstein Equations** in the vacuum

$$\lim_{l\to\infty} G_{\mu\nu}^{[\alpha_l]} = \lim_{\alpha_l \to 0} G_{\mu\nu}^{[\alpha_l]} \equiv G_{\mu\nu} = 0 \tag{23}$$

are brought about in the low-energy limit.
Naturally, the right side of Einstein Equations [33] should be dependent on α_l as

$$(8\pi T_{\mu\nu} - \Lambda g_{\mu\nu})^{[\alpha_l]} \equiv (8\pi T_{\mu\nu} - \Lambda g_{\mu\nu})[\alpha_l]. \tag{24}$$

Therefore, Einstein Equations with a nonzero right side are of the following form:

$$\lim_{\alpha_l \to 0} G_{\mu\nu}^{[\alpha_l]} = \lim_{\alpha_l \to 0} (8\pi T_{\mu\nu} - \Lambda g_{\mu\nu})^{[\alpha_l]}. \tag{25}$$

Of course, at low energies, i.e. for

$$l \gg l_P \tag{26}$$

or,that is the same with a very high accuracy, for

$$\alpha_l \approx 0, \tag{27}$$

the function of α_l may be disregarded and in this case, with a very high accuracy, we can obtain the well-known Einstein Equations

$$G_{\mu\nu}^{[\alpha_l]} \approx G_{\mu\nu} = (8\pi T_{\mu\nu} - \Lambda g_{\mu\nu}) \approx (8\pi T_{\mu\nu} - \Lambda g_{\mu\nu})^{[\alpha_l]}.$$

All the scales (energy), at which Einstein Equations have been studied until the present time, satisfied (26),(27), being far away from the Planck scale $l_P \propto 10^{-33} cm$, and in fact had no α_l–dependence.
But on going to the high-energy limit

$$l \dashrightarrow 2l_{min} \propto l_P; \alpha_l \dashrightarrow 1/4 \tag{28}$$

there appears a nontrivial α_l–deformation of Einstein Equations, later referred to as $\alpha-$ deformation

$$G_{\mu\nu}^{[\alpha_l]} = (8\pi T_{\mu\nu} - \Lambda g_{\mu\nu})^{[\alpha_l]}. \tag{29}$$

Note that from [25] (practically from formula (7),(8)) we have found: with the canonical measuring procedure (7), the minimal length l_{min} **is unattainable** and **a minimal measurable length**, denoted as l_{min}^{measur}, is the quantity

$$l_{min}^{measur} = 2l_{min} \tag{30}$$

in accordance with (28).
Consider two examples of the $\alpha-$ deformation of Einstein Equations.

E1.Phenomenological Markov's Model [49].
This example is taken from Section 3 of [50].
Let us dwell on the work [49], where it is assumed that "by the universal decree of nature a quantity of the material density ϱ is always bounded by

its upper value given by the expression that is composed of fundamental constants" ([49], p.214):

$$\varrho \leq \varrho_P = \frac{c^5}{G^2\hbar}, \tag{31}$$

with ϱ_P as "Planck's density".
It is clearly seen that, proceeding from the involvement of the fundamental length on the order of the Planck's $l_{min} \sim l_P$, one can obtain ϱ_P (31) up to a constant. Indeed, within the scope of GUP (12) (but not necessarily) we have $l_{min} \propto l_P$ and then, as it has been shown in [26], (12) may be generalized to the corresponding relation of the pair "energy - time" as follows:

$$\Delta t \geq \frac{\hbar}{\triangle E} + \lambda t_p^2 \frac{\triangle E}{\hbar}. \tag{32}$$

This directly suggests the existence of the "minimal time" $t_{min} \propto t_P$ and of the "maximal energy" corresponding to this minimal time $E_{max} \sim E_P$. Clearly, this maximal energy is associated with some "maximal mass" M_{max}:

$$E_{max} = M_{max}c^2, M_{max} \sim M_P. \tag{33}$$

Whence, considering that the existence of a minimal three-dimensional volume $V_{min} = l_{min}^3 \sim V_P = l_P^3$ naturally follows from the existence of $l_{min} \sim l_P$, we immediately arrive at the "maximal density" ϱ_P (31) but only within the factor determined by λ

$$\frac{M_{max}}{V_{min}} = \varrho_{max} \sim \varrho_P. \tag{34}$$

Actually, the quantity

$$\wp_\varrho = \varrho/\varrho_P \leq 1 \tag{35}$$

in [49] is the deformation parameter as it is used to construct the deformation of Einstein's equation ([49],formula (2)):

$$R_\mu^\nu - \frac{1}{2}R\delta_\mu^\nu = \frac{8\pi G}{c^4}T_\mu^\nu(1 - \wp_\varrho^2)^n - \Lambda\wp_\varrho^{2n}\delta_\mu^\nu, \tag{36}$$

where $n \geq 1/2$, T_μ^ν–energy-momentum tensor, Λ– cosmological constant. The case of the parameter $\wp_\varrho \ll 1$ or $\varrho \ll \varrho_P$ correlates with the classical Einstein equation, and the case when $\wp_\varrho = 1$ – with the de Sitter Universe. In this way (36) may be considered as $\wp_\varrho$-deformation of the General Relativity.

As it has been noted before, the existence of a maximal density directly, up to a constant, follows from the existence of a fundamental length (31). It is clear that the corresponding deformation parameter $\wp_\varrho$ (35 may be obtained from the deformation parameter α_x (9). In fact, since $\alpha_x = l_{min}^2/x^2$, we have

$$\alpha_x^{3/2} = \frac{l_{min}^3}{x^3} \sim \frac{V_{min}}{V}, \tag{37}$$

where V is the three-dimensional volume associated with the linear dimension x.

As α_x may be represented in the form [24]–[32]:

$$\alpha_x = E^2/E_{max}^2, \tag{38}$$

$E_{max} \sim E_P$, and $V_{min} \sim V_P = l_P^3$, then from (33)–(35),(37),(38) we get

$$\wp_\varrho \sim \frac{E/V}{E_{max}/V_{min}} = \frac{\varrho}{\varrho_{max}} = \alpha_x^2. \tag{39}$$

Of course, the proportionality factor in (39) is model dependent. Specifically, if QMFL is related to GUP, this factor is depending on λ (12). But the deformation parameters $\wp_\varrho$ and α are differing considerably: the limiting value $\wp_\varrho = 1$ is obviously associated with singularity, whereas originally (by the approach involving the density matrix deformation [25]–[27],[32]) no consideration has been given to the deformation parameter $\alpha = 1$ associated with singularity,(formula (30))).

So, $\wp_\varrho$-deformation of the General Relativity [49] may be interpreted as α-deformation.

E2.Spherically-symmetric horizon spaces [51].

As shown in [51], the Einstein Equation for horizon in this case may be written as a thermodynamic identity (the first principle of thermodynamics): ([51], formula (119))

$$\underbrace{\frac{\hbar c f'(a)}{4\pi}}_{k_B T} \underbrace{\frac{c^3}{G\hbar} d\left(\frac{1}{4} 4\pi a^2\right)}_{dS} \underbrace{- \frac{1}{2}\frac{c^4 da}{G}}_{-dE} = \underbrace{P d\left(\frac{4\pi}{3} a^3\right)}_{P\,dV}, \tag{40}$$

where a static, spherically symmetric horizon in space-time is described by the metric

$$ds^2 = -f(r)c^2dt^2 + f^{-1}(r)dr^2 + r^2 d\Omega^2, \tag{41}$$

and the horizon location will be given by simple zero of the function $f(r)$ ($f(a) = 0$, $f'(a) \neq 0$) at $r = a$.(Here $r = a$ is the radius of a sphere.) And $P = T_r^r$ is the trace of the momentum-energy tensor and radial pressure.
In Sections 5 and 6 of [50] first the Einstein Equations on horizon (40) have been written in terms of the parameter α_a, next the high-energy ($\alpha_a \to 1/4$), α_a – deformation of these equations has been derived in two different cases: equilibrium and nonequilibrium thermodynamics.
The latter case is distinguished from the first one by the dynamic cosmological term dependent on α_a, appearing with the corresponding factor in the right side of high-energy deformed (40) as follows:

$$\Lambda \equiv \Lambda[\alpha_a]. \tag{42}$$

4 Comments and Conclusion

In this way we can conclude that

C1) with inclusion of the space-time quantum fluctuations (e.g., in the form of (2) or (3), we can naturally assume that in the most general case of Einstein Equations there is a dependence on the small dimensionless parameter α_l, infinitesimal at normal energies to be neglected but important at high energies which are on the order of the Planck energy.

C2) The parameter α_l is a deformation parameter on going from the well-known quantum theory to a quantum theory of the Early Universe (Planck's scales)and hence the above-mentioned dependence of Einstein Equations on this parameter may be considered as α_l – deformation of the General Relativity whose well-known, i.e. canonical, Einstein Equations are brought about in the low-energy limiting transition.

The foregoing results are rather important for better understanding and investigation of the cosmological term Λ, especially in view of the Dark Energy Problem [52]–[56].
In principle, they may be used to answer the question whether $\Lambda = const$ or $\Lambda = \Lambda(t)$ is a time-variable quantity.
Despite the fact that the works taking Λ as $\Lambda(t)$, i.e. as a dynamic quantity, are numerous(for example, [57]– [60]) quite forceful arguments are given against this point of view (for example, [61]).
Indeed, according to the General Relativity, the cosmological term Λ has

been considered constant $\Lambda = const$ as, due to the Bianchi identities [33],

$$\nabla^{\mu} G_{\mu\nu} = 0. \tag{43}$$

But in this work it has been demonstrated that, actually, Bianchi identities (43) are introduced at the low-energy limit only

$$\lim_{\alpha_l \to 0} \nabla^{\mu} G^{[\alpha_l]}_{\mu\nu} = \nabla^{\mu} G_{\mu\nu} = 0. \tag{44}$$

Because of this, the really measured cosmological term Λ in fact is dynamic $\Lambda = \Lambda[\alpha_l(t)]$, practically invariable in the modern epoch, i.e. at low energies, due to slow variations of the deformation parameter $\alpha_l(t)$ at low energies and due to its very small value.
In the works [62]–[64] a behavior of the term Λ has been studied reasoning from $\alpha_l(t)$ on the assumption that it is dynamic, similar to the case proven in [62] GUP for the pair of conjugate variables (Λ, V), where V is the space-time volume, as with the holographic principle applied to the whole Universe [65]. The main difference of these two cases is in the leading order of expansion $\Lambda[\alpha]$ in terms of α. In the first case it is the second

$$\Lambda^{GUP}(\alpha) \propto (\alpha^2 + \eta_1 \alpha^3 + ...)\Lambda_p, \tag{45}$$

whereas in the second case it is the first

$$\Lambda^{Hol}(\alpha) \propto (\alpha + \xi_1 \alpha^2 + ...)\Lambda_p, \tag{46}$$

where $\Lambda_p = \Lambda_{\alpha \to 1/4}$ – cosmological term at Planck's scales.
As Λ^{Hol} is practically coincident with the experimental value of the cosmological term Λ_{exper}, a holographic model is preferable – model B) of Section 2 developed for quantum fluctuations is supported experimentally.
In conclusion, let us state some important problems of the particular concern:

A) What is the way to derive, in the most general case and in the explicit form, the high-energy $(\alpha_l \to 1/4)$ α_l - representation or, that is the same, the high-energy α_l - deformation of Einstein Equations?

B) Provided the foregoing representation is derived, is it possible to have its logical series expansion in terms of α_l? Note that we must allow for the following: α_l may be considered continuous with a high accuracy only at low energies. Obviously, at high energies it is discrete as the length l

is comparable to the minimal length $l \propto l_{min}$, i.e. in fact to the Planck's length $l \propto l_P$.
As noted in point IV of Section 2, on approximation of the Planck energies, models (A) and (B) for the space-time fluctuations are practically coincident. Because of this, we can raise the following questions:

C_1) Is there some **"critical measure"** or **"critical index"** γ_{crit}: $\gamma = 2/3 < \gamma_{crit} < \gamma = 1$ – minimal bound, beginning from which models (A) and (B) are practically identical at high energies, between the coefficients $\gamma = 2/3$ and $\gamma = 1$ in formulae (3) and (3)? If such a **"critical index"** exists, what is it like? This may be of great importance for answering the question that concerns the **"phase transition"**, i.e. the minimal energies, beginning from which one should take into account the quantum-gravitational effects.

Another but similar problem:

C_2) concerns a minimal bound for α_l (denoted by $\alpha_l^{crit} = l_{min}^2/l_{crit}^2$), above which models (A) and (B) actually result in the same physics. It is clear that the problem at hand is associated with derivation of the corresponding energy: $E_{crit} \sim 1/l_{crit}$.

And, finally,
(D) it is interesting how the high-energy α_l - deformation of Einstein Equations is related to the adequate selection of a model for the space-time foam. Is it representing a set of micro worm holes(for example, [3]–[6]), micro black holes [7]– [9] or something else?
The author is planning to answer these questions, at least some of them, in his future works.

References

[1] J. A. Wheeler, *Geometrodynamics* (Academic Press, New York and London, 1962).

[2] C. W. Misner, K. S. Thorne, and J. A. Wheeler, *Gravitation* (Freeman, San Francisco, 1973).

[3] Remo Garattini, *Int. J. Mod. Phys. D* **4** (2002) 635.

[4] Remo Garattini, *Entropy* **2** (2000) 26.

[5] Remo Garattini, *Nucl.Phys.Proc.Suppl.* **88** (2000) 297.

[6] Remo Garattini, *Phys.Lett.B* **459** (1999) 461.

[7] Fabio Scardigli,*Class.Quant.Grav.* **14** (1997) 1781.

[8] Fabio Scardigli,*Phys.Lett.B* **452** (1999) 39.

[9] Fabio Scardigli, *Nucl.Phys.Proc.Suppl.* **88** (2000) 291.

[10] Luis J. Garay,*Phys.Rev. D* **58** (1998) 124015.

[11] Luis J. Garay, *Phys.Rev.Lett.* **80** (1998) 2508.

[12] Y. J. Ng and H. van Dam, *Found. Phys.* **30** (2000) 795.

[13] Y. J. Ng, *Int. J. Mod. Phys. D* **11** (2002) 1585.

[14] Y. J. Ng, *Mod.Phys.Lett.A* **18** (2003) 1073

[15] Y. J. Ng, gr-qc/0401015.

[16] Y. J. Ng, H. van Dam,*Int.J.Mod.Phys.A* **20** (2005) 1328.

[17] W.A. Christiansen, Y. Jack Ng, H. van Dam, *Phys.Rev.Lett.* **96** (2006) 051301

[18] Y. Jack Ng, *Phys.Lett.B* **657** (2007) 10.

[19] Y. Jack Ng, *AIP Conf.Proc.* **1115** (2009) 74.

[20] A. Wayne Christiansen, David J. E. Floyd, Y. Jack Ng, Eric S. Perlman, *Phys.Rev.D* **83** (2011) 084003.

[21] G. Amelino-Camelia, *Nature* **398** (1999) 216.

[22] L. Diosi and B. Lukacs, *Phys. Lett.* **A142** (1989) 331.

[23] L.Faddeev, *Priroda* **5** (1989) 11.

[24] A.E. Shalyt-Margolin and J.G. Suarez, *gr-qc/0302119.*

[25] A.E. Shalyt-Margolin and J.G. Suarez, *Intern. Journ. Mod. Phys D* **12** (2003) 1265.

[26] A.E. Shalyt-Margolin and A.Ya. Tregubovich, *Mod. Phys.Lett. A* **19** (2004) 71.

[27] A.E. Shalyt-Margolin, *Mod. Phys. Lett. A* **19** (2004) 391.

[28] A.E. Shalyt-Margolin, *Mod. Phys. Lett. A* **19** (2004) 2037.

[29] A.E. Shalyt-Margolin, *Intern. Journ. Mod.Phys D* **13** (2004) 853.

[30] A.E. Shalyt-Margolin, *Intern.Journ.Mod.Phys.A* **20** (2005) 4951.

[31] A.E. Shalyt-Margolin and V.I. Strazhev, The Density Matrix Deformation in Quantum and Statistical Mechanics in Early Universe. In *Proc. Sixth International Symposium "Frontiers of Fundamental and Computational Physics"*,ed. B.G. Sidharth (Springer, 2006) p. 131.

[32] A.E. Shalyt-Margolin, The Density matrix deformation in physics of the early universe and some of its implications. In *Quantum Cosmology Research Trends*,ed. A. Reimer (Horizons in World Physics. **246**, Nova Science Publishers, Inc., Hauppauge, NY,2005) p. 49.

[33] Robert. M. Wald, *General Relativity*, (The University Chicago Press Chicago and London 1984).

[34] E.P. Wigner, *Rev. Mod. Phys.* **29** (1957) 255.

[35] G. 'T. Hooft, *gr-qc/9310026.*

[36] G. 'T. Hooft, *hep-th/0003004*;

[37] L.Susskind, *J. Math. Phys* **36** (1995) 6377.

[38] R. Bousso, *Rev. Mod. Phys* **74** (2002) 825.

[39] R. Bousso, *JHEP* **07** (1999) 004.

[40] E. S. Perlman et al., Astron. J.**124**, 2401–2412 (2002)

[41] G. A. Veneziano, *Europhys.Lett* **2** (1986) 199.

[42] D. Amati, M. Ciafaloni, and G. A. Veneziano, *Phys.Lett.B* **216** (1989) 41.

[43] E.Witten, *Phys.Today* **49** (1996) 24.

[44] R. J. Adler,D. I. Santiago, *Mod. Phys. Lett. A* **14**, 1371 (1999).

[45] D.V.Ahluwalia, *Phys.Lett* **A275** (2000) 31.

[46] D.V.Ahluwalia, *Mod.Phys.Lett* **A17** (2002) 1135.

[47] M. Maggiore, *Phys.Lett B* **319** (1993) 83.

[48] A. Kempf, G. Mangano and R.B. Mann, *Phys.Rev.D* **52** (1995) 1108.

[49] M.A. Markov, *Pis'ma v ZHETF* **36** (1982) 214.

[50] A.E. Shalyt-Margolin, *Intern. J. Mod. Phys. D* **21** (2012) 1250013.

[51] T. Padmanabhan, *Rep. Prog. Phys.* **73** (2010) 046901, arXiv:0911.5004.

[52] S.Perlmutter et al., *Astrophys. J* **517** (1999) 565.

[53] A. G. Riess et al., *Astron. J* **116** (1998) 1009.

[54] A. G.Riess et al., *Astron. J* **117** (1999) 707.

[55] V. Sahni and A. A. Starobinsky, *Int. J. Mod. Phys. D* **9** (2000) 373.

[56] S. M. Carroll, *Living Rev. Rel* **4** (2001)1.

[57] O. Bertolami, *N. Cim. B* **93** (1986) 36.

[58] J.C. Carvalho,J.A.S Lima and I. Waga, *Phys. Rev. D* **46** (1992) 2404.

[59] L.P. Chimento and D. Pavon, *Gen. Rel. Grav.* **30** (1998) 643.

[60] T. Harco and M.K. Mak, *Gen. Rel. Grav.* **31** (1999) 849.

[61] A.D. Dolgov, *Phys.Atom.Nucl* **71** (2008) 651.

[62] A.E. Shalyt-Margolin, *Entropy* **12** (2010) 932.

[63] A.E. Shalyt-Margolin, *Intern. J. Theor. Math. Phys.* **1** (2011) 1.

[64] A.E. Shalyt-Margolin, *Entropy* **14** (2012) 2143.

[65] W. Fischler and L. Susskind, *hep-th/9806039.*

Polarizability of Nucleon in Quantum-Field Approach

V.V. Andreev *, N.V. Maksimenko †, O.M. Deruzhkova ‡

Abstract

On the basis of the relativistic gauge-invariant approach, the solutions of the electromagnetic equations by the covariant method of Green functions and the effective Lagrangians the low-energy Compton scattering amplitudes are determined. Calculations of magnetic and electric quasi-static polarizabilities of spinor particle were evaluated on the based on matrix elements calculation for Compton scattering amplitudes.

Introduction

At present there are many electrodynamic processes on the basis of which experimental data on hadrons polarizabilities can be obtained. In this context, there is a task of covariant determination of the polarizabilities contribution to the amplitudes and cross-sections of electrodynamic hadron processes [1],[2]. This problem can be solved in the framework of theoretical-field covariant formalism of the interaction of electromagnetic fields with hadrons with account for their polarizabilities. In the papers [3]-[6] one can find covariant methods of obtaining the Lagrangians and equations describing interaction of the electromagnetic field with hadrons, in which electromagnetic characteristics of these particles are fundamental. Effective field Lagrangians describing the interaction of low-energy electromagnetic field with nucleons based on expansion in powers of inverse mass

*E-mail:andreev@gsu.by
†E-mail:maksimenko@gsu.by
‡E-mail:dom@gsu.by

of the nucleon have been widely used recently [7]. In Ref. [8] on the basis of correspondence principle between classical and quantum theories an effective covariant Lagrangian describing the interaction of electromagnetic field with particles of spin is presented in the framework of field approach with account for particles polarizabilities.

In this paper, in the framework of the covariant theoretical-field approach based on the effective Lagrangian presented in [8] a set of equations describing the interaction of electromagnetic field with hadrons of spin is obtained taking into account their polarizabilities and anomalous magnetic moments. Using the Greens function method for solving electrodynamic equations [9]-[12], amplitude of Compton scattering on the particles of spin is obtained with account for their polarizabilities. Structures of the amplitude that are similar to polarizabilities, but are caused by electromagnetic interactions, are obtained. The analysis of these structures contributions to hadrons polarizability is performed.

1 The covariant equations of interaction of an electromagnetic field with a nucleon taking into account polarizabilities

To determine the covariant equations describing the electromagnetic field interaction with nucleon taking into account anomalous magnetic moments and polarizabilities we use the following effective Lagrangian:

$$L = -\frac{1}{4}F_{\mu\nu}F^{\mu\nu} + \frac{1}{2}\overline{\Psi}\left(i\widehat{\overrightarrow{D}} - m\right)\Psi - \frac{1}{2}\overline{\Psi}\left(i\widehat{\overleftarrow{D}} + m\right)\Psi. \qquad (1)$$

The following notations were introduced:

$$\widehat{\overrightarrow{D}} = \eta_{\sigma\nu}\gamma^{\sigma}\overrightarrow{\partial}^{\nu} + \frac{ie\kappa}{4m}\sigma^{\mu\nu}F_{\mu\nu} + ie\widehat{A}, \qquad (2)$$

$$\widehat{\overleftarrow{D}} = \overleftarrow{\partial}^{\nu}\gamma^{\sigma}\eta_{\sigma\nu} - \frac{ie\kappa}{4m}\sigma^{\mu\nu}F_{\mu\nu} - ie\widehat{A}, \qquad (3)$$

$$\eta_{\sigma\nu} = g_{\sigma\nu} + \frac{2\pi}{m}\left[\alpha F_{\sigma\mu}F^{\mu}_{\nu} + \beta\widetilde{F}_{\sigma\mu}\widetilde{F}^{\mu}_{\nu}\right]. \qquad (4)$$

If we substitute expressions (2)-(4) into (1), the effective Lagrangian will have the form:

$$L = -\frac{1}{4}F_{\mu\nu}F^{\mu\nu} + \frac{i}{2}\overline{\Psi}\widehat{\overrightarrow{\partial}}\Psi - m\overline{\Psi}\Psi - e\overline{\Psi}\widehat{A}\Psi - \frac{e\kappa}{4m}\overline{\Psi}\sigma^{\mu\nu}\Psi F_{\mu\nu} + K_{\sigma\nu}\Theta^{\sigma\nu}, \qquad (5)$$

where

$$K_{\sigma\nu} = \frac{2\pi}{m}\left[\alpha F_{\sigma\mu}F^{\mu}_{\nu} + \beta\widetilde{F}_{\sigma\mu}\widetilde{F}^{\mu}_{\nu}\right], \quad \Theta^{\sigma\nu} = \frac{i}{2}\overline{\Psi}\gamma^{\sigma}\overleftrightarrow{\partial}^{\nu}\Psi, \quad \overleftrightarrow{\partial}^{\nu} = \overrightarrow{\partial}^{\nu} - \overleftarrow{\partial}^{\nu}.$$

We separate the part related to nucleon polarizabilities in the Lagrangian (5)

$$L^{(\alpha,\beta)} = -\frac{2\pi}{m}\left[\alpha F_{\mu\sigma}F^{\mu}_{\nu} + \beta\widetilde{F}_{\mu\sigma}\widetilde{F}^{\mu}_{\nu}\right]\Theta^{\sigma\nu},$$

$$\widetilde{F}_{\mu\sigma}\widetilde{F}^{\mu\nu} = F_{\mu\sigma}F^{\mu\nu} - \frac{1}{2}\delta^{\nu}_{\sigma}F_{\mu\rho}F^{\mu\rho}, \tag{6}$$

$$L^{(\alpha,\beta)} = -\frac{2\pi}{m}\left[(\alpha+\beta)\,F_{\mu\sigma}F^{\mu\nu}\Theta^{\sigma}_{\nu} - \frac{\beta}{2}\Theta^{\sigma}_{\sigma}F_{\mu\nu}F^{\mu\nu}\right]. \tag{7}$$

Expression for the Lagrangian (7) is consistent with the effective Lagrangian presented in [13]. Formula (7) is a relativistic field-theoretic generalization of the non-relativistic relation

$$\mathrm{H} = -L^{(\alpha,\beta)} = -2\pi\left(\alpha\vec{E}^{2} + \beta\vec{H}^{2}\right),$$

which corresponds to the polarizabilities of induced dipole moments in a constant electromagnetic field [14]. In the case of a variable electromagnetic field the signs of polarizabilities in the Lagrangian (in the non-relativistic approximation) will change [15]. However, the structure of tensor contraction in (7) does not change.

In order to obtain the equations for interaction of the electromagnetic field with nucleons, we use the effective Lagrangian (1) and Euler-Lagrange equations:

$$\partial_{\mu}\left(\frac{\partial L}{\partial\left(\partial_{\mu}A_{\nu}\right)}\right) - \frac{\partial L}{\partial A_{\nu}} = 0,$$

$$\partial_{\mu}\left(\frac{\partial L}{\partial\left(\partial_{\mu}\overline{\Psi}\right)}\right) - \frac{\partial L}{\partial\overline{\Psi}} = 0,$$

$$\partial_{\mu}\left(\frac{\partial L}{\partial\left(\partial_{\mu}\Psi\right)}\right) - \frac{\partial L}{\partial\Psi} = 0.$$

As a result we get:

$$\partial_{\mu}F^{\mu\nu} = e\overline{\Psi}\gamma^{\nu}\Psi - \partial_{\mu}\left[\frac{e\kappa}{2m}\overline{\Psi}\sigma^{\mu\nu}\Psi + G^{\mu\nu}\right], \tag{8}$$

$$\left(i\overrightarrow{\partial} - m\right)\Psi =$$

$$= e\widehat{A}\Psi - \frac{i}{2}\left[\partial^{\nu}\left(K_{\sigma\nu}\gamma^{\sigma}\Psi\right) + K_{\sigma\nu}\gamma^{\sigma}\partial^{\nu}\Psi\right] + \frac{e\kappa}{4m}\sigma^{\mu\nu}F_{\mu\nu}\Psi, \qquad (9)$$

$$\overline{\Psi}\left(i\overleftarrow{\partial} + m\right) =$$

$$= -\overline{\Psi}e\widehat{A} - \frac{i}{2}\left[\partial^{\nu}\left(\overline{\Psi}\gamma^{\sigma}K_{\sigma\nu}\right) + \left(\partial^{\nu}\overline{\Psi}\right)\gamma^{\sigma}K_{\sigma\nu}\right] - \overline{\Psi}\frac{e\kappa}{4m}\sigma^{\mu\nu}F_{\mu\nu}. \qquad (10)$$

If equations (9) and (10) above is not limited to members of the second-order frequency of the radiation, they may be represented as:

$$\left(i\overrightarrow{D} - m\right)\Psi = 0, \quad \overline{\Psi}\left(i\overleftarrow{D} + m\right) = 0,$$

where $\overrightarrow{D}$ and $\overleftarrow{D}$ defined in (2) and (3). Anti-symmetric tensor $G^{\mu\nu}$ in (8) is:

$$G^{\mu\nu} = -\frac{\partial L^{(\alpha,\beta)}}{\partial\left(\partial_{\mu}A_{\nu}\right)} = \frac{4\pi}{m}\left[(\alpha+\beta)\left(F^{\mu}_{\rho}\widetilde{\Theta}^{\rho\nu} - F^{\nu}_{\rho}\widetilde{\Theta}^{\rho\mu}\right) - \beta\Theta^{\rho}_{\rho}F_{\mu\nu}\right], \qquad (11)$$

where $\widetilde{\Theta}^{\rho\nu} = \frac{1}{2}\left(\Theta^{\rho\nu} + \Theta^{\nu\rho}\right)$. With the anti-symmetric tensor (11), the effective Lagrangian (7) can be represented as follows:

$$L^{(\alpha,\beta)} = -\frac{1}{4}F_{\mu\nu}G^{\mu\nu}.$$

If equations (9) and (10) to limit the contribution of the charge and magnetic moment, we obtain the well-known equation given, for example, [12].

To identify the physical meaning of tensor $G^{\mu\nu}$ lets use Gordon decomposition [16]. Current density j^{μ} of Dirac particles with the help of Gordon decomposition can be represented as follows:

$$j^{\mu} = e\overline{\Psi}\gamma^{\mu}\Psi = \frac{e}{2m}\overline{\Psi}i\overleftrightarrow{\partial}^{\mu}\Psi - \partial_{\nu}\left[\frac{e}{2m}\overline{\Psi}\sigma^{\nu\mu}\Psi\right],$$

where the notation

$$G_0^{\nu\mu} = \frac{e}{2m}\overline{\Psi}\sigma^{\nu\mu}\Psi, \quad j_e^{\mu} = \frac{e}{2m}\overline{\Psi}i\overleftrightarrow{\partial}^{\mu}\Psi.$$

The components of $G_0^{\mu\nu}$ tensor, which is called anti-symmetric dipole tensor, are static dipole moments of point-like particles. With the help of this tensor we can define the current

$$j_m^\mu = -\partial_\nu G_0^{\nu\mu}.$$

In the rest frame of the particle, we have the following relations:

$$m_0^i = \frac{i}{2}\varepsilon^{ijk}G_{0jk}, \quad d_0^i = G^{i0}.$$

Components 4-dimensional current can be defined by the dipole moments

$$\rho_0 = -\left(\overrightarrow{\partial}\,\overrightarrow{d}_0\right), \quad \overrightarrow{j}_0 = \partial_t \overrightarrow{d}_0 + \left[\overrightarrow{\partial}\,\overrightarrow{m}_0\right].$$

The Lagrangian of the interaction of electromagnetic fields with a charged particle with a static dipole moment is:

$$L_I = -j_e^\mu A_\mu - \frac{1}{2}G_0^{\nu\mu}F_{\nu\mu}. \tag{12}$$

By using Lagrangian (12), and the Lagrangian $L = -\frac{1}{4}F_{\mu\nu}F^{\mu\nu}$ of the form based on the Euler-Lagrange equations, we get

$$\partial_\mu F^{\mu\nu} = j_e^\mu - \partial_\nu G_0^{\nu\mu}.$$

In relativistic electrodynamics is introduced tensor similar to induced dipole moments [17]. The current density and moments are expressed through $G^{\mu\nu}$ the following

$$j^\mu = -\partial_\nu G_0^{\nu\mu}, \quad d^\mu = G^{\mu\nu}U_\nu, \quad m^\mu = \frac{i}{2}\varepsilon^{\mu\nu\rho\sigma}G_{\nu\rho}U_\sigma. \tag{13}$$

Relations (13) satisfies the tensor form:

$$G^{\mu\nu} = (d^\mu U^\nu - U^\mu d^\nu) + \varepsilon^{\mu\nu\rho\sigma}m_\rho U_\sigma.$$

In the quantum description of the structural particles induced dipole moments pass to the operator form [18]:

$$\widehat{\overrightarrow{G}}^{\mu\nu} = -\frac{i}{2m}\left[\left(\widehat{d}^\mu\overrightarrow{\partial}^\nu - \widehat{d}^\nu\overrightarrow{\partial}^\mu\right) + \varepsilon^{\mu\nu\rho\sigma}\widehat{m}_\rho\overrightarrow{\partial}_\sigma\right],$$

$$\widehat{\overleftarrow{G}}^{\mu\nu} = \frac{i}{2m}\left[\left(\overleftarrow{\partial}^{\nu}\widehat{d}^{\mu} - \overleftarrow{\partial}^{\mu}\widehat{d}^{\nu}\right) + \varepsilon^{\mu\nu\rho\sigma}\overleftarrow{\partial}_{\sigma}\widehat{m}_{\rho}\right],$$

where $\widehat{d}^{\mu}$ and $\widehat{m}^{\mu}$ - operators of the induced dipole moments, which are dependent on the electromagnetic field tensor. If you require that the low-energy theorem for Compton scattering, then these operators can be defined as

$$\widehat{d}^{\mu} = 4\pi\alpha\widehat{F}^{\mu\nu}\gamma_{\nu}, \quad \widehat{m}^{\mu} = 4\pi\beta\widehat{\widetilde{F}}^{\mu\nu}\gamma_{\nu}.$$

Thus, the expression (11) is anti-symmetric tensor of the induced dipole moments of the nucleon. In this case, the interaction Lagrangian is defined as follow

$$L_I = -j_e^{\mu}A_{\mu} - \frac{1}{2}G_0^{\mu\nu}F_{\mu\nu} - \frac{1}{4}G^{\mu\nu}F_{\mu\nu},$$

which implies the Maxwell equation of the form:

$$\partial_{\nu}F^{\nu\mu} = j_e^{\mu} - \partial_{\nu}G_0^{\nu\mu} - \partial_{\nu}G^{\nu\mu}.$$

2 Covariant representation of the amplitude of Compton scattering on the nucleon, with input from the polarizabilities

We define the contribution of electric and magnetic polarizabilities of the amplitude of Compton scattering. To do this, use the method of Green's function [10]-[12]. We represent the differential equation (9), which will take into account the contributions of the polarizabilities in integral form:

$$\Psi(x) = \Psi^{(0)}(x) + \int S_F(x - x')\, V^{(\alpha,\beta)}(x')\, dx', \tag{14}$$

where $V^{(\alpha,\beta)}(x') = -\frac{i}{2}\left[\partial^{\nu}\left(K_{\sigma\nu}(x')\gamma^{\sigma}\Psi(x')\right) + K_{\sigma\nu}(x')\gamma^{\sigma}\partial^{\nu}\Psi(x')\right]$.

We define the matrix element S_{fi} of the scattering of photons on a nucleon. To do this, we turn (14), $\overline{\Psi}_{p_2}^{(r_2)}(x)$ when $t \to +\infty$ we use the relation

$$\int \overline{\Psi}_{p_2}^{(r_2)}(x)\, S_F(x - x')\, d^3x\,|_{t\to+\infty} = (-i)\,\overline{\Psi}_{p_2}^{(r_2)}(x'),$$

where

$$\overline{\Psi}_{p_2}^{(r_2)} = \frac{1}{(2\pi)^{\frac{3}{2}}}\sqrt{\frac{m}{E_2}}\overline{U}^{(r_2)}(\overrightarrow{p}_2)\, e^{ip_2x'}.$$

As a result, we get:

$$S_{fi} = (-i) \int \overline{\Psi}_{p_2}^{(r_2)}(x') V^{(\alpha,\beta)}(x') d^4x'. \tag{15}$$

Using the boundary conditions and the symmetry of the cross, the expression (15) can be represented as:

$$S_{fi} = \left(-\frac{1}{2}\right) \int \overline{\Psi}_{p_2}^{(r_2)}(x') \left\{ \partial^\nu \left(K_{\sigma\nu}^{21}(x') \gamma^\sigma \Psi_{p_1}^{(r_1)}(x') \right) + \right.$$

$$\left. + K_{\sigma\nu}^{21}(x') \gamma^\sigma \partial^\nu \Psi_{p_1}^{(r_1)}(x') \right\} d^4x'. \tag{16}$$

Integrating by parts and using the definition of the electromagnetic field tensor in (16) we get:

$$S_{fi} = \frac{2\pi i}{m} \int \left[(\alpha+\beta) \left(F_{\sigma\mu}^{(2)} F_{(1)}^{\mu\nu} + F_{\sigma\mu}^{(1)} F_{(2)}^{\mu\nu} \right) \Theta_{(21)\nu}^{\sigma} + \right.$$

$$\left. + \beta \left(F_{\mu\nu}^{(2)} F_{(1)}^{\mu\nu} \right) \Theta_{(21)\rho}^{\rho} \right] d^4x'. \tag{17}$$

If we consider the wave functions of the nucleon and the photons in the initial and final states, the expression (17) takes the form:

$$S_{fi} = \frac{im\delta(k_1 + p_1 - k_2 - p_2)}{(2\pi)^2 \sqrt{4\omega_1\omega_2 E_1 E_2}} M, \tag{18}$$

where in M in the amplitude (18) is as follows:

$$M = \frac{2\pi}{m} \overline{U}^{(r_2)}(\vec{p}_2)(\alpha+\beta) \left\{ \left[\hat{k}_2 e_\mu^{(\lambda_2)} - k_{2\mu} \hat{e}^{(\lambda_2)} \right] \left[k_1^\mu \left(e^{(\lambda_1)} \mathcal{P} \right) - (k_1 \mathcal{P}) e^{(\lambda_1)\mu} \right] + \right.$$

$$\left. + \left[k_2^\mu \left(e^{(\lambda_2)} \mathcal{P} \right) - (k_2 \mathcal{P}) e^{(\lambda_2)\mu} \right] \left[\hat{k}_1 e_\mu^{(\lambda_1)} - k_{1\mu} \hat{e}^{(\lambda_1)} \right] \right\} +$$

$$+ m\beta \left[k_{2\mu} e_\nu^{(\lambda_2)} - k_{2\nu} e_\mu^{(\lambda_2)} \right] \left[k_1^\mu e^{(\lambda_1)\nu} - k_1^\nu e^{(\lambda_1)\mu} \right] U^{(r_1)}(\vec{p}_1). \tag{19}$$

We now define the amplitude (19) in the rest frame of the target and limit in M members are not higher than the second frequency radiation. In this case, we have [19]:

$$M = 4\pi\omega^2 \chi^{(r_2)+} \left[\alpha \left(\vec{e}^{(\lambda_2)} \vec{e}^{(\lambda_1)} \right) + \beta \left(\left[\vec{n}_2 \vec{e}^{(\lambda_2)} \right] \left[\vec{n}_1 \vec{e}^{(\lambda_1)} \right] \right) \right] \chi^{(r_1)}.$$

If the amplitude of M along with the contribution of the polarizabilities α and β take into account the contribution of the electric charge, then M can be represented as follows:

$$M = \chi^{(r_2)+} \left[\left(-\frac{e^2}{m} + 4\pi\omega^2\alpha \right) \left(\overrightarrow{e}^{(\lambda_2)} \overrightarrow{e}^{(\lambda_1)} \right) + \right.$$

$$\left. + 4\pi\omega^2\beta \left(\left[\overrightarrow{n}_2 \overrightarrow{e}^{(\lambda_2)} \right] \left[\overrightarrow{n}_1 \overrightarrow{e}^{(\lambda_1)} \right] \right) \right] \chi^{(r_1)}. \quad (20)$$

Differential Compton cross section, for example at an angle $\theta = 0$, computed using (20) has the form [19]:

$$\frac{d\sigma}{d\Omega} = \left(\frac{\alpha_e}{m} \right)^2 - 2\frac{\alpha_e}{m} (\alpha + \beta)\, \omega^2,$$

where $\alpha_e = \frac{e^2}{4\pi}$.

3 Quasi-static polarizability of particles spin $\frac{1}{2}$ in QED

We find the quasi-static polarizability structureless fermions, which appear in the Compton scattering due to higher orders. In general, the AKP T forward ($\theta = 0$) and backward ($\theta = \pi$) up ω^2 can be written as:

$$T^{\lambda',\sigma'}_{\lambda,\sigma}(\theta = 0) = 8\pi m_f \omega^2 (\alpha_E + \beta_M)\, \delta_{\lambda,\lambda'} \delta_{\sigma,\sigma'},$$

$$T^{\lambda',\sigma'}_{\lambda,\sigma}(\theta = \pi) = 8\pi m_f \omega^2 (\alpha_E - \beta_M)\, \lambda \delta_{-\lambda,\lambda'} \delta_{\sigma,-\sigma'}.$$

On the other hand it is possible to calculate the matrix elements, respectively, the amplitude of Compton scattering in the framework of QED, including next to the Born-order perturbation theory in the coupling constant α_{QED} (see, e.g., [20], [21]). In [22] developed a method of calculating the polarizabilities of fermions in the framework of quantum field models and theories by comparing the corresponding matrix elements. The outcome of this procedure in this case is the ratio:

$$\alpha_E^{q-s} + \beta_M^{q-s} = \frac{\alpha_{QED}^2}{3\pi m_f^3} \frac{11}{6} + \frac{8\alpha_{QED}^2}{3\pi m_f^3} \ln \frac{2\omega}{m_f}, \quad (21)$$

$$\alpha_E^{q-s} - \beta_M^{q-s} = -\frac{\alpha_{QED}^2}{3\pi m_f^3} \frac{59}{6} + \frac{4\alpha_{QED}^2}{3\pi m_f^3} \ln \frac{2\omega}{\lambda}, \quad (22)$$

where the parameter λ is an infinitely small mass of the photon.

As follows from (21) and (22) in addition to the quasi-static polarizability of the permanent members and contain non-analytic terms $\sim \ln\omega$, which differ in the Thomson limit $\omega \to 0$. This property was the reason that the work [23], [24] structure (21) and (22) were identified quasistatic polarizabilities. From (21) and (22) it is easy to find the electric (α_E^{q-s}) and magnetic (β_M^{q-s}) quasi-static polarizability and assess their contribution to the polarizability of the "Dirac" proton (point of zero fermion anomalous magnetic moment):

$$\alpha_E^{q-s} + \beta_M^{q-s} \approx -5,8 \cdot 10^{-7} Fm^3. \tag{23}$$

The experimental values [25]:

$$\alpha_E^{q-s} + \beta_M^{q-s} = (13,8 \pm 0,4) \cdot 10^{-4} Fm^3. \tag{24}$$

Numerical estimates are consistent with estimates of [26].

Conclusion

In the framework of the gauge-invariant approach we obtain the covariant equations of motion of a nucleon in the electromagnetic field, taking account of its electric and magnetic polarizabilities. Based on the decision of electrodynamic equations of motion of the nucleon obtained by the Green's function, it is shown that the developed covariant formalism of Lagrange interaction of low-energy photons with nucleons is consistent with the low-energy theorem of Compton scattering. Based on an original technique reproduced the known result for the combination of quasi-static polarizabilities $\alpha_E^{q-s}+\beta_M^{q-s}$ in QED framework and obtain a new expression for $\alpha_E^{q-s} - \beta_M^{q-s}$. The apparent advantage of method of defining "polarizabilities" referred to in Section 3, is its relative simplicity. This approach opens up more opportunities for the study of the internal structure of nucleons and can be applied in various quantum field theories and models.

References

[1] Carlson, C.E. Constraining off-shell effects using low-energy Compton scattering / C.E. Carlson, M. Vanderhaeghen // [Electronic resource].

- 2011. - Mode of access: http://physics.atom-ph/1109.3779. - Date of access: 04.10.2011.

[2] Birse, M.C. Proton polarizability contribution to the Lamb shift in muonic hydrogen at fourth order in chiral perturbation theory / M.C. Birse, J.A. McGovern //Europen Phys. Journal A. - 2012. - Vol. 48. - P. 120-128.

[3] Moroz, L.G. Scattering matrix taking into account the interaction Pauli / L.G. Moroz, F.I. Fedorov // ZhETF. - 1960. - Vol. 39. - N 2. - P. 293-303.

[4] Krylov, V. Spin particles in the field of a plane electromagnetic wave / B.V. Krylov, A.F. Raduyk, F.I. Fedorov // Preprint of the Academy of Sciences of BSSR. In-t fiziki. - 1976. - N 113. - 60 p.

[5] Maksimenko, N.V. Polarizability and elementary particles / N.V. Maksimenko, L.G. Moroz // problems of atomic science and technology. Series: General and nuclear physics. - 1979. - N 4(10). - P. 26-27.

[6] Levchuk, M.I. nucleon as one of the characteristics of its electromagnetic structure / M.I. Levchuk, L.G. Frost // Proc. Academy of Sciences of BSSR. Ser. fiz.-mat. navuk. - 1985. - N 1. - P. 45-54.

[7] Hill, R.J. The NRQED lagrangian at order $\frac{1}{M^4}$ / R.J. Hill, G. Lee, G. Paz, M.P. Solon // Phys. Rev. - 2013. - Vol. D87 . - P. 053017.

[8] Maksimenko, N.V. Phenomenological description polarizabilities of elementary particles in a field-theory / N.V. Maksimenko, L.G. Moroz // Proceedings of the XI International young scientists school on high energy physics and relativistic nuclear physics. D2-11707, JINR, Dubna. - 1979. - P. 533-543.

[9] Baryshevsky, V.G. Nuclear optics of polarized media / V.G. Baryshevsky. - M.: Energoatomizdat, 1995. - 315 p.

[10] Bogush, A.A. Introduction to the theory of classic fields / A.A. Bogush, L.G. Moroz. - Minsk: Science and technology, 1968. - 387 p.

[11] Bogush, A.A. Introduction in the calibration of the field theory of electroweak interactions / A.A. Bogush. - Minsk: Science and technology, 1987. - 359 p.

[12] Bjorken, J.D. Relativistic quantum field theory / J.D. Bjorken, E.D. Drell. - M: Science. - 1978. - Vol. 1. - 295 p.

[13] L'vov, A.I. Theoretical aspects of the polarizability of the nucleon / A.I. L'vov // Jnter. Journ. Mod. Phys. A. - 1993. - Vol. 8. - N 30. - P. 5267-5303.

[14] Schumacher, M. Dispersion theory of nucleon Compton scattering and polarizabilities / M. Schumacher // [Electronic resource]. - 2013. - Mode of access: http:// hep-ph/1301.1567. pdf . - Date of access: 03.02.2013.

[15] Detmold, W. Electromagnetic and spin polarisabilities in lattice QCD / W.Detmold, B.C. Tiburzi, A. Walker-Loud // PoS. - 2006. - Vol. Lat2006. - P. 103-110.

[16] Itzykson, C. Quantum field theory / C. Itzykson, J.-B. Zuber. - McGraw-Hill, 1984. - Vol. II. - 400 p.

[17] De Groot, S.R. Electrodynamics / S.R. de Groot, L.G. Sattorp. - M.: Nauka, 1982. - 560 p.

[18] Maksimenko, N.V. Covariant gauge-invariant Lagrangian formalism with the polarizabilities of the particles / N.V. Maksimenko, O.M. Deryuzhkova // Vestsi NAS Belarusy, ser. fiz.-mat. navuk. - Mn.: "Belarusian Navuka", 2011. - N 2. - P. 27-30.

[19] Petrunkin, V.A. Electrical and magnetic polarizabilities of hadrons / V.A. Petrunkin / / Fiz. - 1981. - Vol. 12. - P. 692-753.

[20] Tsai, W.-Y. Compton scattering. ii. differential cross-sections and left-right asymmetry / W.-Y. Tsai, L.L. Deraad, K.A. Milton // Phys. Rev. - 1972. - Vol. D6. - P. 1428-1438.

[21] Denner, A. Complete O(alpha) QED corrections to polarized Compton scattering / A. Denner, S. Dittmaier // Nucl. Phys. - 1999. - Vol. B540. - P. 58-86.

[22] Andreev, V. The invariant amplitudes of Compton scattering in QED / V. Andreev, A.M. Seitliev // Vesti NAS Belarus. Ser. fiz.-mat. navuk. - 2011. - N 3. - P. 60-65.

[23] Llanta, E. Polarizability sum rules in QED / E. Llanta, R. Tarrach // Phys. Lett. - 1978. - Vol. B78. - P. 586-589.

[24] Holstein, B.R. Sum rules for magnetic moments and polarizabilities in QED and chiral effective-field theory / B.R. Holstein, V. Pascalutsa, M. Vanderhaeghen // Phys. Rev. - 2005. - Vol. D72. - N 9. - P. 094014.

[25] Review of Particle Physics / K. Nakamura [et al.] // Journal of Physics G. - 2010. - Vol. 37. - P. 075021.

[26] Gerasimov, S.B. Scattering of light of low frequency and charged particle polarizability / S.B. Gerasimov, L.D. Soloviev // Nucl. Phys. - 1965. - Vol. 74. - P. 589-592.

Numerical Investigation of Bound Relativistic Two-Particle Systems with One-Boson Exchange Potentials

Yury Grishechkin*, Valery Kapshai †
Francisk Scorina Gomel State Univerity, Gomel, Belarus

Abstract

In this paper numerical solutions of quantum field theory equations describing bound s-state systems of two particles are found in the cases of different variants of one-boson exchange potentials. The masses of particles are supposed to be equal and the mass of the exchange boson is equal to zero. Decay widths of fermion-antifermion bound system into two photons are calculated on the basis of solutions found. Comparison of the obtained energy spectrum and decay widths with experimentally measured values for positronium is carried out.

1 Introduction

Quantum field theory two-particle equations of the quasipotential type were obtained in the momentum representation (MR) in the integral form [1, 2]. Later for these equations the relativistic configurational representation (RCR) was found [3], it is actually the relativistic generalization of the quantum mechanical coordinate representation. One of the advantages of the RCR over the MR is transparency of physical meaning of potentials in the equations. For instance, form of the potential in the RCR may indicate the existence of bound states or resonance states by analogy with quantum

*E-mail:ygrishechkin@rambler.ru
†E-mail:kapshai@rambler.ru

mechanics. Moreover, the elastic form-factors and the decay constants in the terms of wave functions have the simplest form in the RCR [4, 5].

In this paper we consider numerical solutions of relativistic integral equations describing bound s-states of two spinless particles and systems of two particles with spin $1/2$ in the cases of one-boson exchange potentials, which were obtained in the framework of different variants of quasipotential approach in quantum field theory. Decay widths of the particle-antiparticle bound state system into two photons are calculated on the basis of obtained solutions. Comparison of the energy spectrum and decay widths found with experimentally measured values for positronium is carried out.

2 Relativistic two-particle equations

Relativistic two-particle equations for bound s-states in the MR have the form [1, 2] ($E_p = \sqrt{m^2+p^2}$, $E_k = \sqrt{m^2+k^2}$, $p = |\mathbf{p}|$, $k = |\mathbf{k}|$)

$$E_p^2\psi(2E,p) + \frac{2\lambda m^2}{\pi}\int_0^\infty V(2E,p,k)\psi(2E,k)\frac{dk}{E_k} = E^2\psi(2E,p), \qquad (1)$$

$$2E_p\psi(2E,p) + \frac{2\lambda m^2}{\pi E_p}\int_0^\infty V(2E,p,k)\psi(2E,k)\frac{dk}{E_k} = 2E\psi(2E,p), \qquad (2)$$

where (1) - is the Logunov-Tavkhelidze equation, (2) - is the Kadyshevsky equation. The value $\psi(2E,p)$ - is the wave function, m - is the mass of each particle, $2E$ - is the two-particle system energy ($0 < 2E \leq 2m$), λ - is the coupling constant, $V(2E,p,k)$ - is the relativistic potential which in the most common case depends on the system energy $2E$ and spin variables.

The normalization conditions of wave functions have a rather cumbersome form for energy dependent potentials [6]. In the s-states case these conditions have the form

$$\int_0^\infty dp\frac{m}{E_p}\psi^2(2E,p) - I = 1 \qquad (3)$$

- for the wave function of equation (1),

$$\frac{m}{E}\int_0^\infty dp\psi^2(2E,p) - I = 1 \qquad (4)$$

- for the wave function of equation (2), where

$$I = \frac{2\lambda m^3}{\pi E}\int_0^\infty \frac{dp}{E_p}\psi(2E,p)\int_0^\infty \frac{dk}{E_k}\psi(2E,k)\frac{\partial}{\partial(2E)}V(2E,p,k). \qquad (5)$$

To find the two-particle equation form in the RCR let us write equations (1), (2) as

$$\psi_{(j)}(2E,p) = \frac{-2\lambda m}{\pi} G^{(j)}(E,p) \int_0^\infty \frac{dk}{E_k} V(2E,p,k)\psi(2E,k), \qquad (6)$$

where the Green function are introduced for the Logunov-Tavkhelidze equation ($j=1$) and the Kadyshevsky equation ($j=2$):

$$G^{(1)}(E,p) = \frac{m}{E_p^2 - E^2}; \quad G^{(2)}(E,p) = \frac{m}{E_p(2E_p - 2E)}. \qquad (7)$$

We also consider the modified Logunov-Tavkhelidze equation ($j=3$) and the modified Kadyshevsky equation ($j=4$), for which Green functions have the following form

$$G^{(3)}(E,p) = \frac{E_p}{E_p^2 - E^2}; \quad G^{(4)}(E,p) = \frac{1}{2E_p - 2E}. \qquad (8)$$

The values in equations (6) are associated with the respective values in the RCR by expressions

$$\psi_{(j)}(w,r) = \int_0^\infty d\chi \sin(\chi m r)\psi_{(j)}(2E, m\sinh\chi), \qquad (9)$$

$$g_{(j)}(w,r,r') = \frac{-2}{\pi} \int_0^\infty \sin(\chi m r) G_{(j)}(2E,p) \sin(\chi m r') d\chi, \qquad (10)$$

$$V(2E,p,k) = \int_0^\infty dr \sin(\chi m r) V(2E,r) \sin(\chi' m r), \qquad (11)$$

where χ - is the rapidity connected with the momentum p by the relation $p = m\sinh\chi$ ($k = m\sinh\chi'$), quantity w is connected with energy by $2E = 2m\cos w$ ($0 \le w < \pi/2$), r - is the modulus of radius-vector in the RCR. Expression (11) is valid for RCR-local potentials $V(2E,r)$. In the nonlocal potential case this expression has more complicated form [3].

Taking into account formulas (9)-(11) equations (6) can be converted into the two-particle equations in the RCR [7]

$$\psi_{(j)}(w,r) = \lambda m \int_0^\infty dr' g_{(j)}(w,r,r') V(r') \psi_{(j)}(w,r'), \qquad (12)$$

in which we will consider the energy independent potentials only ($V(r) \equiv V(2E,r)$).

Substitution of (7), (8) into formula (10) and subsequent calculation of integrals gives the explicit form of the Green functions in the RCR

$$g_{(j)}(w,r,r') = g_{(j)}(w,r-r') - g_{(j)}(w,r+r'), \tag{13}$$

where [7]

$$\begin{aligned}
g_{(1)}(w,r) &= \frac{-1}{m\sin 2w}\frac{\sinh[(\pi/2-w)m\,r]}{\sinh[\pi\,m\,r/2]}; \\
g_{(2)}(w,r) &= \frac{(4m\cos w)^{-1}}{\cosh[\pi\,m\,r/2]} - \frac{1}{m\sin 2w}\frac{\sinh[(\pi-w)m\,r]}{\sinh[\pi\,m\,r]}; \\
g_{(3)}(w,r) &= \frac{-1}{2m\sin w}\frac{\cosh[(\pi/2-w)m\,r]}{\cosh[\pi\,m\,r/2]}; \\
g_{(4)}(w,r) &= \frac{-1}{2m\sin w}\frac{\sinh[(\pi-w)m\,r]}{\sinh[\pi\,m\,r]}.
\end{aligned} \tag{14}$$

It is easy to see that the non-relativistic limit for all four relativistic Green functions (13) ($m \to \infty$, $w \to 0$) gives the Green function of Schrödinger equation in ordinary coordinate representation.

Since we consider the energy independent potentials only the RCR only then normalization condition can be written in the form

$$\int_0^\infty dr\psi^2_{(j)}(w,r) = 1, \tag{15}$$

which is analogous to the non-relativistic one.

3 One-boson exchange potentials

Let us consider solving of equations in the momentum representation (1), (2) and in the RCR (12) with several variants of potentials.

One of the first potentials describing the interaction of two scalar particles which was obtained in the framework of the quasipotential approach is the expression [2]

$$V(2E,\mathbf{p},\mathbf{k}) = \frac{1}{|\mathbf{p}-\mathbf{k}|(E_p+E_k+|\mathbf{p}-\mathbf{k}|-2E)}. \tag{16}$$

It should be noted that this potential was obtained on the basis of the diagram technique of the Hamiltonian formulation of quantum field theory.

The partial expansion of potential (16) by Legendre polynomials leads to the following expression in the s-wave case:

$$V(2E,p,k)=\frac{1}{2}\log\left(\frac{E_p+E_k+|p-k|-2E}{E_p+E_k+p+k-2E}\right). \tag{17}$$

In article [8] one-boson exchange potentials were found on the basis of two the scalar particle system's retarded and causal Green functions calculation:

$$\begin{aligned} V_{ret}(2E,p,k) &= A(2E,p,k)\log\left(\frac{E_p+E_k+|p-k|-2E}{E_p+E_k+p+k-2E}\right) \\ &+B(2E,p,k)\log\left(\frac{E_p+E_k+|p-k|}{E_p+E_k+p+k}\right) \\ &+C(2E,p,k)\left(\frac{1}{E_p+E_k+|p-k|}-\frac{1}{E_p+E_k+p+k}\right), \end{aligned} \tag{18}$$

where

$$\begin{aligned} A(2E,p,k) &= \frac{E_pE_k}{2E^2};\quad B(2E,p,k)=1-\frac{E}{E_p+E_k}-A(2E,p,k); \\ C(2E,p,k) &= \frac{(E_p-E)(E_k-E)}{E} \end{aligned}$$

and

$$\begin{aligned} V_c(2E,p,k) &= \frac{(E_p+E)(E_k+E)}{4E_pE_k}V_{ret}(2E,p,k) \\ &+\frac{(E_p-E)(E_k-E)}{4E_pE_k}V_{ret}(-2E,p,k). \end{aligned} \tag{19}$$

Potentials of two fermion interaction were obtained in article [9] in the cases of different values of total spin and total angular momentum of the system as coefficients of the expansion of three-dimensional potential [10] into spherical spinors. In the case when system's spin is equal to zero the potential has the form

$$V_{S=0}(2E,p,k)=\frac{1}{2m^2}(2E_pE_k-m^2)\log\left(\frac{E_p+E_k+|p-k|-2E}{E_p+E_k+p+k-2E}\right). \tag{20}$$

If the total spin is equal to one the potential has the form [9]

$$
\begin{aligned}
V_{S=1}(2E,p,k) &= \frac{1}{6m^2}\Bigg[F_1(2E,p,k)\log\left(\frac{E_p+E_k+|p-k|-2E}{E_p+E_k+p+k-2E}\right)\\
&+F_3(2E,p,k)\Bigg(\arctan\frac{\sqrt{2E_pE_k+2m^2-p^2-k^2}}{|p-k|}-\\
&-\arctan\frac{\sqrt{2E_pE_k+2m^2-p^2-k^2}}{p+k}\Bigg)\\
&+F_2(2E,p,k)\log\left(\frac{E_pE_k+m^2-pk}{E_pE_k+m^2+pk}\right)\Bigg],
\end{aligned}
\tag{21}
$$

where the following notations are introduced

$$
\begin{aligned}
F_1(2E,p,k) &= 4\frac{2p^2k^2-(E_pE_k+m^2)(p^2+k^2-(E_p+E_k-2E)^2)}{p^2+k^2-(E_p+E_k-2E)^2-2(E_pE_k+m^2)}+\\
&+2E_pE_k+m^2,\\
F_2(2E,p,k) &= 4\frac{p^2k^2-(E_pE_k+m^2)^2}{2(E_pE_k+m^2)-(p^2+k^2-(E_p+E_k-2E)^2)},\\
F_3(2E,p,k) &= F_2(2E,p,k)\frac{2(E_p+E_k-2E)}{\sqrt{2E_pE_k+2m^2-p^2-k^2}}.
\end{aligned}
$$

The potential for pseudoscalar fermion-antifermion bound state was found in article [11] and in the case of scalar boson exchange has the following form

$$
\begin{aligned}
&V(2E,p,k)= \qquad\qquad (22)\\
&=\left(\frac{b(2E,p,k)}{8m^2}+\frac{1}{2}\right)\log\left(\frac{E_p+E_k+|p-k|-2E}{E_p+E_k+p+k-2E}\right)+\frac{a(2E,p,k)}{8m^2},
\end{aligned}
$$

where

$$
\begin{aligned}
a(2E,p,k) &= (2E-E_p-E_k)(|p-k|-(p+k))-2pk,\\
b(2E,p,k) &= 4m^2+(2E)^2-4E(E_p+E_k).
\end{aligned}
$$

Potentials (17)-(22) can not be converted into the RCR in the form of analytical expressions for arbitrary energy value. That is why we considered the solution of equations in the RCR (12) for more simple energy

independent one-boson exchange potential which has in the RCR and in the MR the forms [3]:

$$V(r) = -\frac{\cosh(\pi - \alpha)mr}{r \sinh \pi mr}; V(p,k) = \frac{1}{4} \log \left(\frac{E_p E_k - pk - m^2 \cos\alpha}{E_p E_k + pk - m^2 \cos\alpha} \right), \tag{23}$$

where parameter α is connected with the boson exchange mass μ as $\cos\alpha = 1 - \mu^2/2m^2$. In what follows we consider the case $\mu = 0$. Potential (23) was obtained on the base of using the quasipotential equation for scattering amplitude which is supposed to be given by Feynman diagrams. In the MR potential (23) is singular at $p = k$. Thus solving equations (1), (2) for (23) is much more difficult problem than solving equations (12) in the RCR.

It is not difficult to see that the non-relativistic limit ($m \to \infty$) of expressions (16) - (23) gives the Coulomb potential ($\lim_{m\to\infty} 2E = 2m - \kappa^2/m$, where $\kappa > 0$).

4 Numerical methods of solving

Simple analysis of the wave functions and potentials in the MR (17) - (22) at $k \to \infty$ at fixed p (or at $p \to \infty$ at fixed k) shows that integrals in equations (1), (2) converge which makes solving of these equations possible.

To solve integral equations (1), (2) we used quadrature method [12] after reducing the half-infinite integrate interval to finite one $0 \le x < 1$ by replacing the variable $p/m = Cx/(1-x)$. Selecting the parameter $C > 0$ influences the convergence rate of numerical results to the exact ones at increasing number of nodes.

All considered kernels of integral equations in the MR contain the module of variable difference $|p - k|$, which slows down the convergence of obtained results to the exact ones. Therefore the rectangle quadratures with the number of nodes N and $2N$ were used. Then the Richardson extrapolation process [12] was applied to the obtained solutions: wave functions ψ_N, ψ_{2N} and eigenvalues energy $2E_N$, $2E_{2N}$

$$\psi = 4/3\psi_{2N} - 1/3\psi_N; \quad 2E = (4/3)2E_{2N} - (1/3)2E_N, \tag{24}$$

that allowed to obtain more accurate results.

Solutions of equations in the RCR (12) were found by using the composite Gauss quadrature method after replacing the infinite limit of integration

by a large value R: the integration interval was range into N small pieces, to which the Gauss quadrature formula for M nodes was then applied [12].

There are nonlinear eigenvalue matrix problems for $2E$ after reducing the integral equations to the homogeneous systems of linear algebraic equations. To solve these problems the iteration method was used [13].

5 Results

Solutions were obtained for λ equals to the fine structure constant: $\lambda = 7.2973525698 \times 10^{-3}$ [14]. In figure 1 the wave functions are shown which were found at solving the Logunov-Tavkhelidze equation with potential (19) for $C = 0.005$ and $N = 1000$. The number of curve is equal to the state number n. Figures of wave functions in the other cases have a similar form. Therefore we do not show them. It can be understood from figure 1 that the number of wave functions zeros is equal to the state number.

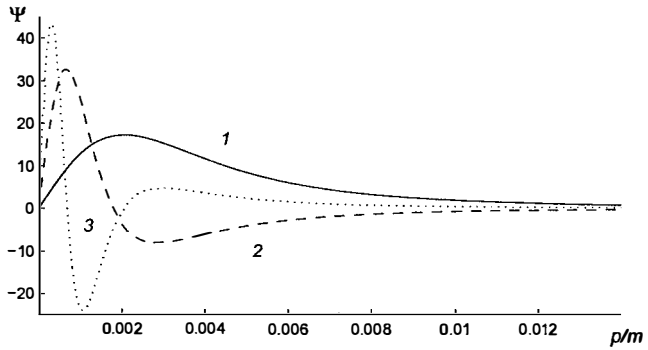

Figure 1: The wave functions for Logunov-Tavkhelidze equation with potential (19)

The results for dimensionless and multiplied by 10^5 binding energy $2E/m - 2$ of the first four states are represented in Table 1. The energy values obtained by Richardson extrapolation (24) of results found for N and $2N$ are given in the columns under each N: $C = 0.01$ for potentials (17) - (21), $C = 0.005$ for potential (22).

It should be noted that to achieve the best accuracy, we chose small values C (about 0.01). As seen in figure 1 this is due to the fact that the

wave functions change is the fastest at small p/m ($p/m \leq 0.005$).

Table 1

Binding energy $(2E/m - 2) \times 10^5$

V	n	Logunov-Tavkhelidze equation		Kadyshevsky equation	
		$N = 1600$	$N = 3200$	$N = 1600$	$N = 3200$
(17)	1	-1.266331	-1.266331	-1.266300	-1.266300
	2	-0.300378	-0.300377	-0.300374	-0.300374
	3	-0.124168	-0.124168	-0.124167	-0.124167
	4	-0.064003	-0.064003	-0.064003	-0.064002
(18)	1	-1.266454	-1.266453	-1.266423	-1.266422
	2	-0.300397	-0.300397	-0.300394	-0.300393
	3	-0.124174	-0.124173	-0.124173	-0.124173
	4	-0.064005	-0.064005	-0.064005	-0.064005
(20)	1	-1.266515	-1.266515	-1.266484	-1.266484
	2	-0.300402	-0.300402	-0.300399	-0.300398
	3	-0.124174	-0.124174	-0.124173	-0.124173
	4	-0.064005	-0.064004	-0.064004	-0.064004
(22)	1	-1.266361	-1.266361	-1.266331	-1.266330
	2	-0.300381	-0.300381	-0.300377	-0.300377
	3	-0.124168	-0.124168	-0.124168	-0.124168
	4	-0.064003	-0.064003	-0.064003	-0.064003
		$N = 800$	$N = 1600$	$N = 800$	$N = 1600$
(19)	1	-1.266396	-1.266392	-1.266365	-1.266361
	2	-0.300391	-0.300387	-0.300388	-0.300384
	3	-0.124175	-0.124171	-0.124174	-0.124170
	4	-0.064008	-0.064004	-0.064007	-0.064004
(21)	1	-1.266437	-1.266432	-1.266406	-1.266402
	2	-0.300397	-0.300393	-0.300394	-0.300389
	3	-0.124176	-0.124172	-0.124175	-0.124171
	4	-0.064008	-0.064004	-0.064008	-0.064004

Transition frequencies of the two-particle systems from the second state (first excited state) to the first state (ground state) are calculated based on the energy values obtained. These frequencies are given in Table 2.

Table 2

Transition frequency, MHz

V	Logunov-Tavkhelidze equation		Kadyshevsky equation	
	$N = 1600$	$N = 3200$	$N = 1600$	$N = 3200$
(17)	1193521990	1193521987	1193488134	1193488121
(18)	1193649720	1193649714	1193615764	1193615758
(20)	1193719570	1193719559	1193685433	1193685431
(22)	1193555894	1193555835	1193521981	1193521930
	$N = 800$	$N = 1600$	$N = 800$	$N = 1600$
(19)	1193585705	1193585495	1193551800	1193551589
(21)	1193629089	1193628884	1193595151	1193594932

The experimentally measured transition frequency for the orthopositronium is equal to 1233607216.4(3.2) MHz [15]. Its comparison with the frequencies from Table 2 shows that the solutions found for potentials (17)-(22) are in satisfactory agreement with the experimental value. It should be noted that, since the orthopositronium - is the system with total spin one, it is preferable to compare the experimental value of the transition frequency with the results obtained for potential (21) than for the other potentials. We will carry out more detailed discussion of these results after investigation the decay widths.

Now let us consider solutions of equations in the RCR (12). The method of solving has been tested in the case of the modified Logunov-Tavkhelidze equation with potential

$$V(r) = -\tanh(\pi m r/2)/r, \tag{25}$$

which allows the exact solutions [16] and which has similar to (23) asymptotic at large r. The exact energy quantization condition in this case has the following form

$$2E_n = \sqrt{4m^2 - \lambda^2/n^2}, \quad n = 1, 2, \ldots \quad . \tag{26}$$

It is easy to see that potential (25) is the difference of two one-boson exchange potentials (23) at $\mu = 0$ and $\mu = 2m$. Moreover, expression (25) is the Coulomb potential in the RCR. In Table 3 we represent the transition frequency between energy levels obtained by solving equations (12) with potentials (23), (25) and potential r^{-1}.

Table 3

Transition frequency, MHz				
j	N	$r^{-1}\tanh(\pi mr/2)$	$r^{-1}\coth(\pi mr)$	r^{-1}
1	400	1233673256	12336956443	12336886274
	800	1233673569	12336954153	12336880641
2	400	1233651095	12336734637	12336664665
	800	1233651664	12336735112	12336661596
3	400	1233708292	12337306742	12337236596
	800	1233701226	12337230675	12337157181
4	400	1233682565	12337049503	12336979345
	800	1233679188	12337010316	12336936813

The transition from the first state to the ground one frequency obtained by exact solution of the Schrödinger equation with the Coulomb potential is 12336907360 MHz. The transition frequency calculated on the basis of the energy quantization condition (26) is 12336958685 MHz. Comparison all these results shows that the best agreement with the experimentally measured value gives the result obtained by solving the Kadyshevsky equation with potential (25).

6 Decay width of two-particle systems

Let us use the obtained numerical wave functions to find another quantity which experimental value is known - the decay width (the decay probability) of parapositronium into two photons. The decay width of fermion-antifermion system into two photons was obtained in the framework of the quasipotential approach in article [5] based on the amplitude of this process and has the form:

$$\Gamma = \frac{8m\lambda^2}{\pi}\left|\int_0^\infty \frac{dp}{E_p}\log\left(\frac{E_p+p}{m}\right)\psi(2E,p)\right|^2 = \frac{4\pi\lambda^2}{m^2}\left|\frac{\partial}{\partial r}\psi(w,r)\right|^2\Big|_{r=0}. \quad (27)$$

It is more correct to calculate the decay widths for potential (22) describing the fermion-antifermion system than for the other potentials. However, we found these quantities for all considered here potentials except (21). Calculated decay widths are represented in table 4. To find the integrals in (27) the same quadratures were used as at solving the equations. For potentials (17) - (19) calculations were carried out at $C = 0.005$, for potential (20) at $C = 0.015$, and for potential (22) at $C = 0.01$.

Table 4

Decay width for parapositronium Γ, μs^{-1}

V	Logunov-Tavkhelidze equation		Kadyshevsky equation	
	$N = 1000$	$N = 2000$	$N = 1000$	$N = 2000$
(17)	7117.719	7117.730	7103.877	7103.883
(18)	7148,564	7148,592	7131,901	7131,915
(19)	7130,939	7130,953	7116,073	7116,081
(20)	7196,282	7196,448	7172,333	7172,449
(22)	7136,326	7136,399	7120,028	7120,077

In table 5 we show the values of the decay widths found on the basis of numerical solutions in the RCR (12) in the cases of potentials (23), (25) and potential r^{-1}.

Table 5

Decay width for parapositronium, Γ, μs^{-1}

j	N	$r^{-1}\tanh(\pi mr/2)$	$r^{-1}\coth(\pi mr)$	r^{-1}
	800	7938.39	7966.34	7395.60
1	1600	7938.47	7966.68	7395.64
	800	7918.82	7942.44	7933.91
2	1600	7918.91	7942.71	7934.23
	800	7995.24	8059.11	8031.52
3	1600	7995.03	8060.68	8032.98
	800	7966.67	8012.48	7993.61
4	1600	7966.60	8013.42	7994.52

Substitution of the exact non-relativistic wave function of the ground state for the Coulomb potential [17] in (27) gives the value of decay width $8032.5\mu s^{-1}$. Substitution of the exact wave function obtained from the modified Logunov-Tavkhelidze equation solution for potential (25) [16] in formula (27) gives $7995.18\mu s^{-1}$. The experimental value of the decay width for parapositronium is equal to $7990.9(1.7)\mu s^{-1}$ [18]. It is easy to see that the best agreement with the experimentally measured result is given by the solution of the modified Kadyshevsky equation for potential r^{-1} and the modified Logunov-Tavkhelidze equation for superposition of one-boson exchange potentials (25).

Let us note that the results for the potentials that admit transformation into the RCP (23), (25) and r^{-1} coincide with the experimental values better than the results for more cumbersome, but received more

strongly potentials (17) - (22). This is the additional argument in favor of the investigation of phenomenological potentials, especially admiting exact solutions of equations.

7 Conclusion

In this paper numerical solutions of quantum field theory equations are found for bound s-states of two scalar particle system and system of two particles with spin 1/2. Solutions are obtained for different variants of one-boson exchange potentials, the superposition of these potentials and for potential r^{-1}. On the basis of the solutions found the decay widths of particle-antiparticle bound state into two photons are calculated. The energy spectrum and decay widths obtained in this approximation are compared with the experimentally measured values for positronium.

References

[1] *Logunov A.A., Tavkhelidze A.N.*, Quasi-Optical Approach in Quantum Field Theory // Nuovo Cimento. - 1963. - V.29, N2. - P.380-399.

[2] *Kadyshevsky V.G.*, Quasipotential Type Equation for the Relativistic Scattering Amplitude // Nucl. Phys. - 1968. - V.B6, N1. - P.125-148.

[3] *Kadyshevsky V.G., Mir-Kasimov R.M., Skachkov N.B.*, Quasi-Potential Approach and the Expansion in Relativistic Spherical Functions // Nuovo Cimento. - 1968. - V.LV.A., N2. - P.233-257.

[4] *Scachkov N.B., Solovtsov I.L.*, Description of the Formfactor of Relativistic Two-Particle System in the Covariant Hamiltonian Formulation of Field Theory // TMF. - 1980. - V.43, N3. - P.330 - 342.

[5] *Kozlov G.A., Kuleshov S.P., Savrin V.I., Sanadze V.V., Skachkov N.B.*, On the Decay of a Bound State of a $\mu^+\mu^-$-Pair into an e^+e^--Datitz Pair and a γ-Quantum // TMF. - 1984. - V.60, N1. - P.24 - 36.

[6] *Faustov R.N.*, Quasipotential Method in the Bound State Problem // TMF. - 1970. - V.3, N2. - P.240 - 254.

[7] *Kapshai V.N., Alferova T.A.*, Relativistic Two-Particle One-Dimensional Scattering Problem for Superposition of δ-Potentials // J. Phys. A: Math. Gen. - 1999. - V.32. - P.5329-5342.

[8] *Kapshai V.N., Savrin V.I., Scachkov N.B.*, On the Dependence of Quasipotential on Total Energy of Two-Particle System // TMF. - 1986. - V.69, N3. - P.400 - 410.

[9] *Dvoeglazov V.V., Scachkov N.B., Tyukhtyaev Yu.N., Hudyakov S.V.*, Relativistic Partial Wave Integral Equations for the Two-Fermion Wave Function // Journal of Nuclear Physics. - 1991. - V.54, N3. - P.658 - 668.

[10] *Arhipov A.A.*, One-Gluon Exchange Approximation for the Quasipotential of Two Quark Interaction in Quantum Chromodinamics // TMF. - 1990. - V.83, N3. - P.358 - 373.

[11] *Kapshai V.N., Tyumenkov G.Yu.*, Boson Exchange Quasipotentials for a Pseudoscalar Fermion-Antifermion Bound State // Russ. Phys. J. - 1991. - V.40, N7. - P.587 - 589.

[12] *Landau R.*, Computational Physics. Problem Solving with Computers, published J. Wiley and Sons, 1997.

[13] *Solov'eva T.M, Zhidkov E.P.*, Iteration Method of Solving the Integral Equation with Nonlinear Dependence on Spectral Parameter // Computer Physics Communications - 2000. - V.126. - P.168 - 177.

[14] *Mohr P.J., Taylor B.N. and Newell D.B.*, CODATA Recommended Values of the Fundamental Physical Constants: 2010. Gaithersburg: National Institute of Standards and Technology, 2012. - 94 p.

[15] *Fee M.S., Mills A.P., Jr. Chu et. al.*, Measurement of the Positronium $1^3S_1 - 2^3S_1$ Interval by Continuous-Wave Two-Photon Exitation // Phys. Rev. Lett. - 1993. - V.70, N10. - P.1397 - 1400.

[16] *Kapshai V. N. and Alferova T. A.* Analog of the Frobenius Method for Solving Homogeneous Integral Equations of the Quasi-Potential Approach in a Relativistic Configurational Representation // Russ. Phys. J. - 1997. - V.40, N7. - P.641 - 648.

[17] *Griffiths D.*, Introduction to Quantum Mechanics, published Prentice Hall, 1995.

[18] *Al-Ramadhan A.H. and Gidley D.W.*, New Precision Measurement of the Decay Rate of Singlet Positronium // Phys. Rev. Lett. - 1994. - V.72, N11. - P.1632-1635.

Covariant equations of the pion interaction with the electromagnetic field in the formalism Duffin-Kemmer

Vakulina E.V.,*
I.G. Petrovsky Bryansk State University, Russia
Maksimenko N.V.
Gomel State University, Physics Department, Gomel, Belarus

Abstract

The Lagrangian in the covariant form and the equation of motion of the pion in the electromagnetic field, taking into account its electric and magnetic polarizabilities were defined in the formalism of Duffin-Kemmer on the basis of the principle of gauge invariance. The amplitude of Compton scattering was defined on the basis of the solution of the equation of the interaction of the pion with the electromagnetic field produced by the method of Greens function, taking into account the impact and polarizabilities of the pion.

1 Introduction

Low-energy theorems which are based on general principles of relativistic quantum field theory and the expansion of the amplitude of Compton scattering on the frequency of the photons play an important role in understanding the structure of hadrons. According to the low-energy theorem, the amplitude of Compton scattering depends not only on the charge and magnetic moment of hadrons, but also to other significant electromagnetic characteristics, such as the anomalous magnetic moments, electric and magnetic polarizabilities. Recently measurement polarizabilities realized

*E-mail:elvakulina@yandex.ru

not only by Compton scattering experiments, but also in other processes electrodynamic [1, 2]. Description of the contribution of the polarizabilities in the amplitude and the cross section of two-photon electrodynamic processes can be performed in sequential relativistic field-theoretic approach [3, 4]. In the papers [4, 5] have been developed methods for obtaining covariant Lagrangians and equations of two-photon amplitudes of electrodynamic processes in view of the polarizabilities of hadrons. In the development of this approach, the problem arises of determining the universal covariant Lagrangians and amplitudes of hadron electrodynamics with the polarizabilities of hadrons for different spins. In this paper, in the framework of the covariant field-theoretical approach, using the method of [4], obtained by the Lagrangian equations and the interaction amplitude of the electromagnetic field with zero spin hadrons in the Duffin-Kemmer formalism, which opens up the possibility of field-theoretical description of the polarizabilities of hadrons, such as spin unit.

2 Description of the polarizability of the pion in the formalism of the Duffin-Kemmer

Using a relativistic field-theoretic properties of the fields in the formalism of the Duffin-Kemmer may establish new structural properties of the polarizabilities of the particles [6]. Duffin-Kemmer for free scalar particles are:

$$(\beta_\mu \overrightarrow{\partial}_\mu + m)\psi(x) = 0, \tag{1}$$

$$\overline{\psi}(x)(\overleftarrow{\partial}_\mu \beta_\mu - m) = 0, \tag{2}$$

where $\psi(x)$ and $\overline{\psi}(x)$ - five-dimensional wave functions of scalar particles, as determined by the components of the four-momentum $a_\mu\{\overrightarrow{a}\, a_4 = ia_0\}$.

In the equations (1) and (2) five-dimensional matrix $\beta_\mu = \beta_\mu^{(5)}$ are the matrices of the Duffin-Kemmer and satisfy the commutation relations:

$$\beta_\mu\beta_\nu\beta_\rho + \beta_\rho\beta_\nu\beta_\mu = \delta_{\mu\nu}\beta_\mu + \delta_{\rho\nu}\beta_\mu. \tag{3}$$

Covariant formalism of Lagrange that equation (1) and (2) follow from the Lagrangian

$$L = -\frac{1}{2}\overline{\psi}(\beta_\mu \overrightarrow{\partial}_\mu + m)\psi(x) + \frac{1}{2}\overline{\psi}(\overleftarrow{\partial}_\mu \beta_\mu - m)\psi(x). \tag{4}$$

To get the equations of the electromagnetic field interactions with peonies in the Duffin-Kemmer formalism based on their polarizabilities, we use the principle of gauge invariance. To do this, according to [7], the Lagrangian (4) must be entered

$$L^{(\gamma)} = -\frac{1}{4}F_{\mu\nu}F_{\mu\nu}$$

and the substitution of derivatives $\overrightarrow{\partial}_\mu$ and $\overleftarrow{\partial}_\mu$ on elongated derivatives

$$\overleftarrow{D} = \overleftarrow{\partial}_\nu\beta_\sigma\eta_{\sigma\nu} + ie\hat{A}, \tag{5}$$

$$\overrightarrow{D} = \eta_{\sigma\nu}\beta_\sigma\overrightarrow{\partial}_\nu - ie\hat{A}, \tag{6}$$

$$\eta_{\sigma\nu} = \delta_{\sigma\nu} + \frac{2\pi}{m}[\alpha_E F_{\sigma\mu}F_{\mu\nu} + \beta_M\tilde{F}_{\sigma\mu}\tilde{F}_{\mu\nu}]. \tag{7}$$

In (5) - (7) $F_{\mu\nu} = \partial_\mu A_\nu - \partial_\nu A_\mu$ - tensor, and $\tilde{F}_{\mu\nu} = \frac{i}{2}\varepsilon_{\mu\nu\rho\sigma}F_{\rho\sigma}$ - dual tensor of the electromagnetic field. If in (4) to take into account (5) - (7), we obtain

$$L = -\frac{1}{4}F_{\mu\nu}F_{\mu\nu} - \frac{1}{2}\overline{\psi}\overleftrightarrow{\partial_\mu}\beta_\mu\psi - m\overline{\psi}\psi + ie\overline{\psi}\hat{A}\psi + K_{\sigma\nu}\theta_{\sigma\nu}. \tag{8}$$

In (8) the following notation:

$$K_{\sigma\nu} = \frac{2\pi}{m}[\alpha_E F_{\sigma\mu}F_{\mu\nu} + \beta_M\tilde{F}_{\sigma\mu}\tilde{F}_{\mu\nu}],$$

$$\theta_{\sigma\nu} = \frac{1}{2}\overline{\psi}\beta_\sigma\overleftrightarrow{\partial_\mu}\psi.$$

The arrows above the derivatives indicate their effect on the wave functions of the pion in the five-dimensional space, and α_E and β_M - electric and magnetic polarizabilities of the pion.

We distinguish in equation (8) part of the Lagrangian associated with the polarizabilities of the pion:

$$L^{(\alpha_E,\beta_M)} = K_{\sigma\nu}\theta_{\sigma\nu}. \tag{9}$$

In the rest frame of the pion Lagrangian (9) takes the form:

$$L^{(\alpha_E,\beta_M)} = -H^{(\alpha_E,\beta_M)} = 2\pi(\alpha_E\overrightarrow{E}^2 + \beta_M\overrightarrow{H}^2),$$

where $H^{(\alpha_E,\beta_M)}$ - the Hamiltonian of the interaction of electromagnetic fields with a peony with the induced dipole moments in the static limit.

We now see that the amplitude of Compton scattering polarizability are included in accordance with the low-energy theorem. To do this, we obtain the equation of the pion interaction with the electromagnetic field with the polarizabilities using the Lagrangian (8)

$$(\hat{\partial} + m)\psi = ie\hat{A}\psi - \frac{1}{2}[\partial_\mu(K_{\sigma\mu}\beta_\sigma\psi) + K_{\sigma\mu}\beta_\sigma\partial_\mu\psi]. \qquad (10)$$

We represent the differential equation (10), which will take into account the contributions of the polarizabilities in integral form:

$$\psi(x) = \psi 0(x)^+ \int S(x - x')V^{(\alpha_E,\beta_M)}(x')dx',$$

where the potential is of the form:

$$V^{(\alpha_E,\beta_M)}(x') = -\frac{1}{2}[\partial_\mu(K_{\sigma\mu}\beta_\sigma\psi) + K_{\sigma\mu}\beta_\sigma\partial_\mu\psi],$$

and the Green's function $S(x - x')$ satisfies the equation

$$(\hat{\partial} + m)S(x - x') = \delta(x - x').$$

We define the matrix element S_{fi} scattering of photons by pioneers following [8-10]. To do this, use the formula:

$$\int \overline{\psi}_{p_2}(x)S(x - x')d^3x|_{t\to\infty} = (-i)\overline{\psi}_{p_2}(x'),$$

where $\overline{\psi}_{p_2}(x') = \frac{1}{\sqrt{(2\pi)^3}}\sqrt{\frac{m}{E_2}}\overline{\varphi}_{\overrightarrow{p}_2}e^{-ip_2x}$.

The function $\overline{\varphi}_{\overrightarrow{p}_2}$ - the momentum representation of the wave function $\overline{\psi}_{p_2}(x)$, which is in the Duffin-Kemmer formalism is defined as follows:

$$\overline{\varphi}_{\overrightarrow{p}_2} = -\frac{i}{2}|Bigr(\varepsilon^{10} - \frac{i}{m}p_{2\mu}\varepsilon^{1\mu}\Big),$$

where ε^{AB} - elements of the full matrix algebra, which satisfy:

$$(\varepsilon^{AB})_{DC} = \delta_{AD}\delta_{BC}, \quad \varepsilon^{AB}\varepsilon^{DC} = \delta_{BC}\varepsilon^{AD},$$

indices A, B, C, D run from 0 to 4.

As a result, we obtain

$$S_{fi} = (-i) \int \overline{\psi}_{p_2}(x') V^{(\alpha_E, \beta_M)}(x') d^4x'. \tag{11}$$

Using the boundary conditions [8-10], and the symmetry of the cross, the expression (11) can be written as:

$$S_{fi} = \frac{im\delta(k_1 + p_1 - k_2 - p_2)}{(2\pi)^2 \sqrt{4\omega_1 \omega_2 E_1 E_2}} M. \tag{12}$$

In (12) the amplitude of Compton scattering of M is given by:

$$M = \frac{2\pi}{m} \overline{\varphi}(p_2) \{ [\hat{k}_2 e_\mu^{(\lambda_2)} + k_{2\mu} \hat{e}^{(\lambda_2)}][k_{1\mu}(e^{(\lambda_1)} P) - (\hat{k}_1 P) e_\mu^{(\lambda_1)}] +$$

$$+ [k_{2\mu}(e^{(\lambda_2)} P) - (\hat{k}_2 P) e_\mu^{(\lambda_2)}][\hat{k}_1 e_\mu^{(\lambda_1)} - k_{1\mu} \hat{e}^{(\lambda_1)}] \} (\alpha_E + \beta_M) \varphi(p_1) + \tag{13}$$

$$+ 2\pi \beta_M \overline{\varphi}(p_2) [k_{2\mu} e_\nu^{(\lambda_2)} - k_{2\nu} e_\mu^{(\lambda_2)}][k_{1\mu} e_\nu^{(\lambda_1)} - k_{1\nu} e_\mu^{(\lambda_1)}] \varphi(p_1).$$

In this expression $e_\mu^{(\lambda_1)}$ and $e_\mu^{(\lambda_2)}$ - the polarization vectors of the initial and final photons, $P = \frac{1}{2}(p_1 + p_2)$, k_1, p_1 and k_2, p_2 - momenta of the initial, final photons and pions, respectively.

In the rest frame of the initial pion amplitude M with the electric charge and polarizabilities up to the second order in the frequency of the photons takes the form [11]:

$$M = (-\frac{e^2}{m} + 4\pi\omega^2 \alpha_E)(\overrightarrow{e}^{(\lambda_2)} \overrightarrow{e}^{(\lambda_1)}) + 4\pi\omega^2 \beta_M [\overrightarrow{n_2} \overrightarrow{e}^{(\lambda_2)}][\overrightarrow{n_1} \overrightarrow{e}^{(\lambda_1)}], \tag{14}$$

where $\overrightarrow{n_1}$ and $\overrightarrow{n_2}$ - the unit vectors directed along the $\overrightarrow{k_1}$ and $\overrightarrow{k_2}$, which is consistent with the low-energy theorem of Compton scattering on the pion.

3 Conclusion

In the formalism of the Duffin-Kemmer on the basis of the principle of gauge invariance defined in covariant form of the Lagrangian and the equation of motion of the pion in the electromagnetic field, taking account of its electric and magnetic polarizabilities. On the basis of the solution of the pion interaction with the electromagnetic field produced by the method of

Green's function is defined amplitude of Compton scattering, taking into account the impact and polarizabilities of the pion. It is shown that the covariant formalism developed by Lagrange interaction of low-energy photons from the pion is consistent with the low-energy theorem of Compton scattering.

References

[1] Carlson, C.E. Constraining off-shell effects using low-energy Compton scattering / C.E. Carlson, M. Vanderhaeghen // [Electronic resource]. - 2011. - Mode of access: http://physics.atom-ph/1109.3779. - Date of access: 04.10.2011.

[2] Birse, M.C. Proton polarisability contribution to the Lamb shift in mnonic hydrogen at fourth order in chiral perturbation theory / M.C. Birse, J.A. McGovern // [Electronic resource]. - 2012. - Mode of access: http:// hep-ph/1206.3030. - Date of access: 15.08.2012].

[3] Moroz, L.G. Scattering matrix taking into account the interaction Pauli / L.G. Moroz, F.I. Fedorov // ZhETF. - 1960. - 39. - Vol. 2. - P. 293-303.

[4] Maksimenko, N.V. Polarizability and gyration elementary particles / N.V. Maksimenko, L.G. Moroz // Problems of atomic science and technology. Series: General and nuclear physics. - 1979. - 4(10). - P. 26-27.

[5] Levchuk, M.I. The nucleon gyration as one of nucleon electromagnetic structure characteristics / M.I. Levchuk, L.G. Moroz // Proc. Academy of Sciences of BSSR. Ser. fiz.-mat. navuk. - 1985. - 1. - P. 45-54.

[6] Maksimenko, N.V. Covariant determination of the polarizability of hadrons with spin one / N.V. Maksimenko // Proc. Academy of Sciences of BSSR. Ser. fiz.-mat. navuk. - 1992. - . 36. - 6. - . 508-510.

[7] ndreev, V.V. Covariant equations of motion in the electromagnetic field of spin 1?2 taking into account the polarizabilities / V.V. ndreev, N.V. Maksimenko, .. Deruzkova // 4 Congress physicists Belarus. Editor in chief S. Ya. Kilin and other. - ins: Kovcheg, 2013. -19-20.

[8] Baryshevsky, V.G. Nuclear optics of polarized media / V.G. Baryshevsky // M.: Energoatomizdat, 1995. - 315 p.

[9] Bogush, A.A. Introduction in the calibration of the field theory of electroweak interactions / .. Bogush // Minsk: Science and technology, 1987. - 359 p.

[10] Bjorken, J.D. Relativistic quantum field theory / J.D. Bjorken, E.D. Drell // M: Science. - 1978. - Vol. 1. - 295 p.

[11] Petrunkin, V.A. Electrical and magnetic polarizabilities of hadrons / V.A. Petrunkin // Fiz. - 1981. - Vol. 12. - 692-753 p.

The Search of Critical Parameter Values for Semirelativistic Coulomb Problem

Andreev V.V. *, Babich K.S.
Fransick Skorina Gomel State University, Physics Department,
Gomel, Belarus
Chebotareva E.S.
I.G. Petrovsky Bryansk State University, Russia

Abstract

The paper presents the new calculation method of upper bounds of critical values for the semirelativistic Coulomb problem with the trial pseudoColumb wave functions.

1 Introduction

One of the main problems of relativistic quantum mechanics is the solution of Salpeter-like equation

$$\hat{H}\Phi_n = \left[\sqrt{\mathbf{k}^2 + m_1^2} + \sqrt{\mathbf{k}^2 + m_2^2} + V(|\mathbf{r}|)\right]\Phi_n = E_n\Phi_n\,, \qquad (1)$$

which describes a system of two particles with a total energy E_n. The interaction is determined centrally symmetric potential $V(|\mathbf{r}|)$. The most common method of solving (1) is a variational method. In this approach the solution of equation (1) reduces to an eigenvalue problem

$$\sum_{k=0}^{\infty} a_k \langle\Psi_k|\,\hat{H}\,|\Psi_{k'}\rangle \equiv \sum_{k=0}^{\infty} \langle H\rangle_{k\,k'}\, a_{k'} = E\, a_k \qquad (2)$$

*E-mail:vik.andreev@gsu.by

by expanding the initial wave function (WF) with respect to some complete set of trial wave function Ψ

$$\Phi = \sum_{k=0}^{\infty} a_k \Psi_k \ . \tag{3}$$

For an approximate solution of the series (3) terminate at a value $N-1$ and get the eigenvalue problem

$$\sum_{k=0}^{N-1} a_k \left\langle \Psi_k \right| \hat{H} \left| \Psi_{k'} \right\rangle = \hat{E}_n \ a_{k'} \tag{4}$$

for the matrix $\langle H \rangle_{k\,k'}$. Moreover, according to the variation of Rayleigh-Ritz technique condition for spectrum $E_0 \leq E_1 \leq \ldots, E_k \leq \hat{E}_k, \ k = 0, \ldots n-1$ is satisfied. In other words, the solution of (4) allows us to find the upper limits E_n for (1). Entries of the matrix $\left\langle \Psi_n \right| \hat{H} \left| \Psi_{n'} \right\rangle = \langle H \rangle_{n\,n'}$, after calculating the angle part with the trial wave functions

$$\Psi_{n,\ell m}(\mathbf{r}) = \psi_{n\ell}(\mathrm{r}) \mathcal{Y}_{\ell m}(\Omega_r) \ , \quad \widetilde{\Psi}_{n,\ell m}(\mathbf{k}) = \widetilde{\psi}_{n\ell}(\mathrm{k}) \mathcal{Y}_{\ell m}(\Omega_k) \tag{5}$$

represent the integrals of the form

$$\langle H \rangle_{n\,n'} = \int_0^{\infty} \widetilde{\psi}^*_{n\,\ell}\,(\mathrm{k}) \left[\sqrt{\mathrm{k}^2 + m_1^2} + \sqrt{\mathrm{k}^2 + m_2^2} \right] \widetilde{\psi}_{n'\,\ell}\,(\mathrm{k})\, \mathrm{k}^2 \mathrm{dk} +$$

$$+ \int_0^{\infty} \psi^*_{n\,\ell}\,(\mathrm{r})\, V\,(\mathrm{r})\, \psi_{n'\,\ell}\,(\mathrm{r})\, \mathrm{r}^2 \mathrm{dr} \ , \quad \mathrm{r} = |\mathbf{r}| \, , \ \mathrm{k} = |\mathbf{k}| \ . \tag{6}$$

There $\widetilde{\psi}^*_{n\,\ell}\,(\mathbf{k})$ - Fourier transform of the wave function $\psi^*_{n\,\ell}\,(\mathrm{r})$. Obviously, the most accurate solution of (1) requires the matrix elements with large n and n'. The aim of this work is to find the critical values α of the Coulomb potential $V\,(r) = -\alpha/r$, $\alpha > 0$ for (1) of equal mass that is $m_1 = m_2 = m$, using the test WF pseudo Coulomb type

$$\psi^{\mathrm{C}}_{n\ell}(\mathrm{r}) = N^{\mathrm{C}}_{n\ell}\,(2\beta)^{3/2} \ (2\beta \mathrm{r})^{\ell} e^{-\beta \mathrm{r}} L_n^{2\ell+2}(2\beta \mathrm{r}) \ , N^{\mathrm{C}}_{n\ell} = \sqrt{\frac{n!}{(n+2\ell+2)!}} \ , \tag{7}$$

$$\tilde{\psi}^{\mathrm{C}}_{n\ell}(\mathrm{k}) = \tilde{N}^{\mathrm{C}}_{n\ell} \left(\frac{\beta}{\mathrm{k}^2 + \beta^2} \right)^{\ell+2} (\mathrm{k})^{\ell} P_n^{(}\ell + 3/2, \ell + 1/2)(\frac{\mathrm{k}^2 - \beta^2}{\mathrm{k}^2 + \beta^2}) \ , \tag{8}$$

$$\tilde{N}^{\rm C}_{n\ell} = \frac{2\sqrt{\beta n!(n+2\ell+2)!}}{\Gamma(n+\ell+3/2)} \ .$$

In (7),(8) $L^{\ell}_{n}(z)$ are Laguerre polynomials; $P^{\mu,\nu}_{n}(z)$ are Jacobi polynomials; number $n, \ell \geq 0$, and β is variational parameter of WF.

2 Searching of the critical values α

In quantum systems with Coulomb potential there is a critical value where there is a discrete energy spectrum. In [1] (see also the references in [2]) have shown that relativistic generalization of the Schrödinger equation (1) - spinless Salpeter equation will also be critical.

We present a new method of estimating the critical values based on the variation problem. Using the variational method with the trial wave function (7) to equation (4) with the Coulomb potential and equal masses $m_1 = m_2 = m$ leads to the eigenvalue problem

$$\mathrm{Det}\|\langle H(\alpha,\beta)\rangle - I \times \tilde{E}\| = 0 \ . \tag{9}$$

We make the transition to dimensionless variables by the relations: $\langle H\rangle \longrightarrow \beta\langle\tilde{H}\rangle$ and $E \longrightarrow \beta\tilde{E}$, where β is parameter of WF (7). Then (9) reduces to the solution of the equation

$$\mathrm{Det}\|\langle H(\alpha, m/\beta)\rangle - I \times \tilde{E}\| = 0 \ . \tag{10}$$

since $\beta \neq 0$. The critical value of the Coulomb parameter $\alpha = \alpha_{crit.}$ corresponds to the limit as $\beta \longrightarrow \infty$ [2]. In this case, there is no minimum value of the function $E(\beta)$ and the spectrum of the Hamiltonian equation (1) gives a negative value. Performing the limit $\beta \longrightarrow \infty$ in (10) we obtain the equation

$$\mathrm{Det}\|\langle H(\alpha_{crit.},0)\rangle\| = \mathrm{Det}\|\langle\tilde{T}((m/\beta)=0) + \alpha_{crit.}\tilde{V}()\rangle\| = 0 \ . \tag{11}$$

where

$$\left\langle\tilde{H}\right\rangle_{n\,n'} = \frac{2}{\beta}\int\limits_0^\infty \tilde{\psi}^{C}_{n\,\ell}(\mathrm{k},\beta)\tilde{\psi}^{C}_{n',\,\ell}(\mathrm{k},\beta)\mathrm{k}^3\mathrm{dk} - \frac{\alpha_{crit.}}{\beta}\int\limits_0^\infty \psi^{C}_{n\,\ell}(\mathrm{r},\beta)\psi^{C}_{n',\,\ell}(\mathrm{r},\beta)\mathrm{rdr} \ . \tag{12}$$

It can be shown that (12) for $\langle \tilde{H} \rangle_{n\,n'}$ does not explicitly depend on the variational parameter β. Indeed, performing the replacement to the dimensionless variables $\tilde{\mathrm{r}} = \beta \mathrm{r}, \tilde{\mathrm{k}} = \mathrm{k}/\beta$, arrive at the relationship

$$\left\langle \tilde{H} \right\rangle_{n\,n'} = 2 \int_0^\infty \tilde{\psi}^C_{n\,\ell}(\tilde{\mathrm{k}}) \tilde{\psi}^C_{n'\,\ell}(\tilde{\mathrm{k}}) \tilde{\mathrm{k}}^3 \mathrm{d}\tilde{\mathrm{k}} - \alpha_{crit.} \int_0^\infty \psi^C_{n\,\ell}(\tilde{\mathrm{r}}) \psi^C_{n'\,\ell}(\tilde{\mathrm{r}}) \tilde{r} \mathrm{d}\tilde{\mathrm{r}} \,, \qquad (13)$$

with dimensionless wave functions

$$\psi^C_{n\,\ell}(\tilde{\mathrm{r}}) = \sqrt{\frac{8n!}{(n+2\ell+2)!}} (2\tilde{\mathrm{r}})^\ell e^{-\tilde{\mathrm{r}}} L_n^{(2\ell+2)}(2\tilde{\mathrm{r}}) \,. \qquad (14)$$

$$\tilde{\psi}^C_{n\,\ell}(\tilde{\mathrm{k}}) = \frac{2\sqrt{n!(n+2\ell+2)!}}{\Gamma(n+\ell+3/2)} \left(\frac{1}{\tilde{\mathrm{k}}^2+1} \right)^{\ell+2} (\tilde{\mathrm{k}})^\ell P_n^{(\ell+3/2,\ell+1/2)} \left(\frac{\tilde{\mathrm{k}}^2-1}{\tilde{\mathrm{k}}^2+1} \right) \,. \qquad (15)$$

Therefore, equation (11) with the matrix elements (15) defines a set of n critical values $\alpha_{crit.}$ for n energy levels E. To solve this equation we need the matrix elements of the various n and n' with the wave function (7) or (15).

3 Calculation of matrix elements $\langle \tilde{H} \rangle_{n\,,n'}$

To test the WF pseudo Coulomb type (7), the potential of equation (6) $V(\mathrm{r}) = \mathrm{r}^p$ written in the form

$$\langle r^p \rangle_{n\ell\,,n'} = \int_0^\infty \psi^C_{n\,\ell}(\mathrm{r},\beta) r^p \psi^C_{n'\,\ell}(\mathrm{r},\beta) \mathrm{r}^2 \mathrm{dr} =$$

$$= N^C_{n\,\ell} N^C_{n'\,\ell} (2\beta)^{2\ell+3} \int_0^\infty \mathrm{dr} \mathrm{r}^{2\ell+2+p} e^{-2\beta \mathrm{r}} L_n^{2\ell+2}(2\beta\mathrm{r}) L_{n'}^{2\ell+2}(2\beta\mathrm{r}) \,. \qquad (16)$$

After the change of variables $z = 2\beta\mathrm{r}$ in (16)we obtain the expression

$$\langle \mathrm{r}^p \rangle_{n\ell\,,n'} = \frac{N^C_{n\,\ell} N^C_{n'\,\ell}}{(2\beta)^p} \int_0^\infty \mathrm{d}z\, z^{2\ell+2+p} e^{-z} L_n^{2\ell+2}(z) L_{n'}^{2\ell+2}(z) \,. \qquad (17)$$

Next, using the ratio of the Chu-Vandermonde with parameters $\alpha = 2\ell+2$, $\beta = 2\ell + 2 + p$ [3],

$$L^{\alpha}_{n-1}(z) = \sum_{j=1}^{n} \frac{(\alpha-\beta)_{n-j}}{(n-j)!} \times L^{\beta}_{j-1}(z) \,, \tag{18}$$

where $(z)_N$ - Pochhammer symbol and the orthogonality relation for the Laguerre polynomials

$$\int_0^{\infty} dz z^{\beta} e^{-z} L^{\beta}_{j}(z) L^{\beta}_{j'}(z) = \frac{\Gamma(j+\beta+1)}{j!} \delta_{j\,j'} \tag{19}$$

obtain a general expression for the integral (16)

$$\langle \mathrm{r}^{p} \rangle_{n,n'} = \frac{1}{(2\beta)^{p}} \sqrt{\frac{n!\,n'!}{(n'+2\ell+2)!(n+2\ell+2)!}} \times$$
$$\times \sum_{j=1}^{n+1} \frac{(-p)_{n+1-j}\,(-p)_{n'+1-j}}{(n+1-j)!\,(n'+1-j)!} \frac{\Gamma\,(2\ell+1+p+j)}{(j-1)!} \,, \quad n \le n' \,. \tag{20}$$

Formula (20) generalizes the relation [4], where the calculations were made for special cases with $p = -1$ and $p = 1$. For the case $\ell = 0$ and $p = -1$ have

$$\langle 1/r \rangle_{n,n'} = \beta \sqrt{\frac{(n+1)(n+2)}{(n'+1)(n'+2)}} \,, \quad n \le n' \,. \tag{21}$$

Part associated with the kinetic energy can be calculated exactly. For example, we present the answers to the case $n = \ell = 0$ and $n' = \{0, 1, 2, 3\}$:

$$\left\langle \tilde{\mathrm{k}} \right\rangle_{n=\ell=0,n'=\{0,1,2,3\}} = \int_0^{\infty} \tilde{\psi}^{C}_{n\ell}(\tilde{\mathrm{k}}) \tilde{\psi}^{C}_{n'\ell}(\tilde{\mathrm{k}}) \tilde{\mathrm{k}}^{3} \mathrm{d}\tilde{\mathrm{k}} = \frac{8}{3\pi} \left\{ 1, \frac{1}{\sqrt{3}}, \frac{\sqrt{2}}{5\sqrt{3}}, \frac{\sqrt{2}}{5\sqrt{5}} \right\} \,. \tag{22}$$

4 The calculation of the critical values

For the simplest case $n = \ell = 0$, $n' = 0$ the upper limit $\alpha_{crit.}$ can be easily calculated analytically. The resulting value $\alpha_{crit.} = 16/(3\pi)$ coincides with

the results of [2], which indirectly confirms the method. The calculations for different n and n' up to $n = n' = 30$ using (20) and (22) show that there is convergence of the calculation results and the relative error

$$\delta_n = \frac{\alpha_{crit.}(n-2) - \alpha_{crit.}(n)}{\alpha_{crit.}(n)} \tag{23}$$

and for $n = 30$ is $\delta_{30} = 1,11\%$. Estimate for the critical value is then equal to

$$\alpha_{crit.} \leq 1,09\ , \tag{24}$$

roughly agrees with the estimate $\alpha_{crit.} \leq 1$, obtained in [5].

5 Conclusion

The paper presents a method of calculating the upper limit of the critical value of the Coulomb parameter α for the spinless Salpeter equation (1). In contrast to [2] (see also other works of these authors), this approach does not require the computation of eigenvalues $E = E(\beta)$ then calculating the limit $\lim\limits_{\beta\to\infty} E(\beta)$ in order to obtain the equation for the critical value $\alpha_{crit.}$.

The proposed method of solution of (11) immediately allows to find an estimate $\alpha_{crit.}$, which greatly simplifies the computational cost. Obviously, in the case of different masses, as the derivation of (11) and (13), the estimate of the critical value is the same as for the case of equal masses, because of (11) and (13) remain unchanged.

References

[1] Herbst, I. Spectral Theory of the perator $(p^2+m^2)^{1/2}-Ze^2/r/$ I.Herbst //Commun.Math.Phys. – 1977. – Vol. 53. – P.285-294.

[2] Lucha, W. Relativistic Coulomb problem: Energy levels at the critical coupling constant analytically /W.Lucha, F.F.Schoberl //Phys.Lett. – 1996. – Vol. B387. – P. 573-576.

[3] Gradstein, I. Tables of integrals, sums, series and products/ I.S. Gradstein, I.M.Ryzhik. - 4th revised. - Moscow: Gos.izd of Sci. literature, 1963. – 1110 p.

[4] Fulcher, L. P. Energies of quark - anti-quark systems, the Cornell potential, and the spinless Salpeter equation / L. P. Fulcher, Z. Chen, K. C. Yeong// Phys. Rev. – 1993. – Vol. D47.–P.4122-4132.

[5] Martin, A. Semirelativistic stability and critical mass of a system of spinless bosons in gravitational interaction/A.Martin, S.M.Roy//Phys.Lett. – 1989. – Vol. B233.– P.407-412.

Resonance Width Consideration for Compton Rotation in Magnetic Field

A.I. Sery*
Brest State Pushkin University, Brest, Belarus

Abstract

In the framework of tree approximation a formula is obtained for the calculation of Compton rotation angle of the plane of linear polarization of photons per unit path in electron gas with high degree of spin polarization of electrons. The finite width of resonance on intermediate virtual Landau level is taken into account, averaging on the momenta of electrons is performed in zero temperature approximation.

1 Introduction

In present work the research is done according to the suggestion of V.G. Baryshevsky and V.V. Tikhomirov. The effect of Compton rotation of the plane of polarization of hard X-(soft gamma-) photons in the absence of magnetic field was theoretically predicted by V.G. Baryshevsky and V.L. Luboshitz in 1965 and experimentally tested at early 1970s [1, 2, 3, 4].

In [5], using the approach of [6], a formula was obtained for the calculation of Compton rotation angle of the plane of linear polarization of photons per unit path in electron gas with total spin polarization of electrons ($p_{0e} = 1$), though the finite width of resonance on intermediate virtual Landau level was not considered:

$$\frac{d\varphi}{dl} = \frac{(\pi\hbar c)^2 n_e \alpha \cos\beta}{\hbar\omega(\varepsilon_0 + \hbar\omega)} \exp\left(-\frac{\phi}{2}\right) \sum_{n=1}^{\infty} \phi^{n-1}(\Xi_n(g) - \Xi_n(f)), \alpha = \frac{e^2}{\hbar c},$$

*E-mail:alexey_ sery@mail.ru

$$\phi = \frac{\hbar\omega^2 \sin^2\beta}{cBe}, \Xi_n(\lambda) = \frac{c\lambda_0\varepsilon_0 - \lambda_3 p_z c^2 - m^2c^4}{c^2\lambda_0^2 - \varepsilon_{n\lambda}^2 - i\cdot 0},$$
$$\varepsilon_0 = \sqrt{m^2c^4 + p_z^2c^2}, \varepsilon_{n\lambda} = \sqrt{m^2c^4 + 2ne\hbar Bc + \lambda_3^2c^2}. \quad (1)$$

Here n_e is electron density, m, p_z are electron's mass and momentum along z axis, respectively; μ_B is Bohr magneton, e is electric charge, $\hbar\omega$ is photon's energy, $\vec{B}$ is magnetic field strength, β is the angle between the wave vector of photon $\vec{k}$ and $\vec{B}$; $\varepsilon_{n\lambda}$ is energy of virtual electron on intermediate nth Landau level. For such an electron in R-process ($\lambda = g$) and S-process ($\lambda = f$) we have

$$cg_0 = \varepsilon_0 + \hbar\omega, cg_3 = p_z c + \hbar\omega\cos\beta, cf_0 = \varepsilon_0 - \hbar\omega, cf_3 = p_z c - \hbar\omega\cos\beta. \quad (2)$$

Formulas (1) are applicable if spin polarization of electrons $p_{0e} = 1$ which corresponds to

$$2^{2/3} m\mu_B B \geq \pi^{4/3}\hbar^2 n_e^{2/3}. \quad (3)$$

2 Consideration of resonance width on Landau level

If $\hbar\omega < \varepsilon_0$ (which corresponds to X-photons), then the width Γ_n of resonance on nth Landau level in R-process must be considered, but the resonance in S-process is absent. Removing the poles from the real axis in $\Xi_n(g)$ and extracting the real part, we obtain

$$\varepsilon_{ng} \to \varepsilon_{ng} - i\Gamma_n/2, \Gamma_n \approx \frac{16(2n-1)\alpha(\mu_B B)^2}{3mc^2}, \quad (4)$$
$$Re(\Xi_n(g)) = \frac{(cg_0\varepsilon_0 - g_3 p_z c^2 - m^2c^4)G_n}{G_n^2 + \Gamma_n^2\varepsilon_{ng}^2}, G_n = c^2 g_0^2 - \varepsilon_{ng}^2 + \frac{\Gamma_n^2}{4}. \quad (5)$$

Numerical calculations show that similar consideration of Γ_n in S-process is not important, at least, at $\hbar\omega < mc^2$.

3 Averaging of amplitudes over momenta at T=0 K

Let's average (1) over electron momenta p_z at T=0 K, using the formula for electron state density per unit volume [7] and the formula for the averaging

of an arbitrary function f:

$$\frac{dN_e}{V} = \frac{eBdp_z}{(2\pi\hbar)^2 c} \Rightarrow \langle f \rangle = \frac{1}{2w_1} \int\limits_{-w_1}^{w_1} f(w)dw, w = \frac{p_z}{mc}, w_1 = \frac{\pi^2(\hbar c)^3 n_e}{(mc^2)^2 \mu_B B}, \quad (6)$$

$$\frac{d\varphi}{dl} = \frac{e^2 m \mu_B B cos\beta}{4\hbar^3 \omega} \exp\left(-\frac{\phi}{2}\right) \sum_{n=1}^{\infty} \phi^{n-1} \int\limits_{-w_1}^{w_1} (R_n - S_n)dw,$$

$$R_n = \frac{f_1(w) f_2(w)}{f_3(w)\left(f_1^2(w) + \frac{\Gamma_n^2}{\hbar^2\omega^2}\left(1 + 4n\frac{\mu_B B}{mc^2} + (w + tcos\beta)^2\right)\right)},$$

$$S_n = \frac{1}{f_3(w)}\left(1 - \frac{Q_n}{Q_n - f_2(w)}\right), Q_n = tsin^2\beta - 4n\frac{\mu_B B}{\hbar\omega},$$

$$f_1(w) = Q_n + f_2(w) + \frac{\Gamma_n^2}{4\hbar\omega mc^2}, f_2(w) = 2(\sqrt{1+w^2} - wcos\beta),$$

$$f_3(w) = \sqrt{1+w^2} + t, t = \frac{\hbar\omega}{mc^2}. \quad (7)$$

The integrals can be taken numerically or analytically, and for S-process we obtain (analytical expressions for R-process are very complicated):

$$S_n = 2arsh(w_1) - \frac{4ty_1}{\sqrt{1-t^2}} - Q_n I_n, \quad (8)$$

$$2I_n(1-t)^2 cos\beta = (1-t)y_3 - 2t\left(\sigma_2 y_3 cos\beta - \frac{2\sigma_2 y_1}{\sigma_1}\right), Q_n = -2; \quad (9)$$

$$I_n = \frac{4t}{\Omega_{1n}}\left(\gamma_{1n}\left(\frac{4\xi_n y_2}{\nu_n} + ln\left|\frac{\tau_{n+}}{\tau_{n-}}\right|\right) - \frac{8\gamma_{2n}y_2}{\nu_n} + \frac{2\gamma_{3n}y_1}{\sigma_1}\right) +$$

$$+\frac{16y_2}{(1-t)(Q_n+2)\nu_n}, Q_n \neq -2, \mu_n = 0; \quad (10)$$

$$I_n = \frac{1}{\Omega_{1n}}\left(\frac{8t\gamma_{3n}y_1}{\sigma_1} + 2t\gamma_{1n} ln\left|\frac{y_2^2 + \xi_n y_2 + q_n}{y_2^2 - \xi_n y_2 + q_n}\right|\right) +$$

$$+\frac{2\Omega_{2n}}{\Omega_{1n}}\left(arctg\left(\frac{\tau_{n+}}{\sqrt{|\mu_n|}}\right) - arctg\left(\frac{\tau_{n-}}{\sqrt{|\mu_n|}}\right)\right)\theta(\mu_n) +$$

$$+\frac{\Omega_{2n}}{\Omega_{1n}} ln\left|\frac{\left(2y_2 - \sqrt{|\mu_n|}\right)^2 - \xi_n^2}{\left(2y_2 + \sqrt{|\mu_n|}\right)^2 - \xi_n^2}\right|\theta(-\mu_n), Q_n \neq -2, \mu_n \neq 0; \quad (11)$$

$$\sigma_1 = \sqrt{\frac{1+t}{1-t}}, \sigma_2 = \frac{cos\beta}{\sigma_1^2 cos^2\beta + 1}, \xi_n = -\frac{4cos\beta}{2+Q_n}, q_n = \frac{2-Q_n}{2+Q_n},$$

$$\gamma_{1n} = \frac{\xi_n}{\gamma_{4n}}, \gamma_{2n} = \frac{\xi_n^2}{\gamma_{4n}} - \gamma_{3n}, \gamma_{3n} = \frac{q_n - \sigma_1^2}{\gamma_{4n}}, \gamma_{4n} = (q_n - \sigma_1^2)^2 + \xi_n^2\sigma_1^2,$$

$$\nu_n = 4y_2^2 - \xi_n^2, \mu_n = 4q_n - \xi_n^2, \tau_{n\pm} = \xi_n \pm 2y_2,$$

$$\Omega_{1n} = (1-t)^2(Q_n + 2), \Omega_{2n} = \frac{2(2\gamma_{2n} - \xi_n\gamma_{1n} + 1)t - 2}{\sqrt{|\mu_n|}},$$

$$y_1 = arctg\left(\frac{y_2}{\sigma_1}\right), y_2 = \frac{w_1 + \sqrt{1+w_1^2} - 1}{w_1 + \sqrt{1+w_1^2} + 1}, y_3 = ln\left|\frac{1 - y_2 cos\beta}{1 + y_2 cos\beta}\right|. \quad (12)$$

Here $\theta(\eta)$ is Heaviside function.

4 Numerical results and applications

For example, if $n_e \sim 10^{23}$ cm^{-3}, $\hbar\omega \sim 0.1$ MeV (hard X-region), $B \sim 10^{13}$ Gs (close to the pole of a neutron star), then $d\varphi/dl \sim 10^2 - 10^3$ rad/cm at the resonance. Besides: 1. Compton rotation can change its sign (like nuclear spin precession of neutrons [1]), that's why the addition of Compton and Faraday rotation can give zero at some ω, B. 2. The increase of β leads to the decrease of the resonant frequency ω_R, but the increase of B leads to the increase of ω_R; in both cases the value of $d\varphi/dl$ decreases at the resonance. In order to obtain more realistic formula for $d\varphi/dl$, finite temperatures must be considered, though the procedure of averaging over p_z becomes more complicated.

Compton rotation is important in some astrophysical problems. One can estimate n_e and the degree of ionization of cosmic plasma from the formula for $d\varphi/dl$ where other quantities can be measured or estimated: 1. The value of ϕ can be measured at different ω. 2. B, T can be estimated by different methods. 3. If $B > 10^{10}$ Gs, then the degree of ionization is about unity, almost all electrons are free and Faraday rotation is absent; otherwise,if $B < 10^9$ Gs, the difference of estimations of n_e from the formulas for $d\varphi/dl$ in cases of Faraday and Compton rotation helps to estimate the degree of ionization.

Besides, photon magnetic splitting becomes very important at $B \sim 10^{12} - 10^{13}$ Gs, that's why Compton rotation dominates at $B \sim 10^{10} - 10^{11}$ Gs in comparison with photon splitting and Faraday rotation.

5 Summary. The main results

Considering the finite width of resonance on intermediate Landau level for a virtual electron, in the framework of tree approximation a formula is obtained for the calculation of Compton rotation angle of the plane of linear polarization of photons per unit path in electron gas with high degree of spin polarization of electrons. Averaging on the momenta of electrons is performed in zero temperature approximation, where integration is performed for S-diagram of Compton scattering.

References

[1] V.G. Baryshevskii. *Nuclear Optics of Polarized Media* [in Russian] (Energoatomizdat, Moscow, 1995).

[2] V.M. Lobashov *et al.*,[in Russian] Sov. JETP Lett. **14** (1971) 373.

[3] V.M. Lobashov *et al.*,[in Russian] Sov. JETP **68** (1975) 1220.

[4] P. Bock and P. Luksch, Lett. Nuovo cimento **2** (1972) 1081.

[5] A.I. Sery. To the Problem of Compton Rotation of the Plane of Polarization of X-photons in Magnetic field // Actual Problems of Microworld Physics: Proceedings of International School-Seminar, Gomel, Belarus, August 1–12, 2011, (Dubna, 2013) 230.

[6] P.I. Fomin and R.I. Kholodov, JETP. **90**, 2 (2000) 281.

[7] L.D. Landau, E.M. Lifshitz. *Quantum Mechanics (Course of theoretical physics, Vol 3, 3rd ed.)* [transl. from the Russian by J.B. Sykes and J.S. Bell] (Pergamon Press, 1977).

3 Soft and Hard QCD Processes

The QCD analysis of xF_3 structure function based on the analytic approach

A. V. Sidorov *
Bogoliubov Laboratory of Theoretical Physics, JINR, 141980 Dubna, Russia
O. P. Solovtsova †
Gomel State Technical University, 246746 Gomel, Belarus

Abstract

We apply analytic perturbation theory to the QCD analysis of the xF_3 structure function data of the CCFR collaboration. We use a different approaches for the leading order Q^2 evolution of xF_3 structure function and compare the extracted values of the parameter Λ and the shape of the higher twist contribution. Our consideration is based on the Jacobi polynomials expansion method of the unpolarized structure function. The analysis shows that the analytic approach provides a reasonable results in the leading order QCD analysis.

1 Introduction

The data on xF_3 structure function [1] provides a possibility for the precise test of the perturbative QCD predictions for the Q^2 evolution of this structure function. The analysis of xF_3 data simplified because one do not need to parameterize gluon and see quark contributions and could parameterize the shape of the xF_3 structure function itself at some value Q_0^2. For the kinematics region of this data $Q^2 \geq 1.3$ GeV^2 the higher twists contribution (HT) to the structure function should be taken into account.

*E-mail: Sidorov@theor.jinr.ru
†E-mail: olsol@theor.jinr.ru

This allows to study from the above-mentioned data both the perturbative part and HT correction related to each other. Here, we'll focus our attention on the interplay of the different approaches to the strong coupling Q^2-behavior and the x-dependence of the HT contribution.

In our investigation we apply the analytic approach in QCD proposed by Shirkov and Solovtsov [2] the so-called analytic perturbation theory (APT) (see also Refs. [3, 4]). This method takes into account basic principles of local quantum field theory which in the simplest cases is reflected in the form of Q^2-analyticity of the Källén–Lehmann type. The key point of APT constructions—the analytic properties of some functions (the two-point correlator of the quark currents, the moments of the structure functions and so on). A overview of the analytic approach to QCD can be found in Ref. [5]. In the framework of the APT in contrast to the infrared behavior of the perturbative (PT) running coupling, the analytic coupling has no unphysical singularities. At low Q^2 scales, instead of a rapidly changing Q^2 evolution as occurs in the PT case, the APT approach leads to a slowly changing functions (see, e.g., Refs. [6, 7]). In the asymptotic region of large Q^2 the APT and the PT approaches coincide. It should be noted that the moments of the structure functions should be analytic functions in the complex Q^2 plane with a cut along the negative real axis (see Ref. [8] for more details), the ordinary PT description violates analytic properties due to the unphysical singularities of PT coupling. On the other hand, the APT support these analytic properties. For fullness, in our analysis, we consider also the recent variant of the model for the freezing-like behaviour coupling – "massive analytic perturbative QCD" (MPT) [9] (see Ref. [10, 11] for a discussion).

In Refs. [12, 13] was made further development of the APT method – the generalization for the fractional powers of the running coupling which called the Fractional Analytic Perturbation Theory (FAPT) (see Ref. [14] as review). The FAPT technique was applied to analyze the F_2 structure function behavior at small x-values [11, 15], to analyze the low energy data on nucleon spin sum rules $\Gamma_1^{p,n}(Q^2)$ [16], to calculate binding energies and masses of quarkonia [17]. Here, we continue applications of the APT/FAPT approach executing the data on xF_3 structure function and investigating how the analytic approach works in this case by comparison with the standard PT analysis.

2 The Method of the QCD analysis

In our analysis we'll follow the well known approach based on the Jacobi polynomial expansion of structure functions. This method of solution of the DGLAP equation was proposed in Ref. [18] and developed both for unpolarized [19] and polarized cases [20]. The main formula of this method allows approximate reconstruction of the structure function through a finite number of Mellin moments of the structure function

$$xF_3^{N_{max}}(x,Q^2) = \frac{h(x)}{Q^2} + x^\alpha(1-x)^\beta \sum_{n=0}^{N_{max}} \Theta_n^{\alpha,\beta}(x) \sum_{j=0}^{n} c_j^{(n)}(\alpha,\beta) M_{j+2}\left(Q^2\right). \tag{1}$$

The Q^2-evolution of the moments $M_N(Q^2)$ in the leading order (LO) perturbative QCD is defined by

$$M_N^{QCD}(Q^2) = \left[\frac{\alpha_s(Q^2)}{\alpha_s(Q_0^2)}\right]^{\frac{\gamma^{(0),N}}{2\beta_0}} M_N^{QCD}(Q_0^2), \quad N = 2,\ 3, \ldots . \tag{2}$$

Here $\alpha_s(Q^2)$ is the QCD running coupling, $\gamma^{(0),N}$ are the nonsinglet leading order anomalous dimensions, $\beta_0 = 11 - 2n_f/3$ is the first coefficient of the renormalization group β-function, n_f denotes the number of active flavors.

Unknown coefficients $M_N^{QCD}(Q_0^2)$ in Eq. (2) could be parameterized as the Mellin moments of some function:

$$M_3^{QCD}(N,Q_0^2) = \int_0^1 dx x^{N-2} A x^a (1-x)^b (1+\gamma\ x), \quad N = 2,3,\ldots\ . \tag{3}$$

The shape of the function $h(x)$ as well as parameters A, a, b, γ, and $\Lambda_{\rm QCD}$ are found by fitting the experimental data on the $xF_3(x,Q^2)$ structure function [1]. Detailed description of the fitting procedure could be found in Ref. [21]. The terms $h(x)/Q^2$ considered as pure phenomenological. The target mass corrections are taken into account to the order $o(M_{nucl}^4/Q^4)$.

3 Analytic approach in QCD

The APT method gives the possibility of combining the renormalization group resummation with correct analytic properties in Q^2-variable some

physical quantities and provides also a well-defined algorithm for calculating higher-loop corrections [4]. As the difference between the APT and PT running couplings becomes significant at low Q^2-scales (see, e.g., Fig. 1 in Ref. [6]) that stimulates applications of the analytic approach for a new analysis [5] especially after the generalization of the APT on the fractional powers of the running coupling (see Refs. [14, 22, 23] for further details).

In the framework of the analytic approach the following modification in the standard PT expression (2) for the Q^2-evolution of the moments $M_N(Q^2)$ is required: $[\alpha_{\rm PT}(Q^2)]^\nu \Rightarrow \mathcal{A}_\nu(Q^2)$. It transforms Eq. (2) as follows[1]

$$\mathcal{M}_N^{QCD}(Q^2) = \frac{\mathcal{A}_\nu(Q^2)}{\mathcal{A}_\nu(Q_0^2)}\,\mathcal{M}_N^{QCD}(Q_0^2)\ , \quad \nu \equiv \frac{\gamma^{(0),N}}{2\beta_0}\,, \tag{4}$$

where analytic function $\mathcal{A}_\nu$ is derived from the spectral representation and correspond to the discontinuity of the ν-th power of the PT running coupling

$$\mathcal{A}_\nu(Q^2) \,=\, \frac{1}{\pi}\int_0^\infty \frac{d\sigma}{\sigma + Q^2}\,{\rm Im}\,\left\{\alpha_{\rm PT}^\nu(-\sigma - {\rm i}\varepsilon)\right\}\,. \tag{5}$$

Note that the function $\mathcal{A}_1(Q^2)$ defines the APT running coupling: $\alpha_{\rm APT}(Q^2) \equiv \mathcal{A}_1(Q^2)$. Mathematical tool for numerical calculations of $\mathcal{A}_\nu$ for any $\nu > 0$ up to four-loop order in the perturbative running coupling is given in Ref. [24].

The 'normalized' analytic function $\bar{\mathcal{A}}_\nu = \beta_0\mathcal{A}_\nu/(4\pi)$ in the leading order (LO) has rather simple form (see, e.g., [14]) and can be writhen as

$$\bar{\mathcal{A}}_\nu^{LO}(Q^2) = \left[\bar{a}_{\rm PT}^{LO}(Q^2)\right]^\nu \,-\, \frac{{\rm Li}_\delta(t)}{\Gamma(\nu)}\,, \tag{6}$$

$$ {\rm Li}_\delta(t) = \sum_{k=1}^{\infty}\frac{t^k}{k^\delta}, \quad t = \frac{\Lambda^2}{Q^2}, \quad \delta = 1-\nu,$$

where 'normalized' PT running coupling $\bar{a}_{\rm PT}^{LO}(Q^2) = \beta_0\alpha_{\rm PT}^{LO}(Q^2)/(4\pi) = 1/\left[\ln(Q^2/\Lambda^2)\right]$ and ${\rm Li}_\delta$ is the polylogarithm function. For $\nu = 1$ the expression (6) leads to well-known one-loop APT result [2]

$$\alpha_{\rm APT}^{LO}(Q^2) = \alpha_{\rm PT}^{LO}(Q^2) + \frac{4\pi}{\beta_0}\,\frac{\Lambda^2}{\Lambda^2 - Q^2}\,. \tag{7}$$

[1]Beyond LO see Ref. [11] and discussion therein.

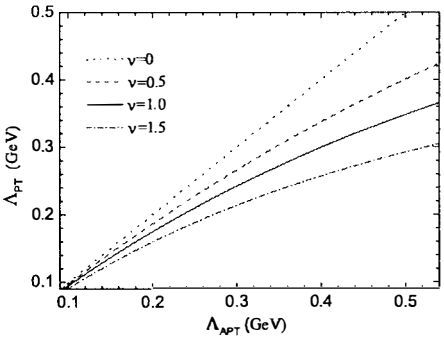

Figure 1: The behavior of the parameter $\Lambda_{\rm PT}$ vs. $\Lambda_{\rm APT}$ in LO for different values of ν at $Q_0^2 = 3$ GeV^2.

One could see, that at large Q^2 the second term in the r.h.s. of (7) is negative. It was confirmed qualitatively in the phenomenological analysis of the xF_3 data in Ref. [25].

It should be stressed that values of the QCD scale parameter Λ are different in PT and APT approaches. In order to illustrate this, in Fig. 1, we present the behavior following from the condition $\left[\alpha_{\rm PT}^{LO}(Q_0^2, \Lambda_{\rm PT})\right]^{\nu} = \mathcal{A}_{\nu}^{LO}(Q_0^2, \Lambda_{\rm APT})$ of the parameter $\Lambda_{\rm PT}$ vs. $\Lambda_{\rm APT}$ for different values of ν.

In short, one-loop modification of the QCD coupling within the MPT approach, which is considered by us further corresponds to the replacement of the logarithm in the $\alpha_{\rm PT}^{LO}(Q^2)$ to the "long logarithm" with the "effective gluonic mass" m_{gl}: $\ln(Q^2/\Lambda^2) \Rightarrow \ln[(Q^2 + m_{gl}^2)/\Lambda^2]$ (see, Refs. [9, 26]).[2]

4 Numerical analysis of experimental data

The results of LO QCD fit in different approaches are presented in Table 1 and Figs. 2–5. Both cases $h(x)$– free and $h(x) = 0$ are considered for $Q_0^2 = 3$ GeV^2, $Q^2 > 1.3$ GeV^2, $n_f = 4$, and $N_{Max} = 12$. In order to reconstruct the x-shape of the HT contribution we have parameterized $h(x)$ in the number of points $x_i = 0.015, 0.045, 0.080, 0.125, 0.175, 0.225,$

[2]The parameter of "effective mass" serves as an infrared regulator and typically of the order $m_{gl} = 500 \pm 200$ MeV (see, e.g., Ref. [27]).

Table 1: The results for the QCD leading order fit (with TMC) of xF_3 data [1] ($Q_0^2 = 3$ GeV^2, $Q^2 > 1$ GeV^2, $n_f = 4$, and $N_{Max} = 12$).

	$h(x) = 0$		$h(x)$–free	
Approach	Λ (MeV)	$\chi^2_{d.f.}$	Λ (MeV)	$\chi^2_{d.f.}$
PT	291 ± 36	1.35	363 ± 170	0.984
APT	275 ± 39	1.42	350 ± 145	0.980
MPT	299 ± 38	1.35	351 ± 128	0.985
"naive" analyt.	417 ± 83	1.34	412 ± 240	0.980

0.275, 0.35, 0.45, 0.55, 0.65 - one per x-bin. The values of A, a, b, γ, x_i and Λ are consider as a free parameter.

As can be seen from the Table 1, the values of Λ's for the case $h(x) = 0$ are smaller in comparison with the case of nonzero HT contribution. The difference of the Λ's values for the APT and PT are smaller in the analysis with HT contribution: $(\Lambda_{\rm PT} - \Lambda_{\rm APT})_{h(x)=0} > (\Lambda_{\rm PT} - \Lambda_{\rm APT})_{h(x)\neq 0}$. The LO $h(x) = 0$ results for Λ's values are consistent within errors. If one add the HT contribution, the values of parameter Λ and their errors are higher than $h(x) = 0$ case. For illustrative purposes we present in the last line of the Table 1 the result corresponding to the use in the analysis of "naive analytization" when the perturbative coupling is replaced by the analytic

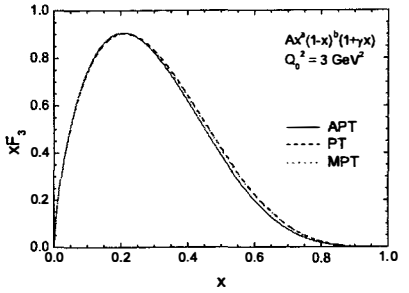

Figure 2: Comparison of parametrizations of xF_3 in PT, APT and MPT approaches for $h(x) = 0$.

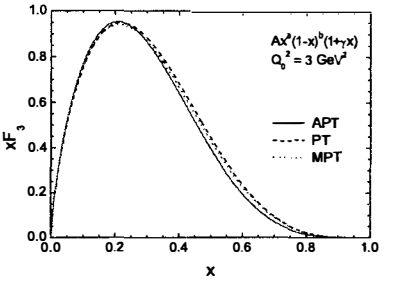

Figure 3: Comparison of parametrizations of xF_3 in PT, APT and MPT approaches for $h(x) \neq 0$.

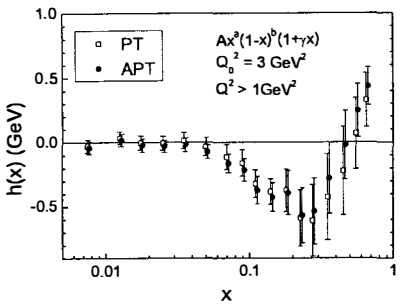

Figure 4: Higher twist contribution resulting from LO QCD analysis of xF_3 data [1] for PT and APT approaches.

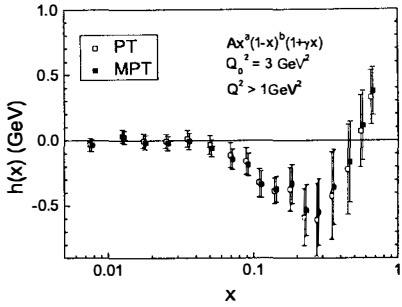

Figure 5: Higher twist contribution resulting from LO QCD analysis of xF_3 data [1] in PT and MPT approaches.

coupling: $\alpha_{\rm PT}(Q^2) \to \alpha_{\rm APT}(Q^2)$ (see Ref. [12] and references therein).

Figures 2–3 show the xF_3-shape obtained in the APT, PT and MPT approaches without taken into account the HT term (Fig. 2) and with the HT (Fig. 3). In both cases, the result for the APT approach slightly higher than for the PT and MPT ones for small x and less for small x.

Figures 4–5 demonstrate HT contributions. From Fig. 4 one can see, that for $x > 0.3$ we obtained $h^{APT}(x) > h^{PT}(x)$. This inequality is in qualitative agreement with the result obtained in LO for the shape of the HT contribution for non-singlet part of F_2 structure function (see Table 3 in Ref. [11]). Opposite inequality we obtain for small values $x < 0.2$: $h^{APT}(x) < h^{PT}(x)$. Figure 5 shows that the central values of $h^{PT}(x)$ and $h^{MPT}(x)$ are very close to each other.

5 Conclusion

We performed the QCD analysis of xF_3 structure function data based on the analytic approach. It should be noted that the wide kinematic region experimental points gave us the possibility to analyze HT contributions of both small and relatively large x and to compare APT and MPT results to the PT one. We have found that in the examined region $Q^2 > 1$ GeV^2 the values of Λ obtained in PT, APT and MPT approaches are close each other. While the "naive analytization" approach leads to the rather large

Λ's value. The shape of HT contributions are in quantitative agreement with the results of the previous analysis of xF_3 structure function data. We made the first step – LO analysis which showed that the analytic approach gives reasonable results. It is important to extend the analysis to higher orders and applied it to the structure function data at low Q^2 region.

Acknowledgments

It is a pleasure for the authors to thank S.V. Mikhailov and O.V. Teryaev for interest in this work and helpful discussions. This work was partly supported by the RFBR grants 11-01-00182 and 13-02-01005 and the BelRFFR-JINR grant F12D-002.

References

[1] CCFR-NuTeV Collab., W.G. Seligman *et al.*, Phys. Rev. Lett. **79**, 1213 (1997).

[2] D.V. Shirkov, I.L. Solovtsov, JINR Rap. Comm. 1996. No. **2**[76]-96, 5 (1996); Phys. Rev. Lett. **79**, 1209 (1997).

[3] K.A. Milton, I.L. Solovtsov, Phys. Rev. D **55**, 5295 (1997).

[4] I.L. Solovtsov, D.V. Shirkov, Theor. Math. Phys. **120**, 1220 (1999).

[5] D.V. Shirkov, I.L. Solovtsov, Theor. Math. Phys. **150**, 132 (2007).

[6] K.A. Milton, I.L. Solovtsov, O.P. Solovtsova, Phys. Rev. D **60**, 016001 (2001).

[7] V.L. Khandramai, R.S. Pasechnik, D.V. Shirkov, O.P. Solovtsova, O.V. Teryaev, Phys. Lett. B **706**, 340 (2012).

[8] I.L. Solovtsov, Part. Nucl. Lett. **4**[101], 10 (2000).

[9] D.V. Shirkov, Phys. Part. Nucl. Lett. **10**, 186 (2013), arXiv:1208.2103 [hep-ph].

[10] F. J. Yndurain, *The Theory of Quark and Gluon Interactions*, 4-th Edition, Springer, Chapt. 4.

[11] A.V. Kotikov, V.G. Krivokhizhin, B.G. Shaikhatdenov, Phys. Atom. Nucl. **75**, 507 (2012).

[12] A.P. Bakulev, S.V. Mikhailov, N.G. Stefanis, Phys. Rev. D **72**, 074014 (2005); *Erratum: ibid.* D **72**, 119908(E) (2005).

[13] A.P. Bakulev, S.V. Mikhailov, N.G. Stefanis, Phys. Rev. D **75**, 056005 (2007); *Erratum: ibid.* D **77**, 079901(E) (2008).

[14] A.P. Bakulev, Phys. Part. Nucl. **40**, 715 (2009).

[15] G. Cvetic, A.Y. Illarionov, B.A. Kniehl, A.V. Kotikov, Phys. Lett. B **679**, 350 (2009).

[16] R.S. Pasechnik, D.V. Shirkov, O.V. Teryaev, O.P. Solovtsova, V.L. Khandramai, Phys. Rev. D **81**, 016010 (2010).

[17] C. Ayala, G. Cvetic, Phys. Rev. D **87**, 054008 (2013).

[18] G. Parisi, N. Sourlas, Nucl. Phys. B **151**, 421 (1979).

[19] I.S. Barker, C.B. Langensiepen, G. Shaw, Nucl. Phys. **B 186**, 61 (1981);
V.G. Krivokhizhin *et al.*, Z. Phys. C **36**, 51 (1987), Z. Phys. C **48**, 347 (1990);
A.V. Kotikov, G. Parente, J. Sanchez-Guillen, Z. Phys. C **58**, 465 (1993);
A.L. Kataev, A.V. Sidorov, Phys. Lett. B **331**, 179 (1994);
A.L. Kataev *et al.*, Phys. Lett. B **388**, 179 (1996);
A.V. Sidorov, Phys. Lett. B **389**, 379 (1996); JINR Rapid Comm. **80** (1996) 11 [hep-ph/9609345].

[20] E. Leader, A.V. Sidorov, D.B. Stamenov, Int. J. Mod. Phys. A **13**, 5573 (1998); Phys. Rev. D **58** (1998) 114028;
C. Bourrely *et al.*, Phys. Lett. B **442** (1998) 479.

[21] A.L. Kataev *et al.*, Phys. Lett. B **417**, 374 (1998).

[22] G. Cvetic, A.V. Kotikov, J. Phys. G **G39**, 065005 (2012).

[23] N.G. Stefanis, Acta Phys. Polon. Supp. **6**, 71 (2013).

[24] A.P. Bakulev, V.L. Khandramai, Comput. Phys. Commun. **184**, 183 (2013).

[25] A.V. Sidorov, Nuovo Cim. A **112**, 1527 (1999).

[26] G. Cvetic, arXiv:1309.1696 [hep-ph].

[27] E.G.S. Luna, A.A. Natale, A.L. dos Santos, Phys. Lett. B **698**, 52 (2011).

Low-energy QCD Calculations with Package "FAPT"

Viacheslav Khandramai*, Dmitry Prokopenko
Gomel State Technical University, Gomel 246746, Belarus

Abstract

We consider computational problems in the framework of non-power Analityc Perturbation Theory and Fractional Analytic Perturbation Theory that are the generalization of the standard QCD perturbation theory. The singularity-free, finite couplings $\mathcal{A}_\nu(Q^2)$, $\mathfrak{A}_\nu(s)$ appear in these approaches as analytic images of the standard QCD coupling powers $\alpha_s^\nu(Q^2)$ in the Euclidean and Minkowski domains, respectively. We provide a package "FAPT" based on the system Mathematica for QCD calculations of the images $\mathcal{A}_\nu(Q^2)$, $\mathfrak{A}_\nu(s)$ up to N^{3}LO of renormalization group evolution. Application of these approaches to Bjorken sum rule analysis and Q^2-evolution of higher twist μ_4^{p-n} is considered.

1 Introduction

The QCD perturbation theory (PT) in the region of space-like momentum transfer $Q^2 = -q^2 > 0$ is based on expansions in a series in powers of the running coupling $\alpha_s(\mu^2 = Q^2)$ which in the one-loop approximation is given by $\alpha_s^{(1)}(Q^2) = (4\pi/b_0)/L$ with b_0 being the first coefficient of the QCD beta function, $L = \ln(Q^2/\Lambda^2)$, and Λ is the QCD scale. The one-loop solution $\alpha_s^{(1)}(Q^2)$ has a pole singularity at $L = 0$ called the Landau pole. The ℓ-loop solution $\alpha_s^{(\ell)}(Q^2)$ of the renormalization group (RG) equation has an ℓ-root singularity of the type $L^{-1/\ell}$ at $L = 0$, which produces the pole as well in the ℓ-order term $d_\ell\, \alpha_s^\ell(Q^2)$. This prevents the application

*E-mail:v.khandramai@gmail.com

of perturbative QCD in the low-momentum space-like regime, $Q^2 \sim \Lambda^2$, with the effect that hadronic quantities, calculated at the partonic level in terms of a power-series expansion in $\alpha_s(Q^2)$, are not everywhere well defined.

In 1997, Shirkov and Solovtsov discovered couplings $\mathcal{A}_1(Q^2)$ free of unphysical singularities in the Euclidean region [1], and Milton and Solovtsov discovered couplings $\mathfrak{A}_1(s)$ in the Minkowski region [2]. Due to the absence of singularities of these couplings, it is suggested to use this systematic approach, called Analytic Perturbation Theory (APT), for all Q^2 and s. The APT yields a sensible description of hadronic quantities in QCD (see reviews [3, 4, 5]), though there are alternative approaches to the singularity of effective charge in QCD — in particular, with respect to the deep infrared region $Q^2 < \Lambda^2$. One of the main advantages of the APT analysis is much faster convergence of the APT nonpower series as compared with the standard PT power series (see [6]). Recently, the analytic and numerical methods, necessary to perform calculations in two- and three-loop approximations, were developed [7, 8, 9]. The APT approach was applied to calculate properties of a number of hadronic processes, including the width of the inclusive τ lepton decay to hadrons [10, 11, 12, 13, 14], the scheme and renormalization-scale dependencies in the Bjorken [15, 16] and Gross–Llewellyn Smith [17] sum rules, the width of Υ meson decay to hadrons [18], meson spectrum [19], etc.

The generalization of APT for the fractional powers of an effective charge was done in [20, 21] and called the Fractional Analytic Perturbation Theory (FAPT). The important advantage of FAPT in this case is that the perturbative results start to be less dependent on the factorization scale. This reminds the results obtained with the APT and applied to the analysis of the pion form factor in the $O(\alpha_s^2)$ approximation, where the results also almost cease to depend on the choice of the renormalization scheme and its scale (for a detailed review see [22] and references therein). The process of the Higgs boson decay into a $b\bar{b}$ pair of quarks was studied within a FAPT-type framework in the Minkowski region at the one-loop level in [23] and within the FAPT at the three-loop level in [21]. The results on the resummation of nonpower-series expansions of the Adler function of scalar D_S and a vector D_V correlators within the FAPT were presented in [24]. The interplay between higher orders of the perturbative QCD expansion and higher-twist contributions in the analysis of recent Jefferson Lab data on the lowest moment of the spin-

dependent proton structure function, $\Gamma_1^p(Q^2)$, was studied in [25] using both the standard PT and APT/FAPT. The FAPT technique was also applied to analyse the structure function $F_2(x)$ behavior at small values of x [26, 27] and calculate binding energies and masses of quarkonia [28]. All these successful applications of APT/FAPT necessitate to have a reliable mathematical tool for extending the scope of these approaches. In this paper, we present the theoretical background which is necessary for the running of $\mathcal{A}_\nu[L]$ and $\mathfrak{A}_\nu[L]$ in the framework of APT and its fractional generalization, FAPT, and which is collected in the easy-to-use Mathematica package "FAPT" [29]. This task has been partially realized for APT as the `Maple` package `QCDMAPT` in [30] and as the `Fortran` package `QCDMAPT_F` in [31]. We have organized "FAPT" in the same manner as the well-known package "RunDec" [32]. A few examples of APT and FAPT applications are given.

2 Theoretical framework

Let us start with the standard definitions used in "FAPT" for standard PT calculations. The QCD running coupling, $\alpha_s(\mu^2) = \alpha_s[L]$ with $L = \ln[\mu^2/\Lambda^2]$, is defined through

$$\frac{d\alpha_s[L]}{dL} = \beta\left(\alpha_s[L]; n_f\right) = -\alpha_s[L] \sum_{k\geq 0} b_k(n_f) \left(\frac{\alpha_s[L]}{4\pi}\right)^{k+1}, \quad (1)$$

where n_f is the number of active flavours. The β-function coefficients are given by (see [33])

$$\begin{aligned}
b_0(n_f) &= 11 - \frac{2}{3} n_f\,, \\
b_1(n_f) &= 102 - \frac{38}{3} n_f\,, \\
b_2(n_f) &= \frac{2857}{2} - \frac{5033}{18} n_f + \frac{325}{54} n_f^2\,, \\
b_3(n_f) &= \frac{149753}{6} + 3564\,\zeta_3 - \left[\frac{1078361}{162} + \frac{6508}{27}\,\zeta_3\right] n_f \\
&\quad + \left[\frac{50065}{162} + \frac{6472}{81}\,\zeta_3\right] n_f^2 + \frac{1093}{729} n_f^3\,. \qquad (2)
\end{aligned}$$

ζ is Riemann's zeta function. We introduce the following notation:

$$\beta_f \equiv \frac{b_0(n_f)}{4\pi}, \quad a(\mu^2; n_f) \equiv \beta_f \, \alpha_s(\mu^2; n_f) \quad \text{and} \quad c_k(n_f) \equiv \frac{b_k(n_f)}{b_0(n_f)^{k+1}}. \quad (3)$$

Then Eq. (1) in the l-loop approximation can be rewritten as:

$$\frac{da_{(\ell)}[L; n_f]}{dL} = -\left(a_{(\ell)}[L; n_f]\right)^2 \left[1 + \sum_{k\geq 1}^{\ell} c_k(n_f) \left(a_{(\ell)}[L; n_f]\right)^k\right]. \quad (4)$$

In the one-loop ($\ell = 1$) approximation ($c_k(n_f) = b_k(n_f) = 0$ for all $k \geq 1$) we have the solution

$$a_{(1)}[L] = \frac{1}{L} \quad (5)$$

with the Landau pole singularity at $L \to 0$. In the two-loop ($\ell = 2$) approximation ($c_k(n_f) = b_k(n_f) = 0$ for all $k \geq 2$) the exact solution of Eq. (1) is also known [34]

$$a_{(2)}[L; n_f] = \frac{-c_1^{-1}(n_f)}{1 + W_{-1}(z_W[L])} \quad \text{with} \quad z_W[L] = -c_1^{-1}(n_f)\, e^{-1-L/c_1(n_f)}, \quad (6)$$

where $W_{-1}[z]$ is the appropriate branch of the Lambert function.

The three- ($c_k(n_f) = b_k(n_f) = 0$ for all $k \geq 3$) and higher-loop solutions $a_{(\ell)}[L; n_f]$ can be expanded in powers of the two-loop one, $a_{(2)}[L; n_f]$, as has been suggested and investigated in [8, 9, 14]:

$$a_{(\ell)}[L; n_f] = \sum_{n\geq 1} C_n^{(\ell)} \left(a_{(2)}[L; n_f]\right)^n. \quad (7)$$

The coefficients $C_n^{(\ell)}$ can be evaluated recursively. As has been shown in [9], this expansion has a finite radius of convergence, which appears to be sufficiently large for all values of n_f of practical interest. Note here that this method of expressing the higher-ℓ-loop coupling in powers of the two-loop one is equivalent to the 't Hooft scheme, where one puts by hand all coefficients of the β-function, except b_0 and b_1, equal to zero and effectively takes into account all higher coefficients b_i by redefining perturbative coefficients d_i (see for more detail [35]).

The basic objects in the Analytic approach are the analytic couplings in the Euclidian $\mathcal{A}_\nu^{(\ell)}[L; n_f]$ and Minkowskian $\mathfrak{A}_\nu^{(\ell)}[L_s; n_f]$ domains calculated

with the spectral densities $\rho_\nu^{(\ell)}(\sigma; n_f)$ which enter into the Källen–Lehmann spectral representation:

$$\mathcal{A}_\nu^{(\ell)}[L; n_f] = \int_0^\infty \frac{\rho_\nu^{(\ell)}(\sigma; n_f)}{\sigma + Q^2}\, d\sigma = \int_{-\infty}^\infty \frac{\rho_\nu^{(\ell)}[L_\sigma; n_f]}{1 + \exp(L - L_\sigma)}\, dL_\sigma\,, \quad (8)$$

$$\mathfrak{A}_\nu^{(\ell)}[L_s; n_f] = \int_s^\infty \frac{\rho_\nu^{(\ell)}(\sigma; n_f)}{\sigma}\, d\sigma = \int_{L_s}^\infty \rho_\nu^{(\ell)}[L_\sigma; n_f]\, dL_\sigma\,. \quad (9)$$

It is convenient to use the following representation for spectral functions:

$$\rho_\nu^{(\ell)}[L; n_f] \equiv \frac{1}{\pi}\, \mathbf{Im}\left(\alpha_{\rm s}^{(\ell)}\,[L - i\pi; n_f]\right)^\nu = \frac{\sin[\nu\, \varphi_{(\ell)}[L; n_f]]}{\pi\, (\beta_f\, R_{(\ell)}[L; n_f])^\nu}\,. \quad (10)$$

In the one-loop approximation the corresponding functions have the simplest form

$$\varphi_{(1)}[L] = \arccos\left(\frac{L}{\sqrt{L^2 + \pi^2}}\right)\,, \quad R_{(1)}[L] = \sqrt{L^2 + \pi^2}\,, \quad (11)$$

whereas at the two-loop order they have a more complicated form

$$R_{(2)}[L; n_f] = c_1(n_f)\left|1 + W_1\left(z_W[L - i\pi; n_f]\right)\right|, \quad (12)$$

$$\varphi_{(2)}[L; n_f] = \arccos\left[\mathbf{Re}\left(\frac{-R_{(2)}[L; n_f]}{1 + W_1\left(z_W[L - i\pi; n_f]\right)}\right)\right] \quad (13)$$

with $W_1[z]$ being the appropriate branch of Lambert function.

In the three- ($\ell = 3$) and four-loop ($\ell = 4$) approximation we use Eq. (7) and then obtain

$$R_{(\ell)}[L] = \left|\frac{e^{i\,\varphi_{(2)}[L]}}{R_{(2)}[L]} + \sum_{k\geq 3} C_k^{(\ell)}\, \frac{e^{i\,k\,\varphi_{(2)}[L]}}{R_{(2)}^k[L]}\right|^{-1}\,, \quad (14)$$

$$\varphi_{(\ell)}[L] = \arccos\left[\frac{R_{(\ell)}[L]\cos\left(\varphi_{(2)}[L]\right)}{R_{(2)}[L]} + \sum_{k\geq 3} C_k^{(\ell)}\, \frac{R_{(\ell)}[L]\cos\left(k\,\varphi_{(2)}[L]\right)}{R_{(2)}^k[L]}\right] \quad (15)$$

Here we do not show explicitly the n_f dependence of the corresponding quantities — it goes inside through $R_{(2)}[L] = R_{(2)}[L; n_f]$, $\varphi_{(2)}[L] = \varphi_{(2)}[L; n_f]$, $C_k^{(3)} = C_k^{(3)}[n_f]$, $C_k^{(4)} = C_k^{(4)}[n_f]$, $c_k = c_k(n_f)$. The Figure 1

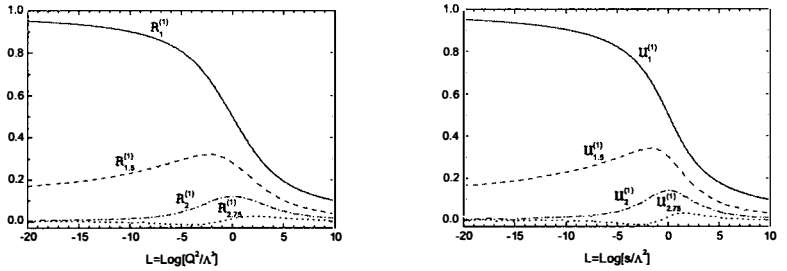

Figure 1: The one-loop analytic functions $\mathcal{A}_\nu^{(1)}[L]$ (left) and $\mathfrak{A}_\nu^{(1)}[L]$ (right) for $n_f = 3$ and different values of ν.

shows the behavior of the one-loop analytic images in the space- and time-like domains for different values of ν. It should be note the following properties of the one-loop $\mathcal{A}_\nu[L]$ and $\mathfrak{A}_\nu[L]$:

$$\mathcal{A}_0[L] = \mathfrak{A}_0[L] = 1; \tag{16}$$

$$\mathcal{A}_m[\pm\infty] = \mathfrak{A}_m[\pm\infty] = 0 \quad \text{for} \quad m \geq 2\,,\ m \in \mathbb{N}; \tag{17}$$

$$\begin{pmatrix} \mathcal{A}_m[-L] \\ \mathfrak{A}_m[-L] \end{pmatrix} = (-1)^m \begin{pmatrix} \mathcal{A}_m[L] \\ \mathfrak{A}_m[L] \end{pmatrix} \quad \text{for} \quad m \geq 2\,, m \in \mathbb{N}; \tag{18}$$

$$\begin{pmatrix} \mathcal{A}_{-m}[L] \\ \mathfrak{A}_{-m}[L] \end{pmatrix} = \begin{pmatrix} L^m \\ \frac{1}{\pi(m+1)}\,\mathbf{Im}\left[(L+i\pi)^{m+1}\right] \end{pmatrix} \quad \text{for} \quad m \geq 2\,, m \in \mathbb{N}\,. \tag{19}$$

Thus, "inverse powers" $\mathcal{A}_{-m}[L] = L^m$ coincide with the inverse powers of the effective charge $a^{-m}[L] = L^m$, while for the "inverse degrees" arise additions in the form of lower degree L with π^2-factors in the Minkowski domain.

The package "FAPT" performs the calculations of the basic required objects: $\left(\alpha_s^{(\ell)}[L, n_f]\right)^\nu$ in Eqs. (5), (6) and (7), $\mathcal{A}_\nu^{(\ell)}[L, n_f]$ in Eq. (8) and $\mathfrak{A}_\nu^{(\ell)}[L, n_f]$ in Eq. (9) up to the N^{3}LO approximation ($\ell = 4$) with a fixed number of active flavours n_f and the global one with taking into account all heavy-quark thresholds (for more details and description of procedures see [29]). As an example, we present here the following **Mathematica** realizations for analytic coupling $\mathcal{A}_\nu^{(\ell)}[L, n_f]$ and $\mathfrak{A}_\nu^{(\ell)}[L, n_f]$:

- `AcalBarℓ[L,Nf,Nu]` computes the ℓ-loop n_f-fixed analytic coupling $\mathcal{A}_\nu^{(\ell)}[L, n_f]$ in the Euclidean domain, where the logarithmic argument

L=ln[Q^2/Λ^2], the number of active flavors Nf=n_f, and the power index Nu=ν;

- UcalBarℓ[L,Nf,Nu] computes the ℓ-loop n_f-fixed analytic coupling $\mathfrak{A}_\nu^{(\ell)}[L, n_f]$ in the Minkowski domain, where the logarithmic argument L=ln[s/Λ^2], the number of active flavors Nf=n_f, and the power index Nu=ν.

3 APT and FAPT applications

As an example of the APT application, we present the Bjorken sum rule (BSR) analysis (see for more details [39]). The BSR claims that the difference between the proton and neutron structure functions integrated over all possible values

$$\Gamma_1^{p-n}(Q^2) = \int_0^1 \left[g_1^p(x,Q^2) - g_1^n(x,Q^2)\right] dx\,, \tag{20}$$

of the Bjorken variable x in the limit of large momentum squared of the exchanged virtual photon at $Q^2 \to \infty$ is equal to $g_A/6$, where the nucleon axial charge $g_A = 1.2701 \pm 0.0025$ [33]. Commonly, one represents the Bjorken integral in Eq. (20) as a sum of perturbative and higher twist contributions

$$\Gamma_1^{p-n}(Q^2) = \frac{g_A}{6}\left[1 - \Delta_{\rm Bj}(Q^2)\right] + \sum_{i=2}^{\infty} \frac{\mu_{2i}^{p-n}}{Q^{2i-2}}\,. \tag{21}$$

The perturbative QCD correction $\Delta_{\rm Bj}(Q^2)$ has a form of the power series in the QCD running coupling $\alpha_{\rm s}(Q^2)$. At the up-to-date four-loop level in the massless case in the modified minimal subtraction ($\overline{\rm MS}$) scheme, for three active flavors, $n_f = 3$, it looks like [36]

$$\Delta_{\rm Bj}^{\rm PT}(Q^2) = 0.3183\,\alpha_{\rm s}(Q^2) + 0.3631\,\alpha_{\rm s}^2(Q^2) + 0.6520\,\alpha_{\rm s}^3(Q^2) + 1.804\,\alpha_{\rm s}^4(Q^2). \tag{22}$$

The perturbative representation (22) violates analytic properties due to the unphysical singularities of $\alpha_{\rm s}(Q^2)$. To resolve the issue, we apply APT. In particular, the four-loop APT expansion for the perturbative part $\Delta_{\rm Bj}^{\rm PT}(Q^2)$ is given by the formal replacement

$$\Delta_{\rm Bj}^{\rm PT}(Q^2) = \sum_{k\le 4} c_k\,\alpha_{\rm s}^k(Q^2) \quad \Rightarrow \quad \Delta_{\rm Bj}^{\rm APT}(Q^2) = \sum_{k\le 4} c_k\,\mathcal{A}_k(Q^2)\,. \tag{23}$$

Clearly, at low Q^2 a value of α_s is quite large, questioning the convergence of perturbative QCD series (22). The qualitative resemblance of the coefficients pattern to the factorial growth did not escape our attention although more definite statements, if possible, would require much more efforts. This observation allows one to estimate the value of $\alpha_s \sim 1/3$ providing a similar magnitude of three- and four- loop contributions to the BSR. To test that, we present in Figures 2 and 3 the relative contributions of separate i-terms in the four-loop expansion in Eq. (22) for the PT case and in Eq. (23) for APT. As it is seen from Figure 2, in the

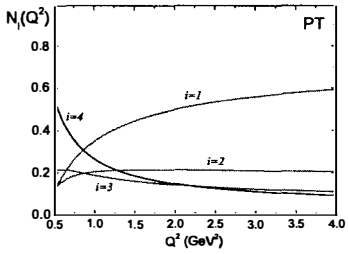

Figure 2: The Q^2-dependence of the relative contributions at the four-loop level in the PT approach.

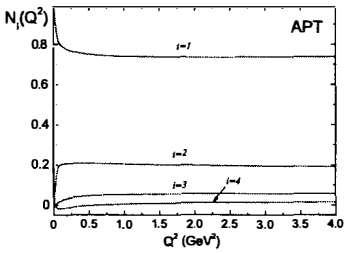

Figure 3: The Q^2-dependence of the relative contributions of the perturbative expansion terms in Eq. (23) in the APT approach.

region $Q^2 < 1\,\mathrm{GeV}^2$ the dominant contribution to the pQCD correction $\Delta_{\mathrm{Bj}}(Q^2)$ comes from the four-loop term $\sim \alpha_s^4$. Moreover, its relative contribution increases with decreasing Q^2. In the region $Q^2 > 2\,\mathrm{GeV}^2$ the situation changes – the major contribution comes from one- and two-loop orders there. Analogous curves for the APT series given by Eq. (23) are presented in Figure 3.

Figures 2 and 3 demonstrate the essential difference between the PT and APT cases, namely, the APT expansion obeys much better convergence than the PT one. In the APT case, the higher order contributions are stable at all Q^2 values, and the one-loop contribution gives about 70 %, two-loop – 20 %, three-loop – not exceeds 5%, and four-loop – up to 1 %.

One can see that the four-loop PT correction becomes equal to the three-loop one at $Q^2 = 2\,\mathrm{GeV}^2$ and noticeably overestimates it (note that the slopes of these contributions are quite close in the relatively wide Q^2 region) for $Q^2 \sim 1\,\mathrm{GeV}^2$ which may be considered as an extra argument supporting an asymptotic character of the PT series in this region. In the APT case, the contribution of the higher loop corrections is not so large as in the PT one. The four-loop order in APT can be important, in principle, if the theoretical accuracy to better than 1 % will be required.

Now we briefly discuss how the APT applications affect the values of the higher-twist coefficients μ_{2i}^{p-n} in Eq. (21) extracted from Jlab data. Previously, a detailed higher-twist analysis of the four-loop expansions in powers of α_s was performed in [39]. In Figures 4 and 5 we present the results of 1- and 3-parametric fits in various orders of the PT and APT. The corresponding fit results for higher twist terms μ_{2i}^{p-n}, extracted in different orders of the PT and APT, are given in Table 1 (all numerical results are normalized to the corresponding powers of the nucleon mass M). From

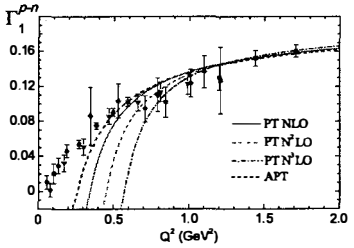

Figure 4: The one-parametric μ_4^{p-n}-fits of the BSR JLab data in various (NLO, N^{2}LO, N^{3}LO) orders of the PT and the all-order APT expansions.

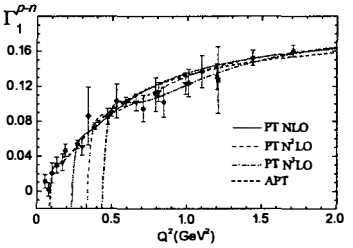

Figure 5: The three-parametric $\mu_{4,6,8}^{p-n}$-fits of the BSR JLab data in various (NLO, N^{2}LO, N^{3}LO) orders of the PT and the all-order APT expansions.

these figures and Table 1 one can see that APT allows one to move down up to $Q^2 \sim 0.1\,\mathrm{GeV}^2$ in description of the experimental data [39]. At the same time, in the framework of the standard PT the lower border shifts up to higher Q^2 scales when increasing the order of the PT expansion. This is caused by extra unphysical singularities in the higher-loop strong coupling. It should be noted that the magnitude of μ_4^{p-n}/M^2 decreases

Table 1: Results of higher twist extraction from the JLab data on BSR in various (NLO, N^2LO, N^3LO) orders of the PT and all orders of APT.

Method	Q^2_{min},	μ_4^{p-n}/M^2	μ_6^{p-n}/M^4	μ_8^{p-n}/M^6
The best μ_4^{p-n}-fit results				
PT NLO	0.5	−0.028(5)	–	–
PT N^2LO	0.66	−0.014(7)	–	–
PT N^3LO	0.71	0.006(9)	–	–
APT	0.47	−0.050(4)	–	–
The best $\mu_{4,6,8}^{p-n}$-fit results				
PT NLO	0.27	−0.03(1)	−0.01(1)	0.008(4)
PT N^2LO	0.34	0.01(2)	−0.06(4)	0.04(2)
PT N^3LO	0.47	0.05(4)	−0.2(1)	0.12(6)
APT	0.08	−0.061(4)	0.009(1)	−0.0004(1)

with an order of the PT and becomes compatible to zero at the four-loop level. It is interesting to mention that a similar decreasing effect has been found in the analysis of the experimental data for the neutrino-nucleon DIS structure function xF_3 [37] and for the charged lepton-nucleon DIS structure function F_2 [38].

Consider the application of the FAPT approach by the example of the RG-evolution of the non-singlet higher-twist $\mu_4^{p-n}(Q^2)$ in Eq. (21). The evolution of the higher-twist terms $\mu_{6,8,...}^{p-n}$ is still unknown. The RG-evolution of $\mu_4^{p-n}(Q^2)$ in the standard PT reads

$$\mu_{4,PT}^{p-n}(Q^2) = \mu_{4,PT}^{p-n}(Q_0^2)\left[\frac{\alpha_s(Q^2)}{\alpha_s(Q_0^2)}\right]^{\nu}, \tag{24}$$

$$\nu = \gamma_0/\left(8\pi\beta_0\right), \gamma_0 = \frac{16}{3}C_F, C_F = \frac{4}{3}. \tag{25}$$

In the framework of FAPT the corresponding expression reads as follows:

$$\mu_{4,APT}^{p-n}(Q^2) = \mu_{4,APT}^{p-n}(Q_0^2)\frac{\mathcal{A}_\nu^{(1)}(Q^2)}{\mathcal{A}_\nu^{(1)}(Q_0^2)}. \tag{26}$$

We present in Table 2 the best fits for $\mu_4^{p-n}(Q_0^2)$ taking into account the corresponding RG-evolution with $Q_0^2 = 1\,\mathrm{GeV}^2$ as a normalization point

Table 2: Results of higher twist extraction from the JLab data on BSR with inclusion and without inclusion of the RG-evolution of $\mu_4^{p-n}(Q^2)$ normalized at $Q_0^2 = 1\,\mathrm{GeV}^2$.

Method	Q^2_{min}, GeV^2	μ_4^{p-n}/M^2	μ_6^{p-n}/M^4	μ_8^{p-n}/M^6
	0.47	−0.055(3)	0	0
NNLO APT	0.17	−0.062(4)	0.008(2)	0
no evolution	0.10	−0.068(4)	0.010(3)	−0.0007(3)
	0.47	−0.051(3)	0	0
NNLO APT	0.17	−0.056(4)	0.0087(4)	0
with evolution	0.10	−0.058(4)	0.0114(6)	−0.0005(8)

and without the RG-evolution. We do not take into account the RG-evolution in μ_4^{p-n} for the standard PT calculations and compare with FAPT since the only effect of that would be the enhancement of the Landau singularities by extra divergencies at $Q^2 \sim \Lambda^2$, whereas at higher $Q^2 \sim 1\,\mathrm{GeV}^2$ the evolution is negligible with respect to other uncertainties. We see from Table 2 that the fit results become more stable with respect to Q_{min} variations, which reduces the theoretical uncertainty of the BSR analysis.

4 Summary

To summarize, APT and FAPT are the closed theoretical schemes without unphysical singularities and additional phenomenological parameters which allow one to combine RG-invariance, Q^2-analyticity, compatibility with linear integral transformations and essentially incorporate nonperturbative structures. The APT provides a natural way for the coupling constant and related quantities. These properties of the coupling constant are the universal loop-independent infrared limit and weak dependence on the number of loops. At the same time, FAPT provides an effective tool to apply the Analytic approach for RG improved perturbative amplitudes. This approaches are used in many applications. In particular, in this paper we consider the application of APT and FAPT to the RG-evolution of nonsinglet structure functions and Bjorken sum rule higher-twist analysis at the scale $Q^2 \sim \Lambda^2$ considered.

The singularity-free, finite couplings $\mathcal{A}_\nu(Q^2), \mathfrak{A}_\nu(s)$ appear in APT/FAPT as analytic images of the standard QCD coupling powers $\alpha_s^\nu(Q^2)$ in the Euclidean and Minkowski domains, respectively. In this paper, we presented the theoretical background, used in a package "FAPT" [29] based on the system Mathematica for QCD calculations in the framework of APT/FAPT, which are needed to compute these couplings up to N^{3}LO of the RG running. We hope that this will expand the use of these approaches.

Acknowledgments

I would like to thank Alexander Bakulev, Sergei Mikhailov and Andrei Kataev for stimulating discussions and useful remarks. This work was supported in part by the Belarussian state fundamental research programm "Convergency", BelRFBR grants under Grant No. F12D-002 and No. F13M-143 and by RFBR Grant No. 11-01-00182.

References

[1] D.V.Shirkov, I.L. Solovtsov, Phys. Rev. Lett. **79**, 1209 (1997).

[2] K.A. Milton, I.L. Solovtsov, Phys. Rev. **D55**, 5295 (1997).

[3] I.L. Solovtsov, D.V. Shirkov, Theor. Math. Phys. **120**, 1220 (1999).

[4] D.V. Shirkov, Theor. Math. Phys. **127**, 409 (2001).

[5] D.V. Shirkov, I.L. Solovtsov, Theor. Math. Phys. **150**, 132 (2007).

[6] D.V. Shirkov, Nucl. Phys. Proc. Suppl. **225-227**, 5 (2012).

[7] B.A. Magradze, Int. J. Mod. Phys. **A15**, 2715 (2000).

[8] D.S. Kourashev, B.A. Magradze, Theor. Math. Phys. **135**, 531 (2003).

[9] B.A. Magradze, Few Body Syst. **40**, 71 (2006).

[10] K.A. Milton, I.L. Solovtsov, O.P. Solovtsova, V.I. Yasnov, Eur. Phys. J. **C14**, 495 (2000).

[11] K.A. Milton, I.L. Solovtsov, O.P. Solovtsova, Phys. Rev. **D65**, 076009 (2002).

[12] G. Cvetic, C. Valenzuela, Phys. Rev. **D74**, 114030 (2006).

[13] G. Cvetic, R. Kogerler, C. Valenzuela, J. Phys. **G37**, 075001 (2010).

[14] B.A. Magradze, Few Body Syst. **48**, 143 (2010).

[15] K.A. Milton, I.L. Solovtsov, O.P. Solovtsova, Phys. Lett. **B439**, 421 (1998).

[16] R.S. Pasechnik, D.V. Shirkov, O.V. Teryaev, Phys. Rev. **D78**, 071902 (2008).

[17] K.A. Milton, I.L. Solovtsov, O.P. Solovtsova, Phys. Rev. **D60**, 016001 (1999).

[18] D.V. Shirkov, A.V. Zayakin, Phys. Atom. Nucl. **70**, 775 (2007).

[19] M. Baldicchi, A.V. Nesterenko, G.M. Prosperi, D.V. Shirkov, C. Simolo, Phys. Rev. Lett. **99**, 242001 (2007).

[20] A.P. Bakulev, S.V. Mikhailov, N.G. Stefanis, Phys. Rev. **D72**, 074014 (2005); *Erratum: ibid.* **D72**, 119908(E) (2005).

[21] A.P. Bakulev, S.V. Mikhailov, N.G. Stefanis, Phys. Rev. **D75**, 056005 (2007); *Erratum: ibid.* **D77**, 079901(E) (2008).

[22] A.P. Bakulev, Phys. Part. Nucl. **40**, 715 (2009).

[23] D.J. Broadhurst, A.L. Kataev, C.J. Maxwell, Nucl. Phys. **B592**, 247 (2001).

[24] A.P. Bakulev, S.V. Mikhailov, N.G. Stefanis, JHEP **1006**, 085 (2010).

[25] R.S. Pasechnik, D.V. Shirkov, O.V. Teryaev, O.P. Solovtsova, V.L. Khandramai, Phys. Rev. **D81**, 016010 (2010).

[26] G. Cvetic, A.Y. Illarionov, B.A. Kniehl, A.V. Kotikov, Phys. Lett. **B679**, 350 (2009).

[27] A.V. Kotikov, V.G. Krivokhizhin, B.G. Shaikhatdenov, Phys. Atom. Nucl. **75**, 507 (2012).

[28] C. Ayala, G. Cvetic, Phys. Rev. **D87**, 054008 (2013).

[29] A.P. Bakulev, V.L. Khandramai, Comput. Phys. Commun. **184**, 183 (2013).

[30] A.V. Nesterenko, C. Simolo, Comput. Phys. Commun. **181**, 1769 (2010).

[31] A.V. Nesterenko, C. Simolo, Comput. Phys. Commun. **182**, 2303 (2011).

[32] K.G. Chetyrkin, J.H. Kühn, M. Steinhauser, Comput. Phys. Commun. **133**, 43 (2000).

[33] J. Beringer *et al.* (Particle Data Group Collaboration), Phys. Rev. **D86**, 010001 (2012).

[34] E. Gardi, G. Grunberg, M. Karliner, JHEP **07**, 007 (1998).

[35] A.V. Garkusha, A.L. Kataev, Phys. Lett. **B705**, 400 (2011).

[36] P.A. Baikov, K.G. Chetyrkin, J.H. Kühn, Phys. Rev. Lett. **104**, 132004 (2010).

[37] A.L. Kataev, G. Parente, A.V. Sidorov, Phys. Part. Nucl. **34**, 20 (2003).

[38] J. Blumlein, Prog. Part. Nucl. Phys. **69**, 28 (2013).

[39] V.L. Khandramai, R.S. Pasechnik, D.V. Shirkov, O.P. Solovtsova, O.V. Teryaev, Phys. Lett. **B706**, 340 (2012).

A high statistics study of the beta-function in the SU(2) lattice theory

S. S. Antropov*, V. V. Skalozub†
Oles Honchar Dnipropetrovsk National University,
Dnipropetrovsk, Ukraine
O. A. Mogilevsky‡
Bogolyubov Institute for Theoretical Physics of the National Academy
of Sciences of Ukraine, Kiev, Ukraine

Abstract

The beta-function is investigated on the lattice in $SU(2)$ gluodynamics. It is determined within a scaling hypothesis while a lattice size fixed to be taken into account. The functions calculated are compared with the ones obtained in the continuum limit. Graphics processing units (GPU) are used as a computing platform that allows gathering a huge amount of statistical data. Numerous beta-functions are analyzed for various lattices. The coincidence of the lattice beta-function and the analytical expression in the region of the phase transition is shown. New method for estimating a critical coupling value is proposed.

1 Introduction

The beta-function is one of the main objects in quantum field theory. It defines scaling properties of the theory in different regions of dynamic

*E-mail:santrop_2@yahoo.com
†E-mail:skalozubv@daad-alumni.de
‡E-mail:mogilevsky.oleg@gmail.com

variables. It is defined as

$$\beta_f(g_\mu) = \mu^2 \frac{\partial \overline{g}(\mu^2)}{\partial(\mu^2)}, \tag{1}$$

where $\beta_f(g_\mu)$ – beta-function, $g_\mu \equiv \overline{g}(\mu^2)$ – effective coupling constant, μ – normalizing momentum.

For the case of the Monte-Carlo (MC) calculations in $SU(N)$ lattice gluodynamics the beta-function has the form

$$\beta_f(g) = -a \frac{dg}{da}, \tag{2}$$

where a replaces the parameter μ^2, a - is lattice spacing. Lattice spacing is a free parameter of the theory. In particular, calculation of $\beta_f(g)$ is one of the ways to define a.

In analytical approach, the beta-function described by an expansion as power series of coupling constant. In the cases of quantum chromodynamics or $SU(N)$ lattice gluodynamics, a non-perturbative beta-function attracts the most interest.

In ref. [6] a new special method was developed. Namely, the effects connected with the final sizes of a lattice were taken into account, and scaling near the critical point of $SU(N)$ lattice gauge theories has been considered without attempt to reach a continuum limit.

The goal of the present paper is the detailed investigation and development of this approach. In $SU(2)$ gluodinamics, we calculate the beta-functions on different lattices and compare their values with those obtained in a continuum limit.

2 Analytical expression

The beta-function describes the dependence of the lattice spacing a on a coupling constant g

$$\beta_f(g) = -a \frac{dg}{da}. \tag{3}$$

Our calculations are based on the special form of the definition of the beta-function [6]. Let us consider a transformation

$$a \to a' = ba = (1 + \Delta b)a. \tag{4}$$

Under this transformation the definition (3) becomes

$$-a\frac{dg}{da} = -\lim_{b\to 1}\left(a\frac{g(ba)-g(a)}{ba-a}\right) = -\lim_{b\to 1}\frac{dg}{db} = \beta_f(g). \tag{5}$$

The singular part of the free energy density can be described by the universal finite-size scaling function [9]

$$f(t,h,N_\sigma,N_\tau) = \left(\frac{N_\sigma}{N_\tau}\right)^{-3} Q_f\left(g_t\left(\frac{N_\sigma}{N_\tau}\right)^{1/\nu}, g_h\left(\frac{N_\sigma}{N_\tau}\right)^{\frac{\beta+\gamma}{\nu}}\right), \tag{6}$$

where β, γ, ν are the critical indexes of the theory. Due to the finite size scaling hypothesis, these indexes coincide with the critical indexes of 3-d Ising model. The scaling function Q_f depends on the reduced temperature $t = \frac{T-T_c}{T_c}$ and the external field strength h through thermal and magnetic scaling fields

$$\begin{aligned} g_t &= c_t t(1+b_t t), \\ g_h &= c_h h(1+b_h t) \end{aligned} \tag{7}$$

with non-universal coefficients c_t, c_h, b_t, b_h still carrying a possible N_τ.

The existence of the scaling function Q [7], [8] allows developing a procedure to renormalize the coupling constant g^{-2} by using two different lattice sizes N_σ, N_τ and N'_σ, N'_τ (N_σ - number of lattice nods in spatial directions, N_τ - number of lattice nods in time direction). Let us fix $\frac{N'_\tau}{N_\tau} = \frac{N'_\sigma}{N_\sigma} = b$ and make a scale transformation

$$\begin{aligned} a &\to a' = ba, \\ N_\sigma &\to N'_\sigma = \frac{N_\sigma}{b}, \\ N_\tau &\to N'_\tau = \frac{N_\tau}{b}. \end{aligned} \tag{8}$$

Then the phenomenological renormalization is defined by the following equation

$$Q(g^{-2}, N_\sigma, N_\tau) = Q\left((g')^{-2}, \frac{N_\sigma}{b}, \frac{N_\tau}{b}\right). \tag{9}$$

It means that the scaling function Q remains unchanged if the lattice size is rescaled by a factor b and the inverse coupling g^{-2} is shifted to $(g')^{-2}$

simultaneously. Taking the derivative with respect to the scale parameter b of the both sides of (9) and using (5) we obtain the expression

$$a\frac{dg^{-2}}{da} = \frac{\frac{\partial Q(g^{-2},N_\sigma,N_\tau)}{\partial lnN_\sigma} + \frac{\partial Q(g^{-2},N_\sigma,N_\tau)}{\partial lnN_\tau}}{\frac{\partial Q(g^{-2},N_\sigma,N_\tau)}{\partial g^{-2}}}. \tag{10}$$

Fourth derivative of f in h taken at $h = 0$ and divided by $\chi^2(\frac{N_\sigma}{N_\tau})^3$ is called the Binder cumulant [10]

$$g_4 = \frac{\frac{\partial^4 f}{\partial h^4}}{\chi^2(\frac{N_\sigma}{N_\tau})^3}\Bigg|_{h=0}. \tag{11}$$

It identically coincides with the scale function [10]

$$g_4 = Q_{g_4}\left(g_t\left(\frac{N_\sigma}{N_\tau}\right)^{\frac{1}{\nu}}\right). \tag{12}$$

Binder cumulant g_4 is calculated through the Polyakov loops on a lattice [10]

$$g_4 = \frac{\langle P^4\rangle}{\langle P^2\rangle^2} - 3. \tag{13}$$

We get the expression for the beta-function

$$a\frac{dg^{-2}}{da} = \frac{\frac{\partial g_4}{\partial lnN_\sigma} + \frac{\partial g_4}{\partial lnN_\tau}}{\frac{\partial g_4}{\partial g^{-2}}} = \frac{1}{4}\frac{\frac{\partial g_4}{\partial lnN_\sigma} + \frac{\partial g_4}{\partial lnN_\tau}}{\frac{\partial g_4}{\partial \beta}}. \tag{14}$$

3 Lattice observables

Let us calculate beta-function using (14). As the lattice size is discrete, it is necessary to replace the derivatives in (14) by the finite differences which are calculated on lattices with the closest N_σ, N_τ (and corresponding $g_4(N_\sigma, N_\tau)$):

$$\begin{aligned}\frac{\partial g_4(\beta,N_\sigma,N_\tau)}{\partial lnN_\sigma} &\to \frac{g_4(\beta,N'_\sigma,N_\tau) - g_4(\beta,N_\sigma,N_\tau)}{ln(\beta,N'_\sigma/N_\sigma)},\\ \frac{\partial g_4(\beta,N_\sigma,N_\tau)}{\partial lnN_\tau} &\to \frac{g_4(\beta,N_\sigma,N'_\tau) - g_4(\beta,N_\sigma,N_\tau)}{ln(\beta,N'_\tau/N_\tau)}.\end{aligned} \tag{15}$$

Such replacement,

$$\frac{\partial g_4}{\partial \beta} \to \frac{\Delta g_4}{\Delta \beta}, \tag{16}$$

leads to huge computing errors. Near the phase transition area, the dispersion is increased and the substitution (16) becomes not reasonable. For different lattices investigated, the amount of data near the critical region varies from 120 up to 600 points, but the error for (16) remains large.

Table 1. Tested fitting curves

Function	*Parameters*
$A_1 + \frac{A_2 - A_1}{1+10^{(\beta_0-\beta)*p}}$	A_1, A_2, β_0, p
$\frac{A_1-A_2}{1+(\frac{\beta}{\beta_0})^p} + A_2$	A_1, A_2, β_0, p
$\frac{A_1-A_2}{1+e^{(\beta-\beta_0)/p}} + A_2$	A_1, A_2, β_0, p

Our the best fits (see Fig. 1, Tab. 2) are reached for the function

$$g_4 = A1 + (A2 - A1)/(1 + 10^{(\beta_0-\beta)*p}), \tag{17}$$

where $A1, A2, \beta_0, p$ - fitting parameters.

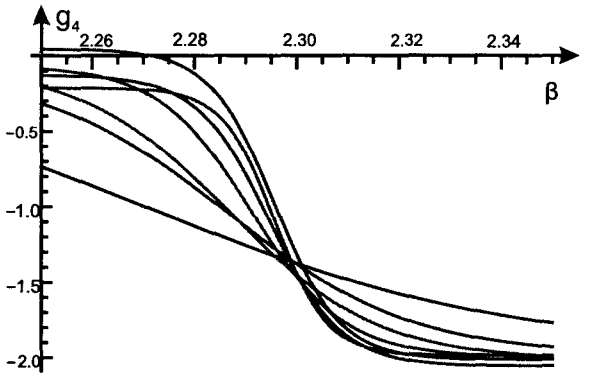

Figure 1. Binder cumulants. Cumulants are received on lattices with $N_\tau = 4$, and $N_\sigma = 8$, 12, 16, 24, 28, 32. The higher number of nods in the lattice corresponds with the sharper step. All curves intersect each other in a local area and as it comes from the theory these curves should intersect in one point (the critical point).

If one knows g_4 in an analytical form, it is possible to calculate $\frac{\partial g_4}{\partial \beta}$ straightforwardly. However, the result of g_4 calculations is a set of points. To reveal a functional dependence on this sequence, it is necessary to apply some fitting procedure. For this procedure we chose the step functions, since the critical area of g_4 is a steplike (see Tab. 1).

In Tab. 2 best fits for number of lattices are represented. We have analyzed up to 600 points for some lattices and have reached small values (down to 10^{-3}) of χ^2 function.

Table 2. Fitting of Binder cumulants by $A_1 + \frac{A_2 - A_1}{1+10^{(\beta_0-\beta)*p}}$

	Parameters						Fitting range	
Lattice	χ^2	A_1	A_2	β_0	p	**Number of points**	β_{min}	β_{max}
$N_\tau = 4, N_\sigma = 8$	0.009	−1.953	−0.0523	2.2705	−12	126	1.7	2.95
$N_\tau = 4, N_\sigma = 8$	0.012	−1.957	−0.0507	2.2747	−11	26	1.7	2.95
$N_\tau = 4, N_\sigma = 12$	0.025	−1.98	−0.1	2, 286	−24	253	1.7	2.95
$N_\tau = 4, N_\sigma = 12$	0.011	−2	−0.04	2, 289	−16	26	1.7	2.95
$N_\tau = 4, N_\sigma = 16$	0.029	−2.01	−0.066	2.287	−30.1	236	1.7	2.95
$N_\tau = 4, N_\sigma = 16$	0.013	−1.99	−0.05	2.292	−30.9	26	1.7	2.95
$N_\tau = 4, N_\sigma = 20$	0.055	−2	−0.065	2.291	−48	246	1.7	2.95
$N_\tau = 4, N_\sigma = 24$	0.1	−2.0098	0.044	2.296	−68	126	1.7	2.95
$N_\tau = 4, N_\sigma = 24$	0.006	−2.001	0.061	2.291	−27	26	1.7	2.95
$N_\tau = 4, N_\sigma = 28$	0.089	−2.05	−0.13	2.29	−62	626	1.7	2.95
$N_\tau = 4, N_\sigma = 28$	0.012	−1.99	$-8 \cdot 10^{-5}$	2.28	−21	26	1.7	2.95
$N_\tau = 4, N_\sigma = 32$	0.12	−1.984	−0.2	2.3	−84	626	1.7	2.95
$N_\tau = 4, N_\sigma = 32$	0.01	−1.988	0.014	2.27	−28	26	1.7	2.95
$N_\tau = 4, N_\sigma = 36$	0.19	−2	−0.27	2.3	−105	600	2.28	2.31
$N_\tau = 16, N_\sigma = 20$	0.094	−1.17	−0.017	2.68	−7	126	1.7	2.95
$N_\tau = 16, N_\sigma = 24$	0.054	−1.7	0.04	2.75	−6	26	1.7	2.95
$N_\tau = 16, N_\sigma = 28$	0.021	−1.6	−0.017	2.67	−17	26	1.7	2.95
$N_\tau = 16, N_\sigma = 32$	0.021	−1.7	0.03	2.69	−23	126	1.7	2.95

Now we turn to an interesting features of these fits. Parameters of the curve, which based on 600 data points, are nearly the same as parameters (especially β_0) of the curve, which based on 25 data points. The parameter

β_0 coincides (to within 2 up to 3 digits) with an inverse critical coupling constant for a corresponding lattice (see Tab. 3, ref. [9], [12]).

Table 3. Values of the inverse coupling constant

N_τ	2	4	6	8
β_c	1.875	2.301	2.422	2.508

It is common to use linear fits for finding of critical point on the lattice. Because of the dispersion in critical region these fits need a lot of data to be performed. Using both listed above properties one can estimate the inverse critical coupling using just few points. For more precise calculations one can use function (17) with data, which are from above and below critical region. Dispersion for these data is much less than for data, which are near critical area, so one need much less statistics than usually.

The expression for the beta-function in lattice variables reads:

$$\beta_f(\beta) = \frac{1}{\beta^{3/2}} \cdot \frac{\frac{g_4(\beta,N'_\sigma,N_\tau)-g_4(\beta,N_\sigma,N_\tau)}{ln(N'_\sigma/N_\sigma)} + \frac{g_4(\beta,N_\sigma,N'_\tau)-g_4(\beta,N_\sigma,N_\tau)}{ln(N'_\tau/N_\tau)}}{\frac{\partial g_4(\beta,N_\sigma,N_\tau)}{\partial\beta}}. \qquad (18)$$

It will be used below.

4 Calculation of the beta-function

We chose the heat-bath as working algorithm in MC procedure. We use standard form of Wilson action of the $SU(2)$ lattice gauge theory. In the MC simulations, we use the hypercubic lattice $L_t \times L_s^3$ with hypertorus geometry.

We use the General Purpose computation on Graphics Processing Units (GPGPU) technology allowing studying large lattices on personal computers. Performance analysis indicates that the GPU-based MC simulation program shows better speed-up factors for big lattices in comparing with the CPU-based one. For the majority lattice geometries the GPU vs. CPU (single-thread CPU execution) speed-up factor is above 50 and for some lattice sizes could overcome the factor 100.

The plots of dependencies of the beta-function on the inverse coupling constant are shown below.

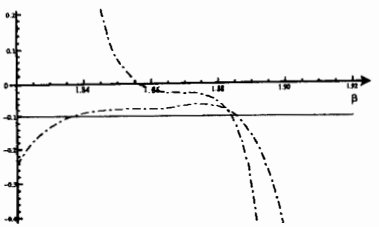

Figure 2. The solid line represents the beta-function in asymptotic expansion. Dashed lines with a point - the beta-functions (18), $N_\tau = 2$, $N_\sigma = 8, 16, 20$, $\Delta N_\tau = N'_\tau - N_\tau = 2$, $\Delta N_\sigma = N'_\sigma - N_\sigma = 4$.

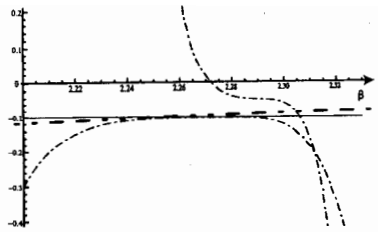

Figure 3. Same as above. Dashed lines with a point - the beta-functions (18), $N_\tau = 4$, $N_\sigma = 12, 20$, $\Delta N_\tau = N'_\tau - N_\tau = 2$, $\Delta N_\sigma = N'_\sigma - N_\sigma = 4$. The Dashed line with two points - the beta-function is received in ref. [1].

Standard deviation of the function (18) is smallest near critical point. It comes from analysis of Binder cumulants. Cumulants decrease linearly in the critical area and change little above and belove that area. Therefore $\frac{\partial g_4(\beta,N_\sigma,N_\tau)}{\partial\beta}$ in the bottom of (18) comes to 0 and leads (18) to infinity. Beta-function values which are calculated near critical point are in good agreement with known results [1].

5 Conclusions

We have performed high-statistics calculations of the beta-function in $SU(2)$ lattice gluodynamics. These calculations became possible due to technology of GPU calculations.

The key point for our investigations is definition (5) [6]. It gives a possibility to analyze a finite size of the lattice.

We have constructed and analyzed the lattice beta-functions for a wide range of different lattices.

Values of all beta-functions in critical region are the same for different functions. In particular, the values of the beta-functions (18) in critical region are almost the same as the values obtained in ref. [1]. The fast method of determination of the inverse critical constant on a lattice based on the formula (17) is proposed.

References

[1] J. Engels, F. Karsch and K. Redlich, Nucl. Phys. B **435**, 295 (1995) [hep-lat/9408009].

[2] R. Sommer, Nucl. Phys. B **411**, 839 (1994) [hep-lat/9310022].

[3] Y. Aoki, Z. Fodor, S. D. Katz and K. K. Szabo, Phys. Lett. B **643**, 46 (2006) [hep-lat/0609068].

[4] Y. Aoki, S. Borsanyi, S. Durr, Z. Fodor, S. D. Katz, S. Krieg and K. K. Szabo, JHEP **0906**, 088 (2009) [arXiv:0903.4155 [hep-lat]].

[5] J. B. Kogut, Rev. Mod. Phys. **55**, 775 (1983).

[6] O. Mogilevsky, Ukr.J.Phys. Vol.51 8, 820-823 (2006).

[7] M. N. Barber, Phase Transitions and Critical Phenomena Vol. 8, ed. C. Domb and J. Lebowitz, Academic Press (1981).

[8] V. Privman, Finite-Size Scaling and Numerical Simulations of Statistical Systems, World Scientific Publishing Co. (1990).

[9] J. Fingberg, U. M. Heller and F. Karsch, Nucl. Phys. B **392**, 493 (1993) [hep-lat/9208012].

[10] K. Binder, Phys. Rev. Lett. **47**, 693 (1981).

[11] V. Demchik and A. Strelchenko, arXiv:0903.3053 [hep-lat].

[12] A. Velytsky, Int. J. Mod. Phys. C **19**, 1079 (2008) [arXiv:0711.0748 [hep-lat]].

[13] K. Binder, Z. Phys. B **43**, 119 (1981).

[14] K. Binder and E. Luijten, Phys. Rept. **344**, 179 (2001).

Научное издание

Actual Problems of Microworld Physics

Proceedings of XII International School-Seminar

V. 1

Актуальные проблемы физики микромира

Труды XII международной школы-семинара

Т. 1

E1,2-2015-42

Сборник отпечатан методом прямого репродуцирования
с оригиналов, предоставленных оргкомитетом.

Подписано в печать 11.06.2015.
Формат 60 × 90/16. Бумага офсетная. Печать офсетная.
Усл. печ. л. 14,13. Уч.-изд. л. 15,46. Тираж 170 экз. Заказ № 58547.

Издательский отдел Объединенного института ядерных исследований
141980, г. Дубна, Московская обл., ул. Жолио-Кюри, 6.
E-mail: publish@jinr.ru
www.jinr.ru/publish/